UNIVERSITÀ DEGLI STUDI DI SASSARI

DIPARTIMENTO DI CHIMICA E FARMACIA

DOTTORATO DI RICERCA IN

SCIENZE E TECNOLOGIE CHIMICHE

INDIRIZZO IN SCIENZE CHIMICHE

XXVI CICLO

SYNTHESIS AND CHARACTERIZATION OF NEW POLYMERIC MATERIALS FOR ADVANCED APPLICATIONS

DR.SSA ROBERTA SANNA

TUTOR: PROF. ALBERTO MARIANI

COORDINATORE: PROF. STEFANO ENZO

A.A. 2012/2013

INDEX

ABBREVIATIONS

AAc	acrylic acid
AAm	acrylamide
AFM	atomic force microscopy
AIBN	2, 2'- azobisisobutyronitrile
AmPS	ammonium persulfate
AMPSA	2-acrylamido-2-methylpropanesulfonic acid
APS	aliquat persulfate
BD	1,4-butanediol
BET	Brunauer–Emmett–Teller
BIS	*N,N*-methylene *bis*-acrylamide
Bis-GMA	bisphenol A glycerolate dimethacrylate
BNC	bacterial nanocellulose
BPO	benzoyl peroxide
CMC	carboxymethyl cellulose
CNC	cellulose nanocrystals
CVD	chemical vapor deposition
DBTDAc	dibutyltin diacetate
DCP	dielectrophoretic
DCPD	dicyclopentadiene
DFT	density functional theory
DMF	dimethylformamide
DMSO	dimethylsulfoxide
DMTA	dynamic mechanical thermal analysis
DP	degree of polymerization
DSC	differential scanning calorimetry
DSSC	dye sensitized solar cells

DXRL	deep X-ray lithography beam line
EG	exfoliated graphite
EtOH	ethanol
FE-SEM	field-effect scanning electron microscopy
FET	field effect transistors
FP	frontal polymerization
FT-IR	Fourier transform infrared
G’	storage modulus
G’’	loss modulus
GFET	graphene field effect transistors
GIC	graphite intercalation compound
GNR	graphene nanoribbon
GO	graphite oxide
GPL	graphene platelet
HDI	1,6-hexane diisocyanate
HEA	2-hydroxyethyl acrylate
HEMA	2-hydroxyethylmethacrylate
HOPG	highly ordered pyrolytic graphite
IPDI	isophorone diisocyanate
IPN	interpenetrating polymer network
ITO	indium tin oxide
LCST	lower critical solution temperature
LDPE	low density polyethylene
LEED	low-energy electron diffraction
LODP	degree of polymerization level-off
MAP	magnetophoretic
MFC	microfibrillated cellulose

MWCNT	multi-walled carbon nanotube
NIPAAm	*N*-isopropylacrylamide
NMP	*N*-methylpyrrolidone
NVCL	*N*-vinylcaprolactam
NVP	1-vinyl-2-pyrrolidone
OLED	organic light-emitting diode
PAAc	poly (acrylic acid)
PAAm	poly(acrylamide)
PAMPSA	poly(2-acrylamido-2-methylpropanesulfonic acid)
PANI	polyaniline
PBT	Bis-GMA/TEGDA copolymer
PC	polycarbonate
PCC	pyrocatechol
PCL	polycaprolactone
PDEAEMA	poly(*N,N*-diethylaminoethylmethacrylate)
PDMAEMA	poly(*N,N*-dimethylaminoethylmethacrylate)
PE	polyethylene
PECDV	plasma enhanced chemical vapor deposition
PEG	poly(ethyleneglycol)
PEO	poly(ethylene oxide)
PHEA	poly(2-hydroxyethyl acrylate)
PHEMA	poly(hydroxyethylmethacrylate)
PLA	polylactic acid
PMAAc	poly(methacrylic acid)
PMMA	poly(methylmethacrylate)
PMVE	poly(methylvinylether)
PNIPAAm	poly(*N*-isopropylacrylamide)

PNVCL	poly(*N*-vinylcaprolactam)
poly(S-co-BuA)	poly(styrene-co-butylacrylate)
PP	polypropylene
PPO	poly(propylene oxide)
PS	polystyrene
PTEGDA	poly(tetraethyleneglycol diacrylate)
PTFE	poly(tetrafluoroethylene)
PU	polyurethanes
PVA	poly(vinyl alchol)
PVC	poly(vinyl chloride)
PVDF	poly(vinylidene fluoride)
PVP	poly(vinylpyrrolidone)
QED	quantum electrodynamic
QHE	quantum hall effect
r-GO	reduced graphene oxide
RWC	relative weight change
SAXS	small Angle X-ray scattering
SEM	scanning electron microscopy
SHS	self-propagating high temperature synthesis
SP	spontaneous polymerization
SR%	swelling ratio
SWCNT	single-walled carbon nanotube
TC	transparent conductor
TEGDA	tetraethylenglycoldiacrylate
TEGDMA	triethyleneglycol dimethacrylate
TEM	transmission electron microscopy
TEMPO	2,2,6,6-tetramethylpiperidine-1-oxyl

TETDPPS	trihexyltetradecylphosphonium persulfate
TEtOSi	tetraethoxy silane
T_g	glass transition temperature
TGA	thermogravimetric analysis
THF	tetrahydrofuran
T_m	melting temperature
T_{max}	maximum temperature
3-TMeOSi	3-(trimethoxysilyl)propyl methacrylate
TPU	thermoplastic polyurethane
TRG	thermally reduced graphene
UCST	upper critical solution temperature
UDP	uridine diphosphate
V_f	front velocity
$V_{interface}$	volume of the interfacial material
$V_{particle}$	volume of the particle
WCA	water contact angle
WPU	waterborne polyurethane
XPS	X-ray photoelectron spectroscopy
XRD	X-rays diffraction

INTRODUCTION

The main aim of this thesis was to synthesize and characterize new kinds of polymeric nanocomposite materials, including *stimuli responsive* hydrogels, polyacrylates and polyurethanes. In particular, the work was divided in two main threads: the first was about the development of new *stimuli responsive* systems (pH-, temperature- and electrical field- responsive hydrogels) and the improving of their properties through the introduction of different nanofillers, such as graphene or nanocellulose. The second one was focused on the development of a simple and efficient method for the production of graphene in high concentration, and the synthesis and characterization of different polymer nanocomposites containing such nanofiller. Finally, this last method was used for the obtainment of mesoporous films made of nanocrystalline TiO_2 doped with exfoliated graphene sheets, which can found application in photocatalytic field.

Polymer hydrogels are highly crosslinked materials having a tridimensional and flexible structure, able to swell when they are immersed in aqueous solutions. Indeed, chemical or physical crosslinking avoids their solubilization, since water can penetrate through the network without breaking the strong interactions that bind the polymer chains together. Some hydrogels can also change their own volume in response to external *stimuli* such as solvents, temperature, pH, ionic force, electric field, light irradiation, and salt concentration. Because of these peculiar features, most hydrogels are developed for uses in pharmaceutical and biological fields, such as for contact lenses, reconstruction of cartilages, artificial tendons and organs, drug delivery systems. A detailed state of art on hydrogels is presented in Chapter I of this thesis.

In this work, pH-responsive hydrogels of poly(acrylic acid-co-2-hydroxyethyl acrylate) were prepared by using the frontal polymerization (FP) as synthetic technique. Their swelling behavior as a function of the external stimulus, and the thermal and morphological properties were also investigated (see paragraph VII.1). Moreover, new polyacrylamide-based hydrogels containing 3-(trimethoxysilyl)propyl methacrylate and/or tetraethoxy silane as sol-gel reactants were synthesized. These materials are both organic-inorganic interpenetrating polymer networks (IPNs) and hybrid polymers at the same time. The term hybrid hydrogel is referred to systems that possess organic and inorganic moieties covalently interconnected. IPNs are a class of polymer blends that can be defined as a combination of two (or more) polymers in a network form, in which one is synthesized or cross-linked in the presence of the other(s) (see paragraph VII.2).

One of the most critical drawbacks in the use of polymer hydrogels is related to their poor mechanical properties. The weak and brittle nature of such systems is due to the random nature of the crosslinking reactions produced by a large number of organic crosslinkers, which strongly limits their use in applications requiring significant stress or strain applied. For such a reason, different nanofillers (i.e. silicates, ceramics,

metals, magnetic particles) have been introduced into the hydrogel matrices thus obtaining the corresponding nanocomposites. In Chapter IV, a description of nanocomposite polymer materials is reported.

Taking into account the above considerations, we studied how the introduction of graphene or cellulose nanocrystals (CNC) into the polymer matrix could improve the mechanical properties of two different systems: the poly(2-acrylamido-2-methyl-1-propanesulfonic acid), which is able to change its volume as a function of both electric field and ionic force, and the poly(*N*-vinylcaprolactam), PNVCL, known as a valid alternative to poly(*N*-isopropylacrylamide) (PNIPAAm), the most studied thermoresponsive hydrogel. In fact, PNVCL is a very interesting material because of its stability against hydrolysis, which makes it more biocompatible than PNIPAAm, whose degradation products are toxic. Moreover, it is characterized by a lower critical solution temperature at 34 °C, which is even closer to the physiological one than that of PNIPAAm itself. For both systems, the influence of the nanofillers on the swelling behavior, on the thermal and morphological properties was also investigated.

In this study, the nanofillers chosen for the synthesis of the nanocomposite hydrogels were CNC and graphene.

CNC are the main building blocks of wood cellulose and are constituted of rodlike cellulose crystals, having a width of 5-70 nm and a length included between 100 nm and several micrometers. In recent years, thanks to an increasing interesting toward environmental issues, the use of these natural fibers as fillers in polymer nanocomposites has gained much attention. In fact, nanocellulose represents an appropriate filler for hydrogels because of its good mechanical properties, biodegradability and biocompatibility, and renewability. Properties, applications and methods for CNC production are widely described in Chapter III.

Graphene is a planar monolayer of sp^2-hybridized carbon atoms arranged into a two-dimensional honeycomb lattice, with a carbon-carbon bond length of 0.142 nm. When compared with the other allotropic forms of carbon, this material exhibits peculiar characteristics that are object of study and development in all the most advanced technological fields. For this reason, over the past decade, the interest of the scientific community toward this innovative material has increased exponentially. Indeed, graphene is characterized by high electron mobility at room temperature, extraordinary thermal and electric conductivity and outstanding mechanical properties. All these features make graphene one of the best candidates for numerous applications for functional devices such as energy storage systems, photovoltaics, field-effect transistors, gas sensor, transparent conducting electrodes and polymer nanocomposites. In particular, the production of polymer nanocomposites containing graphene has gained a lot of attention during the latest years. Most of the synthetic techniques developed until now are particularly complicated and the obtained graphene is characterized by the presence of defects, such as heteroatoms and/or epoxy residues, which not preserve its aromatic structure, thus leading to a reduction

of graphene properties. In this work, a very simple and cheap method for graphene production in high concentration has been developed. Defect-free graphene was produced by sonication of graphite in different liquid media, and, for the first time, directly in a monomer, thus further simplifying the route for the synthesis of nanocomposites. A detailed description of properties, applications and synthetic methods for graphene production is presented in Chapter II.

In the second part of this thesis, the method described above was also used for dispersing graphene in some reactive media such as organosilanes (see paragraph VII.6), diacrylates (see paragraph VII.7 and VII.8), diisocyanates or diols (see paragraph VII.9). In particular, the last three systems were directly employed for the preparation of the corresponding polymer nanocomposites, whose thermal, mechanical and morphological features were fully investigated as a function of graphene content. In fact, graphene was usually introduced into the polymer matrices to further improve their properties: these are strongly affected by the distribution of graphene layers in the polymer matrix as well as by interfacial bonding between graphene layers and polymer matrix. In Chapter IV, a detailed description of nanocomposite polymer materials and graphene containing nanocomposites is reported.

A further purpose of this thesis was to apply the method developed for graphene production to the obtainment of highly ordered mesoporous films made by nanocrystalline TiO_2 doped with such nanofiller, which find application in photocatalytic field (see paragraph VII.10). In fact, carbon-based nanostructures, such as nanotubes and graphene sheets, have recently shown to strongly improve the functional properties of hybrid organic-inorganic nanocomposites due to their extraordinary electron mobility.

Most of the systems studied during this thesis were prepared by using FP as the synthetic technique. This technique exploits the heat released during the polymerization reaction for promoting the formation of a hot front that can sustain itself and propagate throughout the reactor, thus converting monomer into polymer. If compared with the traditional polymerization methods, FP generally exhibits many advantages that make it a “green” technique for macromolecular synthesis. Indeed, it is characterized by shorter reaction times and lower energy consumption. Moreover, the protocols used are very simple and easily applicable even without special apparatuses and generally without involving the use of solvents. A detailed description of FP is reported in Chapter V.

In Chapter VI, the experimental procedures used for the preparation of all the samples are described, while in Chapter VII the obtained results are widely discussed. In the final part, the general conclusions of this PhD thesis are reported.

CHAPTER I

THE HYDROGELS

Hydrogels are highly crosslinked polymeric materials having a tridimensional and flexible structure, able to absorb and retain aqueous solutions within their network, without dissolving. Polymer hydrogels are crosslinked to form a network via chemical or physical interactions. In particular, chemically crosslinked hydrogels are prepared either through water-soluble polymer crosslinking or by converting hydrophobic into hydrophilic polymers, which in turn are then crosslinked to form a network.[1-3] This structure allows hydrogels swelling or deswelling by retaining or expelling a large quantity of water in the network without dissolving. Chemical hydrogels are also non homogeneous and usually contain regions of low water swelling and high crosslinking density, called “clusters”, that are dispersed within regions of high swelling, and low crosslinking density. This may be due to hydrophobic aggregation of multi-functional agents, leading to high crosslinking density clusters.[4]

Conversely, physical crosslinking is due to non-covalent interactions and often is the result of hydrogen bonding, hydrophobic or ionic interactions.[5-9] Physical hydrogels are not homogeneous, since clusters of molecular entanglements, or hydrophobically- or ionically-associated domains can create inhomogeneities.

Hydrogels can be classified in several categories:

- Homopolymer, copolymer, multi-polymer and interpenetrating network (IPN) hydrogels, based on the method of preparation;
- Neutral, anionic, cationic or ampholytic hydrogels, based on the charges on the backbone polymers;
- Amorphous or semi-crystalline hydrogels, based on their physical features;
- Complexation hydrogels, which are held together by different types of secondary forces, such as hydrogen bonding, hydrophobic group associations, and affinity “complexes” (e.g., hetero-dimers (peptide/peptide interactions called “coil–coil”); biotin/streptavidin; cyclodextrin inclusion complexes). Their properties are strongly dependent on the network density of these interactions.[10-12]

Moreover hydrogels can also be divided in stable and degradable, with the latter categorized as hydrolytically or enzymatically degraded.

Synthesis of hydrogels

As indicating previously, chemically crosslinked hydrogels are usually prepared by bringing small multi-functional molecules, such as monomers and oligomers, and reacting them to form a network structure.

This type of crosslinking may be achieved by reaction of two chemical groups on two different molecules, which can be initiated by initiators that are sensitive to temperature, light or other radiation.

There are different methods to form chemically crosslinked hydrogels, even if most of them are based on free radical reactions.

The first method involves copolymerization/crosslinking reaction between one or more monomers, or more monomers and one multi-functional monomer. A similar method allows the crosslinking reaction between two water soluble polymers, through the formation of free radicals on both polymeric chains, which combine to form covalent bonds, and thus a crosslinked structure. The polymerization reactions can be activated by a chemical initiator (peroxide and azo- compounds), or by using UV light or ionizing radiation (electron beams, γ-rays, X-rays),[13-15] and can be carried out in bulk, in solution, or in suspension (Figure I.1.).

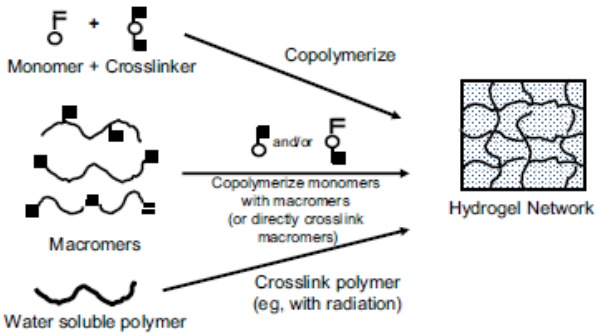

Figure I.1. Synthesis of hydrogels by free radical polymerization and crosslinking reactions.

The second method is based on the reaction of linear or branched polymer with a di-functional or multi-functional, small molecular weight crosslinking agent. This agent usually links two larger molecular weight chains through its di- or multi-functional groups. In a related method, it can be obtain a crosslinked hydrogel by reaction of a bi-functional crosslinking agent and polymeric chains, having reactive groups such as –OH, $–NH_2$, NCO, or –COOH on their backbone, which are crosslinked by the bi-functional molecule (Figure I.2.).

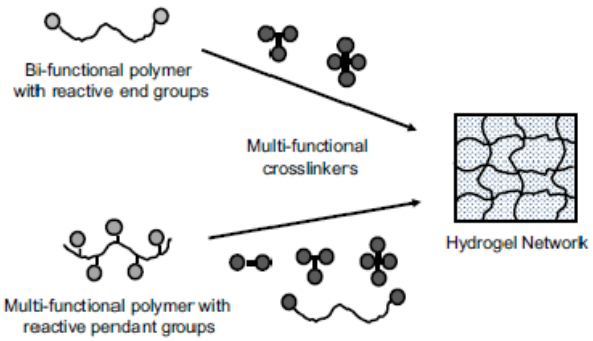

Figure I.2. Synthesis of hydrogels by crosslinking reactive polymers with multi-functional crosslinkers**.**

Furthermore, covalently crosslinked hydrogels can be obtain by polymerizing one monomer into a different crosslinked hydrogel network. The monomer polymerizes to form a polymer or a second crosslinked network, which is intermeshed with the first network. These types of compounds are named IPNs.

On the other hand, physical hydrogels are obtained when the networks are held together by molecular entanglements, and/or secondary forces including ionic, H-bonding or hydrophobic forces. They are prepared by heating or cooling a polymer solution (e.g., poly(ethylene oxide)-poly(propylene oxide)-poly(ethylene oxide)[PEO-PPO-PEO] block copolymers in H_2O),[12] or by decreasing the pH of the mixture to form an H-bonded gel between two different polymers in the same aqueous solution (e.g., PEO and poly(acrylic acid), PAAc,) (Figure I.3.).[12]

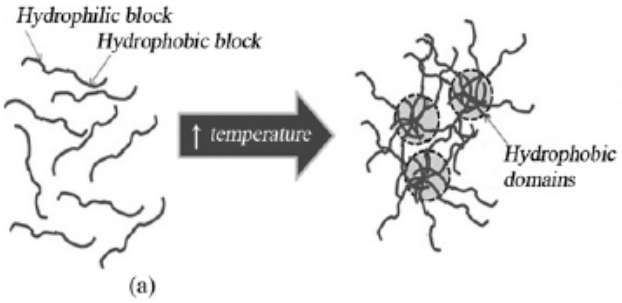

Figura I.3. Hydrophobic interactions drive in situ physical gelation.

An alternative method to synthesize physically crosslinked hydrogels involves the combination of a polyelectrolyte solution with a multivalent ion of opposite charge, obtaining the so called “ionotropic hydrogel” (e.g., calcium alginate).[12] Moreover, if polyelectrolytes of opposite charge are mixed, they may gel or precipitate, forming ion-crosslinked systems, known as complex coacervates, polyion complexes, or polyelectrolyte complexes (e.g., sodium alginate plus polylysine; Figure I.4.).[16]

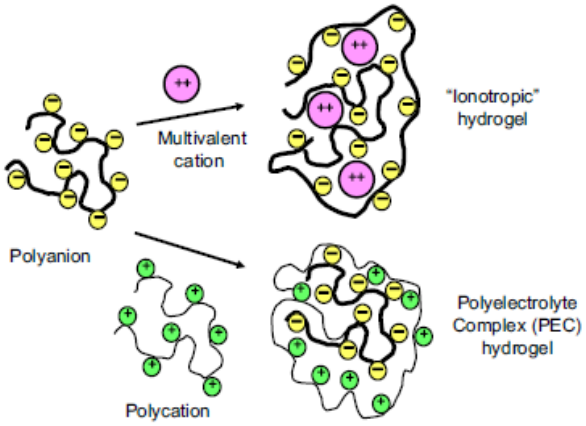

Figure I.4. Formation of ionic hydrogels.

Swelling theory

The swelling behavior in aqueous solutions is an important parameter in designing polymer hydrogels. In fact one of their main applications is in controlled drug delivery systems.

When a hydrogel is immersed in solution, the hydrophilic polymeric chains, which constituted the network, create an osmotic pressure within the hydrogel, leading to the swelling of the matrix.[17]

The swelling process takes place in three different steps: (a) diffusion of water molecules through the matrix, (b) relaxation of polymer chains via hydration, and (c) expansion of polymer network upon relaxation.[18,19]

Hydrogels absorb water to a maximum degree possible, the so-called equilibrium water content. This degree is defined as the balance between osmotic pressure and the elastic retractive forces of the polymer chains in the three-dimensional network. The stretching of polymer chains increases elastic retractive forces as a counteraction for the network expansion. When these forces are balanced, the network expansion stops and comes to equilibrium. When either the osmotic pressure changes, e.g. due to protonation of amino groups in the network due to a shift in pH, or the crosslinking density changes, this balance is broken and the hydrogel exhibits a change in the degree of swelling. The most widely used theory to explain the swelling in neutral hydrogels is the equilibrium swelling theory of Flory and Rehner.[20,21] This theory is an ideal thermodynamic description of polymer solutions, and does not consider network imperfections or the real, finite volumes of network chains and crosslinks, and in the case of aqueous solutions does not consider the presence of “bound” (versus “free”) water around the network chains. It can be used to calculate thermodynamic quantities related to that mixing process.

In 1953 Flory developed the initial theory of the swelling of crosslinked polymer gels using a Gaussian distribution of the polymer chains. His model, describing the equilibrium degree of crosslinked polymers, postulated that the degree to which a polymer network swelled was governed by the elastic retractive forces of the polymer chains and the thermodynamic compatibility between polymer and solvent molecules.[23] Accordingly, the total free energy change of a neutral hydrogel (ΔG) upon swelling can be expressed as:

$$\Delta G = \Delta G_{el} + \Delta G_{mix} \qquad (1)$$

where ΔG_{el} represents the contribution of elastic refractive forces, and ΔG_{mix} is the thermodynamic compatibility of polymer and solvent.

This equation can be rewritten in terms of chemical potentials. At the equilibrium conditions, the total chemical potential (μ) has to be equal to zero:

$$\mu = \mu_{el} + \mu_{mix} = 0 \qquad (2)$$

At equilibrium, the chemical potentials of water inside and outside of the hydrogel must be equal. Therefore, the elastic and mixing contributions to the chemical potential will balance each other at equilibrium. The change in chemical potential due to elastic forces can be expressed by using the theory of rubber elasticity,[23] while the contribution of mixing to chemical potential change is determined using the heat and the entropy of mixing.[24]

If these two contributions are equalized, the molecular weight between two crosslinks ($\overline{M_c}$) in absence of a solvent can be expressed as:

$$\frac{1}{\overline{M_C}} = \frac{2}{\overline{M_N}} = \frac{\left(\frac{\bar{v}}{V_1}\right)[\ln(1-v_{2,s}) + v_{2,s} + \chi_1 v^2_{2,s}]}{v^{1/3}_{2,s} - (v_{2,s}/2)} \quad (3)$$

where $\overline{M_N}$ is the average molecular weight of the polymer chains prepared in absence of a crosslinker, $\bar{v}$ and V_1 are the specific and the molar volume of water, respectively, $v_{2,s}$ is the polymer volume fraction in the fully swollen state, and χ_1 is a parameter related to polymer–solvent interaction.

However, the presence of water changes the chemical potential, so that a new term is required for the volume fraction density of the polymer chains. Thus, the above original Flory–Rehner model can be rewritten by incorporating a term, $v_{2,r}$, that describes the polymer fraction in the relaxed state according to the theory of Peppas and Merril.[26]

$$\frac{1}{\overline{M_C}} = \frac{2}{\overline{M_N}} = \frac{\left(\frac{\bar{v}}{V_1}\right)[\ln(1-v_{2,s}) + v_{2,s} + \chi_1 v^2_{2,s}]}{v_{2,r}[v^{1/3}_{2,s} - (v_{2,s}/2v_{2,r})]} \quad (4)$$

If the polymeric backbone contains ionic groups, the swelling equilibrium of the network becomes more complicated, and new terms, related to ionic force and dissociation constant K_a and K_b, have to be added in the previous equation.

The swelling behavior is influenced by different physical and chemical parameters, and structural factors.[27-30] One of them is the crosslinking degree, that is the ratio between the moles of crosslinking agent and the repetitive units of polymer. The higher the crosslinking density is, the lower swelling is. Highly crosslinked hydrogels exhibit a smaller mesh size and swell less in comparison to loosely crosslinked ones. As a matter of fact, crosslinking hinders chains mobility, decreasing the extent of the swelling. Another parameter that modulates the swelling behavior of hydrogels is the nature of the polymers: hydrogels containing hydrophilic functional groups, which are able to establish hydrogen bonds with water molecules, swell more than those containing hydrophobic groups, which tend to minimize the interactions with the solvent.

As well as swelling behavior, swelling kinetic represents an important parameter in hydrogel characterization, especially for those designed for biomedical applications. Swelling kinetic is affected by

the mechanism of solvent penetration into the matrix, and can be either diffusion-controlled or relaxation-controlled.[31,32] In the first case diffusion of water molecules through hydrogel matrix occurs much faster than the relaxation of the polymer chains, and the swelling is controlled by a concentration gradient. However, in the second case the swelling is controlled by the rate of polymer relaxation.

Applications of hydrogels

In the past decade hydrogels have been a topic of intensive research, especially in biomedical and pharmaceutical field. In fact, because of their optimal features (e.g. soft and rubbery consistency, large water content, low interfacial tension with water or biological fluids), these polymers exhibit physical properties closely to those of living tissues, if compared with the other synthetic materials. In particular, the hydrophilic and mostly inert nature of hydrogels, often leads to minimized non specific interactions with proteins and cells, making them ideal candidates for numerous bio-related applications. In particular they are used in soft contact lenses, because of their relatively good mechanical stability and favorable refractive index,[33,34] blood-contacting biomaterials,[35,36] artificial tendons and tissues, reconstruction of cartilage,[37] in controlled drug delivery systems[38-40] and in biosensors.[41]

The most widely used hydrogel, which is able to swell in water, is crosslinked poly(hydroxyethylmethacrylate), PHEMA. Introduced by Wichterle and Lim in 1960, PHEMA represents the first example of synthetic polymer hydrogel.[42]

This hydrogel is characterized by inertia to normal biological processes and resistance to degradation, it is permeable to metabolites, is not absorbed by the body, is biocompatible, withstands heat sterilization without damage, and can be prepared in a variety of shapes and forms.

Other hydrogels of biomedical interest include polyacrylamides and their derivatives,[43,44] poly(vinyl alcohol) (PVA),[45] poly(ethyleneglycol) (PEG) and PEO.[46]

Because of the large number of functional groups available in a very small molecular volume, dendrimers and stars polymer have achieved more interest as new exciting material for polymer hydrogels.[47] Griffith and Lopina prepared hydrogels of controlled structure and large biological functionality by irradiation of PEO star polymers.[48] Such structures could have particularly promising drug delivery applications when combined with emerging new technologies such as molecular imprinting.

I. 1 *STIMULI* RESPONSIVE HYDROGELS

In the latest years a particular class of polymer hydrogels has gained more interest in the scientific community: the so called *smart*, *stimuli responsive* or *environment sensitive* hydrogels, which are polymers that undergo relatively large and sharp volume change in response to environmental changes (Figure I.5.).

These polymers recognize a *stimulus* as a signal, value its magnitude, and then change their chain conformation in direct response.[49]

The volume phase transitions, which take place in *stimuli* responsive hydrogels, can be classified according to the nature of intermolecular forces that determine them. Four different types of interactions can be identified:

- Van der Waals interaction, which causes a phase transition in hydrophilic gels in mixed solvents, such as a polyacrylamide gel in an acetone–water mixture. The non-polar solvent is needed to decrease the dielectric constant of the solvent.
- Attractive ionic interaction: it is responsible for the pH-driven phase transition, such as in poly(acrylamide-sodium acrylate)/poly(methacrylamidopropyltrimethyl ammonium chloride) gels.
- Hydrophobic interaction: hydrophobic gels, such as N-isopropylacrylamide (NIPAAm) gels, undergo a phase transition in pure water, from a swollen state at low temperature to a collapsed state at high temperature.
- Hydrogen bonding with change in ionic interactions: gels with cooperative hydrogen bonding, such as an IPN–of PAAc and poly(acrylamide) (PAAm), undergo a phase transition in pure water (the swollen state at high temperatures). The repulsive ionic interaction determines the transition temperature and the volume change at the transition.

Stimuli can be classified as either chemical or physical: the first, such as pH, ionic factors, and chemical agents, change the interactions between polymer chains or between polymer chains and solvents at the molecular level; physical *stimuli*, such as temperature, pressure, electric or magnetic fields, and mechanical stress, affect the level of various energy sources.

Moreover, some systems have been developed to combine two or more *stimuli*-responsive mechanisms into one polymer system. For instance, temperature-sensitive polymers may also respond to pH changes.[50-52] Recently, dual or ternary *stimuli* responsive polymer hydrogel microspheres were prepared and applied in various fields, especially in controlled release drug delivery systems.[53-56]

Because of these peculiar features, *stimuli* responsive hydrogels have found a lot of applications in biomedical and pharmaceutical fields, where they are used for reconstruction of cartilages,[57,58] artificial tendons and organs,[59,61] soft contact lens,[62] and self-regulated, pulsatile or oscillating drug delivery systems.[63-67] Furthermore, they have also found application in medicine for making chemical valves,[68] immobilization of enzymes and cells,[69-72] concentrating dilute solutions in bioseparation,[73,74] and in bulk engineering for microfluidic devices,[75] motors/actuators,[76] and sensors.[77,78]

Subsequently, the main types of *stimuli* responsive hydrogels, temperature-, pH-, electric and magnetic sensitive hydrogels will be described.

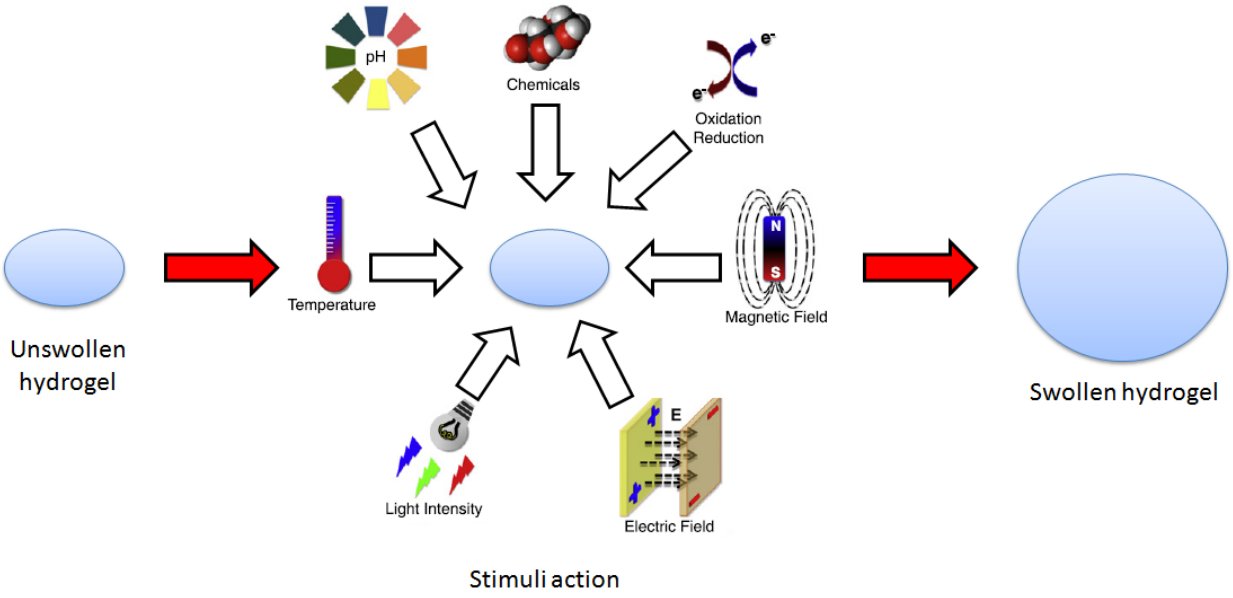

Figure I.5. Stimuli responsive hydrogels.

I. 1. 1 THERMO-RESPONSIVE HYDROGELS

Temperature responsive polymers are the most studied class of *stimuli* sensitive polymer systems, especially in drug delivery research. The change in temperature is relatively easy to control and also applicable both in vitro and in vivo.

More specifically, temperature responsive hydrogels are materials that show a volume change at a certain temperature, at which a sharp alteration in the solvation state occurs: a small temperature variation across the critical solution temperature (CST) results in contraction or expansion of the polymer chain structure, as a consequence of the optimization of the hydrophobic and hydrophilic interactions between polymer chains and aqueous solution.

Thermodynamics can explain this with a balance between entropic effects, due to the dissolution process itself and due to the ordered state of water molecules near the polymer. Enthalpic effects are due to the balance between intra- and intermolecular forces and due to solvation, e.g. hydrogen bonding and hydrophobic interaction. The transition is then accompanied by coil-to-globule transition (Figure I.6.).

The CST, at which the volume phase transition occurs, is therefore an important parameter for describing thermoresponsive polymer systems. Polymer hydrogels that are deswollen below a given temperature exhibit an upper critical solution temperature (UCST) while a lower critical solution temperature (LCST) characterizes those that are swollen below a given temperature.

Polymer hydrogels having a LCST, show a swelling behavior know as inverse, or negative temperature dependence. They are made of polymer chains having either relatively hydrophobic groups or containing a

mixture of hydrophilic and hydrophobic segments. At low temperature, hydrogen bonding between hydrophilic segments of the polymer chains and water molecules are prevalent, leading to enhanced swelling or dissolution in water. As temperature increase, however, hydrophobic interactions among hydrophobic segments become stronger, while hydrogen bonding becomes weaker. The net result is the contraction of the hydrogels. In general, increasing hydrophobic units along the polymer chains, LCST becomes lower.[79]

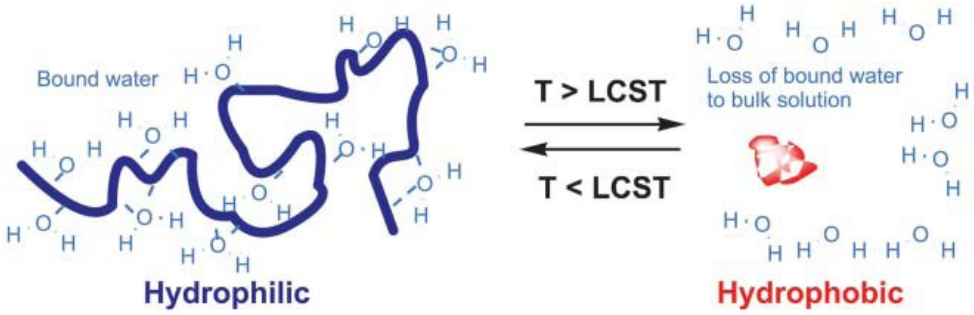

Figure I.6. Coil-to-globule transition for a thermoresponsive hydrogel.

The LCST can be changed by balancing between hydrophilic and hydrophobic segments of the polymer chain. For instance, it can be varied LCST of a polymer making copolymers of hydrophobic (e.g. NIPAAm) and hydrophilic (e.g. acrylic acid, AAc) monomers. The LCST of the PNIPAAm can be also changed by incorporating ionic groups into the gel network[80,81] or by changing solvent composition.[82]

Another parameter that influenced the thermoresponsive behavior and volume phase transition of hydrogel is the presence of additives in solution, such as salts, co-solvents and surfactants. They, in fact, can alter the solvent quality and therefore modify the interactions between polymer and solvent.

Some particular hydrogels can also exhibit both UCST and LCST: these materials swell when they are heated up to temperature above UCST or are cooled down below LCST, whereas they contract when the temperature is between UCST and LCST.

There are many polymers belonging to the family of thermo-responsive polymer hydrogels, systems mainly characterized by the presence of hydrophobic groups, such as methyl, ethyl and propyl groups. Among them, PNIPAAm, which shows an LCST of 32 °C close to the body temperature, is the most extensively used.[83-86] Other polymer having an LCST are poly(*N,N'*-diethylacrylamide),[87,88] poly(*N*-acryloyl-*N'*-propylpiperazine),[89] PNVCL,[90-92] and poly(methylvinylether) (PMVE),[93,94] while a typical UCST systems is based on a combination of acrylamide (AAm) and AAc (Figure I.7.).[96]

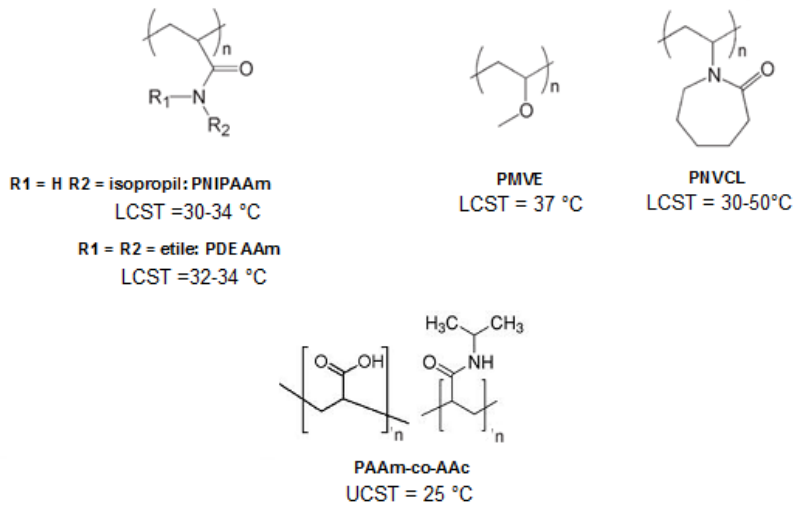

Figure I.7. Chemical structure of LCST and UCST polymers

I. 1. 1. 1 PNIPAAm HYDROGELS

The most popular thermoresponsive polymer hydrogel is PNIPAAm, which possesses a sharp phase transition in water at around 32–33 °C.

The phase transition, and hence the origin of the *smart* behavior, arises from the entropic gain as water molecules associated with the side-chain isopropyl moieties are released into the bulk aqueous phase as the temperature increases past a critical point. In fact, below the LCST, PNIPAAm assumes a flexible and extended coil conformation, while, at the LCST, it becomes hydrophobic and the polymer chains seem to collapse prior to aggregation in globular structures.[96,97] Coil-to-globule transition of PNIPAAm in water was investigated by Wang et al.[98] They observed two intermediate states, which gives in total four different, thermodynamically stable states: coil, crumpled coil, molten globule, globule. The fully collapsed globule still contains ca. 66% water in its hydrodynamic volume. Wang also found that a change in the solvent quality can alter the volume phase transitions, e.g. the replace of water with deuterated water causes an increase in the LCST of 1–2 K, indicating that D_2O is a better solvent than water.[99]

The LCST of PNIPAM is not influenced by the molecular weight and the concentration, but it can be changed upon varying the hydrophilic/hydrophobic balance. As previously reported, this can be achieved by copolymerization of NIPAAm with a second monomer: if NIPAAm is copolymerized with a more hydrophilic monomer, the overall hidrophilicity of the polymer increases and the polymer-water interactions became stronger, leading to an increase in the LCST. Likewise, copolymerization with a more hydrophobic monomer results in a lower LCST than PNiPAAm.[100]

The transition temperature of PNIPAAm, extremely close to the physiological one, makes this polymer suitable for such biomedical and pharmaceutical applications such as for cell encapsulation,[101] cell culture surfaces [102] and for drug delivery systems. [103,104]

I. 1. 1. 2 PNVCL HYDROGELS

Recently, another thermoresponsive polymer hydrogel, the poly(*N*-vinylcaprolactam), has attracted great interest. PNVCL is a non-ionic, biodegradable, water-soluble, non-adhesive polymer, belonging to the same family of poly(vinylpyrrolidone), PVP. [105-109]

PNVCL is non-toxic and stable against hydrolysis: unlike PNIPAAM, which produces small toxic amide compounds in strong acid conditions, its degradation results in a polymeric carboxylic acid.[110] Moreover PNVCL exhibits an LCST at about 32–34 °C, very close to the physiological one, making it a valid alternative to PNIPAAm, and an interesting candidate for biomedical and pharmaceutical applications, such as in controlled drug-delivery systems,[111-113] in the immobilization of enzymes,[114] and in separation science.[115]

Many authors have investigated different systems based on PNVCL. Solomon et al. have studied the bulk polymerization of NVCL in the presence of different initiators in nitrogen or in air atmosphere.[116] They found that, in a temperature range included between 60 to 80 °C, high conversions of polymer can be obtained by using low concentrations of 2,2'- azobisisobutyronitrile (AIBN), one the most used radical initiators. Moreover Solomon et al. were able to prepare PNVCL by radical polymerization of NVCL in homogeneous solution.[117,118]

Cheng et al. reported the polymerization of NVCL by radiation in water. The effects of radiation dose and total dose on the viscosity of polymer were studied.[119]

Lozinsky et al. reported the polymerization of NVCL by emulsion polymerization using water as solvent and ammonium persulphate/tertiary amine as redox initiator. The molecular weight and molecular weight distribution, their temperature-dependent solution behaviors and the thermodynamic parameters of phase segregation process of polymer have been studied by using size exclusion chromatography and differential scanning calorimetry (DSC).[120]

Law and Wu reported the synthesis and characterization of PNVCL with a higher molar mass by the free-radical bulk polymerization.[92] Pich et al. prepared reactive microgel particles with tunable swelling degree and modulated separation properties as smart enzyme carriers.[121] Loos et al. prepared thermoresponsive hydrogels based on PNVCL and inorganic crosslinked silica phases by sol-gel technology.[122] Some authors added PEO molecules and its derivatives in the recipes because it increases the biocompatibility of the final polymer. [123,124]

I. 1. 1. 3 OTHER THERMO-RESPONSIVE POLYMER HYDROGELS

PMVE has a transition temperature at 37 °C, which makes it very interesting for biomedical applications. It is synthesized by cationic polymerization using inert conditions. Nucleophiles, such as alcohol or amino groups cannot be tolerated during the synthesis, which limits the potential of PMVE.[125]

Poly (N-acryloyl-N'-alkylpiperazine) was recently reported as another temperature responsive polymer. [126] It showed a LCST at 37 °C, while introducing methyl or ethyl groups instead of the propyl one, resulted in the loss of the LCST.[127]

Poly(N-ethyl oxazoline) has a transition temperature around 62 °C, which is too high for any drug delivery application. However, their copolymer with NIPAAm are very interesting because they tend to aggregate into micelle above the LCST.[128] Unfortunately the poly(oxazoline) chemistry has the disadvantage that it is not very tolerant against unprotected functionalities.

Polypeptides can also show LCST behavior, when hydrophilic and hydrophobic residues are balanced well. A polymer made out of the pentapeptide GVGVP as repeating unit exhibits a volume phase transition at 30 °C.[129]

One of the few examples of polymer hydrogels having an UCST is that of the interpenetrating network of PAAc and PAAm. The transition temperature is at 25 °C .[96] The UCST behavior is caused by the cooperative effects coming from the hydrogen bonding between AAc and AAm units. A similar situation is found for 1:1 copolymers of AAc and AAm.

I. 1. 2 pH-RESPONSIVE HYDROGELS

pH-responsive hydrogels are materials that vary their volume with pH changes: they consist of ionizable groups that can accept or donate protons in response to a pH variation. Polymers with weak ionizable groups show a degree of ionization, which dramatically changes at a specific pH named pK_a (Figure I.8.). The rapid variation in the net charge on the pendant groups causes an alteration of the hydrodynamic volume of the polymer chains. The transition from collapsed to swollen state is due to the osmotic pressure exerted by mobile counterions, which neutralizes the network charges.[130] Polymers having ionizable groups along their chains form polyelectrolytes in aqueous solution.

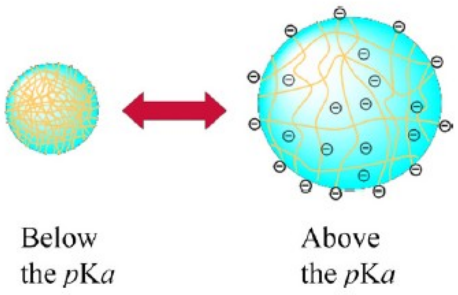

Figure I.8. Schematic illustration of the pH-responsive behavior (below and above the pKa) of a particulate system constituted by a polymer with carboxylic acid segments.

There are two main kinds of pH responsive materials: (i) weak polyacids, which have COOH or SO_3H as acid groups (these materials are generally swollen at high pH and deswell in acid conditions); (ii) the second type, which is characterized by an opposite behavior, is represented by weak polybases bearing basic pendants, like NH_2, and so forth.

The most reported pH-responsive polyacids are PAAc[131-133] and poly(methacrylic acid), PMAAc,[134] weak polyacids bearing carboxylic group with pK_a of around 5-6, which release protons at neutral and high pH (Figure I.9. a and b).

At high pH, these compounds are transformed into polyelectrolytes with electrostatic repulsion forces between the molecular chains. This repulsion force generates a momentum along with the hydrophobic interaction, which govern precipitation/solubilization of molecular chains, deswelling/ swelling of hydrogels, or hydrophobic/hydrophilic characteristics of the surfaces.

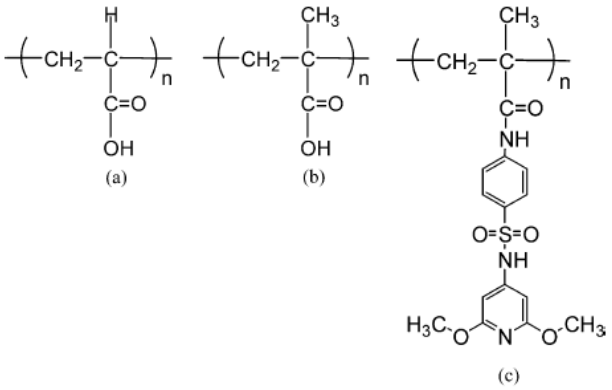

Figure I.9. Representative pH-responsive polyacides; (a) PAAc), (b) PMAAc, (c) polymer containing sulfonamide groups.

Another type of weak polyacid belonging to the pH-responsive family are those containing sulfonamide groups. These compounds show various pK_a values ranging from pH 3 to 11, because of different pendant substituents at the sulfonamide group acting as electron withdrawing or donating groups (Figure I.9. c). The hydrogen atom of the amide nitrogen can be readily ionized to form a weak polyacid. If compared to the traditional carboxylic acid-based polymers, they exhibit a narrow pH range and sensitivity.[135]

On the other hand, typical poly-bases are poly(4-vinylpyridine),[136] poly(N,N-dimethylaminoethylmethacrylate), PDMAEMA,[137] poly(N,N-diethylaminoethylmethacrylate),[138,139] PDEAEMA and poly(vinyl imidazole)[140] which are protonated at high pH and positively ionized at neutral and low pH (Figure I.10.).

PDEAMA undergoes an abrupt precipitation above pH 7.5, due to the deprotonation of the amino group, followed by hydrophobic molecular interactions, while poly(4-vinylpyridine) shows the phase transition at pH lower 5, because of the deprotonation of pyridine groups.

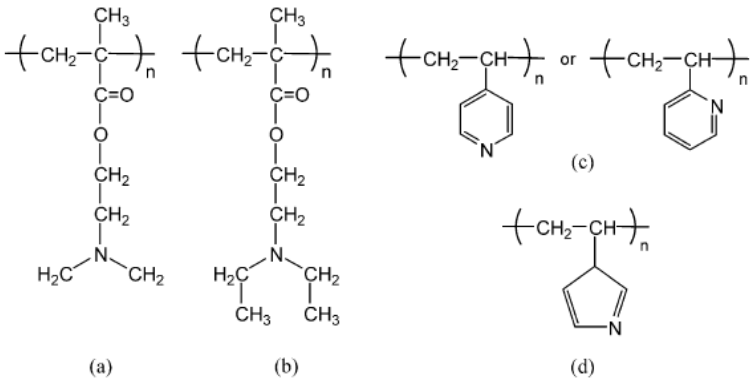

Figure I.10. Representative pH-responsive polybases. (a) PDMAEMA, (b) PDEAEMA), (c) poly(4 or 2-vinylpyridine), (d) poly(vinyl imidazole).

Hydrogels made of crosslinked polyelectrolytes show big differences in swelling properties, depending on the pH of the environment. Ionization on polyelectrolytes, however, is more difficult due to electrostatic effects exerted by other adjacent ionized groups, thus making the apparent dissociation constant (K_a) different from that of the corresponding monoacid or monobase. Since the swelling of polyelectrolyte hydrogels is mainly due to the electrostatic repulsion among charges present on the polymer chain, the extent of swelling is influenced by any condition that reduce electrostatic repulsion, such as pH, ionic strength and type of counter ions.[141]

One of the possible methods to control the pH-responsive properties of the hydrogels is the introduction of a small fraction of hydrophobic repeat units in weak polyacid or polybase hydrogels. In this case hydrophobic groups can aggregate with each other, when the gel is uncharged. These hydrophobic microdomains, acting as additional cross-links, interfere with the network swelling induced by ionization.

pH-sensitive hydrogels are particularly useful, for example, in the delivery of drugs or peptides to a specific site in the gastrointestinal tract or in response to small changes in the pH of blood stream or tissues in a pathological situation, such as a clot or cancer.[142] The range of physiological pH is from 1.2 to 7.4, and different body part may have a special pH surroundings. For example, the stomach possesses pH 1.2 while the pH of the intestine is 7.4. Moreover, it is known that the extracellular pH of tumors (6.8–6.9) is more acidic than both tumor intracellular pH (7.2) and normal extracellular tissues (7.4).[143] In this sense, pH sensitive polymers seem to have high potential application value as drug delivery agents.[144]

Polycationic hydrogels in the form of semi-IPN have also been used for drug delivery in the stomach. Semi-IPN of crosslinked chitosan and PEO showed more swelling under acidic conditions (as in the stomach). This type of hydrogels would be ideal for localized delivery of antibiotics, such as amoxicillin and metronidazole, in the stomach for the treatment of Helicobacter pylori.[145]

Superporous hydrogels for delivery of drug in the alkaline pH were formulated employing acrylamide and methacrylic acid by free radical polymerization. These swelled only in basic pH and showed very fast swelling kinetics.[146]

pH-sensitive hydrogels have also been used in making biosensors and permeation switches.[147] The pH-sensitive hydrogels for these applications are usually loaded with enzymes that change the pH of the local microenvironment inside the hydrogels. One of the common enzymes used in pH-sensitive hydrogels is glucose oxidase which transforms glucose to gluconic acid. The formation of gluconic acid lowers the local pH, thus affecting the swelling of pH-sensitive hydrogels.

I. 1. 3 ELECTRO-RESPONSIVE HYDROGELS

Electric field responsive hydrogels are polymers that swell, shrink or bend in response to an applied electric field.

They are usually made of polyanions, polycations or amphoteric polyelectrolites, and are thus pH-responsive as well.

Electro-responsive hydrogels can be also prepared by using synthetic as well naturally occurring polymers, either alone or in combination. Among the natural polymers, hyaluronic acid, chondroitin sulfate, agarose, xanthan gum and calcium alginate are the most used; while the synthetic polymers are methacrylate and acrylate derivatives such as partially hydrolyzed PAAm and poly(dimethylaminopropyl acrylamide).

They are synthesized by either chemical–crosslinking of water soluble polymers or by free-radical polymerization of the monomers. Complex multi-component gels or interpenetrating networks have also been prepared in order to enhance the gel electro-responsiveness.[148]

To investigate the electrical response, different experimental set-ups are projected. The gel can or cannot be placed in an electro-conducting medium such as water, saline or buffer. One or both electrodes (e.g., carbon, platinum) may be in contact with the gel (Figures I.11a-c,e). When electrodes are not contacting, the gel is placed in a conducting medium (Figure I.11d), while, when both electrodes are contacting conducting medium is not needed (Fig. I.11e). Sometimes, one end of the gel is fixed to an electrode while the other also end is touching the counter electrode.

Under the influence of an electric field, electric sensitive hydrogels generally deswell or bend, depending on their shape and their position relative to the electrodes. Bending occurs when the main axis of the gel lies parallel to the electrodes, while deswelling occurs when the hydrogels lies perpendicular to the electrodes. The first has mainly been studied for the production of mechanical devices, such as artificial tendons/fingers/hands, soft actuators and molecular machine,[149,150] while the hydrogel deswelling has been used in drug delivery systems.[151] Moreover, there are some polymer systems that swell or erode after the application of an electric field.

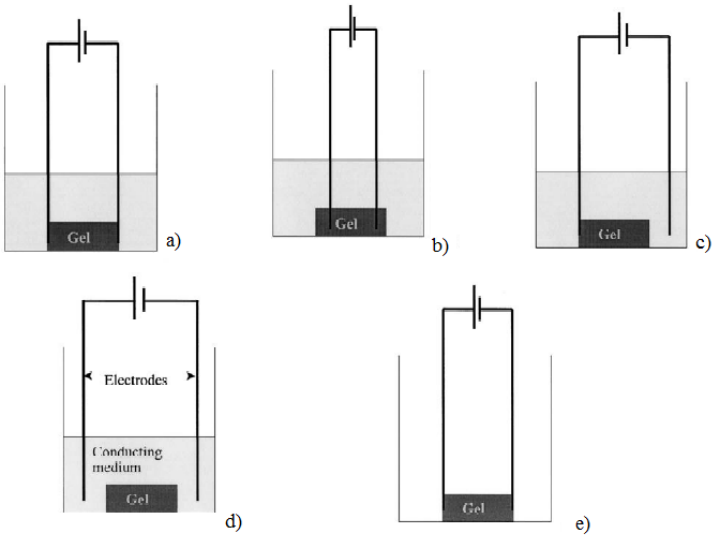

Figure I.11. Examples of the different experimental set-ups that have been used to study electro-responsive hydrogels.

Electro-induced hydrogel bending

Upon the application of the electrical stimulus some hydrogels tend to swelling on one side and deswelling on the other side, resulting in the bending of their structure. Shiga et al. studied the swelling behavior of a copolymer hydrogel of sodium acrylic acid–acrylamide, placed in a water-acetone mixture, without touching the electrodes, under the electric field action.[152] They observed that the type of hydrogel deformation was influenced by the concentration of the electrolytes: in absence of electrolytes or in presence of very low concentration of them, application of an electric field causes the hydrogel to collapse. This is due to the migration of Na^+ to the cathode electrode resulting in changes in the carboxyl groups of the polymer chains from COONa to COOH. In the presence of high concentration of electrolytes in solution, however, more Na^+ enters the hydrogel than migrated from the hydrogel to the cathode. The swelling was more prominent at the hydrogel side facing the anode and this resulted in bending of the hydrogels.

Electro-induced hydrogel deswelling

When the electric field applied to the polyelectrolyte hydrogel exceeds a threshold value, the polymer system generally deswells: anionic hydrogels collapse at the anode[153] while the cationic ones shrink at the cathode.[154]

Since volume changes of responsive hydrogels are usually diffusion-controlled, the deswelling equilibrium is reached slowly.

The gel deswelling may also be accompanied by an increase in gel opacity and it is strongly influenced by the magnitude of the electric field. In fact the extent of the deswelling increases with the electric field, even

if it is not linearly proportional to it. However, at high voltage the capability of the hydrogel response tails off: this is probably due to an increase of resistivity to the charge passage as the content of "free" water decreases.[155,156]

Gong et al. and Budtova et al. have shown that the extent of deswelling depends on the amount of charge transported through the gel, rather than on the applied voltage.[157,158]

When the electric field is removed, the hydrogel absorbs the solution and swells. Thus, upon sequential switching "on" and "off" of the electric field, the hydrogel deswells or swells. The extent of the gel response and the degree of reversibility decrease with time and increase with the number of the on-off cycles performed.

The electrical response of polyelectrolyte hydrogels is influenced by many parameters, such as the shape and the orientation of the gel, its composition (charge density, nature and hidrophilicity of crosslinks, monomers and pendant groups), the nature of the aqueous conducting medium, the eventually presence of electrolytes in the medium and the experimental set up.

Therefore, the same hydrogel can exhibit a different behavior depending on the experimental conditions chosen. For example Tanaka et al. reported that when partially hydrolyzed polyacrylamide hydrogels were immersed in a water-acetone mixture and fixed to the electrodes, 20% of the gel near the anode collapses 200 fold in volume while the rest of the gel remained swollen when a voltage of 1.25 V was applied. When the voltage increased, the other part of the hydrogel shrinks, until to obtain a total collapse of the polymer system at 2.5 V. Conversely, if the water-acetone mixture was changed with pure water, the hydrogel continuously deswells along the whole axis. [153]

Yuk et al. observed different deswelling behaviors when contacting or non-contacting electrodes were used. Contacting electrodes induced bulk shrinkage of calcium alginate /polyacrylic acid composites. In contrast, when non contacting electrodes were used, the effect of the electric field was first felt on the gel surface: therefore the gel surface deswelled, while the bulk of the gel remained in a swollen state.[159]

Furthermore some investigators have reported that gel deswelling at one electrode may be accompanied by gel swelling at the other electrode.

There are three main mechanisms of electro-induce gel deswelling: (i) the establishment of a stress gradient in the gel, (ii) changes in local pH around the electrodes and (iii) electroosmosis of water coupled to electrophoresis.

Electro-induced hydrogel swelling

In addition, there are some polymer systems that swell when an electric field is applied. In these cases, it is needed that the gel is placed at a fixed position away from the electrodes. Sawata et al. studied the swelling behavior of poly(methylmethacrylate), PMMA, as a function of the applied electric field.[160] They

found that PMMA hydrogel, immersed in water or in salt solution, swelled when two polarized electrode faced each other at a certain distance from it. This is probably due to the fact that, upon electrical stimulation, the mobile cations in aqueous medium migrate toward the cathode, penetrating into the PMMA hydrogel network on their way. This phenomenon induces the ionization of the carboxylic groups on the gel network and causes the swelling of the gel on the anode side as the ionic groups became hydrate.
However, electro-induced hydrogel swelling is much rarer than gel deswelling, and it is needed to perform more work before completely understand this phenomenon.

Electro-induced hydrogel erosion

Finally, there are also hydrogels that erode rather deswell when exposed to an electric field. A hydrogel that shows this behavior was studied by Kwon et al.[161,162] The gel is formed when two water-soluble polymers are mixed and interacts either by hydrogen-bonding (PEO and PAAc/PMAAc) or by ionic bonding between two oppositely-charged polymers (polyallylamine and heparin). Complex structures are pH dependent: PEO/PMAAc complex is formed below pH 5, but disintegrates above pH 5.4 when the carboxylic acid groups become ionized and hydrogen bonds are disrupted; beside the polyallylamine / heparin complex is stable over pH range 3–10 and dissociates below pH 2 and above pH 11, when deionization of COO^-, SO_3^- and NH_3^+ groups leads to disruption of the ionic bonds responsible for the gel complex.
When the hydrogel, attached to the cathode and immersed in a conducting medium, with the non contacting anode placed 1 cm away from the cathode, undergoes the electrical stimulus, the gel surface in contact with the cathode starts to dissolve and erode. The production of OH^- ions by electrolysis of water increases the local pH at the cathode, resulting in the disruption of hydrogen-bonding/ ionic bonding between the two polymers and in the disintegration of the polymer complex into its two component polymers.
The degree of hydrogel erosion is measured by the release of anionic polymer (heparin) and is influenced by the extent of the electric field applied, even if it is not linearly proportional to it. Moreover the rate of erosion is constant with time and with the number of on-off cycles of electrical stimulation.
Unlike hydrogel deswelling, gel erosion is not reversible: in fact once the polymer system has eroded, it does not reform when the electric stimulus is removed.

Electro-responsive hydrogels have been mainly applied in controlled drug delivery systems.[151,163,164] Kwon et al.[165] prepared hydrogels of poly(2-acrylamido-2-methylpropane sulfonic acid–co-n-butylmethacrylate) able to release edrophonium chloride and hydrocortisone in a pulsatile manner using electric current. Control of “on–off’ drug release was achieved by varying the intensity of electric stimulation in distilled–

deionized water. For edrophonium, a positively charged drug, the release pattern was explained as an ion exchange between the positively-charged solute and hydrogen ion produced by electrolysis of water.
Electric fields have also been used to control the erosion of hydrogels made of poly(ethyloxazoline)–PMAAc complex in a saline solution.[166] The two polymers form a hydrogel via intermolecular hydrogen bonding between carboxylic and oxazoline groups. When the gel matrix was attached to a cathode surface, application of electric current caused disintegration of the complex into water-soluble polymers at the gel surface facing the cathode. The surface erosion of this polymer system was controlled either in a stepwise or continuous fashion by controlling the applied electrical stimulus. Pulsatile insulin release was achieved by applying a step function of electric current.
Another application of electro-sensitive hydrogels is in biomedical field for the production of artificial muscles and tissues. These types of hydrogel are able to convert chemical energy to mechanical energy.[167]
All living organisms move by the isothermal conversion of chemical energy into mechanical work, e.g. muscular contraction, and flagellar and ciliary movement. Electrically driven motility has been demonstrated using weakly crosslinked poly(2-acrylamido-2-methylpropanesulfonic acid), PAMPSA, hydrogels. In the presence of positively charged surfactant molecules, the surface of the polyanionic hydrogel facing the cathode is covered with surfactant molecules reducing the overall negative charge. This results in local deswelling of the hydrogel, leading to bending of the hydrogel. Application of an oscillating electrode polarity could lead the hydrogel to quickly repeat its oscillatory motion, leading to a worm-like motion.[168]

I. 1. 4 MAGNETIC-RESPONSIVE HYDROGELS

Another type of stimuli responsive hydrogels is that of magnetic sensitive hydrogels, which undergo a volume change after the application of an external magnetic field.
These compounds are generally obtained by incorporating colloidal magnetic solution, named “complex fluid” into the polymer network: through this combination of solid-like and fluid-like behavior, the influence of the external field on the hydrogel properties is enhanced. Electro-rheological fluids, magneto-rheological fluids and ferro-fluids usually contain dispersed small particles in the size range from nanometers to micro-meters, and respond to an applied field by rapidly changing their apparent viscosity and yield stress.
When a magnetic-responsive hydrogel is exposed to an external field, two distinct types of interactions can be identified: field-particle interaction and particle-particle interaction.[169,170] If the field is non uniform, the field-particle interactions are dominant. The particles undergo a dielectrophoretic (DEP) or a magnetophoretic (MAP) force, and are attracted to regions of stronger field intensities. Because of the crosslinking bridges in the network, changes in molecular conformation, due to either DEP or MAP forces can accumulate and lead to macroscopic shape changes and/or motion.

In uniform fields the situation is completely different. Because of the lack of a field gradient, there are no attractive or repulsive field-particle interactions, thus particle-particle interactions become dominant. The applied field induces electric or magnetic dipoles. As a result, mutual particle interactions occur if the particles are so closely spaced that the local field can influence their neighbors. This mutual interaction can be very strong, leading to a significant change in the structure of particle ensembles. The particles attract each other when aligned end to end, and repel each other in the side-by-side situation. Because of the attractive forces, pearl-chain structure develops.

Zrinyi prepared a magnetic field sensitive hydrogels by incorporating colloidal magnetic particles into crosslinked PNIPAAm-co-PVA hydrogels. The gel beads formed straight chainlike structures in uniform magnetic fields, while they aggregated in non homogeneous fields. The rapid and controllable shape changes of these gels would be expected to mimic muscular contraction.[171]

Magnetic sensitive hydrogel have been found useful in biomedical applications, such as cell separation,[172-174] gene and drug delivery, and magnetic intracellular hyperthermia treatment of cancer.[175,176]

Reynolds et al. obtained a thermo-sensitive and magnetically responsive hydrogel composites, based on the temperature sensitivity of PNIPAAm and magnetic properties of iron oxide (Fe_3O_4) nanoparticles. Fe_3O_4 magnetic nanoparticles were used to generate heat through the application of an alternating magnetic field, phenomena at the basis of the use of magnetic particles in hyperthermia treatment. The application of the magnetic field causes a strong volume change in the hydrogel systems through the thermal response of the PNIPAAm component.[177]

I. 2 SUPERABSORBENT POLYMER HYDROGELS

Superabsorbent polymer hydrogels (SPH) are materials that are able to absorb and retain water up to a few hundred times of their own weight: they can imbibe water as high as 1000-100000% (10-1000 g/g) respect to common hydrogels that have an absorption capacity not exceeding 100 % (1 g/g).[178-180]

SPHs are highly hydrophilic crosslinked polymers with a large internal surface having a large number of interconnected pores, which allow absorbing water in extremely short times. Thanks to the capillary attraction forces within the pores, water can be rapidly absorbed, and these polymers can swell to their maximum volume very quickly.[181,182]

The swelling phenomenon is the result of three different processes: (i) physical entrapment of water via capillary forces in their macroporous structure; (ii) hydration of functional groups; (iii) dissolution and thermodynamically favoured expansion of the macromolecular chains limited by crosslinkages.

Another feature that discriminates SHP from the other hydrogels is that the SHP particle shape (granule, fiber, film, etc.) is preserved after water absorption and swelling: the swelling gel strength should be high enough to prevent loosening, mushy or slimy state.

SHPs can be classified in four groups on the basis of the presence or absence of electrical charged groups in the crosslinked chains[183]:

- Non ionic SHPs
- Ionic SHPs
- SHPs formed by amphoteric electrolytes containing both acid and basic groups
- Zwitterionic SHPs containing both anionic and cationic groups in each structural repeating unit.

SHPs are also classified on the basis of the monomeric unit used in their chemical structure. Three distinct categories can be found:

- Crosslinked polyacrylates and polyacrylamide
- Hydrolyzed cellulose-polyacrylonitrile or starch-polyacrylonitrile graft copolymers
- Crosslinked copolymers of maleic anhydride

Taking into account the original sources, SHPs can be also divided into two main classes: synthetic and natural SHPs.

The main monomers used in the obtainment of synthetic SHPs are acrylamide, acrylic acid and its sodium or potassium salts. However, methacrylic acid, methacrylamide, acrylonitrile, 2-hydroxyethylmethacrylate (HEMA), 2-acrylamido-2-methylpropane sulphonic acid (AMPSA), N-vinylpyrrolidone (NVP), vinyl acetate and vinyl sulphonic acid are also used.

N,N-methylene *bis*-acrylamide (BIS) and potassium or ammonium persulfate (AmPS) are the most used water soluble crosslinking agent and initiators, respectively.

SHPs are prepared by free radical polymerization in aqueous solution or by inversion-suspension polymerization.

In the first case, the reactants are dissolved in water at the desired concentrations, and a fast exothermic reaction yields a gel-like elastic product which is dried, pulverized and sieved to obtain the required particle size. The disadvantages of this method are the lack of a sufficient reaction control and non exact particle size distribution.[184,185] However, free radical polymerization is a cheaper and faster technique for the obtainment of SHPs.

In the emulsion polymerization route, aqueous monomer solution drops are dispersed in the hydrocarbon phases before polymerization. The viscosity of the monomer solution, agitation speed, rotor design and dispersant type mainly govern the resin particle size and shape.[186] The resulting microspherical particles are easily removed by filtration or centrifugation from the continuous organic phase. Upon drying, these particles will directly provide a free flowing powder.

This method has different advantages compared to the previous: better control of reaction, heat-removal, *ab initio* regulation of particle size distribution, and further possibilities for adjusting particle structures or morphology alteration.[187]

The final properties of SHPs are influenced by different parameter, such as type of crosslinker, initiator, monomer(s) and their related concentrations, polymerization method and temperature, amount and type of surfactant used, method of drying and post-polymerization treatments.

This kind of hydrogels has found wide application such as sanitary napkins, communication technology, building industry, chromatography, water purification, artificial snows, food storage, gel actuators, water-bloking tapes, medicine for drug delivery systems.[178,186,188-194]

SHPs have also found interesting applications in agricultural field, where they have been successfully used as soil amendments, to improve the physical properties of soil in view of increasing their water-holding capacity and/or nutrient retention of sandy soils to be comparable to silty clay or loam.[195,196] They are able to reduce irrigation frequency and compaction tendency, stop erosion and water run off, and increase the soil aeration and microbial activity.[197]

SHPs can be also used as retaining materials in the form of seed additives (to aid in germination and seedling establishment), seed coatings, root dips, and for immobilizing plant growth regulator or protecting agents for controlled release.[195]

REFERENCES

[1] Trabbic-Carlson, K.; Setton, L. A.; Chilkoti, A. *Biomacromolecules* 2003, 4, 572–580.
[2] Ossipov, D. A.; Hilborn, J. *Macromolecules* 2006, 39, 1709–1718.
[3] Topuz, F.; Okay, O. *Reactive and Functional Polymer* 2009, 69, 273–280.
[4] Drumheller, P.; Hubbell, J.A. *J. Biomed. Mater. Res.* 1995, 29, 201–215.
[5] Campoccia, D.; Doherty, P.; Radice, M.; Brun, P.; Abatangelo, G.; Williams, D.F. *Biomaterials* 1998, 19, 2101–2127.
[6] Prestwich, G.D.; Marecak, D.M.; Marecak, J.F.; Vercruysse, K.P.; Ziebell, M.R. *J. Controlled Release* 1998, 53, 93–103.
[7] Sanabria-DeLong, N.; Crosby, A. J.; Tew, G. N. *Biomacromolecules* 2008, 9, 2784–2791.
[8] Branco, M. C.; Nettesheim, F.; Pochan, D. J.; Schneider, J. P.; Wagner, N. J. *Biomacromolecules* 2009, 10, 1374–1380.
[9] Xu, Y. X.; Sheng, K. X.; Li, C.; Shi, G. Q. ACS Nano 2010, 4, 4324–30.
[10] Peppas, N. A.; Merrill, E. W. *J. of Polym. Sci. Part A: Polym. Chem.* 1976, 14, 441-457.
[11] Hoffman, A. S. *Advanced Drug Delivery Reviews* 2002, 43, 3-12.
[12] Hoffman, A. S. *Advanced Drug Delivery Reviews* 2012, 64, 18-23.
[13] TanakaT. *Phys.Rav.* 1978, 40, 820-823.
[14] Das ,A.; Wadhwa, S.; Srivastava, A. K. *Drug Del.* 2006, 13, 139-142.
[15] Chapiro, A. In Radiation Chemistry of Polymeric Systems. New York, USA: Interscience, 1962.
[16] Lim, F.; Sun, A.M. *Science* 1980, 210, 908–910.
[17] Eichler, S.; Ramon, O.; Cohen, Y.; Mizrahi, S. *International Journal of Food Science & Technology* 2002, 37, 245–53.
[18] Ganji, F.; Vasheghani-Farahani, S.; Vasheghani-Farahani, E. *Iranian Polymer Journal* 2010, 19,375–398.
[19] Gemeinhart, R. A.; Guo, C. In Fast swelling hydrogel systems. In: Yui N, Mrsny RJ, Park K, editors. Reflexive polymers and hydrogels: understanding and designing fast responsive polymeric systems. Boca Raton: CRC Press; 2004.
[20] Flory, P. J.; Rehner J. *J. of Chem. Physics* 1943, 11,521–526.
[21] Flory, P.J. *J. of Chem. Physics* 1950, 18, 108–111.
[22] Flory, P. J. In Principles of Polymer Chemistry. Ithaca, NY: Cornell University Press. 1953.
[23] Edwards, S. F. *British Polymer Journal* 1977, 9,140–143.
[24] Peppas, N. A. Hydrogels. In: Ratner BD, Hoffman AS, Schoen FJ, Lemons JE, editors. Biomaterial science: an introduction to materials in medicine. 2nd ed. California: Academic Press; 2004.
[25] Peppas, N. A.; Merrill, E. W. *J. App. Polym. Sci.* 1977, 21, 1763–1770.
[26] Pourjavadi, A.; Salimi, H. Indust. & Engin. Chem. Res. 2008, 47, 9206–9213.
[27] Swann, J. M. G.; Bras, W.; Topham, P. D.; Howse, J. R.; Ryan, A. J. *Langmuir* 2010, 26, 10191–10197.
[28] Gao, M.; Gawel, K.; Stokke, B. T. *Soft Matter* 2011, 7, 1741–1746.
[29] Donati, I.; Morch, Y. A.; Strand, B. L.; Skjak-Braek, G.; Paoletti, S. *J. Phys. Chem B* 2009, 113, 12916–12922.
[30] Kudaibergenov, S. E.; Sigitov, V. B. *Langmuir* 1999, 15, 4230–4235.
[31] Peppas, N. A.; Khare, A. R. *Adv. Drug Deliv. Rev.* 1993, 11, 1–35.
[32] Peppas, N. A.; Colombo, P. J. of Control. Releas 1997, 45, 35–40.
[33] Michalek, J.; Hobzova, R.; Pradny, M.; Duskova, M. Hydrogel Contact Lenses. In R. M. Ottenbrite, K. Park, & T. Okano (Eds.), Biomedical Applications of Hydrogels Handbook (pp. 303–316). New York, USA: Springer, 2010.
[34] Ostrovidova, G. Material. Sci. and Engin. C 2003, 23, 545–550.
[35] Merrill, E. W.; Pekala, P. W.; Mahmud, N. A. In Hydrogels for Blood Contact. In N. A. Peppas (Ed.), Hydrogels in Medicine and Pharmacy, Boca Raton, FL: CRC Press, 1987.
[36] Tae, G.; Kim, Y. J.; Choi, W. I.; Kim, M.; Stayton, P. S. et al. *Biomacromolecules* 2007, 8, 1979–1986.
[37] Park, K. In Controlled Release: Challenges and Strategies; Park, K. (Purdue University), Ed.; American Chem Society: Washington, DC, USA, 1997.
[38] Schmaljohann, D. *Adv Drug Deliv Rev* 2006, 58, 1655–1670.
[39] Jeonga, B.; Kimb, S. W.; Baeb, Y. H. *Adv Drug Deliv Rev* 2002, 54, 37–51.

[40] Bajpai, A. K.; Shukla, S. K.; Bhanu, S.; Kankane, S. *Prog Polym Sci* 2008, 33, 1088–1118.
[41] Buengera, D.; Topuza, F.; Grollb, *J. Progr. Polym. Sci.* 2012, 37, 1678–1719.
[42] Wichterle, O.; Lim, D. *Nature* 1960, 185, 117–118.
[43] Tanaka, T. *Polymer* 1979, 20, 1404–1412.
[44] Murosaki, T.; Gong, J. P. In Double Network Hydrogels as Tough, Durable Tissue Substitutes. In R. M. Ottenbrite, K. Park, & T. Okano (Eds.), Biomedical Applications of Hydrogels Handbook, New York, USA: Springer, 2010.
[45] Hassan, C. M.; Peppas, N. A. *J. Appl. Polym. Sci.* 2000, 76, 2075–2079.
[46] Oishi, M.; Nagasaki, Y. In Stimuli-responsive PEGylated Nanogels for Smart Nanomedicine. In R. M. Ottenbrite, K. Park, & T. Okano (Eds.), Biomedical Applications of Hydrogels Handbook , New York, USA: Springer, 2010.
[47] Wang, Q.; Mynar, J. L.; Yoshida, M.; Lee, E.; Lee, M.; Okuro, K.; Kinbara, K.; Aida, T. *Nature* 2010, 463, 339-343.
[48] Griffith, L., Lopina, S. T. Macromolecules 1995, 28, 6787–6794.
[49] Okano T. In Biorelated Polymers and Gels; Academic Press: San Diego, CA, 1998.
[50] Peng, T.; Cheng, Y. L. Polymer 2001, 4, 2091–2100.
[51] Bignotti, F.; Penco, M.; Sartore, L.; Peroni, I.; Mendichi, R.; Casolaro, M.; D'Amore, A. Polymer 2000, 41, 8247–8256.
[52] Tengfei, F.; Mingjun, L; Xuemin, W.; Min, L.; Yan, W. *Colloids and Surfaces B: Biointerfaces* 2011, 88, 593–600.
[53] Bromberg, L.; Temchenko, M.; Hatton, T. A. *Langmuir* 2002, 18, 4944-4952.
[54] Torres-Lugo, M.; Garcia, M.; Record, R.; Peppas, N. A. *Biotechnol. Prog.* 2002, 18, 612-616.
[55] Schilli, C. M.; Zhang, M. F.; Rizzardo, E.; Thang, S. H.; Chong, Y. K.; Edwards, K.; Karlsson, G.; Müller, A. H. E. *Macromolecules* 2004, 37, 7861-7866.
[56] Garbern, J. C. ; Hoffman, A. S.; Stayton, P. S. *Biomacromolecules* 2010,11, 1833-1839.
[57] Peppas, N. A.; Langer, R. Science 1994, 263, 1715–1720.
[58] Park K (1997) In Controlled Release: Challenges and Strategies. American Chem Society: Washington, DC.
[59] Ueoka, Y.; Gong, J.; Osada, Y. *J. Intelligent Mater. Syst. Struct.* 1997, 8, 465–471.
[60] Liu, Z. S.; Calvert, P. *Adv. Mater.* 2000, 12, 288–291.
[61] Vernon, B.; Kim, S. W.; Bae, Y. H. *J. Biomed. Mater. Res.* 2000, 51, 69–79.
[62] Liu, T. Y.; Hu, S. H.; Liu, D. M.; Chen, S. Y.; Chen, W. I. Nano Today 2009, 4, 52–65.
[63] Yoshida, R.; Okano, T. In Stimuli-Responsive Hydrogels and their Application to Functional Materials. In R. M. Ottenbrite, K. Park, & T. Okano (Eds.), Biomedical Applications of Hydrogels Handbook New York, USA: Springer, 2010.
[64] Gupta, P.; Vermani, K.; Garg, S. *Drug Discov Today* 2002, 7, 569–79.
[65] Jhaveri, S. J.; Hynd, M. R.; Dowell-Mesfin, N.; Turner, J. N.; Shain, W.; Oberet, K. *Biomacromolecules* 2009, 10, 174–183.
[66] Hoffman, A. S. *J. Controlled Release* 2008, 132, 153–163.
[67] Bayer, C. L.; Peppas, N. A. *J. Controlled Release* 2008, 132, 216–221.
[68] Osada, Y.; Hasebe, M. *Chem. Lett.* 1985, 69, 1285–1288.
[69] Chen, J. P.; Sun, Y. M.; Chu, D. H. *Biotechnol. Prog.* 1998, 14, 473–478.
[70] Shiroya, T.; Tamura, N.; Yasui, M.; Fujimoto, K.; Kawaguchi, H. *Colloids Surf. B* 1995, 4, 267–274.
[71] Dobson, J. *Drug Dev. Res.* 2006, 67, 55-60.
[72] Ruel-Gariépy, E.; Leroux, J. C. *Eur. J. Pharm. Biopharm.* 2004, 58, 409-426.
[73] Gehrke, S. H.; Andrews, G. P.; Cussler, E. L. *Chem. Eng. Sci.* 1986, 41, 2153–2169.
[74] Cussler, E. L.; Stokar, M. R.; Varberg, J. E. *AIChE J*. 1984, 30, 578–582.
[75] Barker, S. L. R.; Ross, D.; Tarlov, M. J.; Gaitan, M.; Locascio, L. E. *Anal. Chem.* 2000, 72, 5925–5929.
[76] Hoffmann, J.; Plotner, M.; Kuckling, D.; Fischer, W. J. Sens. Actuators A 1999, 77, 139–140.
[77] Sorber, J.; Steiner, G.; Schulz, V.; Guenther, M.; Gerlach, G.; Salzer, R.; Arndt, K. F. *Analytical Chemistry* 2008, 80, 2957-2962.
[78] Buengera, D.; Topuza, F.; Grollb, J. *Prog. Polym. Sci.* 2012, 37, 1678– 1719.
[79] Schild, H. G. *Prog. Polym. Sci.* 1992, 17, 163–249.
[80] Hirotsu, S.; Hirokawa, Y.; Tanaka, T. *J. Chem. Phys.* 1987, 87, 1392–1395.
[81] Yu, H.; Grainger, D. W. *J. Appl. Polym. Sci.* 1993, 49, 1553–1563.

[82] Suzuki, Y.; Tomonaga, K.; Kumazaki, M.; Nishio, I. *Polym. Gels Netw.* 1996, 4, 129–142.
[83] Gil, E.; Hudson, S. *Prog. Polym. Sci.* 2004, 29, 1173-1222.
[84] Dautzenberg, H.; Gao, Y.; Hahn, M. *Langmuir* 2000, 16, 9070-9081.
[85] Schild, H. G. *Prog. Polym. Sci.* 1992, 17, 163-249.
[86] Ju, X. J.; Chu, L. Y.; Zhu, X. L.; Hu, L.; Song, H.; Chen, W. M. *Smart Mater. Struct.* 2006, 15, 1767-1774.
[87] Qiu. Y.; Park, K. *Adv Drug Deliv Rev* 2001, 53, 321–39.
[88] Idziak, I.; Avoce, D.; Lessard, D.; Gravel, D.; Zhu, X.X. *Macromolecules* 1999*,* 32, 1260-1263.
[89] Gan, L. H.; Gan, Y. Y.; Deen, G. R. *Macromolecules* 2000, 33, 7893–7897.
[90] Van Durme, K.; Verbrugghe, S.; Du Prez, F. E.; Van Mele, B. *Macromolecules* 2004, 37,1054-1061.
[91] Makhaeva, E.E.; Tenhu, H.; Khokhlov, A.R. *Macromolecules* 1998, 31, 6112-6118.
[92] Andy, C. W.; Wu, L.; Wu, C. *Macromolecules* 1999, 32, 581-584.
[93] Maeda, Y. *Langmuir* 2001, 17, 1737–1742.
[94] Mikheeva, L. M.; Grinberg, N. V.; Mashkevich, A. Y.; Grinberg, V. Y.; Thanh, L. T. M.; Makhaeva, E. E.; Khokhlov, A. R. *Macromolecules* 1997, 30, 2693-2699.
[95] Aoki, T.; Kawashima, M.; Katono, H.; Sanui, K.; Ogata, N.; Okano, T.; Sakurai, Y. *Macromolecules* 1994, 27, 947-952.
[96] Schild, H. G. *Prog. Polym. Sci.* 1992, 17, 163–249.
[97] Zhang, X. Z.; Yang, Y. Y.; Chung, T. S.; Ma, K. X. *Langmuir* 2001, 17, 6094–6099.
[98] Wang, X.; Qiu, X.; Wu, C. *Macromolecules* 1998, 31, 2972-2976.
[99] Wang, X.; Wu, C. *Macromolecules* 1999, 32, 4299-4201.
[100] Feil, H.; Bae, Y. H.; Feijen, J.; Kim, S.W. *Macromolecules* 1993, 26, 2496–2500.
[101] Na, K.; Park, J. H.; Kim, S. W.; Sun, B. K.; Woo, D. G.; Chung, H. M.; Park, K. H. *Biomaterials* 2006, 27, 5951–5957.
[102] Hatakeyama, H.; Kikuchi, A.; Yamato, M.; Okano, T. *Biomaterials* 2006, 27, 5069–5078.
[103] Liu, Y. Y.; Shao, Y. H.; Lü , J. *Biomaterials* 2006, 27, 4016–4024.
[104] Coughlan, D. C.; Quilty, F. P.; Corrigan, O. I. *J. Control. Release* 2006, 98, 97–114.
[105] Vihola, H.; Laukkanen, A.; Valtola, L.; Tenhu, H. *Biomaterials* 2005, 26, 3055-3064.
[106] Laukkanen, A.; Wiedmer, S. K.; Varjo, S.; Riekkola, M. L.; Tenhu, H. Colloid Polym. Sci. 2002, 280, 65-70.
[107] Verbrugghe, S.; Laukkanen, A.; Aseyev, V.; Tenhu, H.; Winnik, F. M. *Polymer* 2003, 44, 6807-6814.
[108] Vihola, H.; Laukkanen, A.; Tenhu, H. *J. Pharm. Sci*. 2008, 97, 4783-4793.
[109] Imaz, A.; Forcada, J. *J. Polym. Sci., Part A: Polym. Chem.* 2008, 46, 2766-2775.
[110] Lau, A. C. W.; Wu, C. *Macromolecules* 1999, 32, 581-584.
[111] Mardyani, S.; Chan, W. C. W.; Kumacheva, E. *Adv. Mater.* 2006, 18, 80–83.
[112] Soppimath, K. S.; Tan, D. C. W.; Yang, Y. *Adv. Mater.* 2005, 17, 318–323.
[113] Liang, X.; Kozlovskaya, V.; Chen, Y.; Zavgorodnya, O.; Kharlampieva, E. *Chem. of mater.* 2012, 24, 3707−3719.
[114] Guiseppi-Elie, A.; Sheppard, N. F.; Brahim, S.; Narinesingh, D. *Biotechnol. Bioeng* 2001, 75, 475–484.
[115] Kawaguchi, H.; Fujimoto, K. S. *Bioseparation* 1998, 4, 253–258.
[116] Solomon, O.F.; Corciovei, M.; Boghina, C *J. Appl. Polym. Sci.* 1968, 12, 1835-1842.
[117] Solomon, O.F.; Corciovei, M.; Boghina, C *J. Appl. Polym. Sci.* 1968, 12, 1843-1851.
[118] Solomon, O.F.; Vasilescu, D. S.; Tatarescu, T. *J. Appl. Polym. Sci.* 1969, 13, 1-7.
[119] Cheng, S. C.; Feng, W.; Pashikh, I. I.; Yuan, L. H.; Deng, H. C.; Zhou, Y. *Radiation Physics and Chemistry* 2002, 63, 517-519.
[120] Lozinsky, V. I.; Simenel, I. A.; Kurskaya, E. A.; Kulakova, V. K.; Galeav, I.Y.; Mattiasson, B.; Grinberg, V. Y.; Khoklov, A. R. *Polymer* 2000, 41, 6507-6518.
[121] Pich, A.; Tessier, A.; Boyko, V.; Ly, Y.; Adler, H. J. P. *Macromolecules* 2006, 39, 7701–7707.
[122] Loos, W.; Verbrugghe, S.; Goethals, E. J.; Du Prez, F. E.; Bakeeva, I. V.; Zubov, V. P. *Macromol Chem Phys* 2003, 204, 98–103.
[123] Van Durme, K.; Verbrugghe, S.; Du Prez, F. E.; Van Mele, B. *Polymer* 2003, 44, 6807–6814.
[124] Laukkanen, A.; Hietala, S.; Maunu, S. L.; Tenhu, H. *Macromolecules* 2000, 33, 8703–8708.

[125] R. Moerkerke, F. Meeussen, R. Koningsveld, H. Berghmans, W. Mondelaers, E. Schacht, K. Dusek, K. Solc, *Macromolecules* 1998, 31, 2223-2229.
[126] Gan, L. H.; Roshan Deen, G.; Loh, X. J.; Gan, Y.Y. *Polymer* 2001, 42, 65–69.
[127] Gan, L. H; Gan, Y. Y.; Deen, G. R. *Macromolecules* 2000, 33, 7893–7897.
[128] Rueda, J.; Zschoche, S.; Komber, H.; Schmaljohann, D.; Voit, B. *Macromolecules* 2005, 38, 7330–7336.
[129] Urry, D.W. *J. Phys. Chem. B* 1997, 101, 11007-11028.
[130] Tonge, S. R.; Tighe, B. J. *Adv. Drug Delivery Rev.* 2001, 53, 109–122.
[131] Philippove, O. E.; Hourdet, D.; Audebert, R.; Khokhlov, A. R. *Macromolecules* 1997, 30, 8278–8285.
[132] Pojman, J. A.; Griffith, J.; Nichols, H. A. *e-Polymers* 2004, 13, 1–7.
[133] Perry, M. F.; Volpert, V. A.; Lewis, L. L.; Nichols, H. A.; Pojman, J. A. *Macromol. Theory Simul.* 2003, 12, 276–286.
[134] Torres-Lugo, M.; Peppas, N. A. *Macromolecules* 1999, 32, 6646–6651.
[135] Kang, S. I.; Bae, Y. H. *J. Control. Release* 2003, 86, 115–21.
[136] Pinkrah, V. T.; Snowden, M. J.; Mitchell, J. C.; Seidel, J.; Chowdhry, B. Z.; Fern, G. R. *Langmuir* 2003, 19, 585–590.
[138] Schacher, F.; Müllner, M.; Schmalz, H.; Müller, A. H. E. *Macromol. Chem. Phys.* 2009, 210, 256–262.
[138] Lee, A. S.; Butun, V.; Vamvakaki, M.; Armes, S. P.; Pople, J. A.; Gast, A. P. *Macromolecules* 2002, 35, 8540–8551.
[139] Schmalz, A.; Hanisch, M.; Schmalz, H.; Müller, A. H. E. *Polymer* 2010, 51, 1213–1217.
[140]Sutton, R. C.; Thai, L.; Hewitt, J. M.; Voycheckand, C. L.; Tan, J. S. *Macromolecules* 1988, 21, 2432-2439.
[141] Firestone, B. A.; Siegel, R. A. *J. Polym. Sci. Part A: Polym. Chem.* 1991, 43, 901-914.
[142] Alvarez-Lorenzo, C.; Concheiro, A. *J. Control. Release* 2002, 80, 247–257.
[143] Yan, G.; Robinson, L.; Hogg, P. *Radiography* 2007, 13, e5–e19.
[144] Liu, C.; Shan, Y.; Zhu, Y.; Chen, K *Thin Solid Films* 2009, 518, 324–327.
[145] Patel, V. R.; Amiji, M. M. *Pharm. Res.* 1996, 13, 588-593.
[146] Gupta, V; Shivakumar, N.; Shivakumar, H. G. *Curr. Drug Deliv.* 2009, 6, 505-510.
[147] Hoffman, A. S. In Intelligent Polymers, Controlled Drug Delivery: Challenge and Strategies. American Chemical Society, Washington DC, USA, 1997.
[148] Yuk, S. H.; Cho, S. H.; Lee, H.B. *Pharm. Res.* 1992, 9, 955–95.
[149] Osada, Y.; Hasebe, M. *Chem. Lett.* 1985, 9, 1285–1288.
[150] Osada, Y.; Gong, J.P. *Adv. Mater.* 1998, 10, 827–837.
[151] Guiseppi-Elie, A. *Biomaterials* 2010, 31, 2701–2716.
[152] Shiga, T.; Hirose, Y.; Okada, A.; Kurauchi, T. *J. Appl. Poly. Sci.* 1992, 46, 635–640.
[153] Tanaka, T.; Nishio, I.; Sun, S. T.; Ueno-Nishio, S. *Science* 1982, 218, 467–469.
[154] Ramanathan, S.; Block, L. H. *J. Control. Release* 2001, 70, 109–123.
[155] Jensen, M.; Hansen, P. B.; Murdan, S.; Frokjaer, S.; Florence, A.T. *Eur. J. Pharm. Sci.* 2002, 15, 139–148.
[156] Yang, Y.; Engberts, J. B. F. N. *Coll. Surf. A: Physicochem. Eng. Aspects* 2000, 169, 85–94.
[157] Gong, J .P.; Nitta, T.; Osada, Y. *J. Phys. Chem.* 1994, 98, 9583– 9587.
[158] Budtova, T.; Suleimenov, I.; Frenkel, S. *Polym. Gels Networks* 1995, 3, 387–393.
[159] Yuk, S. H.; Cho, S. H.; Lee, H. B. *Pharm. Res.* 1992, 9, 955–957.
[160] Sawahata, K.; Hara, M.; Yasunaga, H.; Osada, Y. *J. Control. Release* 1990, 14, 253–262.
[161] Kwon, I. C.; Bae, Y. H.; Kim, S. W. *Nature* 1991, 354, 291–293.
[162] Kwon, I. C.; Bae, Y. H.; Kim, S. W. *J. Control. Release* 1994, 30, 155–159.
[163] Yoshida, R.; Sakai, K.; Okano, T.; Sakurai, Y. *Adv. Drug Deliv. Rev.* 1993, 11, 85–108.
[164] Sawahata, K.; Hara, M.; Yasunaga, H.; Osada, Y. *J. Controlled Release* 1990, 14, 253–262.
[165] Kwon, I. C.; Bae, Y. H.; Okano, T.; Kim, S.W. *J. Controlled Release* 1991, 17, 149–156.
[166] Kwon, I. C.; Bae, Y. H.; Kim, S. W. *Nature* 1991, 354, 291–293.
[167] Kajiwara, K.; Ross-Murphy, S.B. *Nature* 1992, 355, 208–209.
[168] Osada, Y.; Okuzaki, H.; Hori, H. *Nature* 1992, 355, 242–244.
[169]Rosenweig, R. E. (1985) Ferrohydrodynamics. Cambridge University Press, Cambridge.
[170] Jones, T. B. In Electromechanics of particles. Cambridge University Press, UK, 1995.
[171] Zrinyi, M. *Colloid Polym Sci* 2000, 278, 98–103.

[172] Chatterjee, J.; Haik, Y.; Ching, J. C. *J Magn Magn Mater* 2001, 225, 21–29.
[173] Popovic, Z.; Sjostrand, J. *Vision Res* 2001, 41, 1313–1319.
[174] Liberti, P. A.; Rao, C. G.; Terstappen, L. W. M. *J Magn Magn Mater* 2001, 225, 301–307.
[175] Shinkai, M.; Yanase, M.; Suzuki, M.; Honda, H.; Wakabayashi, T.; Yoshida, J. et al. *J Magn Magn Mater* 1999, 194, 176–184.
[176] Golui, S.; Datta, D.; Bohadur, D. In Studies on sol–gel derived and melt quenched magnetic oxide base bioceramics in $CaO–Na_2–O–P_2O_5–Fe_2O_3–SiO_2–B_2O_3$ system. In: Ferrites proceedings of the eighth international convence on ferrites (ICF8) 2000, vol. 115. 2001).
[177] Reynolds, A. Frimpong, Stew Fraser, J. Zach Hilt 2006 DOI: 10.1002/jbm.a.30962.
[178] Buchholz, F. L.; Graham, A. T. In Modern Superabsorbent Polymer Technology, Wiley- VCH, New York, USA, 1998.
[179] Brannon-Peppas, L.; Harland, R. S. In Absorbent Polymer Technology, Elsevier, Amsterdam, Netherland, 1990.
[180] Chen, J.; Park, K. J. *Biomed Mater Res* 1999, 44, 53-62.
[181] Van Dijk-Wolthuis, W. N. E.; Tsang, S. K. Y.; Kettenes-Van den Bosch, J. J.; Hennink, W. E. *Polymer* 1997, 38, 6235-6242.
[182] Lee, Y. M.; Soo Kim, S. *Polymer* 1997, 38, 2415-2420.
[183] Zohuriaan-Mehr, M. J. In Super-Absorbents (in Persian), Iran Polymer Society, Tehran, 2-4, 2006.
[184] Omidian, H.; Hashemi, S. A.; Askari, F.; Nafisi, S. *J. Appl. Polym. Sci.* 1994, 54, 241-249.
[185] Omidian, H.; Hashemi, S. A.; Askari, F.; Nafisi, S. *J. Appl. Polym. Sci.* 1994, 54, 251-256.
[186] Buchholz, F. L.; Peppas, N. A. In Superabsorbent Polymers Science and Technology, ACS Symposium Series, 573, American Chemical society, Washington DC, USA, 1994.
[187] Trijasson, P.; Pith, T.; Lambla, M. *Macromol Chem Macromol Symp* 1990, 35/36, 141-169.
[188] Das, A.; Kothari, V. K.; Makhija, S.; Avyaya, K. *J. Appl. Polym. Sci*. 2008, 107, 1466-1470.
[189]Dorkoosh, F. A.; Brussee, J.; Verhoef, J. C.; Borchard, G.; Tehrani, M. R.; Junginger, H. E. *Polymer* 2000, 41, 8213–8220.
[190] Ende, M.; Hariharan, D.; Peppas, N. A. *React Polym* 1995, 25, 127–137.
[191] Raju, K. M.; Raju, M. P.; Mohan, Y. M. *Polym Int* 2003, 52, 768–772.
[192] Shiga, T.; Hirose, Y.; Okada, A.; Kurauchi, T. *J. Appl. Polym. Sci*. 1992, 44, 249–253.
[193] Jong, H. P.; Dukjoon, K. *J. Appl. Polym. Sci*. 2001, 80, 115-121.
[194] Omidian, H.; Roccaa, J. G.; Park, K. *J Controlled Release* 2005, 102, 3-12.
[195] Wu, L.; Liu, M. Polym Adv Tech, 2008, in press (DOI:10.1002/pat.1034).
[196] Abedi-Koupai, J.; Sohrab, F. *J Polym Sci Technol (Persian)* 2004, 17, 163-173.
[197] Abd El-Rehim, H. A.; Hegazy, E. S. A.; Abd El-Mohdy, H. L. *J Appl Polym Sci* 2004, 93, 1360-1371.

CHAPTER II

GRAPHENE

Graphene is a planar monolayer of sp^2-hybridized carbon atoms, arranged into a two-dimensional honeycomb lattice,[1] with a carbon-carbon bond length of 0.142 nm.[2] Each carbon atom in the lattice has a π orbital that contributes to a delocalized network of electrons. In fact, each electron belonging to a non hybridized p orbital is shared with the other carbon atoms and fits in a semi-full π band, thus making graphene a zero gap semi-conductor.

Graphene can be defined in different ways as a function of the number of layers: *single* layer graphene is a single two-dimensional hexagonal sheet of carbon atoms, *bi*-layer and *few*-layer graphenes have 2 and 3-to-10 layers of such two-dimensional sheets, respectively. In *bi*- and *few*-layer graphene, carbon atoms can be stacked in different ways, generating hexagonal or AA stacking, Bernal or AB stacking and rhombohedral or ABC stacking (Figure II.1.).

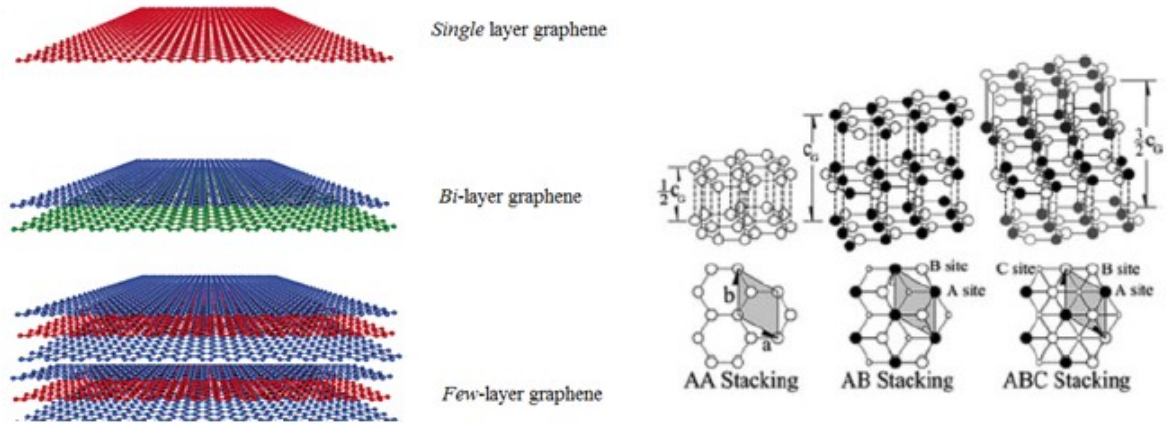

Figure II.1 The three most common structures and stacking sequences of graphene

Therefore, graphene represents the first example of two-dimensional atomic crystal. Even if the bi-dimensionality is preserved until a maximum of 10 layers, graphene properties are strongly influenced by the number of the layers:[3] when the number of layers goes from 2 to 3, there are a significant change in the physical and chemical properties of the material, while, if they increase from 3 to 10 the properties do not vary.[1]

History of graphene

Although the use of graphite started 6000 years ago, the research about graphene dates back to the birth and developing of graphite intercalation compounds (GICs). The earliest reports of GICs can be traced back

to the 1840s, when the German scientist Schafhaeutl reported the intercalation, which is the insertion of small-molecule species (acid or alkali metals) between the carbon lamellae, and exfoliation of graphite with sulfuric and nitric acids.[4] Lately, potassium, fluoride salts, transition metals such as iron, nickel,[5,6] and various organic molecules[7] were used as intercalants and exfoliants. In GICs, the stacked structure of graphite is retained while the interlayer spacing is widened by several angstroms, resulting in the electronic decoupling of the individual layers.

In the following years, many scientists tried to modify this method by using strong acids (sulfuric and nitric) or oxidants ($KClO_3$), obtaining not only GICs, but also the chemical oxidation of graphite and the formation of graphite oxide.[8,9] Functionalization of graphite surface in this manner decreases the interplanar forces that cause lamellar stacking; thus, these oxidized layers can be readily exfoliated under ultrasonic, thermal, or other energetic conditions. Consequently, these intercalation and oxidation experiments are the first examples of the delamination of graphite into its constituent lamellae, and a first step toward the obtainment of graphene.

In 1962 Boehm et al. succeeded to produce thin lamellar carbon containing small amounts of hydrogen and oxygen, by chemical reduction of graphite oxide dispersion in dilute alkaline media with hydrazine, hydrogen sulfide and ferrous salts. The thickness was determined by electron-micrograph densitometry measurements and was about 4.6 Å, slightly different from the value observed in previous works (4.0 Å). Nevertheless, Boehm stated that his results confirmed that the thinnest of the lamellae really consisted of *single* carbon layers. However, he obtained the so-called reduced graphene oxide (r-GO) rather than pristine graphene.[10,11]

In 1968, Morgan and Somorjai used low-energy electron diffraction (LEED) to examine the adsorption of various gaseous organic molecules (e.g., CO, C_2H_4, C_2H_2) onto a platinum (100) surface at high temperature.[12] Taking into account the LEED data obtained by Morgan et al., May postulated in 1969 that single, as well as multiple, layers of a material that characterizes a graphitic structure were present on the platinum surface, as a result of these adsorption processes.[13]

Afterward, various techniques were employed to synthesize graphene, such as the method used for the growth of carbon nanotubes,[14] which produced graphite with 100 layers of graphene, the chemical vapor deposition (CVD) on metal surfaces[15,16] or the thermal decomposition of SiC.[17] Although these approaches did not produce perfect monolayer graphene, the studies showed high-charge mobility of a *few* layers of graphene, and the CVD approach has been optimized and become a major technique to produce graphene nowadays.[18-20]

In 1999, a micromechanical approach was used to obtain thin lamellae comprising multiple graphene layers, although these lamellae were not fully exfoliated into their respective monolayers.[21,22] In this

method, lithographic patterning of highly ordered pyrolytic graphite (HOPG) was combined with oxygen-plasma etching to create pillars, which were converted into the thin lamellae by rubbing.

Once understood the extraordinary potential of this mechanical approach, Andre Geim and Konstantin Novoselov, in 2004, demonstrated that graphene can be isolated and its outstanding properties analyzed.[23] They developed a simple and efficient method based on the mechanical exfoliation of graphite: when graphite surface was pressed against a scotch tape and then removed, thin flakes of graphene could be obtained. By repeating many times this operation, they succeeded to isolate graphene layers having infinitesimal thicknesses, which were located by optical microscopy and electrically characterized.

The carbon samples produced by this technique were largely free from the significant presence of functional groups, as determined by X-ray photoelectron spectroscopy (XPS), elemental analysis, and other spectroscopic techniques.

Since then, the research of graphene including the control of the graphene layers on substrates, functionalizing graphene and exploring the applications of graphene has grown exponentially.

The term ‘‘graphene’’ replaced the older term ‘‘graphite layers’’, which was unsuitable in the research of *single* carbon layer structure, because a three-dimensionally stacking structure is identified as ‘‘graphite’’.

The recent definition of graphene can be given as a two-dimensional monolayer of carbon atoms, which is the basic building block of various carbon allotrope materials (i.e. fullerene, carbon nanotube, graphite).

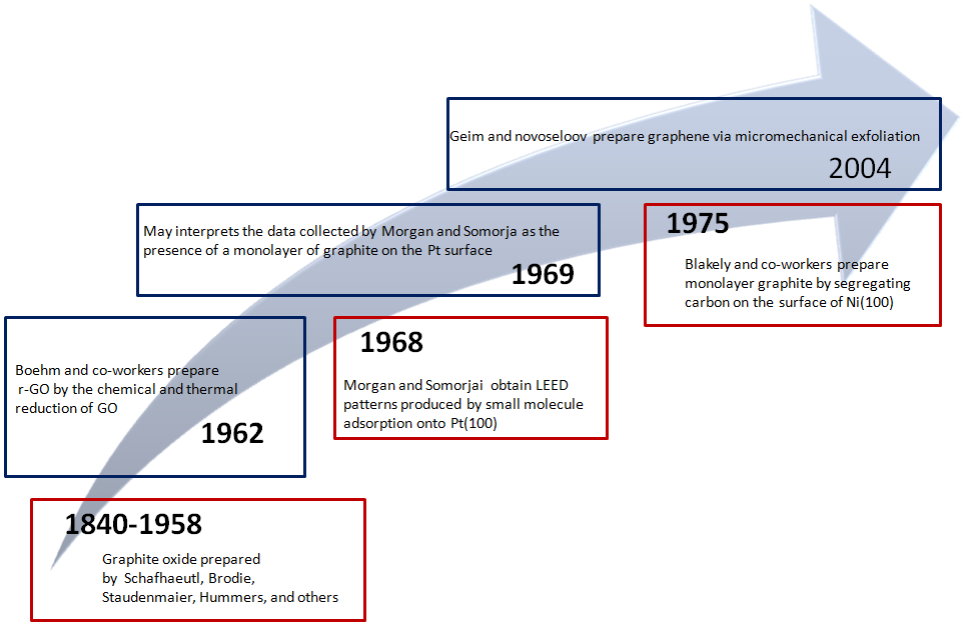

Figure II.2 Timeline of selected events in the history of the preparation, isolation, and characterization of graphene

II. 1 PROPERTIES OF GRAPHENE

If compared with other allotropic forms of carbon, graphene exhibits peculiar features that are object of study and development in all the most advanced technological fields. In fact graphene is characterized by high electron mobility at room temperature, extraordinary thermal and electric conductivity, high Young modulus, and tensile strength, which will be widely discussed in this section.

II.1.1 ELECTRICAL PROPERTIES

Graphene has a unique electronic structure, which leads to a number of extraordinary properties not seen in conventional materials.

To fully understand graphene electron properties is necessary to describe electron behavior by quantum electrodynamic (QED), rather than by traditional quantum mechanics.

Graphene electronic properties vary as a function of layer number and interlayer ordering. *Single* layer graphene exhibits an unusual band structure, where two bands intersect in equivalent point K and K' in the reciprocal space (Figure II.3a). The charge carriers in this structure, known as mass-less Dirac fermions, are electrons losing their rest mass, m_0, and can be described by (2 + 1)-dimensional Dirac equations, rather than Schroedinger classical ones.[24-26]

K and K' are referred as Dirac points, where valence and conduction bands are degenerated, making graphene a zero band gap semiconductor. This unique band structure has made *single* layer graphene a fascinating system for the study of QED.

However, the absence of permanent band gaps in graphene sheets makes their integration into conventional semiconductor device architectures difficult. For such a reason, an increasing number of research projects are focused on the functionalization of graphene, including reactions of graphene and its derivatives with organic and inorganic molecules, and the chemical modification of its large surface.[27-29] Besides, band gap opening of graphene can be obtained by doping, intercalation and striping, making it useful for functional nano-electronic devices.[30,31]

Single layer graphene is also characterized by a high electronic conductivity, ca. 6000 S/cm.[32] This is mainly due to the low defects density of its crystal lattice, and thus to its high quality. Generally, defects can act as scattering sites and inhibit charge transport, by limiting the electron mean free path. There are evidences that pristine graphene is defect free, thus its conductivity must be affected by some extrinsic source, such as interaction with the under laying substrate during measurement, surface charge traps,[33,34] interfacial phonons,[35] and substrate ripples.[36] As a zero band gap semiconductor, graphene displays an ambipolar electric field effect and charge carriers can be continuously tuned between electrons and holes in

concentrations as high as 10^{13} cm^{-2}, with room temperature mobility of up to 15 000 cm^2 V^{-1} s^{-1}, by applying the required gate voltage.[23,37,38]

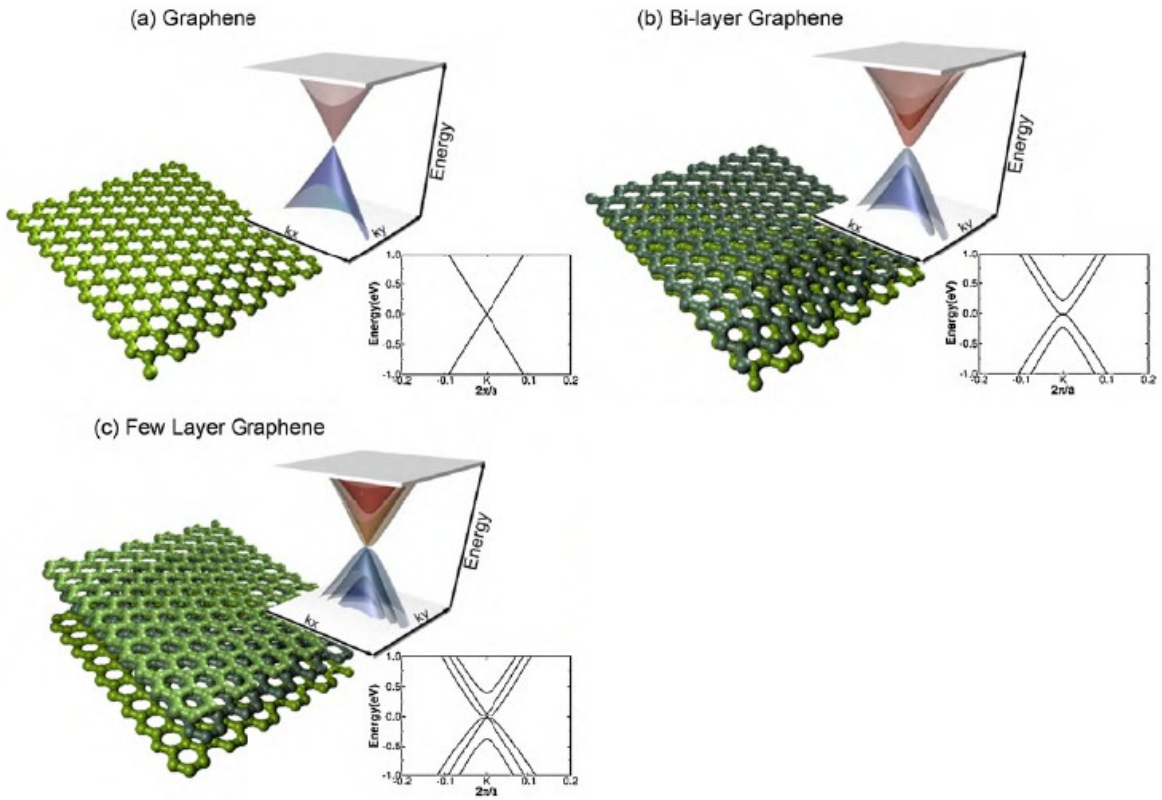

Figure II. 3. Low energy DFT 3D band structure for (a) graphene, (b) *bi*-layer graphene and (c) *tri*-layer graphene. (a) exhibits the characteristic Dirac Point. It is lost in bi-layer graphene (b), but appears again in three-layer graphene (c).

Bi-layer graphene is likewise a zero-gap semiconductor, but its electrons obey to a parabolic energy dispersion (Figure III.3b). In contrast to *single* layer graphene, charge carriers in *bi*-layer graphene have finite mass and are called massive Dirac fermions. The structure also shows an anomalous quantum hall effect (QHE), even if different from that of *single* layer graphene and as a result, it remains metallic at the neutrality points.[39]

Different experiments have also shown that a tunable band gap of several hundred meV can be induced in *bi*-layer graphene by breaking the symmetry between the two graphene layers using a carefully applied gate bias (Figure II.4b).[40] This results in formation of a semiconducting gap and restoration of normal QHE, making *bi*-layer graphene useful for novel optoelectronic applications and future microprocessors.

In contrast, *tri*-layer graphene shows an interesting band structure, which looks like a combination of the *single* and the *bi*-layer ones. It is a semimetal with a band overlap that can be controlled by an external electric field.[41] These properties only hold for multilayer graphene with the Bernal ABAB stacking found in natural graphite. Deviations from this stacking arrangement, both through lateral translation or angular

misorientation, can affect interlayer interactions and sometimes induce behavior similar to that of *single* layer graphene.[42]

In general, for *few*-layer graphene with N layers (AB stacking), there will be a linear band (Dirac fermions) if N is odd.[43] As the number of layers increases, the band structure becomes more complicated, several charge carriers appear[23,44] and the conduction and valence bands start notably overlapping.[23]

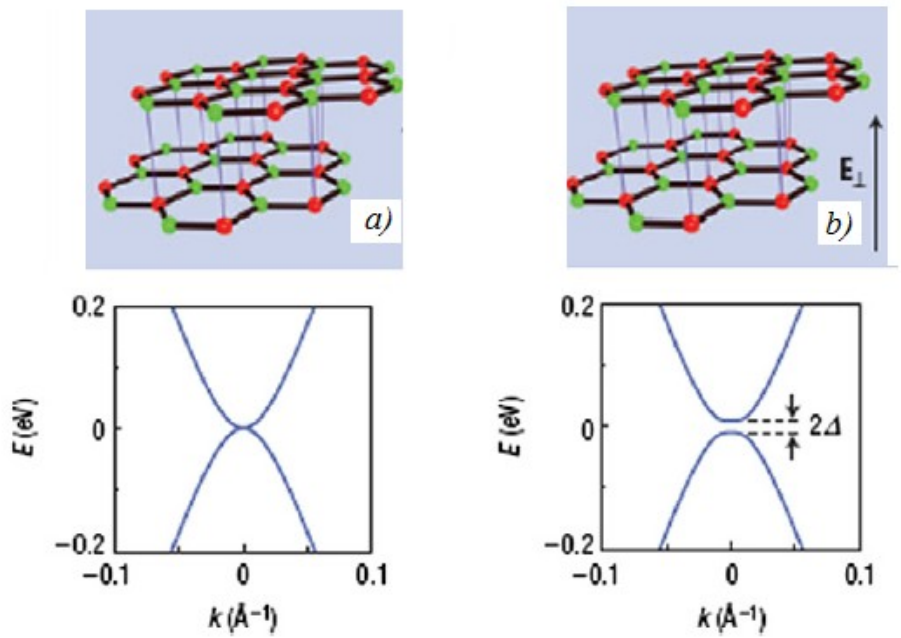

Figure II.4 Schematic diagrams of the lattice structure of bi-layer graphene in absence (a) and in present of perpendicularly applied electric field (b), which opens a band gap in bi-layer graphene, whose size (2D) is modulated by the electric field.

A peculiar feature of graphene is its characteristic Hall effect: in the traditional Hall effect, electric current, flowing on the metal surface under the presence of a transverse magnetic field, produces a potential difference (Hall potential) between the two metal faces. Because of the ratio between the potential difference and the flowing current (Hall resistivity) is directly proportional to the applied magnetic field, Hall effect is usually employed for the measurement of magnetic fields. In a bi-dimensional metal system, at temperature close to the absolute one, Hall resistivity becomes quantized, and assumes values around h/ne^2 (where h is the Plank's constant, n a positive integer number and e is the electric charge). This phenomenon is known as QHE.[47] However, graphene exhibits a different QHE. Because of the quantum-mechanic effect, named Berry's phase, Hall resistivity assumes only values for which n is an odd integer number. These properties was observed for the first time by Novoselov et al. at environmental temperature and not near the absolute zero, as seen in the metals.[48] This is due to the fact that, in graphene, the magnetic energy of electron is 1000 times higher than that of other materials. For *bi*-layer

graphene QHE is different and can be used to discriminate between the different pseudodimensional structures of graphene.

Another key feature of graphene, which is a product of its electron transport chiral nature, is Klein tunneling, as explained by Katsnelson et al.[26] Graphene electrons show a 100% transmission rate through a potential barrier of any size. The quantum mechanical explanation for this phenomenon is that in order for electrons traveling in one direction in a particular valley to be reflected back by the barrier, it must switch orientation, which is inhibited by conservation of chirality.[49,50] This can make working with graphene difficult, as square potential barriers used to form the device channel yield ineffective.

II.1.2 OPTICAL PROPERTIES

Graphene is almost transparent: it absorbs 2.3% of incident light over a broad wavelength range. Graphene transmittance can be well described in terms of fine structure constants. [51,52] The absorption of light was found to be directly proportional to the number of layers[53]: each layer has an absorbance value equal to A = 1- T = $\pi\alpha$ = 2.3%, where $\alpha\sim$ 1/37 is the fine structure constant, which determines the electromagnetic intensity of the material (Figure II.5). Graphene can also become photo-luminescent by inducing a suitable band gap. There are two methods for the obtainment of photo-luminescent graphene: the first method involves cutting graphene in nanoribbons and quantum dots, while the second one is based on the physical or chemical treatment with different gases, to reduce the connectivity of the π electron network.[54,55] For example, Gokus et al. made graphene luminescent by oxygen plasma treatment.[56] This allows to obtain hybrid structures by designing just the top layer, while keeping the underlying layer unaffected.

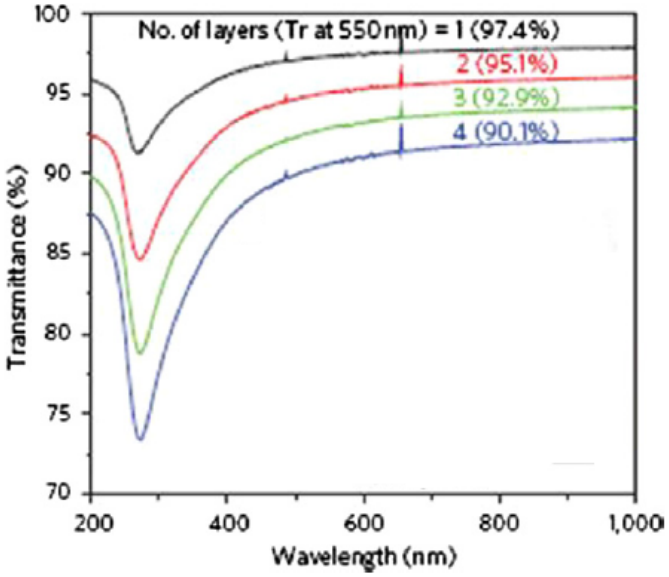

Figure II.5 UV–Vis spectra of roll-to-roll layer-by-layer transferred graphene films on quartz substrates. It can be seen how transmittance decreases with the number of graphene layers.

II.1.3 THERMAL PROPERTIES

Graphene also exhibits extraordinary thermal properties. It has a room temperature thermal conductivity of about 5000 W/mK ,[57,58] higher than that of carbon nanotubes (3000-3500 W/mK)[59] and diamond (2000 W/mK). [60] There are different methods to determine the thermal conductivity of graphene. Among them the opto-thermal Raman technique is the mainly used (Figure II.6). In this method, a suspended graphene layer is heated by laser light (488 nm), the heat propagated laterally towards the sinks on side of the corner of the flakes. The temperature change is determined by measuring the shift in the graphene G peak using confocal micro-Raman spectroscopy which acts as a thermometer.[58,61]

These outstanding thermal properties could be exploited in the fabrication of heat dissipaters and polymer composites with high thermal conduction.

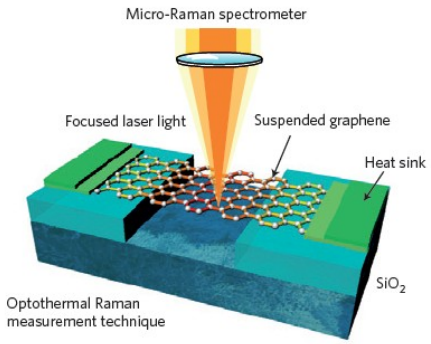

Figure II.6 Schematic experimental setup for measuring the thermal conductivity of graphene.

II.1.4 MECHANICAL PROPERTIES

Graphene is also being recognized as one of the strongest materials. It has a fracture strength of 130 GPa, 200 times higher than that of steel, and a Young modulus of 1 TPa, extremely close to that of diamond (1.2 TPa).[23]

All the mechanical properties can be investigated by atomic force microscopy (AFM) and Raman spectroscopy.

Compressive and tensile strain can be determined using Raman spectroscopy by monitoring changes in the G and 2D peaks with applied stress. Increasing the applied strain the G peak splits, while the 2D peak shifts toward higher wavelength, without splitting for strains < 0.8%.[62] Young's modulus can be estimated by using AFM. Lee et al. use this technique to value the elastic modulus through the nano-indentation of graphene membranes, suspended over holes of 1.0–1.5 μm in diameter on a silicon substrate.[63] They determined the variation of force with indentation depth and derived stress–strain curves by assuming that graphene behaved mechanically as a 2D membrane of thickness 0.335 nm. It was found that failure of

graphene took place by the bursting of the single molecular layer membrane at large displacements, with failure initiating at the indentation point.

Graphene can also be lengthened more than other crystalline materials: its length can be increased of about 20% related to its initial value.[63] Moreover it has unique mechanical properties: it is able to contract with the increase of temperature (expansion thermal coefficient =-7x10^{-6} K^{-1} at 300 K),[64] and it is both flexible and fragile.

II.1.5 MAGNETICAL PROPERTIES

Graphene also exhibits magnetic properties: in its structure there are ferromagnetic domains which coexist with antiferromagnetic ones, like phase separated materials.[65,66] Even if the origin of this magnetic behavior is still unknown, it is probably due to the presence of defects in the structure and irregularities at the edges of the graphene sheet.

II.1.6 CHEMICAL PROPERTIES

Highly crystalline graphene surfaces appear to be chemically inert, and usually interact with other molecules via physical adsorption (π–π interactions). However, it is possible to functionalize graphene surface by anchoring several chemical groups such as carboxyl (COOH), carbonyl (COH), hydrogenated (CH) and amines (NH_2) at the edges, which are more chemically reactive. In 2009, Novoselov et al. reported the obtainment of a fully hydrogenated graphene sheet, termed "*graphane*": the hydrogenation route is reversible at 450 °C, and unlike graphene, *graphane* behaves as a semiconductor (Figure II.7).[26] However, the synthesis of this compound still needs to be improved and further analysis related to the C—H bonding nature using XPS should be carried out.

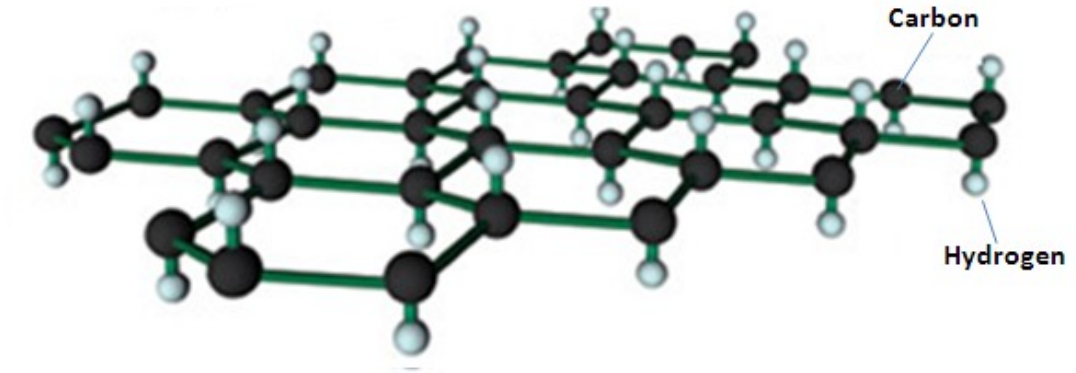

Figure II.7 Graphane structure.

In order to make the graphene surface more chemically reactive, either surface defects or high degrees of curvature need to be introduced. In several studies the graphene reactivity is increased by reacting it with halogen atom such as fluorine.[67]

II.1.7 OTHER PROPERTIES

Graphene has a high theoretical surface area of about 2630 m^2/g, while experimental values, measured by Brunauer–Emmett–Teller (BET) analysis, are included between 270 and 1150 m^2/g. It has also a density of 0.77 mg/m^2.

Another important feature of these extraordinary materials is its gas sensing ability. It was found that adsorbed gas molecules modify the local carrier concentration and a subsequent change in the resistance. Using this property of graphene, Schedin and colleagues prepared micron-level gas sensors, which can detect adsorption and desorption of single molecules of gases like CO, H_2O, NH_3 and NO_2.[68]

Because its honeycomb structure and its chemical inertia, graphene avoids the passage of small gaseous molecules, such as helium. It is an excellent barrier for any gas and can be used both to protect metal from corrosion and as a system for gas storing.

II.2 APPLICATIONS

Thanks to its extraordinary properties, graphene have been found application in field-effect transistors, in transparent conducting electrodes, in functional devices such as energy storage systems and photovoltaics, gas sensors, and in biological field.

Transparent conductors

Transparent conductors (TCs) are an essential part of different electronic devices, such as touch screen displays, electronic papers, organic light-emitting diodes (OLEDs), and other photonic technologies: they require a low sheet resistance with high transmittance (of over 90%) depending on the specific application. With high electrical conductivity, high carrier mobility, and moderately high optical transmittance in the visible range of the spectrum, graphene materials are the best candidates for the development of a new class of TCs. Although graphene meets the electrical and optical requirements, the traditionally used indium tin oxide (ITO) has still demonstrated better characteristic. Nevertheless, graphene is cheaper than ITO and is characterized by mechanical flexibility and chemical durability, important features for flexible electronic devices, in which ITO usually fails.[69] Beside, different researches have demonstrated that

graphene has a transmittance and sheet resistance combination comparable to conventional ITO, and can be a valid alternative to it as transparent conducting coating in electronic devices.

Solar cells and similar light harvesting devices are strongly influenced by the type of TC used. Transparent conducting films of solution-processed[70] and CVD grown graphene[71] have been used and implemented for inorganic,[72] organic,[73] hybrid[74] and dye sensitized solar cells (DSSC).[75] In particular for DSSC, graphene replaces ITO at the anode, reducing the recombination rate and thus improving the efficiency of the device.[76]

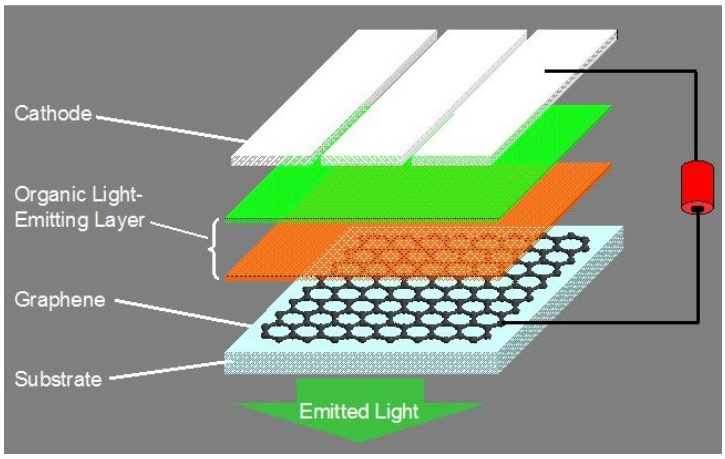

Figure II.8 OLED using graphene as transparent conductor.

Field effect transistors (FETs)

The exceptional carrier mobility and saturation velocity, as well as the bipolar nature of the carries, make graphene a valid alternative to Si in the development of field effect transistors (FETs) (Figure II.9). FETs are widely used in the field of digital electronics, and, although in lesser extent, in analogical electronic systems. FET is made up of a doped semiconductor substrate, usually Si, on which three terminals are applied: gate, sources and drain. The operation of these devices is based on the ability to control the electrical conductivity, and thus the electric current passing through it, by forming an electric field inside the system.

Graphene FET (GFET) devices exhibit better performance than those based on Si: experimental values of the field-effect mobility of graphene are one order of magnitude higher than that of Si. Moreover, the use of graphene affords to achieve chips having lower size than that of traditional FETs. In 2008 the world smallest transistor, having a thickness of one atom and a width of about ten, was created.[77] GFETs having 100 GHz switching frequency are reported by Lin et al.[78] Graphene *p-n* junctions, in which carrier type and density in two adjacent regions were locally controlled by electrostatic gating, have been reported.[79]

Unfortunately, GFETs cannot be turned off effectively due to the absence of a band gap and therefore are not suitable for logic applications. Several researches are being targeted at opening a band gap in

graphene: single electron transistors[77] and nanoribbons formation,[80] bi-layer control[81] and chemically modified graphene.[82] However, all of these approaches have so far been unable to open a band gap wider than 360 meV,[83] limiting the on/off ratio to about 10^3, much less than the required 10^6. Moreover, they can often introduce defects and contaminants into GFETs, damaging its performance.[84]

The issue of the low on/off ratio is resolved in the new transistor designs, which exploits the modulation of the work function of graphene, gaining control over vertical transport through various barriers.[85] Although such devices allow for on/off ratios of 10^6, more work on integration is required to enable the full use of graphene for logic applications.

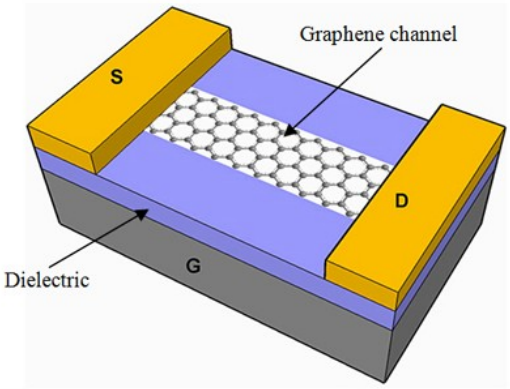

Figure II.9 Structure of field effect graphene: a source and a drain are connected through a graphene channel, which allows the passage of an electron at once.

Chemical and biological sensors

Another interesting application of graphene is in the field of the chemical and biological sensors. Its ultra-sensibility is due to its large surface area, its single-atom thickness and its low electric noise, and can be improved by functionalizing graphene with various organic and inorganic species (atoms, nanoparticles, polypeptides and nucleotides). The atomically thin structure can also enable many novel sensing schemes, such as nanoporous membranes for DNA probing and sequencing.[86,87]

There are two types of chemical sensors based on graphene: the GFETs, in which a variation in the conductivity responds to nearby charge fluctuation brought by molecular binding near or on graphene, and graphene or graphene-derivate electrochemical sensors, which detect redox potential and the current of certain species.

Different studies have shown that graphene molecular sensors are able to detect gases such as NO_2, NH_3, H_2 and CO with a sensibility up to some parts per million.[88]

Lu et al. observed that GFETs, having graphene functionalized with single stranded DNA, are highly sensitized towards vapor analytes.[89]

Graphene is also involved in other sensing schemes such as fluorescence resonance energy transfer sensing and surface acoustic wave transducer-based gas sensors.[90]

To realize biological sensors, graphene has been functionalized with receptors that selectively bind to specific target species. In fact, ultrasensitive devices based on graphene are able to detect a range of biological molecules such as glucose, cholesterol, hemoglobin and DNA. Ohno et al. obtained an aptamer (specific oligonucleotide or peptide filaments) modified GFETs, having a high sensitivity and good selectivity toward immunoglobulin E protein.[91]

Drug delivery systems and bio-applications

Recently, graphene has gained great attention in biologic and biotechnological field due to its large surface area, chemical purity and its ability to be easy functionalized. Graphene can solubilize and bind drug molecules, acting as a drug delivery vehicle: thanks to its lipophilic character, graphene affords the passage of some drugs through biological membranes. Most of the limited work that has been done so far is focused on investigating the loading and in vitro behavior or aromatic anticancer drugs.[92] However, given the safety and regulatory obstacles and long timescale associate with drug development, graphene-based drug delivery systems will be commercially introduced in 15 years.

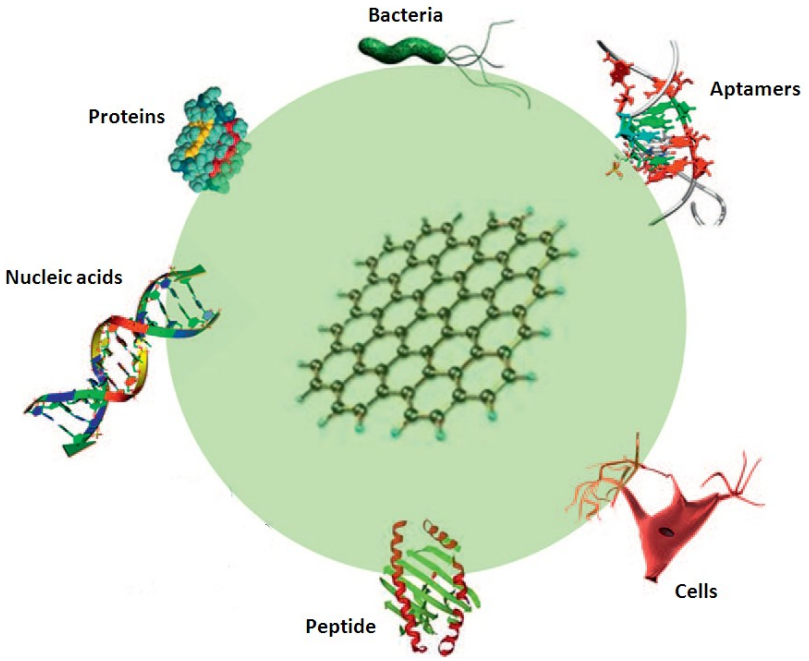

Figure II.10 Graphene and its derivatives have been reported to be functionalized with peptides, DNAs, proteins, aptamers, and cells through physical adsorption or chemical conjugation. The functionalized graphene biosystems with the unique properties have been used to build up biosensors, and biodevices.

Thanks to its extraordinary mechanical properties graphene can also found application in tissue engineering field. In fact graphene could be incorporated into the scaffold material to enhance its mechanical properties and modulate its biological performance in areas such as cell adhesion and proliferation.[92]
Moreover, various graphene-based nanomaterials have been used to fabricate functionalized biosystems integrated with nucleic acids, peptides, proteins and even cells (Figure II.10).[93,94]
Nevertheless, it is important to underline that before graphene can be widely used in such biomedical applications, the understanding of its biocompatibility, biodistribution and its toxicity is needed. There are still few studies related to graphene toxicity, which is strongly influenced by graphene morphology, size and synthetic method.

Electrochemical devices

Recently, graphene has been used as a material for the construction of supercapacitors, thanks to its high intrinsic electrical conductivity, good resistance to oxidative processes, high temperature stability and an accessible and defined pore structure. In 2009, Stoller et al. realized the first prototype of graphene-based electrochemical double-layer capacitors, having an optimal energy and density power (Figure II.11).[95]

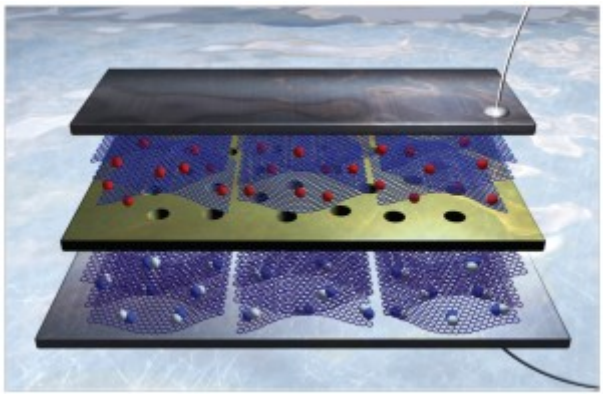

Figure II. 11 In a supercapacitor device two high-surface-area graphene-based electrodes (blue and purple hexagonal planes) are separated by a membrane (yellow). Upon charging, anions (white and blue merged spheres) and cations (red spheres) of the electrolyte accumulate at the vicinity of the graphene surface. Ions are electrically isolated from the carbon material by the electrochemical double layer that is serving as a molecular dielectric.

Graphene nanosheets are also used as support material for platinum catalysis in fuel cells. Due to the strong interaction with platinum and its small particle sizes, graphene leads to an increase of the catalytic activity in methanol fuel cells.[96]
However, in order to replace the common supporting material (activate carbon, carbon black, graphite) in such devices, graphene must be superior in terms of performance and cost.

With its high theoretical surface area and ability to facilitate electrons or hole transfer along its two-dimensional surface, graphene can be also used in lithium ions batteries. The introduction of graphene should help to overcome some issue due to the poor electrical conductivity, and should give rise to novel core–shell or sandwich-type nanocomposite structures.[97] Yoo et al. demonstrated that the use of graphene nanosheets in conjunction with carbon nanotubes and fullerenes increased the battery charge capacity.[98]

Polymer nanocomposites

One of the most important applications of graphene is in the field of polymer nanocomposites, where graphene is introduced as filler with the aim to improve their chemical and physical properties. As will be described in Paragraph IV.2.1 several polymer nanocomposites containing graphene has been prepared, such as polystyrene (PS),[99] PMMA,[94] PVA,[100] polypropylene (PP),[101] epoxy,[102] polyester,[103] silicon foams,[104] polyurethanes (PU)[105] and polycarbonates (PC).[106] The benefits related to the introduction of graphene in nanocomposite systems lead to the obtainment of elastic, lightweight and extremely strong materials, which could be found application in automotive, aerospace and aeronautic field.

II.3 GRAPHENE SYNTHESIS METHODS

As from graphene isolation by Geim and Novoselov, incredible efforts have been made to develop synthetic methods for graphene, in order to achieve high yields of production and also to realize the solution or thin film based process. Among them, four are of great importance: micromechanical exfoliation, CVD, epitaxial growth on crystalline silicon carbide and methods based on the obtainment of graphene colloidal suspensions.

The CVD and the epitaxial growth are both defined as *bottom-up* processes and afford to obtain defect-free graphene, having high surface. On the contrary, the methods based on the obtainment of graphene colloidal suspension are named *top-down* approaches and are advantageous in terms of high yields and easy of implementations.

II.3.1 MICROMECHANICAL EXFOLIATION

Graphite is made up of stacked layers of many graphene sheets, bonded together by week Van der Waals forces.

The first method to be described is that of micromechanical exfoliation, used by Novoselov and Geim to isolate graphene for the first time.[23] The method is based on the use of mechanical energy for breaking the weak Van der Waals forces, which bounded together the many graphene sheets which constitute graphite.

As described previously, this technique, formally known as “Scotch tape method” is quite simple and allows obtaining high quality graphene, having lateral dimensions on the order of tens to hundreds of micrometers. The process was later used to produce two-dimensional atomic crystals of many other materials, including BN and MoS_2.[107] Although the micromechanical exfoliation does not yet appear to be scalable to large area, it is suited for the study of fundamental properties such as ballistic transport,[108] carrier mobility,[109,110] thermal conductivity[111] and so on. In fact, if compared with chemical exfoliation methods, which will be described later on, it preserves the aromatic structure of graphene, and thus its properties.

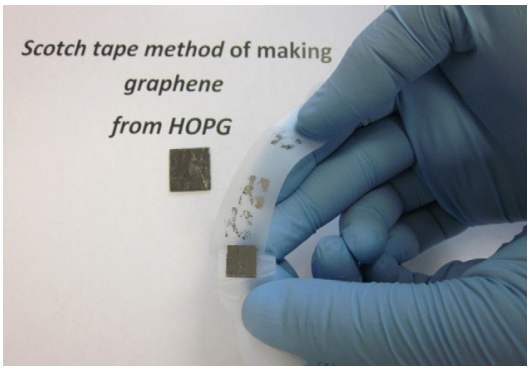

Figure II. 12 Mechanical exfoliation of graphene using scotch tape from HOPG.

II.3.2 CHEMICAL VAPOR DEPOSITION

CVD method has emerged to be one of the most promising techniques for the large-scale production of single and multiple layer graphene films. It consists in the grown of graphene on both single crystal and polycrystalline transition metal surface at high temperature by pyrolysis of hydrocarbon precursors, such as methane.

The first successful synthesis of *few*-layer graphene films using CVD was reported in 2006 by Somani et al., using camphor as precursor on Ni foils. Camphor was first evaporated at 180 °C and then pyrolyzed, in another chamber of the CVD furnace, at 700-850 °C, using argon as the carrier gas. Upon natural cooling to room temperature, *few*-layer graphene sheets were observed on the Ni foils.[112]

The graphene grown mechanism is dependent on the carbon solubility of the metal surface. Using a substrate with a medium carbon solubility, such as Co and Ni, graphene growth happens through diffusion of the carbon into the metal thin film, at high temperature (1000 °C) and pressure (10^3 Torr), and the subsequent precipitation of carbon out of the bulk metal to metal surface upon the cooling.[113,114]

On the other hand, the graphene growth on low carbon solubility substrate, like Cu, mainly happens on the surface through the four-step process[115] (Figure II. 13):

- Catalytic decomposition of methane on Cu to form C_xH_y upon the exposure of Cu to methane and hydrogen;
- Formation of nuclei, as a result of local supersaturation of C_xH_y where undersaturated Cu surface does not form nuclei;
- Nuclei grow to form graphene islands on Cu surface saturated, or supersaturated with C_xH_y species;
- Full Cu surface coverage by graphene under certain temperature, methane flow rate, and methane partial pressure.

Moreover, carbon solubility of the substrate strongly influences the number of graphene layers. With metals having relatively high carbon solubility, it can be possible to obtain graphene having from 1 to 10 layers, with mono-layers domains sizes up to several tens of micrometers in diameters.[116] The thickness and crystal ordering can be controlled by the cooling rate and hydrocarbon gas concentration.

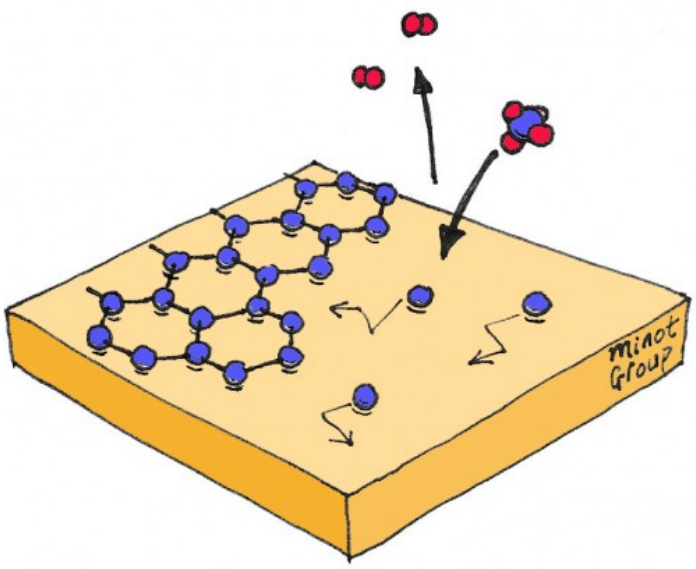

Figure II.13 Representation of the growing process for CVD graphene, at 1000 °C in presence of methane and hydrogen gas.

In contrast, low carbon solubility in certain transition metals allows obtaining *single* layer graphene. This is due to the fact that graphene growth on Cu is a surface-mediated process and this is self-limiting: once the Cu surface is fully covered with graphene, the growth process terminates, obtaining a 100% monolayer coverage.[117] Yan and coworkers avoided the self-limiting effect of this type of process to enable second layer growth on prepared monolayer graphene, using a fresh copper foil placed in the high-temperature upstream regime. *Bi*-layer graphene, with coverage area as high as 67% were prepared.[118]

Although CVD affords to prepare high quality graphene on metal foils, it is not particularly useful for electronic applications without transferring it to an insulating substrate, such as SiO_2, polydimethylsiloxane,

etc. The transfer process adds more complication to the quality and consistency of sample, and needs to be improved and optimized. There are some techniques that eliminate this transfer step, using thin metal films on insulating substrates that are removed during[119] or post growth,[120] or with remote catalysis by Cu atoms in the atmosphere.[121] However, the convenience and practicality of transfer-free growth is at the expense of quality and performance.

CVD is also an expensive route, owing to large energy consumption and because the underlying metal layer has to be removed. A promising approach to isolating CVD graphene from its metallic growth substrate and regain its intrinsic electronic properties is through intercalation with a buffer layer such as Si.[122] Instead, to decrease energy consumption it can be reduce growth temperature: Li et al. have recently been demonstrated that graphene can be grown at a temperature as low as 300 °C using a liquid benzene hydrocarbon source.[123]

Another useful feature of CVD is the ability to dope graphene by introducing other gases during growth, such as ammonia (NH_3) or borane (BH_3). Nitrogen and boron displace normal carbon atoms within the lattice, resulting in a nitrogen- or boron-doped graphene layers, which have demonstrated interesting properties.[124,125]

Plasma enhanced chemical vapor deposition (PECVD)

PECVD is a laser-induced CVD process, which allows to achieve graphene growth at moderate temperature ≈ 700 °C.[126,127] The first report on *single* to *few*-layer graphene by PECVD was found by Wang et al. in 2004.[128,129] A radio frequency PECVD system was used to synthesize graphene on a variety of substrates, such as Si, W, Mo, Zr, 304 types of stainless steel, SiO_2, Al_2O_3, without any special surface preparation operation or catalyst deposition. The graphene sheet was produced in a gas mixture of 5–100% CH_4 in H_2 (total pressure 12 Pa), at 900 W of power and 680 °C substrate temperature, and it was found to have sub-nanometer thickness and erected from the substrate surface.

Despite of traditional CVD, PECVD exhibits short deposition time (< 5 min) and lower growth temperature of 650 °C.

Instead of using the hydrocarbon gases as the carbon precursors, solid state carbon sources such as poly(methyl methacrylate), PMMA, or even table sugar, virtually any carbon-based material, succeeds in producing graphene on select metal substrates at high enough temperature with PECVD methods.[130]

Thanks to its versatility of synthesizing graphene from different substrates, and its low growth temperature used, PECVD can expand drastically its fields of applications.

II.3.3 EPITAXIAL GROWTH ON SiC

Graphene can also be obtained by thermal decomposition of Si on the (0001) surface plane of single crystal of SiC. In the pioneering work, Berker et al. prepared graphene by heating of 6H-SiC in ultrahigh vacuum (UHV), in a temperature range of 1200-1600 °C, for a short time (i.e., 5-20 min).[131] When SiC substrate is heated under UHV, silicon atoms on the surface sublimate, and exposed carbon atoms rearrange into graphene layers. Graphene, epitaxially grown on this surface, typically have 1 to 3 graphene layers. The thickness of graphene, and thus the number of its layers are strongly influenced by the decomposition temperature. It is important to note that epitaxial graphene can grow on both the C-terminated and Si-terminated surfaces, even if the growth on the carbon face is faster than on the silicon one.[132,133]

Moreover, there are a difference between graphene obtained from C-terminated surface and that grown on Si-terminated surface: in the first case there is a weaker coupling of substrate and the next graphene layer rather than the second one. The quality of such graphene can be very largely, with crystallites approaching hundreds of micrometers in size.[133]

Epitaxial growth of graphene on SiC has been an attractive technique especially for semiconductor industry, because the products are obtained on SiC substrates and don't require transfer before processing devices.[136]

Even if this method affords to obtain free-defect graphene, with crystallites approaching hundreds of micrometers in size,[137] it exhibits some drawbacks, such as the high cost of the SiC wafers and the high temperatures (above 1000 °C) used, which are not directly compatible with silicon electronics technologies. Furthermore, there are other problems that need to be resolved, such as the presence of terraces, which contribute to carrier scattering and the increase in size of the crystallites. As a result, the use of graphene on SiC will probably be limited to niche applications.

II.3.4 SOLUTION AND CHEMICAL EXFOLIATION

This method is based on the obtainment of graphene from colloidal suspension and it is that used by our research group. It is a top-down method, based on the exfoliation of graphite, graphite derivates (i.e., graphite oxide) or GICs, and have many advantages, such as high yields, solutions based processability, and ease of implementation.

Graphene from graphite oxide

The production of graphene by chemical modification of graphite is the most suitable technique for the large-scale applications, and it is still the most widely studied.

Graphite oxide is usually synthesized by either the Hummers,[138] Brodie[139] or Staudenmaier methods.[140] Hummers used a combination of potassium permanganate ($KMnO_4$) and concentrated sulfuric acid (H_2SO_4) to oxide graphite, while Brodie or Staudenmaier methods involve treatment of graphite with a mixture of potassium permanganate ($KMnO_4$) and concentrated nitric acid (HNO_3). Graphite oxide has higher oxygen content than pristine graphite, with hydroxyl and epoxy groups on sp^3 hybridized carbon on the basal plane, in addition to carbonyl and carboxyl groups located at the sheet edges on sp^2 hybridized carbon. Subsequently, graphite oxide is highly hydrophilic and can be easily exfoliated in water, yielding brown, stable dispersions, consisting mostly of single layered sheets, the so called graphene oxide (GO). The formation of stable dispersion of GO surface in water is due not only to its hydrophilicity but also to the electrostatic repulsions between the negatively charged groups on the surface. When graphene is dispersed in water, the carboxylic and the phenolic hydroxylic groups are ionized, bearing to a highly negative surface. GO can be also dispersed directly in several polar solvents such as ethylene glycol, dimethylformamide (DMF), N-methylpyrrolidone (NMP) and tetrahydrofuran (THF).[141]

The chemical structure of GO have been studied using NMR ^{13}C-labbelled graphene oxide.[142] It was found that the basal plane of the sheet is characterized by the presence of hydroxyl and epoxy (1,2-ether) functional groups with small amount of lactol, ester, acid and ketone carbonyl groups at the edges.

Because of the presence of these functional groups, irreversible defects and disorders,[143,144] the aromatic structure of GO is not preserved: thus it behaves like an electrical insulating.

To partially restore the conductivity of pristine graphene, GO reduction is needed (Figure III.14). In these years, different types of reduction methods have been reported to obtain r-GO sheets, such as the chemical, photochemical, thermal, micro-wave assisted and electrochemical reductions. Among them, the chemical reduction is the most used and versatile technique, which uses hydrazine,[143-146] dimethylhydrazine,[147] $NaBH_4$,[148] ascorbic acid,[149] *Escherichia coli* (*E. coli)* bacteria[150] and hydriodic acid[151] as reducing agents.

If compared with the other strong reducing agents, hydrazine does not react with water, resulting as the best one in producing very thin and fine graphene-like sheets. During the reduction process, the brown colored dispersion of GO in water turned black and the reduced sheets aggregated and precipitated[143] (Figure II.15): the decrease of hydrophilicity of GO, due to the removal of oxygen atoms, results in precipitation of r-GO sheets.

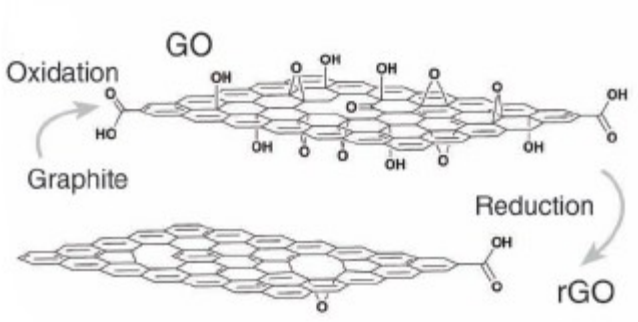

Figure II.14 GO and r-GO showing the remaining oxygen-rich functional groups after reduction.

However, chemical reduction usually cannot completely remove all the oxygen in GO: only the epoxy groups are actually reduced, while carboxy and alkoxy functionalities on the edges are not. In other words, the material obtained from chemical reduction of GO is not "pristine graphene" but chemically modified graphene. In fact, it exhibits thermal and electric properties poorer than that of pristine graphene.[153-154]

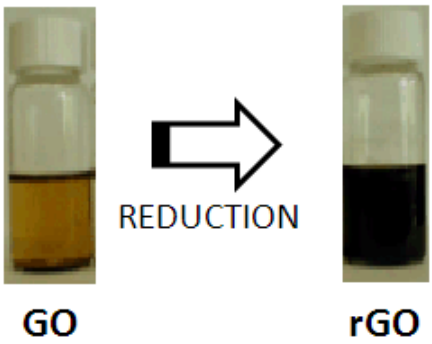

Figure II.15 Comparison between GO (left) and r-GO dispersions (right) in water.

Reduction of GO via thermal treatment has been reported to be an efficient and low cost method, producing r-GO having a BET surface area of 600-900 m^2/g.[155,156] In this technique GO is reduced by heating at high temperature (> 1000 °C), at which oxide functional groups are extruded as carbon dioxide. To achieve more complete removal of oxygen, thermal reduction can be combined with chemical treatments.[157]

An eco-friendly and economical method to obtain r-GO is represented by the electrochemical reduction, which allows producing high-quality r-GO in large scales.[158,159]

Photochemical methods are based on the reducing of GO by UV-irradiation of a mixture with TiO_2 particles suspended in ethanol.[160]

Unfortunately, either in these reduction methods, the reduction reaction is not complete, leading to the obtainment of a chemically modified graphene and not to "*real graphene*".

Graphene directly from graphite oxide

A convenient and promising technique for the production of defect-free graphene directly from pristine graphite is that proposed by Hernandez et al. in 2008,[161] and subsequently widely developed by our research group.[162,163] This method is based on the dispersion and ultrasonic exfoliation of graphite in organic solvent. Hernandez et al. succeeded to obtain graphene from direct ultrasonic exfoliation of graphite in NMP, initially achieving a concentration as low as 0.01 mg/mL.[161] The success of the process is due to the fact that the energy required to exfoliate graphite into single layer graphene was countered by the solvent-graphene interaction, with the solvent having similar surface energy as that of graphene. Therefore, the use of solvents with cohesive forces similar to the surface energy of graphene is needed in order to obtain efficient graphite exfoliation.

Independently of this pioneering work, our research group successfully developed a similar method for obtaining graphene dispersions having the highest concentrations achieved so far in any liquid and, for the first time, also directly in the monomer. Indeed, we were able to disperse graphene in different media, such as 1-hexyl-3-methylimidazolium hexafluorophosphate, with a graphene concentration of 5.33 mg/mL[162] and in NMP (2.21 mg/mL).[163]

Further improvements of this technique have been achieved by increasing the sonication time,[164] controlling the power of sonication[165] and through the use of different dispersing media such as surfactants,[166,167] ionic liquids[162] and solvents having low vapor tension.

If compared with the other described methods, the exfoliation of graphite in organic solvents or directly in the monomers does not require any chemical manipulation, thus preserving the aromatic structure of graphene. It also involves a simpler protocol, lower energy consumption and allows the large-scale production of defect- and oxide-free graphene.

Graphene from graphite derivates

Graphene can be also obtained from graphite derivative, such as GICs and expanded graphite.

Li et al. obtained *single* layer graphene by thermal treatment at high temperature (1000 °C) and for a short time (1 min) of expandable graphite. The key step for high quality graphene was the re-intercalation with *oleum* and the expansion with tetrabutylammonium hydroxide. The final suspension of graphene sheets was thus produced after sonication in a surfactant solution with an almost quantitative yield, as confirmed by AFM measurements.[153]

Colloidal suspensions of graphene were obtained shaking a GIC, for instance a ternary potassium salt, $K(THF)_xC_{24}$, in NMP.[168]

Another technique developed for the preparation of chemically modified graphene is that based on the electrochemical treatment of graphite. Graphite rods are used as anode and cathode electrodes and

immersed in a phase-separated mixture of water and imidazolium based ionic liquids. After the application of potentials of 10–20 V, different ionic-liquid-functionalized graphene sheets are generated at the anode, as a result of the interaction of the aromatic imidazole ring and graphene.[169]

II.4 GRAPHENE CHARACTERIZATION

Because of its atomic thickness and microscopic sizes, graphene is difficult to detect. Therefore, over the years, different techniques have been used and developed in order to determine the number of graphene layers, their dimensions, and to distingue it from GO. The characterization methods most frequently used are optical microscopy, AFM, transmission electron microscopy (TEM) and Raman spectroscopy, which are described below.

II.4. 1 OPTICAL MICROSCOPY

The optical microscopy was the first technique used by Novoselov and Geim to observe graphene. It is a very simple, cheap, non destructive and readily available technique. However, it requires that graphene layers will be disposed on a support, generally a silicon dioxide substrate, to obtain a good contrast imaging. The identification of graphene sheets, down to one layer in thickness, happens through the color contrast caused by the light interference effect on the SiO_2 substrate, which is modulated by the graphene layer.[170-172] In addition to the thickness of the substrate, also the wavelength of the incident light represents another important factor to modulate the optical contrast.[172,173] Blake et al. reported that under normal white light illumination, graphene sheets were invisible on 200 nm SiO_2, while thick and thin sheets were visible on 300 nm SiO_2 by using green light, whereas sheets were visible on 200 nm SiO_2 when blue light was employs.[172]

II.4.2 ATOMIC FORCE MICROSCOPY

AFM is an effective technique for graphene characterization, affording to determine the layers thickness, superficial topology and the eventual presence of defects. Moreover, AFM is able to distinguish between a defect free graphene and its functionalized version. This is due to the variation of the interaction forces between the AFM tip and the attached functional groups.[173] However, it cannot discriminate between GO and graphene layers.

Finally, AFM has been employed for mechanical characterization of graphene as it can resolve the small forces involved in the deformation process.

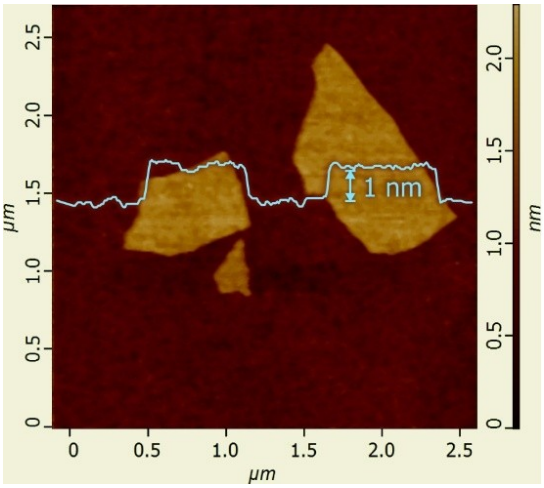

Figure II.16 Topography of a few graphene sheets on top of an atomically smooth surface, determined by AFM.

The main drawback of this characterization method is that sometimes it is not accurate. In fact, due to the varying interactions between the AFM tip and graphene or the supporting substrate, it is difficult to obtain the precise theoretical thickness (0.34 μm). Moreover, it can be even worse if the graphene surface adsorbs a thin layer of water or other contaminants. For such a reason, there are a variety of reported data for *single* layer graphene using AFM, with thicknesses ranging from 0.4 to 1.0 nm.

Furthermore, AFM cannot be used in order to characterize graphene obtained by liquid exfoliation of graphite in highly-boiling liquids. In fact, it was found that, due to the presence of a large number of solvent layers among those of graphene, AFM largely overestimates the height of the steps.[174]

II. 4. 3 TRANSMISSION ELECTRON MICROSCOPY

TEM is a powerful tool, which can resolve the atomic features of graphene: it can not only observe the morphological characteristics of graphene but also determine the number of graphene layers accurately (Figure II.17). However, the use of this technique is limited by the voltage applied during the measures: when the operations are conducted at high voltage the monolayer is damaged. Therefore, TEM analyses are limited by their resolution at low operating voltage. Recently, a new class of TEM, having an aberration correcting system combined with a monochromator, providing a 1 Å resolution at an acceleration voltage of 80 kV, is developed.[175]

The atomic lattice defects and surface contamination can also be observed in high-angle annular dark-field images using scanning transmission electron microscopy and further characterized with electron energy loss spectroscopy.[176,177]

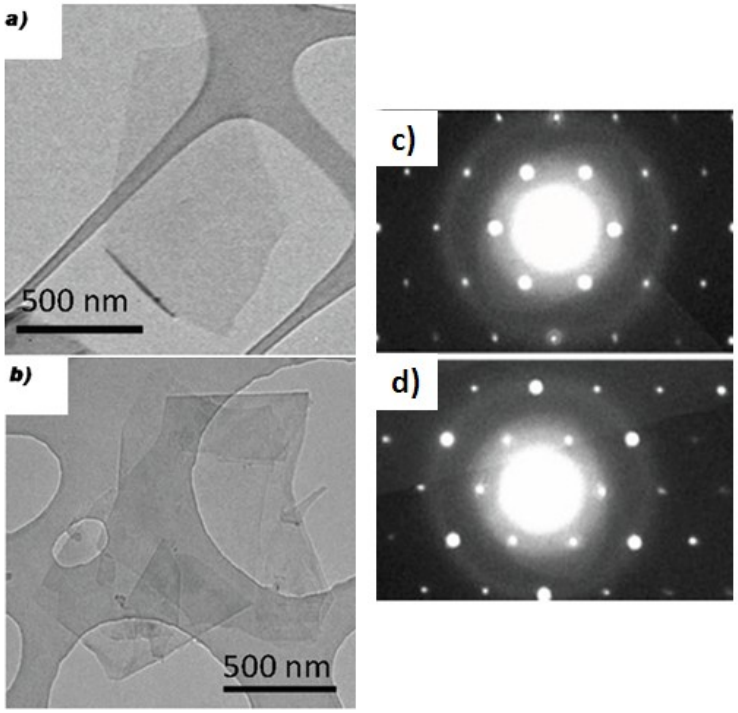

Figure II.17 TEM images of monolayer (a) and multilayer (b) graphene and their corresponding electron diffraction patterns (c,d).[162]

II.4.4 RAMAN SPECTROSCOPY

Raman spectroscopy is a reliable and widely applied technique to investigate graphene structure: it enables to determine the number of layers, their thickness, mechanical strain, edge structures, and to discriminate between graphite and graphene.

Raman spectra are usually carried out on *single*, *bi-* and *multi-* layer graphene deposited on Si + SiO_2. The measurements are performed at room temperature, using an exciting radiation of 532 or 633 nm, with an incident power included between 0.04 and 5 mW.

Raman spectrum of graphene is characterized by three typical bands, namely the D band at 1350 cm^{-1}, the G band at 1580 cm^{-1}, and the 2D band at a frequency at 2700 cm^{-1}. The D band is related to the *breathing mode* of carbon atoms on the aromatic ring[178] and is not always visible; the G peak is determined by in-plane optical vibrations of the sp^2-bonded carbon atoms, whereas the 2D peak is at almost double the frequency of the D band and arises from second order Raman scattering process.

As can be seen in Figures II.18b,c, the 2D band is a diagnostic signal for the identification of graphene, because its shape, width and position differ from that of graphite.

The 2D peak in bulk graphite consists of two components, 2*D*1 and 2D2, of approximately 1⁄4 and 1⁄2 the height of the G peak, respectively;[179] while graphene exhibits a single and sharp 2D peak, about 4 times more intense than the G peak.[180]

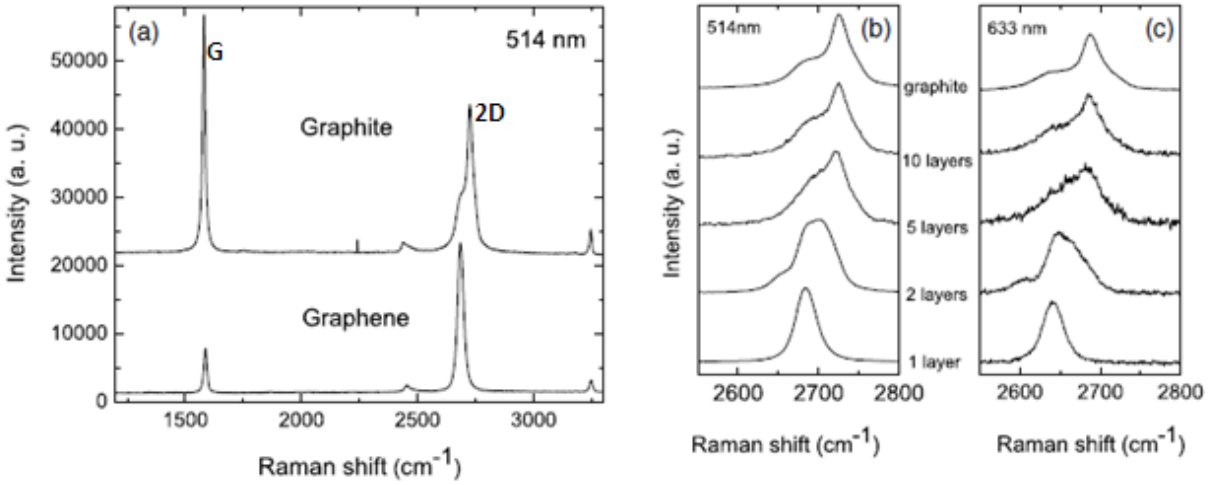

Figure II.18 Comparison of Raman spectra at 514 nm for the graphite and single layer graphene (a). Evolution in 2D band as a function of layers at 514 and 633 nm excitations (b,c).[180]

Moreover the shape and the position of 2D band afford to establish the number of graphene layers. Figures II.18a,b reported the evolution of the 2D peak as a function of the layers for 514 and 633 nm excitations. It can be seen that with the increase of the layers, the 2D band shifts toward upper wavelengths, becomes broader and non-symmetric. Besides, a further increase of the layers leads to a strong decrease of the intensity of the 2D1 peak, which becomes hardly distinguishable from that of bulk graphite with a number of layer higher than 5.

The D band is also known as the related disorder band: it appears when disorder in atomic arrangement or edge defects are presented on graphene. Therefore, the Raman spectrum of free-defect single layer graphene does not show the D peak (Figure II.18a). Besides, the intensity of the D band at armchair type edges is higher than that at zigzag type edges.[181]

Since graphene properties are strongly influenced by the number of the layers and purity, Raman spectra represent a powerful and non destructive tool to characterize *single* and *few*-layers graphene.

II.4.5 X-RAYS DIFFRACTION (XRD)

XRD is use to assess the graphite intercalation. For example, the reflection peak located at $2\theta = 26.3°$ (Cu radiation Kα, X-rays wavelength = 0.154 nm) of graphite shifts to a value of 14.1 -14.9° in graphite oxide.[182]

II.4.6 SUPERFICIAL AREA MEASURES

Even if it is an indirect measure, the superficial area is an indicator of graphite exfoliation: higher the graphite exfoliation is, higher superficial area is. The superficial area can be determined by nitrogen[183] or blue of methylene absorption;[184] however the measure is strongly influenced by compressibility of the obtained graphene.

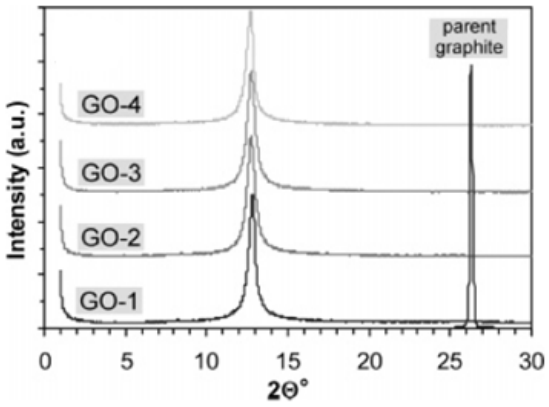

Figure II.19 XRD diffractograms for different types of graphite oxide and graphite (Cu radiation Kα, X-rays wavelength = 0.154 nm)**.**

II.5 GRAPHENE NANORIBBONS (GNRs)

GNR could be defined as one-dimensional sp^2 hybridized carbon crystal, having boundaries that expose non three coordinated carbon atoms and a large aspect ratio. GNRs were originally introduced as a theoretical model by Mitsutaka Fujita et al. to examine the edge and nano-scale size effect on graphene.[185] Their chemical, magnetic and electronic properties are strongly influenced by the structure and topology of the edges, which could be armchair, zigzag or a combination of both (Figure II.20). Moreover, these properties can be modulated by functionalization of the highly reactive sites present on GNRs edges, allowing their use in different systems, such as in sensors, memory and processing devices.[186-188] Unlike graphene, GNRs exhibit band gaps useful for room temperature transistor operations with extraordinary switching speed and high carrier mobility.[189] Theoretical studies determined that zigzag GNRs behave always like a metal while armchairs can be either metallic or semiconducting, depending on their width. In particular, density functional theory (DFT) calculations showed that armchair nanoribbons are semiconducting with an energy gap that increases with the decreasing of GNRs width.[190] Due to their semiconductive properties, GNRs can replace copper in integrated circuit interconnects, and silicon in electronic devices.

GNRs are prepared by using different techniques:

- CVD
- Chemical treatments
- Unzipping of carbon nanotubes

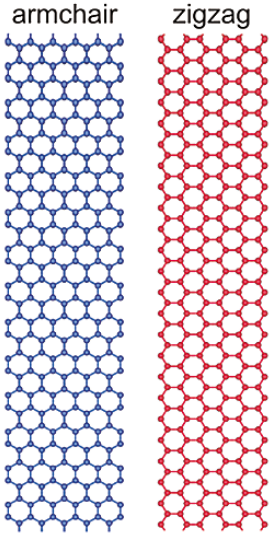

Figure II.20 Typical nanoribbon edge configuration: armchair (left side) and zigzag (right side).

As described in II.3.2 , CVD is based on the precipitation of graphene on metallic surface such as Ni or Cu. The first synthesis of GNRs by CVD dates back to 1990, when Murayama et al. obtained ribbon-like filaments from hydrocarbon decomposition or disproportionation of CO at 400-700 °C. Such ribbons were 10 μm long, 0.1-0.7 μm wide and 10-200 nm thick. They also have a catalyst particle at one side and graphitic layers perpendicular to the filament axis, which are subsequently removed by annealing treatments at 2800 °C.[191]

Recently, Campos-Delgado et al. proposed another CVD method for the synthesis of GNRs.[192] In this work a spray of ferrocene in ethanol and thiophene were carried out by Ar to a furnace having a temperature of 950 °C, producing rippled nanoribbons having a length of several micrometers, a width of 20-300 nm and a thickness less than 15 nm.

GNRs can also be prepared by different chemical techniques. Finkenstadt et al. obtained graphene nanoribbons through exfoliation of expandable graphite by annealing at 1000 °C, followed by 30 min sonication in a solution of dichloroethane and a polymer. GNRs were recovered from the supernatant. [193]

An alternative chemical route exploited the Suzuki-Miyaura linking reaction between tetra- and hexa-phenylbenzenes to produce GNRs. In this work the polyphenylene formed undergoes to a cyclodehydrogenation reaction with $FeCl_3$ as the oxidant, resulting in ribbons with 6 -12 polycyclic aromatic repeating units, and 8-12 nm of length.

This technique represents a bottom-up method for the production of thin and short GNRs with armchair edges.[194]

Finally GNRs can be synthesized through unrolling or unzipping of carbon nanotubes. Among the several method developed until now, the most important are: intercalation-exfoliation of multi-walled carbon nanotubes by treatments in liquid NH_3 and Li, and subsequent exfoliation using HCl and heat treatments;[195] catalytic method, in which metal nanoparticles "cut" the nanotube longitudinally;[196] chemical route, involving acid reactions that break carbon-carbon bonds (e.g. oxidation with H_2SO_4 and $KMnO_4$);[197] physicochemical method by embedding the tubes in a polymer matrix followed by Ar plasma treatment;[198] electrical techniques based on the passage of an electric current through a nanotube.[199]

REFERENCES

[1] Geim, A. K.; Novoselov, K. S. *Nature Materials* 2007, 6, 183-191.
[2] Slonczewski, J. C.; Weiss, P. R. *Phys. Rev.* 1958, 109, 272–279.
[3] Partoens, B.; Peeters, F. M. *Physical Review B* 2006, 74, 075404-075414.
[4] Schafhaeutl, C.; Prakt. J. Chem. 1840, 21, 129-157.
[5] Inagaki, M. *J. Mater. Res.* 1989, 4, 1560-1568.
[6] Sorokina, N. E.; Nikolskaya, I. V.; Ionov, S. G.; Avdeev, V. V. *Russ. Chem. Bull.* 2005, 54, 1749-1767.
[7] Liu, Z.H.; Wang, Z.-M.; Yang, X.; Ooi, K. *Langmuir* 2002, 18, 4926-4932.
[8] Brodie, B. C. *Philos. Trans. R. Soc. London* 1859, 149, 249-259.
[9] Brodie, B. C. *Q. J. Chem. Soc.* 1860, 12, 261-268.
[10] Boehm, H. P.; Clauss, A.; Fischer, G. O.; Hofmann, U.; Naturforschg, Z. *Nature* 1962, 17, 150-157.
[11] Boehm, H. P.; Clauss, A.; Fischer, G.; Hofmann, U. In Proceedings of the Fifth Conference on Carbon, Pergamon Press, Heidelberg, Germany, 1962.
[12] Morgan, A. E.; Somorjai, G. A. *Surf. Sci.* 1968, 12, 405-425.
[13] May, J. W. *Surf. Sci.* 1969, 17, 267-279.
[14] Krishnan, A.; Dujardin, E.; Treacy, M. M. J.; Hugdahl, J.; Lynum, S.; Ebbesen T. W. *Nature* 1997, 388, 451-454.
[15] Land, T. A.; Michely, T.; Behm, R. J.; Hemminger, J. C.; Comsa, G. *Surf Sci* 1992, 264,261-270.
[16] Nagashima, A.; Nuka, K.; Itoh, H.; Ichinokawa, T.; Oshima, C.; Otani, S. *Surf Sci* 1993,291,93-98.
[17] Forbeaux, I.; Themlin , J. M.; Debever, J. M. *Phys Rev B* 1998, 58, 16396-16406.
[18] Berger, C; Song, Z. M.; Li, T. B.; Li, X. B.; Ogbazghi, A. Y.; Feng, R. et al. *J Phys Chem B* 2004, 108, 19912-19916.
[19] Berger, C.; Song, Z.; Li, X.; Wu, X.; Brown, N.; Naud, C. C. et al. *Science* 2006, 312, 1191-1196.
[20] Ohta, T.; Bostwick, A.; Seyller, T.; Horn, K.; Rotenberg, E. Science 2006, 313, 951-954.
[21] Lu, X. K.; Huang, H.; Nemchuk, N.; Ruoff, R. S. *Nanotechnology* 1999, 10, 269-272.
[22] Lu, X. K.; Huang, H.; Nemchuk, N.; Ruoff, R. S. *Appl. Phys.* 1999, 75, 193-195.
[23] Novoselov, K. S.; Geim, A. K.; Morozov, S. V.; Jiang, D.; Zhang, Y.; Dubonos, S. V. et al. *Science* 2004, 306, 666-669.
[24] Rao, C. N. R.; Biawas, K.; Subramanyam, K. S.; Govindaraj, A. *J. Mater. Chem.* 2009, 19, 2457-2469.
[25] Castro Neto, A. H.; Guinea, F.; Peres, N. M. R.; Novoselov, K. S.; Geim, A. K. *Rev. Mod. Phys*. 2009, 81, 109-162.
[26] Katsnelson, M. I.; Novoselov, K. S.; Geim, A. K. *Nature Physics* 2006, 2, 620-625.
[27] Wang, Q. H.; Hersam, M. C. *Nat. Chem.* 2009, 1, 206-211.
[28] Si, Y.; Samulski, E. T. Nano Lett. 2008, 8, 1679-1682.
[29] Elias, D. C.; Nair, R. R.; Mohiuddin, T. M. G.; Morozov, S. V.; Blake, P.; Halsall, M. P.; Ferrari, A. C.; Boukhvalov, D. W.; Katsneltson, M. I.; Geim, A. K.; Novoselov, K. S. *Science* 2009, 323, 610-613.
[30] Cho, K.; Hong, B. H.; Kim, K. S. *J. Phys. Chem. Lett.* 2011, 2, 841-847.
[31] Park, J.; Jo, S. B.; Yu, Y. J.; Kim, Y.; Yang, J, W.; Lee, W. H.; Kim., H. H.; Hong, B. H.; Kim, P.; Cho, K.; Kim, K. S. *Adv. Mater.* 2012, 24, 407-411.
[32] Du, X.; Skachko, I.; Barker, A.; Andrei, E. Y. *Nature Nanotechnology* 2008, 3, 491-495.
[33] Hwang, E. H.; Adam, S.; Das Sarma, S. *Phys Rev Lett* 2007, 98, 186806.
[34] Nomura, K.; MacDonald, A. H. *Phys Rev Lett* 2006, 96, 256602.
[35] Chen, J. H.; Jang, C.; Xiao, S.; Ishigami, M.; Fuhrer, M. S. *Nature Nanotechnology* 2008, 3, 206-209.
[36] Meyer, J. C.; Geim, A. K.; Katsnelson, M. I.; Novoselov, K. S.; Booth, T. J.; Roth, S. *Nature* 2007, 446, 60-63.
[37] Novoselov, K. S.; Geim, A. K.; Morozov, S. V.; Jiang, D. M.; Katsnelson, I.; Grigorieva, I. V.; Dubonos, S. V.; Firsov, A. A. *Nature* 2005 , 438 , 197-200.
[38] Zhang, Y. B.; Tan, Y. W.; Stormer, H. L.; Kim, P. *Nature* 2005, 438, 201-204.
[39] Novoselov, K. S.; McCann, E.; Morozov, S. V.; Ko, V. I.; Katsnelson, M. I.; Zeitler, U.; Jiang, D. et al. *Nature Physics* 2006, 2, 177-180.
[40] Zhang, Y. B.; Tang, T. T.; Girit, C.; Hao, Z.; Martin, M. C.; Zettl, A.; Crommie,M. F.; Shen, Y. R.;Wang, F. *Nature* 2009, 459, 820–823.
[41] Craciun, M. F.; Russo, S.; Yamamoto, M.; Oostinga, J. B.; Morpurgo, A. F.; Tarucha, S. *Nature Nanotechnol.* 2009, 4, 383–388.

[42] Neto, A. H. C.; Guinea, F.; Peres, N. M. R.; Novoselov, K. S.; Geim, A. K. *Rev. Mod. Phys.* 2009, 81, 109–162.
[43] Partoens, B.; Peeters, F.M. *Phys. Rev. B* 2007, 75, 193402.
[44] Partoens, B.; Peeters, F.M. Phys. Rev. B 2006, 74, 075404.
[45] Morozov, S.V.; Novoselov, K.S.; Schedin, F.; Jiang, D.; Firsov, A.A.; Geim, A.K. *Phys. Rev. B* 2005, 72, 201401.
[47] Sarma, S. D.; Pinczuk, A. In Perspectives in Quantum Hall Effects; Wiley. New York, 1997.
[48] Novoselov, K. S.; Jiang, Z. ; Zhang, Y.; Morozov, S. V.; Stormer, H. L.; Zeitler, U.; Maan, J. C.; Boebinger, G. S.; Kim, P.; Geim, A. K. *Science* 2007, 315, 1379.
[49] Young, A. F.; Kim, P. *Nat. Phys.* 2009, 5, 222.
[50] Stander, N.; Huard, B.; Goldhaber-Gordon, D. *Phys. Rev. Lett.* 2009, 102, 026807.
[51] Nair, R. R.; Blake, P.; Grigorenko, A. N.; Novoselov, K. S.; Booth, T. J.; Stauber, T. et al. *Science* 2008, 320, 1308.
[52] Kravets, V. G.; Grigorenko, A. N.; Nair, R. R.; Blake, P.; Anissimova, S.; Novoselov, K. S. et al. *Phys Rev B* 2010, 81, 155413.
[53] Bae, S.; Kim, H.; Lee, Y.; Xu, X.; Park, J. S.; Zheng, Y. et al. *Nature Nanotechnol* 2010, 5, 574-578.
[54] Park, S.; Ruoff, R. S. *Nature Nanotechnol* 2009, 4, 217-224.
[55] Bonaccorso, F.; Sun, Z.; Hasan, T.; Ferrari, A. C. *Nat Photon* 2010, 4, 611-622.
[56] Gokus, T.; Nair, R. R.; Bonetti, A.; Bohmler, M.; Lombardo, A.; Novoselov, K. S. et al. *ACS Nano* 2009, 3, 3963-3968.
[57] Balandin, A. A.; Ghosh, S.; Bao, W.; Calizo, I.; Teweldebrhan, D.; Miao, Feng; Lau, C. N. *Nano Lett.* 2008, 8, 902–907.
[58] Ghosh, S.; Calizo, I.; Teweldebrhan, D.; Pokatilov, E. P.; Nika, D. L.; Balandin, A. A.; Bao, W.; Miao, F.; Lau, C. N. Appl. Phys. Lett. 2008, 92, 151911-151913.
[59] Pop, E., Mann, D., Wang, Q., Goodson, K.; Dai, H. *Nano Lett.* 2006, 6, 96–100.
[60] Dresselhaus, M. S.; Dresselhaus, G.; Eklund, P. C. In Science of Fullerenes and Carbon Nanotubes (Academic Press, 1996).
[61] Ghosh, S. et al. *MRS Proc.* 2010, S6.2, 198.
[62] Mohiuddin, T. M. G.; Lombardo, A.; Nair, R. R.; Bonetti, A.; Savini, G.; Jalil, R.; et al. *Phys Rev B* 2009, 79, 205433.
[63] Lee, C.; Wei, X. D.; Kysar, J. W.; Hone, J. *Science* 2008, 321,385–388.
[64] Bao, W.; Miao, F.; Chen, Z.; Zhang, H.; Jang, W.; Dames, C.; Lau, C. N. Ripple Texturing of Suspended Graphene Atomic Membranes. http://arxiv.org/abs/0903.0414 2009.
[65] Enoki, T.; Kobayashi, Y. *J. Mater. Chem.* 2005, 15, 3999-4002.
[66] Matte, H. S. S. R.; Subrahmanyam, K. S.; Rao, C. N. R. J. of Physic. Chem. C 2009, 113, 9982-9985.
[67] Bon, S.B.; Valentini, L.; Verdejo, R.; Garcia Fierro, J.L.; Peponi, L.; Lopez-Manchado, M.A.; Kenny, J.M. *Chem. Mater.* 2009, 21, 3433-3438.
[68] Schedin, F.; Geim, A. K.; Morozov, S. V.; Hill, E. W.; Blake, P.; Katsnelson, M. I.; Novoselov, K. S. *Nature Materials* 2007, 6, 652-655.
[69] Bae, S.; Kim, H.; Lee, Y.; Xu, X.; Park, J. S.; Zheng, Y.; Balakrishnan, J.; Lei, T.; Kim, H. R. et al. *Nature Nanotechnol.* 2010, 5, 574–578 .
[70] Li, S.S.; Tu , K. H.; Lin, C. C.; Chen, C.W.; Chhowalla, M. *ACS Nano* 2010, 4 , 3169-3174.
[71] Molitor, F.; Jacobsen, A.; Stampfer, C.; Guettinger, J.; Ihn, T.; Ensslin, K. *Phys. Rev. B* 2009, 79, 075426.
[72] Shim, J.P.; Choe , M.; Jeon, S. R.; Seo, D.; Lee, T.; Lee , D. S. *Appl. Phys. Express* 2011 , *4* , 052302.
[73] Park, H.; Rowehl, J. A.; Kim, K. K.; Bulovic, V; Kong, J. *Nanotechnology* 2010, 21, 155202.
[74] Yin, Z.; Wu, S.; Zhou, X.; Huang, X.; Zhang, Q.; Boey, F.; Zhang, H. *Small* 2010, *6*, 307-312.
[75] Wang, X.; Zhi, L.; Muellen, K. *Nano Lett.* 2008, 8, 323-327.
[76] Chen, C.C.; Aykol , M.; Chang, C. C.; Levi, A. F. J.; Cronin, S. B. *Nano Lett.* 2011 , 11, 1863-1867.
[77] Ponomarenko, L. ; Schedin, F.; Katsnelson, M. I.; Yang, R.; Hill, E. W.; Novoselov, K. S.; Geim, A. K. *Science* 2008, 320, 356-358.
[78] Lin, Y.; Dimitrakopoulos, C.; Jenkins, K.A.; Farmer, D.B.; Chiu, H.; Grill, A.; Avouris, P. Science 2010, 327, 662.
[79] Williams, J. R.; DiCarlo , L.; Marcus, C. M. *Science* 2007, 317, 638-641.
[80] Cai, J. M.; Ruffieux, P.; Jaafar, R.; Bieri, M.; Braun, T.; Blankenburg, S. et al. *Nature* 2010, 466, 470–473.
[81] Ohta, T.; Bostwick, A.; Seyller, T.; Horn, K.; Rotenberg, E. *Science* 2006, 313, 951–954.

[82] Elias, D. C.; Nair, R. R.; Mohiuddin, T. M. G.; Morozov, S. V.; Blake, P.; Halsall, M. P.; Ferrari, A. C.; Boukhvalov, D. W.; Katsnelson, M. I.; Geim, A. K.; Novoselov, K. S. *Science* 2009, 323, 610–613.
[83] Kim, K.; Choi, J. Y.; Kim, T.; Cho, S. H; Chung, H. J. *Nature* 2011, 479, 338–344.
[84] Schwierz, F. *Nature Nanotechnol.* 2010, 5, 487–496.
[85] Britnell, L.; Gorbachev, R. V.; Jalil, R.; Belle, B. D.; Schedin, F.; Mishchenko, A.; Georgiou, T.; Katsnelson, M. I. *Science* 2012, 335, 947–950.
[86] Merchant, C. A.; Healy, K.; Wanunu, M.; Ray, V.; Peterman, N.; Bartel, J.; Fischbein, M. D.; Venta, K.; Luo, Z.; Johnson, A. T. C.; Drndic, M. *Nano Lett.* 2010 , 10, 2915-21.
[87] Garaj, S.; Hubbard, W.; Reina, A.; Kong, J.; Branton, D.; Golovchenko, J. A. *Nature* 2010, 467, 190-193.
[88] Yavari, F.; Chen, Z.; Thomas, A. V.; Ren, W.; Cheng, H. M.; Koratkar, N. *Sci. Rep.* 2011, 1, 1-5.
[89] Lu, Y.; Goldsmith, B. R.; Kybert, N. J.; Johnson, A. T. C. *Appl. Phys. Lett.* 2010, 97 , 083107.
[90] Chang, H.; Tang, L.; Wang, Y.; Jiang, J.; Li J. *Anal. Chem.* 2010*, 82*, 2341-2346.
[91] Ohno, Y.; Maehashi, K.; Matsumoto, K. *J. Am. Chem. Soc.* 2010 , *132* , 18012-18013.
[92] Sanchez, V. C.; Jachak, A.; Hurt, R. H.; Kane, A. B. *Chem. Res. Toxicol* 2012, 25, 15–34.
[93] Zhang, H.; Lv, X.; Li, Y.; Wang, Y.; Li, J. ACS Nano 2010, 4, 380–386.
[94] Ramanathan, T. et al. Functionalized graphene sheets for polymer nanocomposites. *Nature Nanotechnol.* 2008, 3, 327–331.
[95] Stoller, M. D.; Park, S. J.; Zhu, Y. W.; An, J. H.; Ruoff, R. S. *Nano Lett.* 2008, 8, 3498–3502.
[96] Yoo, E.; Okata, T.; Akita, T.; Kohyama, M.; Nakamura, J.; Honma, I. *Nano Lett.*2009, 9, 2255–2259.
[97] Yang, S. B.; Feng, X. L.; Ivanovici, S.; Mullen, K. *Angew. Chem. Int. Edn* 2010, 49, 8408–8411.
[98] Yoo, E. Kim, J.; Hosono, E.; Zhou, H. S.; Kudo, T.; Honma, I. *Nano Lett.* 2008, 8, 2277–2282.
[99] Fang, M.K.; Wang, G.; Lu, H. B.; Yang, Y. L.; Nutt, S. *J. Mater. Chem.* 2009, 19, 7098-7105.
[100] Liang, J. J.; Huang, Y.; Zhang , L.; Wang, Y.; Ma, Y. F.; Guo, T. Y.; Chen, Y. S. *Adv. Funct. Mater.* 2009, 19 , 2297-2302.
[101] Kalaitzidou, K.; Fukushima, H.; Drzal, L. T. *Compos. Sci. Technol.* 2007, 67, 2045-2051.
[102] Rafiee , M. A; Rafiee, J.; Yu, Z. Z.; Koratkar, N. *Appl. Phys. Lett.* 2009, *95*, 223103-223107.
[103] Kim, H.; Macosko, C. W. *Macromolecules* 2008, *41*, 3317-3327.
[104] Verdejo, R.; Barroso-Bujans , F.; Rodriguez-Perez, M. A.; De Saja , J. A.; Lopez-Manchado, M. A. *J. Mater. Chem.* 2008, *18*, 2221-2226
[105] Cai, D.; Yusoh, K.; Song, M. *Nanotechnology* 2009, 20, 085712.
[106] Lee, Y. R.; Raghu, A. V.; Jeong, H. M.; Kim, B. K. *Macromol. Chem. Phys.* 2009, 210, 1247-1254.
[107] Novoselov, K. S.; Jiang, D.; Schedin, F.; Booth, T. J.; Khotkevich, V. V.; Morozov, S. V.; Geim, A. K. *PNAS* 2005, 102, 10451-10453.
[108] Du, X.; Skachko, I.; Barker, A.; Andrei, E. Y. *Nature Nanotechnol*. 2008 ,3, 491-495.
[109] Morozov, S. V.; Novoselov, K. S.; Katsnelson, M. I.; Schedin, F.; Elias, D. C.; Jaszczak, J. A.; Geim, A. K. *Phys. Rev. Lett.* 2008, 100, 016602.
[110] Castro, E. V.; Ochoa, H.; Katsnelson, M. I.; Gorbachev, R. V.; Elias, D. C.; Novoselov, K. S.; Geim, A. K.; Guinea, F. *Phys. Rev. Lett.* 2010, 105, 266601.
[111] Balandin, A. A.; Ghosh, S.; Bao, W.; Calizo, I.; Teweldebrhan, D.; Miao, F.; Lau, C. N. *Nano Lett.* 2008, 8, 902-907.
[112] Somani, P. R.; Somani, S. P.; Umeno, M. *Chem Phys Lett* 2006, 430, 56.
[113] Kim, K. S.; Zhao, Y.; Jang, H.; Lee, S. Y.; Kim, J. M.; Kim, K. S. et al. *Nature* 2009, 457, 706-710.
[114] Reina, A.; Jia, X.; Ho, J.; Nezich, D.; Son, H.; Bulovic, V. et al. *Nano Lett* 2009, 9, 30-35.
[115] Li, X; Cai, W; Colombo, L.; Ruoff, R. S. *Nano Lett* 2009, 9, 4268-4272.
[116] Reina, A.; Jia, X.; Ho, J;. Nezich, D.; Son, H.; Bulovic, V.; Dresselhaus, M. S.; Kong, J. *Nano Lett.* 2009, 9, 30-35.
[117] Li, X. S.; Cai, W. W.; Colombo, L.; Ruoff, R. S. *Nano Lett.* 2009, 9, 4268.
[118] Yan, K.; Peng, H.; Zhou, Y.; Li, H.; Liu, Z. *Nano Lett.* 2011 , 11 , 1106-1110.
[119] Ismach, A.; Druzgalski, C.; Penwell, S.; Schwartzberg, A.; Zheng, M.; Javey, A.; Bokor, J.; Zhang, Y. *Nano Lett.* 2010, 10, 1542-1548.

[120] Su, C. Y.; Lu, A. Y.; Wu, C. Y.; Li , Y. T.; Liu, K. K.; Zhang , W.; Lin, S.Y.; Juang, Z. Y.; Zhong, Y. L.; Chen, F. R. Li, L. J. *Nano Lett.* 2011 , 11 , 3612-3616.
[121] Teng, P. Y.; Lu , C. C.; Akiyama-Hasegawa, K.; Lin , Y.C.; Yeh , C. H.; Suenaga, K.; Chiu, P. W. *Nano Lett.* 2012 , 12 , 1379-1384.
[122] Mao, J.; Huang, L.; Pan, Y.; Gao, M.; He, J.; Zhou, H.; Guo, H.; Tian, Y.; Zou, Q.; Zhang, L.; Zhang, H.; Wang, Y.; Du, S.; Zhou , X.; Neto, A. H. C.; Gao, H. J. *Appl. Phys. Lett.* 2012, 100, 093101.
[123] Li, Z.; Wu, P.; Wang, C.; Fan, X.; Zhang, W.; Zhai, X.; Zeng, C.; Li, Z.; Yang, J.; Hou, J. *ACS Nano* 2011, 5, 3385-3390.
[124] Guo, B.; Liu, Q.; Chen, E.; Zhu, H.; Fang, L.; Gong, J. R. *Nano Lett.* 2010, 10, 4975-4980.
[125] Qu, L.; Liu, Y.; Baek, J. B.; Dai, L. *ACS Nano* 2010, 4, 1321-1326.
[126] Vitchev, R.; Malesevic, A.; Petrov, R. H.; Kemps, R.; Mertens, M.; Vanhulsel, A.; Van Haesendonck, C. *Nanotechnology* 2010, 21, 095602.
[127] Zhu, M.; Wang, J.; Holloway, B. C.; Outlaw, R. A.; Zhao, X.; Hou, K.; Shutthanandan, V.; Manos, D. M. *Carbon* 2007, 45, 2229-2234
[128] Wang, J. J.; Zhu, M. Y.; Outlaw, R. A.; Zhao, X.; Manos, D. M.; Holoway, B. C. *Appl. Phys. Lett.* 2004, 85, 1265-1267.
[129] Wang, J. J.; Zhu, M. Y.; Outlaw, R. A.; Zhao, X.; Manos, D. M.; Holoway, B. C. Carbon 2004, 42, 2867-2872.
[130] Ruan, G.; Sun, Z.; Peng, Z.; Tour, J. M. *ACS Nano* 2011, 5, 7601-7507.
[131] Berger, C.; Song, Z. M.; Li, T. B.; Li, X.; Ogbazghi, A. Y.; Feng, R.; Dai, Z. T.; Marchenkov, A. N.; Conrad, E. H.; First, P. N.; De Heer, W. A. *J. Phys. Chem. B* 2004, 108, 19912-19916.
[132] Shivaraman, S.; Barton, R. A.; Yu, X.; Alden, J.; Herman, L.; Chandrashekhar, M. V. S.; Park, J.; McEuen, P. L.; Parpia, J. M.; Craighead, H. G.; Spencer, M. G. *Nano Lett.* 2009, 9, 3100-3105.
[133] Hass, J.; De Heer, W. A.; Conrad, E. H. *J. Phys.: Condens. Matter* 2008, 20, 323202-323229.
[136] Varchon, F.; Feng, R.; Hass, J.; Li, X.; Nguyen, B. N.; Naud, C. et al. *Phys Rev Lett* 2007, 99, 126805.
[137] Virojanadara, C. et al. Homogeneous large-area graphene layer growth on 6HSiC (0001). *Phys. Rev. B* 2008, 78, 245403.
[138] Hummers, W. O. R. *J Am Chem Soc* 1958, 80, 1339.
[139] Brodie, B. C. *Ann. Chim. Phys.* 1860, 59, 466-472.
[140] Staudenmaier, L.; *Ber. Deut. Chem. Ges.* 1898, 31, 1481-1487.
[141] Paredes, J. I.; Villar-Rodil, S.; Martinez-Alonso, A.; Tascón, J. M. D. *Langmuir* 2008, 24, 10560-10564.
[142] Cai, W. W.; Piner, R. D.; Stademann, F. J.; Park, S.; Shaibat, M. A.; Ishii, Y. et al. *Science* 2008, 321, 1815-1817.
[143] Stankovich, S.; Dikin, D. A; Piner, R. D.; Kohlhaas, K. A.; Kleinhammes, A.; Jia, Y. et al. *Carbon* 2007, 45, 1558-1565.
[144] Stankovich, S.; Piner, R. D.; Chen, X. Q.; Wu, N. Q.; Nguyen, S. T.; Ruoff, R. S. *J Mater Chem* 2006, 16, 155-158.
[145] Qi, X.; Pu, K.Y.; Li, H.; Zhou, X.; Wu, S.; Fan, Q.L.; Liu, B.; Boey, F.; Huang, W.; Zhang, H. *Angew. Chem., Int. Ed.* 2010, 49, 9426-9429.
[146] Li, D.; Muller, M. B.; Gilje, S.; Kaner, R. B.; Wallace, G. G.*Nature Nanotechnol.* 2008, 3, 101-105.
[147] Stankovich, S.; Dikin, D.; Dommett, G. H. B.; Kohlhaas, K. M.; Zimney, E. J.; Stach, E. A.; Piner, R. D.; Nguyen, S. T.; Ruoff, R. S. *Nature* 2006, 442, 282-286.
[148] Wang, G.; Yang, J.; Park, J.; Gou, X.; Wang, B.; Liu, H.; Yao, J. J. of Phys. Chem. C 2008, 112, 8192-8195.
[149] Dua, V.; Surwade, S.; Ammu, S.; Agnihotra, S.; Jain, S.; Roberts, K.; Park, S.; Ruoff, R.; Manohar, S. *Angew. Chem., Int. Ed.* 2010, 49, 2154-2157.
[150] Akhavan , E. Ghaderi , *Carbon* 2012, 50, 1853-1860.
[151] Moon, I. K.; Lee, J.; Ruoff, R. S.; Lee, H. *Nat. Commun.* 2010, 1, 73-79.
[152] Gilje, S.; Han, S.; Wang, M.; Wang, K. L.; Kaner, R. B. *Nano Lett.* 2007,7, 3394-3398.
[153] Li, X.; Zhang, G.; Bai, X.; Sun, X.; Wang, X.; Wang, E.; Dai, H. *Nature Nanotechnology* 2008, 3, 538-542.
[154] Vallés, C.; Drummond, C.; Saadaoui, H.; Furtado, C. A.; He, M.; Roubeau, O.; Ortolani, L.; Monthioux, M.; Pénicaud, A. *J. of Am Chem Soc* 2008, 130, 15802-15804.
[155] McAllister, M. J.; Li, J.-L.; Adamson, D. H.; Schniepp, H. C.; Abdala, A. A.; Liu, J.; Herrera-Alonso, M.D.; Milius, L.; Car, R.; Prud'homme, R. K.; Aksay, I. A. *Chem. Mat.* 2007, 19, 4396-4404.

[156] Schniepp, H. C.; Li, J.-L.; McAllister, M. J.; Sai, H.; Herrera-Alonso, M.; Adamson, D. H.; Prud'homme, R. K.; Car, R.; Saville, D. A.; Aksay, I. A. *J. Phys. Chem. B* 2006, 110, 8535-8539.
[157] Wang, X.; Zhi, L.; Muellen, K. *Nano Lett.* 2008, 8, 323-327.
[158] Shao, Y.; Wang, J.; Engelhard, M.; Wang, C.; Lin, Y. *J. Mater. Chem.* 2010, 20, 743-748.
[159] Fan, Z.J.; Kai, W.; Yan , J.; Wei T.; Zhi, L.-J.; Feng, J.; Ren, Y. M.; Song, L. P.; Wei, F. *ACS Nano* 2011, 5, 191-198.
[160] Williams, G.; Seger, B.; Kamat, P. V. *ACS Nano* 2008, 2, 1487.
[161] Hernandez, Y.; Nicolosi, V.; Lotya, M.; Blighe, F. M.; Sun, Z.; De, S.; McGovern, I. T.; Holland, B.; Byrne, M.; Gun'Ko, Y. K.; Boland, J. J.; Niraj, P.; Duesberg, G.; Krishnamurthy, S.; Goodhue, R.; Hutchison, J.; Scardaci, V.; Ferrari, A. C.; Coleman, J. N. *Nature Nanotechnol.* 2008, 3, 563–568.
[162] Nuvoli, D.; Valentini, L.; Alzari, V.; Scognamillo, S.; Bittolo Bon, S.; Piccinini, M.; Illescas, J.; Mariani, A. *J. Mater. Chem* 2011, 21, 3428-3431.
[163] Alzari, V.; Nuvoli, D.; Scognamillo, S.; Piccinini, M.; Gioffredi, E.; Malucelli, G.; Marceddu, S.; Sechi, M.; Sanna, V.; Mariani, A. *J. Mater. Chem.* 2011, 21, 8727–8733.
[164] Khan, U.; O'Neill, A.; Lotya, M.; De, S.; Coleman, J. N. *Small* 2010, 6, 864-871.
[165] Coleman, J. N. *Account of Chemical research* 2013, 46, 14-22.
[166] Lotya, M.; King, P. J.; Khan, U.; De, S.; Coleman, J. N. *ACS Nano* 2010, 4, 3155-3162.
[167] Neill, A. O.; Khan, U.; Nirmalraj, P. N.; Boland, J.; Coleman, J. N. *J. Phys Chem* 2011, 115, 5422-5428.
[168] Li, X.; Wang, X.; Zhang, L.; Lee, S.; Dai, H. *Science* 2008, 319, 1229-1232.
[169] Liu, N.; Luo, F.; Wu, H.; Liu, Y.; Zang, C.; Chen, J. *Adv. Funct. Mater.* 2008, 18, 1518-1525.
[170] Gao, L. B.; Ren, W. C.; Li, F. et al. *ACS Nano*, 2008, 2, 1625-1633.
[171] Ni, Z. H.; Wang, H. M.; Kasim, J. et al. *NanoLetters* 2007, 7, 2758–27639.
[172] Blake, P.; Hill, E. W.; Neto, A. H. C.; Novoselov, K. S.; Jiang, D.; Yang, R. et al. *Appl Phys Lett* 2007, 91, 063124.
[173] Wei, D.; Liu, Y.; Wang, Y.; Zhang, H.; Huang, L.; Yu, G. Nano Lett. 2009, 9, 1752-1758.
[174] Hernandez, Y.; Lotya, M.; Rickard, D.; Bergin, S. D.; Coleman, J. N. *Langmuir* 2009, 26, 3208-3213.
[175] GoÌmez-Navarro, C.; Meyer, J. C.; Sundaram, R. S.; Chuvilin, A.; Kurasch, S.; Burghard, M. et al. *Nano Lett* 2010, 10, 1144-1148.
[176] Huang, P. Y.; Ruiz-Vargas , C. S.; Van der Zande, A. M.; Whitney, W. S.; Levendorf, M. P.; Kevek, J. W.; Garg, S. et al. *Nature* 2011, 469, 389-392.
[177] Meyer, J. C.; Kisielowski, C.; Erni, R.; Rossell, M. D.; Crommie, M. F.; Zettl, A. *Nano Lett.* 2008, 8, 3582-3586.
[178] Tuinstra, F.; Koenig, J. L. *J. Chem. Phys.* 1970, 53, 1126-1130.
[179] Nemanich, R. G.; Solin, S. A. *Physical Review B* 1979, 20, 392-401.
[180] Ferrari, A.; Meyer, J.; Scardaci, V.; Casiraghi, C.; Lazzeri, M.; Mauri, F.; Piscanec, S.; Jiang, D.; Novoselov, K.; Roth, S.; Geim, A. K. *Physical Review Letters* 2006, 97, 1-4.
[181] Casiraghi, C.; Hartschuh , A.; Qian, H.; Piscanec, S. *Nano Lett.* 2009, 9, 1433-41.
[182] Szabó, T.; Berkesi, O.; Forgó, P.; Josepovits, K.; Sanakis, Y.; Petridis, D.; Dékány, I. *Chemistry of Materials* 2006, 18, 2740-2749.
[183] Schniepp, H. C.; Kudin, K. N.; Li, J.-L.; Prud'homme, R. K.; Car, R.; Saville, D. A.; Aksay, I. A. *ACS Nano* 2008, 2, 2577-2584.
[184] Meyer, J. Geim, A. K. Katsnelson, M. Novoselov, K. Obergfell, D. Roth, S. Girit, C.; Zettl, A. *Solid State Communications* 2007, 143, 101-109.
[185] Fujita M.; Wakabayashi K.; Nakada K.; Kusakabe K. *J.of the Physics Society Japan* 1996, 65, 1920-1923.
[186] Boukhvalov, D.W.; Katsnelson, M.I. *Phys. Rev. B* 2008, 78, 085413.
[187] Huang, B.; Li, Z.; Liu, Z.; Zhou, G.; Hao, S.; Wu, J.; Gu, B.; Duan, W. *J. Phys. Chem. C* 2008, 112, 13442-13446.
[188] Kan, E.; Li, Z.; Yang, J.; Hou, J.G. *J. Am. Chem. Soc.* 2008, 130, 4224-4225.
[189] Son, Y.W.; Cohen, M. L.; Louie, S. G. *Phys. Rev. Lett.* 2006, 97, 216803.
[190] Barone, V.; Hod, O.; Scuseria, G. E. *Nano Letters* 2006, 6, 2748–54.
[191] Murayama, H.; Maeda, T. *Nature* 1990, 345, 791-793.
[192] Campos-Delgado, J.; Kim, Y.; Hayashi, T.; Morelos-Gomez, A.; Hofmann, M.; Muramatsu, H.; Endo, M.; Terrones, H.; Shull, R.; Dresselhaus, M.S.; Terrones, M. *Chem. Phys. Lett.* 2009, 469, 177-182.

[193] Finkenstadt, D.; Pennington, G.; Mehl, M.J. *Phys. Rev. B* 2007, 76, 121405.
[194] Yang, X.; Dou, X.; Rouhanipour, A.; Zhi, L.; Rader, H.J.; Mullen, K. *J. Am. Chem. Soc.* 2008, 130, 4216-4217.
[195] Cano-Marquez, A.G.; Rodriguez-Macias, F.J.; Campos-Delgado, J.; Espinosa-Gonzalez, C.G.; Tristan-Lopez, F.; Ramirez-Gonzalez, D. et al. *Nano Lett*. 2009, 9, 1527-1533.
[196] Terrones, M. Nature 2009, 458, 845-846.
[197] Kosynkin, D.V.; Higginbotham, A.L.; Sinitskii, A.; Lomeda, J.R.; Dimiev, A.; Price, B.K.; Tour, J.M. *Nature* 2009, 458, 872-876.
[198] Jiao, L.; Zhang, L.; Wang, X.; Diankov, G.; Dai, H. *Nature* 2009, 458, 877.
[199] Kim, K.; Sussman, A.; Zettl, A. *ACS Nano* 2010, 4, 13626.

CHAPTER III

NANOCELLULOSE

III.1 CELLULOSE

Cellulose is probably one of the most widespread and abundant biopolymer on the planet, a renewable natural resource and an almost inexhaustible raw material.

It is distributed in higher plants, in several marine animals (i.e., tunicates), and to a lesser degree in algae, fungi, bacteria and invertebrates, in which acts as reinforcing material. It has been estimated that 10^{10}-10^{11} tons of cellulose are synthesized and destroyed every year.[1] Due to its abundance, high strength and stiffness, low weight and biodegradability, the industrial use of cellulose is widespread not only in the present age, but also in the past. For millennia, cellulose has been used in products and materials in daily life, such as in energy sources, for building materials and for clothing. One of its first employs dates back to the Egyptian age, where cellulose was used for the production of the so-called "*papyri*", which allowed recording and transmission of the human culture during the centuries. It was first isolated by Anselme Payen in 1838.[2] Subsequently, different studies have been done on the chemical features and reactivity of this material, in order to define and create novel types of materials. In 1870, Hyatt synthesized cellulose nitrate from the reaction between nitric acid and cellulose, reaction at the basis of the formation of celluloid, the first thermoplastic polymeric material. Afterward, researches focused on the chemical modification of cellulose, with the aim of using it for the industrial production of fibers and filaments. Nowadays, cellulose is an important building block for the production of coatings, inks, painting, ropes, sails, boards, textile fibers, chemical precursors, cosmetics and for paper making and food additives.[3,4]

III.1.1 STRUCTURE AND MORPHOLOGY OF CELLULOSE

Cellulose belongs to the family of carbohydrates and exhibits a peculiar and unique feature in that it can be synthesized from, or hydrolyzed to, monosaccharides.[5] It can be defined as a linear homopolysaccharide consisting of β-D-glucopyranose units linked by glycosidic β (1→4) bonds in a $^4C_1$ conformation (Figure III.1). Therefore the repeating unit of the cellulose polymer is known to comprise two anhydroglucose rings joined via a β-1,4 glycosidic linkage (called cellobiose). The two end-groups of this polymer are not chemically equivalent, since one bears the "normal" C4–OH group (non-reducing end), whereas the other has a C1–OH moiety in equilibrium with the corresponding aldehyde function (reducing end).

The number of the glucose units or the degree of polymerization (DP) is influenced by the origin and treatment of the raw material. For cellulose obtained from wood pulp, DP is included between 300 and

1700, while cotton and other fibers have DP values comprised between 8000 and 10000, depending on treatment. Similar values are observed in bacterial cellulose.[6]

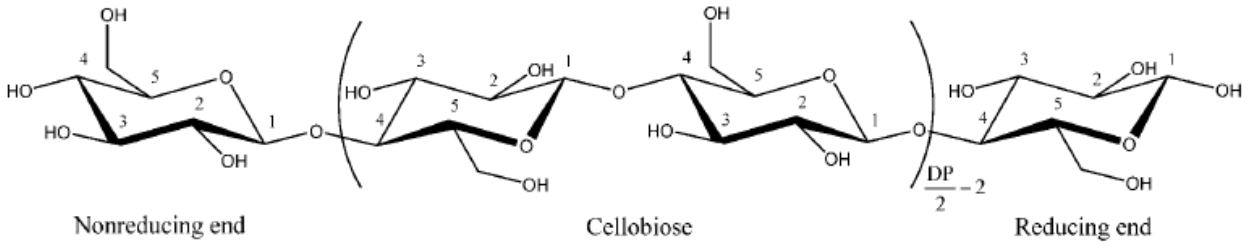

Figure III.1 Chemical structure of cellulose.

The free OH groups on each glycosidic unit have a high possibility to form intra- and intermolecular hydrogen bonds, which impart cellulose a crystalline structure and morphology. The high cohesive energy derived from such physico-chemical interactions explains why cellulose does not show a liquid phase, since its melting temperature is very close to that at which chemical degradation occurs.

Moreover, the strong hydrogen bond network makes cellulose a high stable polymer, which does not ready dissolve in common aqueous and organic solvents, and provides it a high axial stiffness.[7] Mechanical properties of crystalline cellulose can compete with that of glass and steel fibers, commonly used as reinforcing material in engineering field. The value of the elastic modulus of pure crystalline cellulose is not yet well-defined. However several theoretical molecular model and XRD measurements have been allowed to measure the elastic modulus of crystalline cellulose, which is about 140 GPa for a cellulose having a density of 1.5 mg/m^3.[8,9] Moreover, to overcome the issue of the cellulose insolubility in common organic solvent, it is needed to disrupt the hydrogen bonds network. One of the most important solvent systems for cellulose in organic synthesis is the solution of LiCl in dimethylamine.[10] Cellulose is also soluble in tetrabutylammonium fluoride trihydrate/dimethylsufoxide (DMSO),[11] cupriethylenediamine, cadmiumethylenediamine and in *N*-methylmorpholine *N*-oxide.[12]

In nature, it is not possible to observe cellulose as an individual molecule, since it gives rise to assemble of cellulose chains forming fibers. Typically, about 36 single cellulose molecules tend to bind together leading to the formation of larger units, the so called *protofibrils*. These structures pack into bigger units called *microfibrils*, which are in turn assembled into the common cellulose fibers (Figure III.2). Depending on the source, cellulose can occur in different packing. Several methods for the determination of the cellulose hierarchical structure, crystalline structure, crystallite dimensions and defects, etc. have been developed. It has been found that the amorphous regions are distributed as chain dislocations on segments along the elementary fibril, where the microfibrils are distorted by internal strain in the fiber and proceed to tilt and twist.[13]

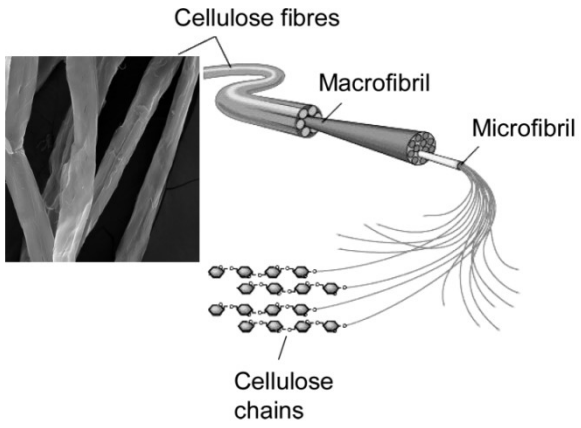

Figure III.2 Hierarchical morphology of a plant cellulose fiber.

In the ordered region, cellulose chains are highly packed together in crystallites, which are stabilized by hydrogen network. However, the proportion of crystalline and amorphous domains in natural cellulose can vary significantly at the macroscopic level of a fiber assembly, but tends to favor the ordered region, since the constitutive elements are progressively refined down to the microfibrils, resulting in an increase of cellulose mechanical properties.

The degree of crystallinity of cellulose is strongly influenced by the origin and the pretreatment of the sample: cellulose obtained from plants has a degree of crystallinity of ca. 40-60% while that of bacterial cellulose is around 60-90%.

According to the change in the hydrogen-bonding network or in the molecular orientation of cellulose, it is possible to identify four cellulose polymorphic or allomorphic forms: cellulose I, II, III and IV.

The cellulose-I crystal form, or native cellulose, has two allomorphs, named cellulose Iα e Iβ. Cellulose Iα has a single chain triclinic structure while Iβ exists in a monoclinic unit cell having two cellulose chains.

The ratio of these allomorphs is strongly influenced by the source of cellulose: bacteria and algae cellulose is rich in Iα while plant and animal cellulose is rich in Iβ.[14] Moreover Iα is a methastable phase and can be converted in Iβ by high temperature annealing in various media.[15]

Unlike cellulose I, where crystal structure has parallel unit cells, cellulose II shows a monoclinic crystal structure with two antiparallel chains in the unit cell.[16] This structural arrangement leads to a more stable structure, which makes it adapt for various textiles and paper materials.

Cellulose II can be obtained by two different processes:

a) By chemical regeneration, which consists in dissolving cellulose I in a solvent (i.e., cupric hydroxide in aqueous ammonia[17] or cupriethylenediamine,[18] ammonia or amine/thiocyanate,[19] hydrazine/thiocyanate,[20] lithium chloride/*N*,*N*-dimethylacetamide[21] and *N*-methylmorpholine-*N*-oxide[22]) then reprecipitating it in water.

b) By mercerization, which consists in the treatment of cellulose with aqueous sodium hydroxide solutions.[23]

Indeed, cellulose III is prepared by heating cellulose I and II with ammonia[24] while cellulose IV is obtained by heating cellulose III up to 260 °C in glycerol.[25]

III.1.2 SYNTEHTIC METHODS

As described previously, cellulose is mainly obtained by natural sources, such as plants, bacteria, fungi and algae. However there are also some synthetic routes that afford to prepare cellulose in vitro.

The obtainment of cellulose by photosynthesis is the dominant route, with an annual production of about 10^{11} ton.[26] Cellulose is in fact the main lignocellulosic component of cell wall in plants (25-50%),[27] where forms a natural composite with hemicellulose, lignin, pectin and wax. The isolation of cellulose from this composite occurs though a large scale chemical-pulping, separation and purification processes.

Apart from plants, the biosynthesis of cellulose takes place also in bacteria (i.e., Acetobacter, Acanthamoeba, and Achromobacter) fungi and algae (Valonia, Chaetamorpha).[28,29]

The synthesis of the bacterial cellulose occurs between the outer and plasma membranes of the cell by cellulose synthesizing complex starting with uridine diphosphate glucose (UDP glucose).[30]

Among the several routes developed for the *in vitro* synthesis of cellulose, the most important are the reaction catalyzed from enzymes and the ring opening polymerization of glucose derivates.

In the first process, cellulose is synthesized by polymerization of β-cellobiosyl fluoride, catalyzed by purified cellulase, in acetonitrile at 30 °C. Cellulose is obtained with yield of 54% and shows a DP of 22 (Figure III.3).[31]

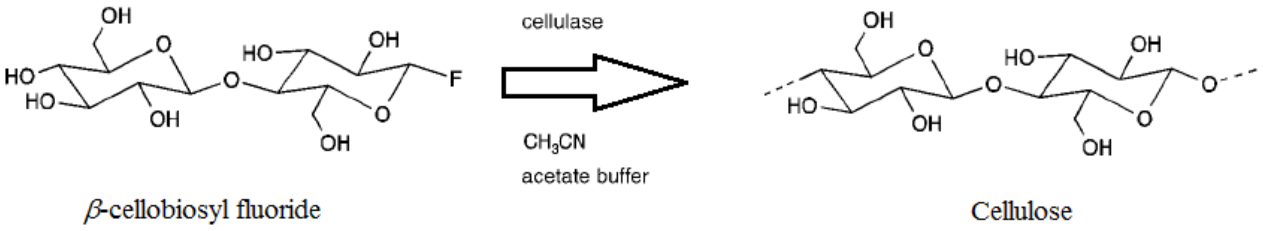

Figure III.3 Enzyme-catalyzed in-vitro synthesis of cellulose.

In the second one, cellulose is prepared by the cationic ring opening polymerization of glucose orthoesters. In 1996, Nakatsubo et al. realized the first chemosynthesis of cellulose through ring opening polymerization of 3-*O*-benzyl-α-d-glucopyranose-1,2,4-orthopivalates with different groups at position 6, followed by deprotection (Figure III.4).[32]

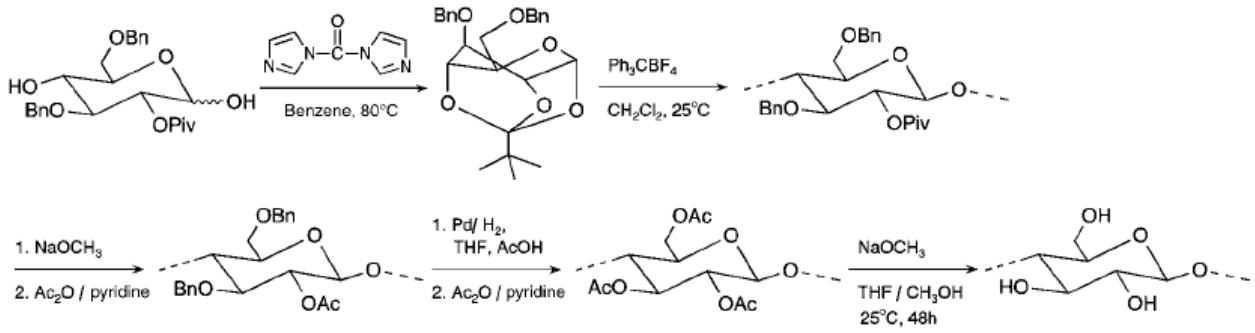

Figure III.4 Chemosynthesis of cellulose by ring-opening polymerization of 3,6-di-O-benzyl-a-d-glucopyranose-1,2,4-orthopivalate.

III.2 NANOCELLULOSE

In the last years, growing worldwide activity has been recorded regarding extensive scientific studies for the synthesis and application of a new type of cellulose-based material, the so-called *nanocellulose*. Such cellulosic material, having almost one dimension in the nanometer range, is able to combine both the typical feature of cellulose, such as hydrophilicity, broad chemical modification capacity, and the formation of semicrystalline fiber morphologies, and the specific properties of nanometric material (i.e., large surface area). Nanocellulose-based materials have gained an enormous success in the material community, due to their important chemical and physical features, renewability and sustainability, in addition to their abundance. In particular, they are mainly used as reinforcing agents in nanocomposites, thanks to their availability, light weight, nanoscale dimensions, renewability and low cost.

Although a well defined nomenclature of nanocellulose does not exist yet, it is possible to identify three types of nanocellulose on the basis of their dimensions, functions and synthetic methods: microfibrillated cellulose (MFC), CNC and bacterial nanocellulose (BNC).

Morphologies, preparation techniques, properties and applications of each type of nanocellulose will be described below.

III.2.1 MICROFIBRILLATED CELLULOSE

MFC is a cellulosic material, composed of aggregates of cellulose microfibrils with a diameter in the range of 20-60 nm and a length of several micrometers.

MFC can be synthesized by chemical and mechanical treatments. The first synthesis of MFC dates back to 1983, when Turbak et al. produced MFC by forcing suspensions of wood-based cellulose fibers through mechanical devices.[33]

Accordingly with this procedure, nowadays MFC is produced by a mechanical treatment consisting of refining and high pressure homogenizing process steps (Figure III.5). The raw cellulosic mass is extracted from wood by chemical treatment with a mixture of NaOH and Na_2S, or with H_2SO_3, leading to the obtainment of the so called *Kraft* and *sulfite* pulp, respectively. After that, the pulp dispersion is introduced in the homogenizer, where it is pumped at high pressure through a spring-loaded valve assembly. As this valve opens and closes in rapid succession, the fibers are subjected to a large pressure drop with shearing and impact forces. This combination of forces promotes high degree of microfibrillation of the cellulose fibers, leading to the production of MFC. [34]

It has been found that sulfite pulps are easier to delaminate than Kraft pulps, and that a high hemicellulose content and or charge density facilitates delamination.[35] Moreover, to enhance delamination of the fiber wall, charged groups (i.e., carboxymethyl groups) are introduced into the pulp fibers.[36] During the delamination process of the cellulose fiber clogging problems could occur. To overcome these issues and improve pulp consistency, hydrophilic polymers such as carboxymethyl cellulose (CMC), methyl cellulose, hydroxypropyl cellulose, PAAc and carrageenin are added to it. [37]

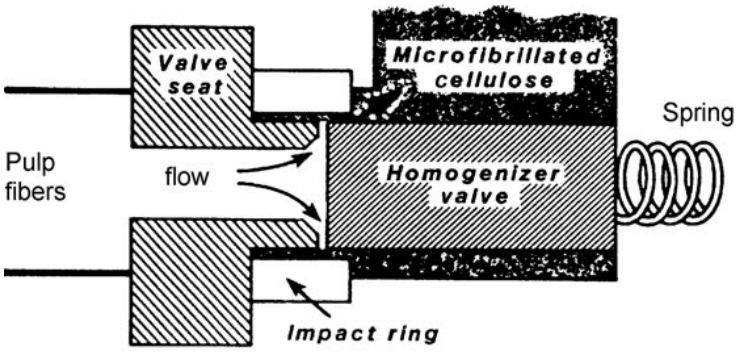

Figure III. 5 Example of high-pressure homogenizer.

However, the delamination process of the cellulose fibers is characterized by a high energy consumption, amounting to over 250000 kWh per ton of MFC, which makes their commercial application and success difficult. To decrease the energy consumption, samples are subjected to chemical or enzymatic pre-treatment before mechanical processing.

The introduction of charge by carboxymethylation is a great method to save energy: with the increasing of the charge density of pulp fibers, charge repulsion leads to a strong decrease in fiber-fiber attrition, and therefore to a reduction of flocculation and clogging phenomena.[38] Moreover, cellulose pre-treatments with alkaline solution, oxidizing agents or enzymes allow reducing the energy consumption to 1000 kWh/ton.[39]

Apart from the high pressure homogenization, MFC can be prepared by compression and roller mechanic techniques, and by cryo-crushing.

In compression mechanical techniques delignified fibers of cellulosic materials are placed in a bed of stripes located between the two plates and subjected to a constant load of 10 tons for 10 seconds. On the contrary, in roller mechanic routes delignified stripes are forced between the two rollers, one of which is fixed while the other is rotating. [40]

Cryo-crushing is an alternative method for producing MFC in which fibers are frozen using liquid nitrogen and then subjected to high speed crushing. The high shear and impact forces acting on the fibers turn them to powder comprising microfibrils.

Another issue related to MFC production, is its difficult redispersion after drying. In fact, MFC gives rise to irreversible aggregation of the fibrils, which can neither be employed in rheological applications nor dispersed for composite applications. This phenomenon is known as *hornification* because these particular aggregates exhibit properties similar to that of ivory. To prevent *hornification*, electrostatic or steric barriers, which are able to block cooperative hydrogen bonding of the cellulose chains, are introduced. The most used additives are carbohydrates, cellulose derivates, oligosaccharides and starches.[41-43] However, large amounts of such compounds are needed to eliminate this phenomenon.

Properties and characterizations

MFC properties are strongly influenced both by the source of cellulose and by the treatment or pre-treatment undergone during the synthesis. Although MFC morphology is almost the same at varying of the source of cellulose, it is drastically influenced by the preparation methods of the sample. Among the most used techniques for the determination of the nanofibers diameters there are TEM, scanning electron microscopy (SEM), field-effect SEM (FE-SEM) and AFM. The measure of MFC lengths is particularly difficult because of the formation of entanglements and because of the fact that the length of fibrils is too big to be observed in its entirety within the microscope reading section. The common practice consists in estimating the fibril length in the order of several micrometers. TEM analysis is the most accurate technique for the determination of MFC dimensions, followed by SEM and AFM. While AFM is an easier and less accurate technique than TEM, FE-SEM analyses afford to an overestimate of fibril diameters, mainly when the analysis requires that the surface is covered with a conductive metallic layer. Recently, to overcome this problem, particular methods which allow determining of MFC morphology by FE-SEM, without using of conductive substrates, have been developed.[44]

As can be seen previously, MFC dimensions depend on both the synthetic method and the typology used in the pre-treatment phase. MFC obtained by high-pressure homogenization shows a diameter of about 20-40 nm and a length of several micrometers. Non pre-treated MFC has a diameter of ca. 15-20 nm,[45] value that decreases down to 3-5 nm when MFC is obtained by a pulp pre-treated with an oxidant agent as 2,2,6,6-tetramethylpiperidine-1-oxyl (TEMPO).[46] This drastic difference is related to the centrifugation steps used

in this method, which leads to the elimination of the fibrils having the largest dimensions. Moreover, AFM images show that carboxymethylated MFC gives rise to fibrils with a diameter lower than those non pre-treated.[47] If the raw cellulose undergoes an enzymatic pre-treatment, the resulting MFC exhibits a diameter of about 20-30 nm.[48] Despite the numerous studies present in literature, it is more difficult to compare the dimensions of particles obtained through the same mechanical method but by different cellulose sources. In fact, the source of the raw cellulose is another important variable for diameter measurement. For example the diameter of MFC derived from wheat straw are more different from those obtained by soy hulls, with value ranging between 10-80 nm and 20-120 nm, respectively. These dimensions are also higher than those obtained by treatment of wood pulp.[49]

MFC properties can be also affected by the presence of lignin and hemicellulose residues: lignin is able to increase MFC dimensions while hemicellulose influences their properties through limiting agglomerate formation.

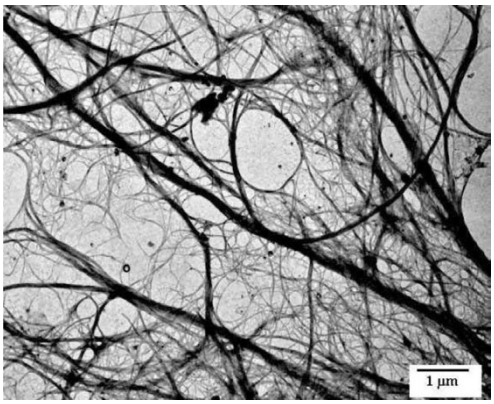

Figure III.6 TEM observation of homogenized MFC suspension obtained from Opuntia ficus-indica.

An extremely important factor in the characterization of such materials is the DP, which is strongly related both to its high aspect ratio and the lengths of the nanofibers. DP of MFC is generally calculated by using a viscosity method with a cupri-ethylene diamine solution. DP is also strongly reduced by the delignification process: MFC produced from wood pulp has a DP of 825, whereas the initial pulp had a DP of 2249.[50]

As all the features of MFC, DP depends by the source of the raw cellulose. Several studies have also shown how DP is related to the nanofiber strength and can be used in the determination of the mechanical properties of such material. However, AFM is the most useful technique for doing it.

Another important parameter for a material characterized by the presence of amorphous and crystalline domains as MFC is the determination of the crystallinity degree, which is measured by XRD. The typically used crystallinity index corresponds to the ratio between the diffracted portion from the crystalline part of the sample and the total diffraction of the same sample. The crystallinity degree also varies with the source of cellulose: it goes from a value of 70-78 % for MFC obtained by wheat and soy,[49] to 30-40 % for that prepared from sugar beet.[51] MFC obtained by wood pulp treated with oxidant agent shows a crystallinity

degree included between 60 and 90 %.[52] Moreover, both DP and the crystallinity degree are physical parameters extremely important in the application of such systems in nanocomposite materials.

As regard the chemical properties, the studies on the chemical surface result extremely important when MFC obtained by pre-treated cellulose are taken into account. One of the methods for the characterization of the MFC surface is the electric conductivity titration, which is able to quantify the aldehyde and carboxylic groups, generated for instance during the oxidative pre-treatment of pulp.

MFC is also characterized by a high specific area. Sisal MFC shows a specific area of 50 m^2/g, which is about 10 times greater than that of the common fibers.[53] Its measure is complex due to the strong aggregation upon drying. An innovative method is that based on its spectrophotometric determination, which measures the maximum UV absorption of the Congo red.[54] By using the following equation it is possible to determine the specific area of such material.

$$Specific\ area = \frac{A_{max} \times N \times SA}{MW * 10^{21}}$$

where A_{max} is the maximum absorbed amount, N is Avogadro's constant, SA is the surface area of a single dye molecule (1.73 nm^2), and MW is the molecular weight of Congo red (696 g/mol).

When MFC is obtained by high pressure homogenization, the specific area increases from 2 to 55 times related to its initial value. In addition, the presence of lignin residues allows decreasing of the specific area regardless of the source of the pulp: this is due to the modification of the internal and external pore structures that accompanies the lignin removal during the process.[54]

Moreover, when suspended in water, MFC exhibits specific rheological features that can be described in terms of pseudoplasticity and shear thinning behavior.

Herrick et al. studied rheological feature of a 2 % MFC suspension in water, measuring a viscosity of 17400, 264 and 136 MPa at 10, 1000 and 5000 s^{-1}, respectively.[55] In 2007, Paaako et al. evaluated the rheological behavior of enzymatic pre-treated MFC suspensions, having concentrations included between 0.12 and 5.9 wt.-%.[48] They show a gel-like behavior and an increase in the storage modulus by five orders of magnitude (Figure III.7).

For example a 3 wt.-% MFC suspension, exhibits a storage modulus of about 10^4 Pa. This phenomenon is due to the long fibrils, which form an inherently entangled network structure. Several experiments reported the pseudoplastic behavior of MFC gels, which show a decreasing of viscosity with increasing shear rate. This might be due to a packing aggregation of MFC, which limits the formation of a continuous network. The viscosity is influenced by the mechanical treatment: in fact it increases with increasing of number of passes through the homogenizer.[56,57]

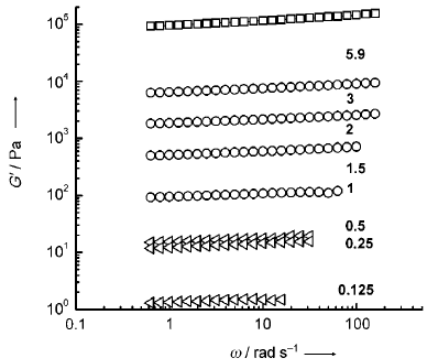

Figure III. 7 Storage modulus for MFC suspensions of various concentrations (wt.-%).[48]

Finally, an important aspect for the application of MFC in nanocomposite material is its toxicity. To define MFC toxicity, it is needed to take into account all the phases for its production and the source of cellulose. Despite all the MFC applications, there are still few studies regarding its toxicity. Recently, a study about the cytotoxic and genotoxic properties of MFC from birch pulp and Arbocel MF40 (produced by Rettenmaier & Sonhe GmbH+CO.KG) was published. The tests showed the absence of toxicity and genotoxicity for both MFC suspensions according to the in vitro methods carried out with human and mouse cells.[58]

MFC films and aerogels

When MFC is dried, aerogels or films can be obtained. MFC aerogels are particularly used in applications such as filtration, liquid storage, grafts, cushioning and catalysis, and are usually prepared by supercritical drying of MFC. There are also two alternative processes, namely cryogenic freeze-drying and vacuum freeze-drying methods, which are cost effective. Crosslinking is not required because the hydrogen bonding network and nanofibers entanglements ensure this.

Aerogels obtained by different sources of cellulose show different properties. Paakko et al. obtained MFC aerogels with a surface area ranging from 250 to 389 m^2/g, low porosity (41-82%) and a density of 0.15-0.85 g/cm^3. These samples are also ductile and flexible.[58] By observing the stress-strain curves it can be noted a linear behavior lasts up to a strain of about 40%, and the maximum compression strain is about 70%.[58] Aerogels have found applications in food packaging and in bio-nanocomposites.

As described above, MFC gels can be converted to films by dilution and dispersion in water and then either cast or vacuum filtration. When the water is removed from the MFC gel, a cellulose nanofiber network is formed with interfibrillar hydrogen bonding. The quality of the MFC film depends on the type of MFC used. Chinga-Carrasco et al. developed a computer-assisted method for determination of the structure, dimensions and specific area of MFC films.[44] Different methods have been developed for the synthesis of MFC films: the vacuum filtration affords to MFC films having a thickness of 60-80 μm[60] while those based

on a solvent exchange process are 70-90 μm thick.[61] Spin-coating allows to obtain MFC films directly on a suitable substrate.[62]

Recently, a new method for the large scale production of wood-based and plastic-like materials has been projected. MFC films are manufactured by evenly coating fibril cellulose on plastic films so that the spreading and adhesion on the surface of the plastic can be controlled.

MFC films show great mechanical properties with a Young's modulus of 20 GPa and a strength of about 240 MPa, and optimal optical features.[63] In fact, films exhibit a transmittance of 70-90%, which is sometimes decreased by the presence of a rough surface.[64]

MFC films have been used as barrier systems in food industry and packaging. In fact, due to relatively high crystallinity and to the ability of the nanofibers to form a dense network, MFC films act as a barrier material. Fukuzumi et al. demonstrated that the introduction of MFC layer into poly(lactic acid), PLA, decreases 700-fold the oxygen permeability of PLA film.[64]

Figure III. 8 Transparent film of MFC.

MFC applications

MFC is mainly used as filler in nanocomposites to increase their mechanical properties, and because of its ability to produce highly transparent and flexible films. Nanocomposites are defined as two phase-materials in which one of the phases has at least one nano-sized dimension (1-100 nm). The introduction of such nanofillers leads to an improvement of both chemical and physical properties: nanocomposite materials show better thermal, mechanical and barrier properties as well as superior transparency, recyclability and low weight, already at low filler concentrations (≤5 wt.-%). Moreover, MFC is also used in biodegradable polymers to improve their low thermal stability, fragility and poor barrier properties. As will be described in Paragraph IV.2.1, several polymer nanocomposites containing MFC has been prepared, such as polyethylene (PE), PP, acrylic and epoxy resins, PUs, and with biodegradable polymers such as PLA, PVA and polycaprolactone (PCL).

MFC has also found applications in food, pharmaceutical and cosmetic field. MFC is used as a low-calorie thickener and suspension stabilizer in food applications.[65,66] Due to its great mechanical properties it has found application in sanitary products,[67,68] coating agents[69] and wound dressing.[70]
MFC dispersions can be used as a component of suspending fluids for drilling and for oil recovery.[71] Dried MFC is also used as a battery separator[72] and as a component of drug tablets.[73]

IV.2.2 CELLULOSE NANOCRYSTALS

CNC, also known as whiskers, are the main building blocks of wood cellulose. They are constituted by rodlike cellulose crystals, having a diameter of 5-70 nm and a length included between 100 nm and several micrometers.
CNC production is based on the removal of amorphous regions of a purified cellulose source (cotton, tunicin, cellulose fibers from lignocellulosic materials, MFC) by acid hydrolysis. This method was first reported by Ränby et al. in 1950, who were able to obtain colloidal suspensions of cellulose by controlled sulfuric acid-catalyzed degradation of cellulose fibers.[74] Amorphous and para-crystalline domains of cellulose are easier to hydrolyze than the crystalline ones, which exhibit a higher resistance to acid attack, remaining intact. The amorphous regions are regularly distributed along the microfibers and therefore they are more susceptible to acid attack than crystalline domains, which are more impervious to attack. Moreover, such behavior can be also attributed to difference in the kinetics of hydrolysis.
Typical procedures employed for the production of CNC consist of subjecting pure cellulosic material to strong hydrolysis with mineral acid, keeping under strict control temperature, agitation and time. The resulting suspension is thus diluted with water and washed through several centrifugations. Then, dialysis against water is performed to eliminate any acid residues from the dispersion. Different additional steps such as filtration or ultrasonication can be carried out to disperse the CNC in a homogeneous stable suspension.
The hydrolysis is usually performed by using mineral acid such as HCl and H_2SO_4, even if H_3PO_4 and HBr are also employed for some purposes. The concentration of sulfuric acid, generally used to prepare NCC, is of ca. 65 wt.-%, while the temperature can vary from 25 up to 70 °C. Moreover, the corresponding hydrolysis time can be varied from 30 min to overnight depending of the chosen temperature. When HCl is used as hydrolyzing agent, the reaction is performed at reflux, with an acid concentration included between 2 and 4 N, and for a time that strongly depends on the source of raw cellulose.
CNC prepared by hydrolysis with HCl are difficult to disperse in water, because they tend to flocculate.[74] Contrarily, the use of H_2SO_4 as hydrolytic agent leads to a good dispersion of CNC in water. In fact, it reacts with the hydroxyl groups on the surface of cellulose yielding to the formation of negatively charged surface

sulfate esters, which, through strong electrostatic repulsion between them, promote the CNC dispersion in water(Figure III.9).[75] However, the introduction of such charged groups compromises the thermostability of the nanocrystals.[76]

Another way to achieve charged CNC consists in the oxidation of the nanocrystalline cellulose surface[77,78] or in the post- treatment of the CNC generated by hydrochloric acid hydrolysis with sulfuric acid.[79,80]

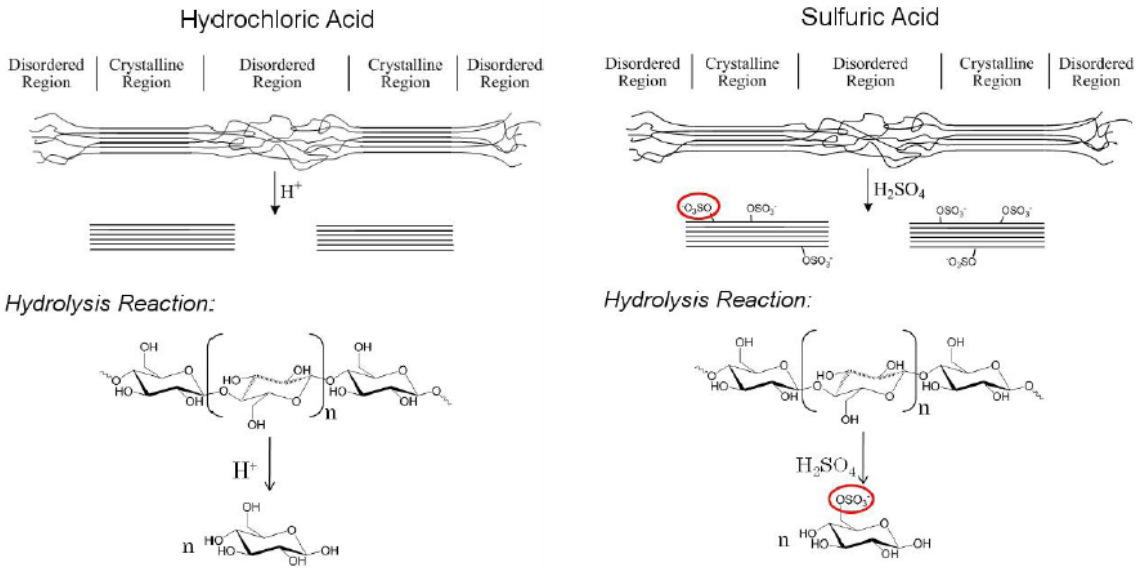

Figure III.9 Schematic representation of the isolation of CNC.

Properties and characterization

The morphological structure and properties of CNC are strongly affected by hydrolysis temperature and time, the type of mineral acid used and its concentration, the intensity of the ultrasonic bath and the source of cellulose.

As described previously, CNC show widths of few nanometers and lengths that span a larger window, from tens of nanometers to several micrometers. Biological cellulose sources particularly influence the dimensions of the CNC: cotton and wood yield to a distribution of highly crystalline nanorods (width: 5–10 nm, length: 100–300 nm),[81] whereas tunicin,[82-84] bacteria[85,86]and algae[87,88] produce crystals with larger polydispersity and dimension (width: 5–60 nm, length: 100 nm to several micrometers). Besides, the aspect ratio, defined as the length-to-width (*L*/*w*), spans a broad range and can vary between 10 and 30 for cotton and ca. 70 for tunicate.

Moreover the source of the raw cellulose influences the geometrical shape of CNC: for example, algal cellulose membrane displays a rectangular structural arrangement, whereas both bacterial and tunicate cellulose chains have a twisted-ribbon geometry.[87,89]

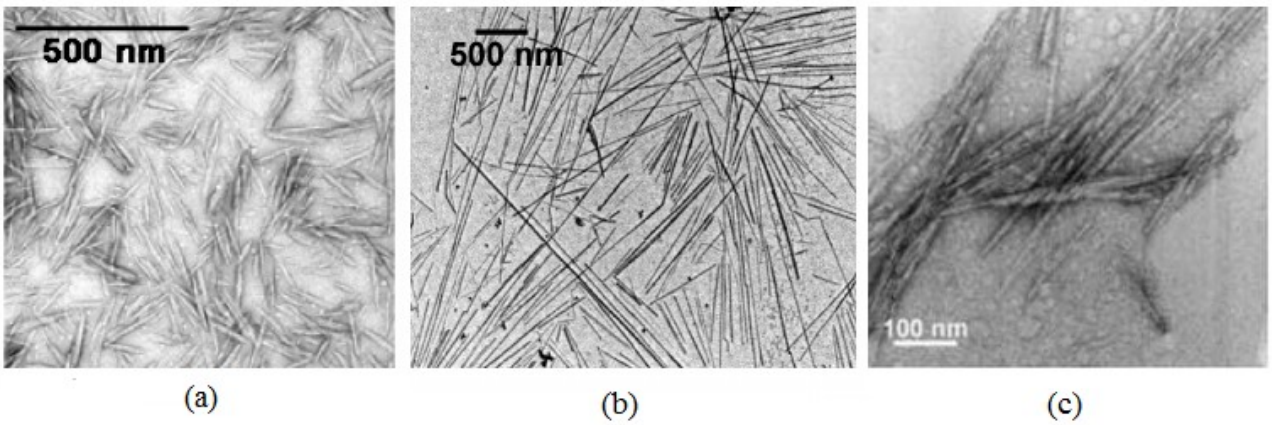

Figure III.10 TEM images of dilute suspension of hydrolyzed (a) cotton, (b) tunicin and (c) MFC.

The dimensions of CNC are also influenced by the reaction conditions, such as the hydrolysis time and temperature. Different studies have demonstrated that the nanocrystal dimensions tend to decrease by increasing the hydrolysis time and temperature. For example, Elazzouzi-Hafraoui et al. studied the size distribution of CNC derived from sulfuric acid over 30 min at different temperatures (42-72 °C), observing a decreasing of CNC dimensions with the increasing of temperature.[87,89] Beck-Candanedo et al. reported that prolonging hydrolysis time it was possible to obtain shorter nanoparticles with narrow size polydispersity.[90]

The morphological structure of CNC are usually investigated by using microscopy (TEM, SEM and AFM) or light scattering techniques, such as small angle neutron scattering and polarized and depolarized dynamic light scattering. Among them, TEM and AFM are the most important.

TEM are used to determine and value the CNC dimensions, even if sometimes it is possible to observe particle aggregates, because of the drying step for the preparation of the specimens after negative staining. Therefore, to prevent aggregation, CNC dimensions are analyzed by using TEM in cryogenic mode.[87]

AFM is used for a rapid indication of surface topography of CNC under ambient conditions and at length scales down to the angstrom level. It is also a valid technique for the determination of CNC mechanical properties and interactions, such as stiffness and adhesion or pull-off forces.[91]

CNC show low dispersibility in aqueous media and in organic solvents with high dielectric constants, such as DMSO, and diethylene glycol, but tend to aggregate in highly hydrophobic solutions.[88]

Dispersion of CNC in low polarity solvents is made possible by coating or chemical functionalization of CNC surface as well as silylation,[92] acylation,[93] carboxylation[94] or esterification.[95]

Bonini et al. obtained stable suspension of CNC in toluene and cyclohexane by coating cotton and tunicin CNC with a surfactant (Beycostat).[96]

Araki et al. prepared sterically stable aqueous and non aqueous CNC suspensions by grafting monoamino oligooxyethylene monomethyl ether on the nanocrystal surface.[77]

Azizi Samir was able to freezing dry CNC samples and redisperse them in DMF after sonication.[97] Goussè et al. succeeded in stabilizing CNC in THF by partial silylation of their surface.[98] However, a potential drawback to surface functionalization is the possibility of losing CNC properties upon modification.

Moreover, CNC have a degradation temperature as low as about 230 °C, which limits their composite processing to temperature below 200 °C.

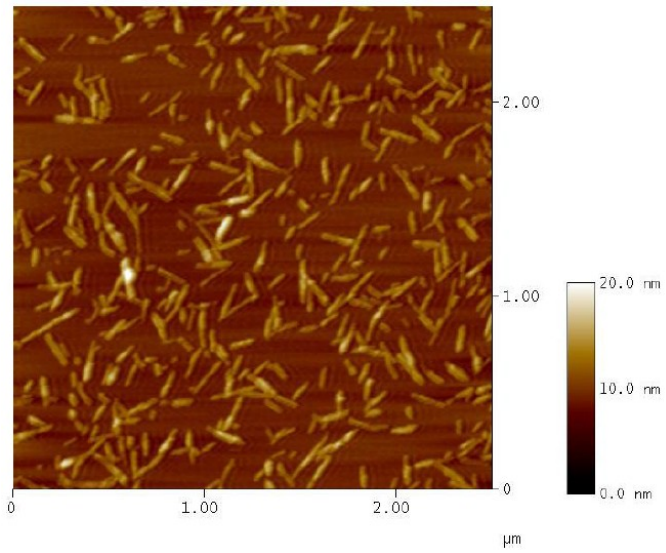

Figure III.11 AFM image of NCC isolated from wood pulp

CNC exhibit large surface area of 13.300 m^2/g [93] and extraordinary mechanical properties with an elastic modulus of 138 GPa[99] and a tensile strength of 10 GPa.[100]

As regarding the DP of CNC, it is lower than that of the native cellulose, which is strongly decreased to the so-called level-off DP (LODP) during the hydrolysis step. LODP is influenced by the source of the raw cellulose: its value is about 250 for NCC derived from cotton, 300 for ramie-CNC[101] and of ca. 6000 for CNC derived from *Valonia*.[102]

CNC are also characterized by a better thermal conductivity than cellulose. This is probably due to smaller phonon scattering in the bundle of crystallized cellulose chains in CNC than the amorphous random chains in cellulose.[103]

CNC aqueous dispersions are also able to self-organize into stable chiral nematic phases. At low concentration, CNC possess random orientation, forming an isotropic phase. As the concentration of CNC increases, for example by water evaporation, CNC orient in the same direction along a vector director resulting in a nematic liquid crystalline alignment. When the suspension reaches a critical concentration CNC can form a chiral nematic ordered phase, having optical characteristics of a typical cholesteric liquid crystal. These phenomena correspond to the helicoidal packing of several nematic planes and have already been observed in other biological systems such as cholesterol, the best known of chiral nematic liquid

crystals, DNA fragments, collagen, and chitin. [104,105] This particular property gives CNC a high optical rotatory power reflecting a circularly polarized light in a limited wavelength band.[106]

As regarding the biocompatibility of CNC, different studies have been demonstrated the non toxicity of CNC. Roman et al. conducted toxicity assessment of CNC in human brain microvascular endothelial cells, concluding that CNC were non-toxic to cell and could be used as carriers in targeted delivery of therapeutics.[107]

CNC applications

One of the main applications of CNC is in the nanocomposite field. It is a better candidate than MFC as filler in nanocomposite systems, because of its lower dimensions and density (1.61 g/cm^3), higher aspect ratio, better dispersibility, larger surface area and higher elastic modulus.

Numerous nanocomposite materials were developed by incorporating CNC into a wide range of polymeric matrices such as polysulfonates,[108] PCL,[109] poly(oxyethylene),[110] PVA,[111] cellulose acetate butyrate,[112] poly(vinyl acetate),[113] epoxides,[114] PE,[115] PP,[116] poly-(vinyl chloride) (PVC),[117] PU.[118] Moreover CNC were also incorporated into biopolymers such as soy protein,[119] chitosan,[120] and biopolymer-like PLA.[121]

CNC have also found application in biomedical and pharmaceutical field for drug delivery systems and protein immobilization. Zhang et al. demonstrated that hydrogels based on cyclodextrin/polymer inclusion can be used as controlled delivery vehicles after introduction of CNC.[122] Mahmoud et al. investigated a new type of nanocomposite consisting of CNC and gold nanoparticles as a matrix for enzyme/protein immobilization.[123]

Moreover CNC have been used as a template in the synthesis of mesoporous materials[124] and as iridescent pigments in biomolecular NMR contrast agents.[125]

In addition, CNC may be used in security paper, based on the solidified liquid crystals property,[126] and in lithium battery products as a mechanical reinforcing agent for low-thickness polymer electrolytes.[127]

III.2.3 BACTERIAL NANOCELLULOSE

The third and last kind of nanocellulose is the bacterial nanocellulose, also called microbial cellulose or biocellulose. BNC is secreted extracellularly by specific bacteria, mainly by *Gluconacetobacter* strains, which are Gram negative, aerobic, rodlike microorganisms, having an untypically acid tolerance, high motility and high ubiquity. In fact, these bacteria are widely spread in nature, where fermentation of sugars and plant carbohydrates takes place, for example, on flowers, on damage fruits and in unpasteurized juice, beer and wine. Generally, bacteria produce nanocellulose for living in different environments and for protecting

themselves from enemies, irradiation, lack of oxygen and food.[128] The synthesis of the bacterial cellulose occurs between the outer and plasma membranes of the cell by cellulose synthesizing complex starting with UDP glucose. Cellulose synthase catalyzes the addition of UDP glucose to the end of the growing cellulose chain, which exits the cell as fibers with diameters of 20-100 nm, then form ribbons and finally a tridimensional network with other cellulose fibrils (Figure III.12).

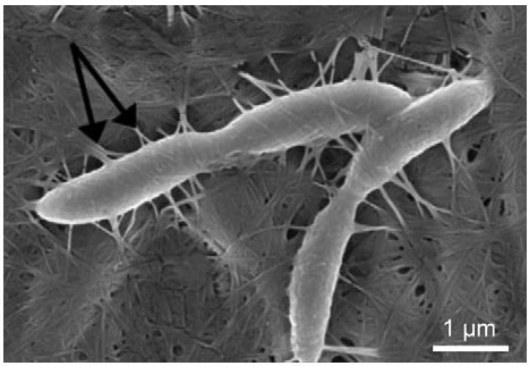

Figure III.12 *Gluconacetobacter* bacteria forming cellulose nanofibers and ribbons.

In contrast to MFC and CNC, which are isolated from different cellulose sources, BNCs are prepared starting from low molecular weight carbon source, such as D-glucose, thus using a *bottom up* method. The bacteria are cultivated in aqueous nutrient medium and BNC is secreted at the interface between liquid and air. (Figure III.13) BNC results as a stable highly swollen network with a distinct tunnel and pore structure, enclosing up to 99% of water.

Residual bacteria and components of the culture medium eventually present can be removed by heating in 0.1 M aqueous sodium hydroxide under reflux for 10–120 min, depending on the thickness of the cellulose body. Under these conditions, no detectable damage to the polymer occurs.

Pure BNC is obtained with a yield higher than 40% (in relation to the bacterial strain), a value particularly elevated for a biotechnological route: it in fact does not contain impurities or functional groups other than the hydroxylic ones.[129]

The efficiency of the process is strongly dependent on several factors such as the type of bacterial strain, the surface structure of the substrate, the component of the culture medium and the temperature used. Moreover, a continuous supply of oxygen and carbon source (D-glucose) is also required.

Over the past few years a sharp enhancement in the studies on BNC synthesis has been recorded, mainly their large scale production. Most of them are based on a combination of static and agitated cultivation. Bungay and Serafica obtained BNC by using a rotary disk reactor. However, this approach leads to a non uniform material due to the aggregation of thin layers or filaments.[130] Kralish et al. developed an alternative route for the cultivation of planar BNC fleeces and films of selectable length and adjustable height, by using a novel horizontal lift reactor.[131]

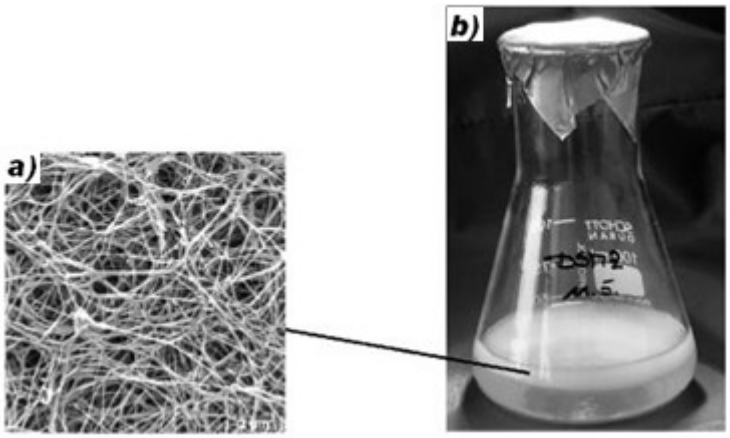

Figure III.13 a) SEM image of freeze-dried nanofiber network (magnification 10 000 X); b) pellicle of BNC from common static culture.

Properties and characterizations

The main features that distinguish BNC from common plant celluloses and other polymers are:

- the synthesis of these materials starting from low molecular weight compounds under laboratory and pilot-plant conditions;
- the direct control of the cellulose synthesis, including shape, structure and composite formation of products during biosynthesis (in situ);
- the direct formation of cellulose bodies as hydrogels and as aerogels (after drying), respectively; specificity of the formed cellulose as nanofiber support useful, e.g., for particles, metals, and proteins.

BNC is characterized by specific and extraordinary properties based on the accessible hydrated nanofibrillated network. Fink et al. elaborated a model of the BNC structure in which anhydrous nanofibrils in the range of 7X13 nm appear hydrated as whole and are aggregated to flat microfibrils with a width of 70-150 nm.[132] This indicates that water is outside of the crystalline cellulose nano-units and between these elements. A shell of non-crystalline cellulose chains passes around neighboring microfibrils to produce a microfibril band (ribbon) with a width of about 0.5 μm. (Figure III.14) The incorporated water plays an important role as spacer element and - as a hydrogen-bond forming partner of cellulose - as a stabilizing agent with respect to the network and pore structure.

BNC is characterized by a high DP in the range of 4000-10000 anhydroglucose units, a high crystallinity of 80-90%, and a small thermal expansion coefficient similar to that of glass. Besides, BNC shows excellent mechanical properties, with a Young's modulus of about 134 GPa and a tensile strength of ca. 2 GPa, value particularly similar to those of the aramid fibers (i.e., Kevlar).[133,134]

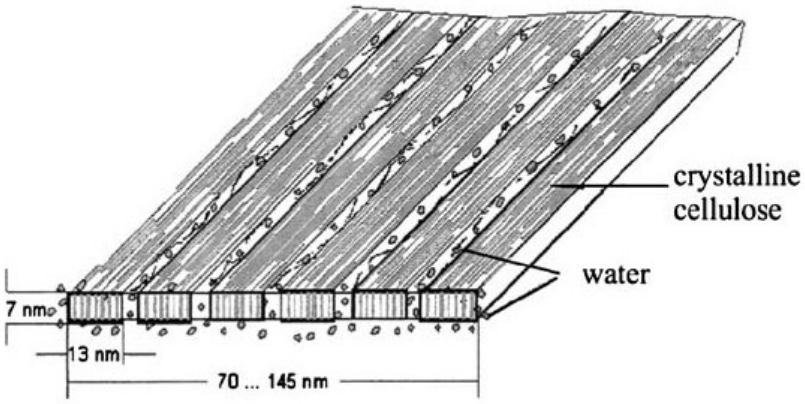

Figure III.14 Model of initially hydrated BC fibrils

As indicated previously, the shape and the supramolecular structure can be directly controlled during the synthesis and are strongly influenced by the bacteria strain used, the composition and the shape of the reactor, and the constituents of culture medium. The shape of BNC changes depending on the reactor used and the modality of cultivation (static or agitated). Flat materials, such as fleeces and foils (Figure III.150a), hollow bodies (i.e., tubes, Figure III.15b) and spheres (Figure III.15c) can be obtained during bacteria cultivation.

Flat products of different geometry are formed during static cultivation in liquid culture medium or in thin layer cultivation on solid phases like agar, silicone, rubber, and different porous membranes. The size and the thickness of the BNC fleeces and foils are influenced by the type of strain, volume of culture medium and cultivation time.[135]

Hollow bodies of different shape are formed by using a matrix in the static culture. Instead, BNC spheres are obtained under agitated cultivation conditions (shaking, stirring).

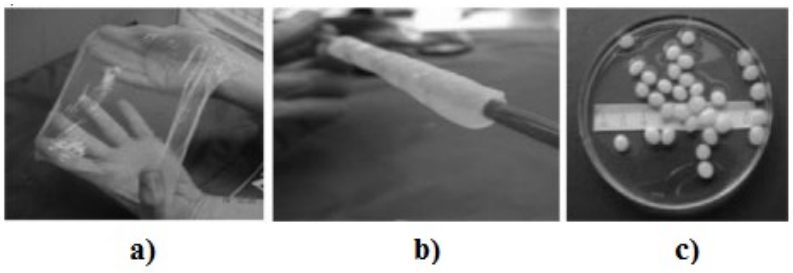

Figure III.15 BNC hydrogels formed in situ. a) Film prepared in a PP container under static conditions; dimensions: 25X25 cm^2, thickness: 200 mm.[137] b) tube as vessel implant (15 cm length, 6mm inner diameter);[137] c) Spheres formed by agitated cultivation with a shaking rate of 80–100 rpm; diameter: 2–3 mm, smooth surface.[137]

This type of cultivation opens the possibility to produce BNC in commercial fermentation equipment, even if there are some restriction such as a limited number of suitable *Gluconoacetobacter* strains, inhibition of BNC formation by share forces resulting in lower yields and change of BNC structure and properties.[136]
As reported in Figure III.16, the fiber network structure of BNC is strongly influenced by the type of *Gluconoacetobacter* chosen. In fact, the obtained BNC hydrogels show different stabilities and network architecture.

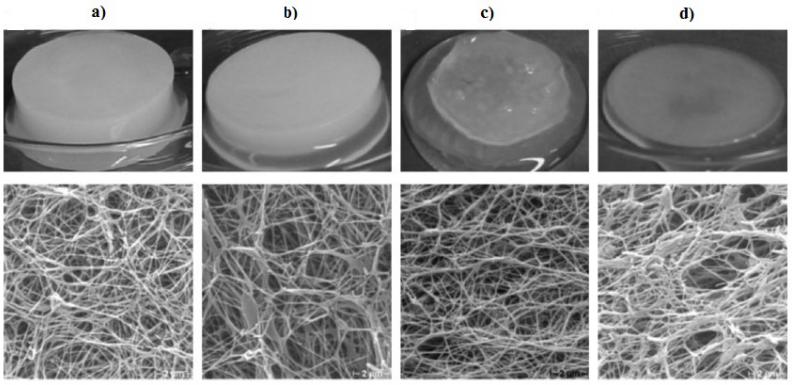

Figure III.16 Fleeces of BNC produced by four different *Gluconacetobacter* strains and their corresponding SEM images (scale bar; 2 μm): a) DSM 14666; b) ATCC 53582; c) ATCC 23769; d) ATCC 10245; DSM= Sammlung für Mikroorganismen und Zellkulturen, Braunschweig, Germany; ATCC=American Type Culture Collection, Manassas, VA, USA right: ATCC 23769.

The structure is also affected by the type of additive used in the culture medium: low molecular weight compounds, such as glycerol, β-cyclodextrin and PEG 400, can modify the network organization, and subsequently be extracted from BNC during the purification step. Therefore, these compounds act as structure-forming auxiliaries. Besides, there are additives such as CMC and some cationic starches that remain partially incorporated in the BNC network because of establishment of strong hydrogen bonds.[138]
Another parameter that can influence the BNC structure is the viscoelasticity of the culture interface. Gong et al. observed an enhancement in the degree of orientation and fibril width with the increasing of the viscosity of the oil interface.[139]

BNC applications

Similarly to MFC and CNC, the bacterial nanocellulose has been used as nanofiller in nanocomposite materials. Different nanocomposite materials have been prepared by using both organic compounds, such as bioactive agents and polymerizable monomers, polymers (i.e., polyacrylate, resins, polysaccharides and proteins), and inorganic substances, such as metal and metal oxides. A more detailed discussion of nanocomposites containing BNC is reported in Paragraph IV.2.1.

In addition to its use in nanocomposite materials, BNC exhibits a great potential as a natural biomaterial for the development of medical devices and applications in healthcare and veterinary medicine. BNC is used as artificial blood vessel and cuff for nerve suturing.[129] This material has substituted the traditional synthetic implant materials made of PE, PU or poly(tetrafluoroethylene), PTFE, which have proved insufficient, often resulting in thrombosis. Several research groups have developed prototypes of BNC tubes in the required diameter range and with a length of 5–25 cm or more. The wall of the tubes is formed by the typical transparent BNC hydrogel and is also characterized by a stable inner lumen, good stability of sutures, essential mechanical strength, and the important feature of being permeable to water, other liquids, ions, and small molecules. The tubes also show very good surgical handling and can be sterilized in standard ways.[129]

Moreover, it has been demonstrated that the use of protective cuff of BNC prevents connective tissue from growing into the nerve gap and favors the adhesion of the fascicles, facilitating early regeneration of the nerve and rapid return of the muscle function. After the observation time included from 4 to 26 weeks post-operatively the BNC tube was covered with connective tissue and small vessels within. Neither an inflammation reaction nor an encapsulation of the implant was observed. BNC are also employed in veterinary medicine for wound suturing.

Because of its high mechanical stability, high wetness with a water content of over 95%, and high purity, BNC has also found application in the cosmetic industry. For instance, two cosmetic tissue products are successful on the market: a series of masks based on BioCellulose and the mask basis material NanoMasque® (Figure III.17).

Figure III.17 Example of cosmetic application of NanoMasque®.

Both tissues are produced from pure BC and alternatively impregnated with active substances applied in cosmetics such as plant extracts, extracts from algae, essential oils, and panthenol. BNC has shown high biocompatibility with cells, with no citotoxic effects.[135,140]

BNC layers have also been investigated as loudspeaker vibration films. It was demonstrated that these films have good mechanical properties and thermal stability, good fundamental characteristics of a sound-vibration film, high specific elasticity and loss factor, and long service life.[141]

Moreover, BNC has been also used in food industry as stabilizer and emulsifier.[142]

REFERENCES

[1] Zimmermann, T.; Bordeanu, N.; Strub, E. Carbohydrate Polymers 2010, 79, 1086-1093.
[2] Payen, A. Compt. Rend. 1838, 7, 1052-1056.
[3] Han, Y.H.; Han, S.O.; Cho, D.; Kim-II, H. Macromolecular Research 2008, 16, 253-260.
[4] Paula, M.P.D.; Lacerda, T.M.; Frollini, E. eXPRESS Polymer Letters, 2008,2, 423-428.
[5] Khadem, H. S. In Carbohydrate chemistry: monosaccharides and their oligomers. Academic Press Ltd., New York, USA, 1988.
[6] Klemm, D.; Heublein, B.; Fink, H. P.; Bohn, A. Angew. Chem. Int. Ed. 2005, 44, 3358 – 3393.
[7] Kroonbatenburg, L. M. J. ; Kroon, J.; Northolt, M. G. Polym Commun 1986, 27, 290-292.
[8] Sachurada, I.; Nukushina, Y.; Ito, T. J. of Polym. Sci. 1962, 52, 651-660.
[9] Tanaka, F.; Iwata, T. Cellulose 2006, 13,509-517.
[10] Dawsey, T. R.; Mc Cormick, C. L. J. Macromol. Sci. Rev. Macromol. Chem. Phys. 1990, 30, 405–440.
[11] Ciacco, G. T.; Liebert, T. F.; Trollini, E.; Heinze, T. J. Cellulose 2003, 10, 125 – 132..
[12] Stenius, Per In Forest Products Chemistry. Papermaking Science and Technology 3. Finland: Fapet OY, 2000.
[13] Rowland, S. P.; Roberts, E. J. J. Polym. Sci., Part A: Polym. Chem. 1972, 10, 2447-2461.
[14] Nishiyama, Y.; Langan, P.; Chanzy, H. J Am Chem Soc 2002, 124, 9074-9082.
[15] Sugiyama, J.; Okano, T.; Yamamoto, H.; Horii, F. Macromolecules 1990, 23, 3196-3198.
[16] Langan, P.; Nishiyama, Y.; Chanzy, H. Biomacromolecules 2001, 2, 410 – 416.
[17] Schweizer, E. J. J. Prakt. Chem. 1857, 72, 109-111.
[18] Jayme, G. In Cellulose and Cellulose DeriVatiVes; Bikales, N. M., Segal, L., Eds.; Wiley: New York, 1971.
[19] Hudson, S. M.; Cuculo, J. A. J. Polym. Sci., Polym. Chem. Ed. 1980, 18, 3469-3481.
[20] Hattori, K.; Cuculo, J. A.; Hudson, S. M. J. Polym. Sci., Part A: Polym. Chem. 2002, 40, 601-611.
[21] Dawsey, T. R.; McCormick, C. L. J. Macromol. Sci., ReV. Macromol. Chem. Phys. 1990, C30, 405-440.
[22] Chanzy, H.; Paillet, M.; Peguy, A. Polym. Commun. 1986, 27, 171-172.
[23] Kuga, S.; Takagi, S.; Brown, R. M., Jr. Polymer 1993, 34, 3293-3197.
[24] Mann, J.; Marrinan, H. J. Chem. Ind. 1953, 1092-1093.
[25] Gardiner, E. S.; Sarko, A. J. Appl. Polym. Sci.: Appl. Polym. Symp. 1983, 37, 303-314.
[26] Sun, J. X.; Sun, X.F.; Zhao, H.; Sun, R.C. Polymer Degradation Stability 2004, 84, 331-339.
[27] Teeri, T.T.; Brumer-III, H.; Daniel, G.; Gatenholm, P. Trends in Biotechnology 2007, 25, 299-306.
[28] Vandamme, E. J.; De Baets, S.; Vanbaelen, A.; Joris, K.; DeWulf, P. Polym. Degrad. Stab. 1998, 59, 93–99.
[29] Jonas, R.; Farah, L. F. Polym. Degrad. Stab. 1998, 59, 101–106.
[30] Jonas, R.; Farah, L. F. Polym. Degrad. Stab. 1998, 59, 101–106.
[31] Kobayashi, S.; Kashiwa, K.; Shimada, J.; Kawasaki, T.; Shoda, S. Macromol. Symp. 1992, 25, 3237-3278.
[32] Nakatsubo, F.; Kamitakahara, H.; Hori, M. J. Am. Chem. Soc. 1996, 118, 1677 – 1681.
[33] Turbak, A. F.; Snyder, F.W.; Sandberg, K. R. J. Appl. Polym. Sci. Appl. Polym. Symp. 1983, 37, 815–827.
[34] Nakagaito, A. N.; Yano, H. Appl Phys A-Mater Sci Process 2004, 78, 547–552.
[35] D. Page, In Fundamentals of Papermaking Fibers: Transactions of the Symposium held at Cambridge, UK, 1989.
[36] Wögberg, L.; Winter, L.; ödberg, L.; Lindström, T. Colloids Surf. 1987, 27, 163–173.
[37] Turbak, A. F.; Snyder, F.W.; Sandberg K. R. (ITT Corp.), US-A 4341807, 1982.
[38] Horvath, E.; Lindström, T. J. Colloid Interface Sci. 2007, 309, 511–517.
[39] Ankerfors, M.; Lindström, T. In On the manufacture and uses of nanocellulose. In the 9th International Conference on Wood & Biofiber Plastic Composites, Madison, 2007.
[40] Stelte, W.; Sanadi, A.R. Industr. Engineer. Chem. Res. 2009, 48, 11211-11219.
[41] Cantiani, R.; Guerin, G.; Senechal, A.; Vincent, I.; Benchimol, J. (Rhodia Chemie), US-B 6231657, 2001.
[42] Cantiani, R.; Guerin, G.; Senechal, A.; Vincent, I.; Benchimol, J. (Rhodia Chemie), US-B 6224663, 2001.
[43] Cantiani, R.; Guerin, G.; Senechal, A.; Vincent, I.; Benchimol, J. (Rhodia Chimie), US-B 6306207, 2001.
[44] Chinga-Carrasco, G.; Syverud, K. Journal of Nanoparticle Research 2010, 12, 841–851.
[45] Uetani, K.; Yano, H. Biomacromolecules 2010, 12, 348–353.

[46] Eichhorn, S. J.; Dufresne, A.; Aranguren, M.; Marcovich, N. E.; Capadona, J. R.; Rowan, S. J. et al. Journal of Materials Science 2010, 45, 1–33.
[47] Aulin, C.; Ahola, S.; Josefsson, P.; Nishino, T.; Hirose, Y.; Osterberg, M. et al. Langmuir 2009, 25, 7675–7685.
[48] Paakko, M.; Ankerfors, M.; Kosonen, H.; Nykanen, A.; Ahola, S.; Osterberg, M. et al. Biomacromolecules 2007, 8, 1934–1941.
[49] Alemdar, A.; Sain, M. Bioresource Technology 2008, 99, 1664–1671.
[50] Zimmermann, T.; Bordeanu, N.; Strub, E. Carbohydrate Polymers 2010, 79, 1086–1093.
[51] Heux, L.; Dinand, E.; Vignon, M. R. Carbohydrate Polymers 1999, 40, 115–124.
[52] Saito, T.; Isogai, A. Biomacromolecules 2004, 5, 1983–1989.
[53] Siqueira, G.; Bras, J.; Dufresne, A. Langmuir 2010, 26, 402–411.
[54] Spence, K. L.; Venditti, R. A.; Habibi, Y.; Rojas, O. J.; Pawlak, J. J. Bioresource Technology 2010, 101, 5961–5968.
[55] Herrick, F. W.; Casebier, R. L.; Hamilton, J. K.; Sandberg, K. R. In Microfibrillated cellulose: Morphology and accessibility. In Presented at the Conference: 9. Cellulose conference (Vol. 37) Syracuse, NY, USA, 1983.
[56] Aulin, C.; Gallstedt, M.; Lindstrom, T. Cellulose 2010, 17, 559–574.
[57] Aulin, C.; Netrval, J.; Wagberg, L.; Lindstrom, T. Soft Matter 2010, 6, 3298–3305.
[58] Pitkanen, M.; Honkalampi, U.; Von Wright, A.; Sneck, A.; Hentze, H. P.; Sievanen, J. et al. (2010). Nanofibrillar cellulose – Assessment of cytotoxic and genotoxic properties in vitro. Nanofibrillar cellulose – In vitro study of cytotoxic and genotoxic properties. In Presented at the 2010 International Conference on Nanotechnology for the Forest Products Industry Espoo, Finland.
[59] Paakko, M.; Vapaavuori, J.; Silvennoinen, R.; Kosonen, H.; Ankerfors, M.; Lindstrom, T. et al. Soft Matter 2008, 4, 2492–2499.
[60] Rodionova, G.; Lenes, M.; Eriksen, O.; Gregersen, O.; Cellulose 2010, 18, 127–134.
[61] Henriksson, M.; Berglund, L. A.; Isaksson, P.; Lindstrom, T.; Nishino, T. Biomacromolecules 2008, 9, 1579–1585.
[62] Aulin, C. In Novel oil resistant cellulosic materials (Pulp and paper technology).: KTH Chemical Science and Engineering Stockholm, Sweden, 2009.
[63] Berglund, L. (2006) New concepts in natural fiber composites. Proceedings of the 27th Ris¢ International Symposium on Materials Science: Polymer Composite Materials for Wind Power Turbines :1-9.
[64] Fukuzumi, H.; Saito, T.; Wata, T; Kumamoto, Y.; Isogai, A. Biomacromolecules 2009, 10, 162–165.
[65] Curtol, F.; Eksteen, N. C. (Pebble Bed Mudular Reactor (Proprietary) Ltd.), US-A 20060006189.
[66] Akimoto, M. (Asahi Kasei Chemicals Corporation), US-A 20080107789, 2008.
[67] K. Sugiyama, Y. Takamatso, R. Kuwabara, M. Tsubata, M. Suzuki (Frommer Lawrence & Haug), US-A 20040039363, 2004.
[68] Sugiyama, K.; Takamutso, Y.; Kuwabara, R.; Tsubata, M.; Suzuki, M. (Frommer Lawrence & Haug), US-A 20080065038, 2008.
[69] Mondet J. (L'Oreal), US-A 6001338, 1999.
[70] Chatterjee, P. K.; Makoui, K. B. (Personal Products Company), US-A 4474949, 1983.
[71] Langlois, B.; Benchimol, J.; Guerin, G.; Vincent, I.; Senechal, A.; Cantiani, R. (Rhodia Chimie), US-B 6348436, 2002.
[72] Cavaille, J. Y.; Dufresne, A.; Paillet, M.; Azizi Samir, M. A. S.; Alloin, F.; Sanchez, J. Y. (Buchanan Ingersoll PC), US-A 20060102869, 2006.
[73] Innami, S.; Fukui, Y. (Daicel Chemical Industries), US-A 4659388, 1987.
[74] Araki, J.; Wada, M.; Kuga, S.; Okano, T. Colloids Surf. A 1998, 142, 75-82.
[75] Revol, J. F.; Bradford, H.; Giasson, J.; Marchessault, R. H.; Gray, D. G. Int. J. Biol. Macromol 1992, 14, 170-172.
[76] Roman, M.; Winter, W. T. Biomacromolecules 2004, 5, 1671-1677.
[77] Araki, J.; Wada, M.; Kuga, S. Langmuir 2001, 17, 21-27.
[78] Isogai, A.; Kato, Y. Cellulose 1998, 5, 153-164.
[79] Araki, J.; Wada, M.; Kuga, S.; Okano, T. J. Wood Sci. 1999, 45, 258-261.
[80] Araki, J.; Wada, M.; Kuga, S.; Okano, T. Langmuir 2000, 16, 2413.
[81] Dong, X. M.; Kimura, T.; Revol, J. F.; Gray, D. G. Langmuir 1996, 12, 2076 – 2082.
[82] Favier, V.; Chanzy, H.; Cavaille, J. Y. Macromolecules 1995, 28, 6365 – 6367.

[83] Petersson, L.; Kvien, I.; Oksman, K. Compos Sci Technol 2007, 67, 2535 – 2544.
[84] Terech, P.; Chazeau, L.; Cavaille, J. Y. Macromolecules 1999, 32, 1872 – 187.
[85] Tokoh, C.; Takabe, K.; Fujita, M.; Saiki, H. Cellulose 1998, 5, 249 – 261.
[86] Grunert, M.; Winter, W. T. J Polym Environ 2002, 10, 27 – 30.
[87] Elazzouzi-Hafraoui, S.; Nishiyama, Y.; Putaux, J. L.; Heux, L.; Dubreuil, F.; Rochas, C. Biomacromolecules 2008, 9, 57 – 65.
[88] Klemm, D.; Kramer, F.; Moritz, S.; Lindstrom, T.; Ankerfors, M.; Gray, D.; Dorris, A. Angew Chem Int Ed 2011, 50, 5438 – 5466.
[89] Itoh, T.; Brown, R. M. Protoplasma 1988, 144, 160 – 169.
[90] Beck-Candanedo, S.; Roman, M.; Gray, D. G. Biomacromolecules 2005, 6, 1048-1054.
[91] Lahiji, R. R.; Reifenberger, R.; Raman, A.; Rudie, A.; Moon, R. J. NSTI Nanotech, Nanotechnol. Conf. Trade Show, Tech. Proc. 2008, 2, 704-707.
[92] Roman, M.; Winter, W. T. In Cellulose Nanocomposites: Processing, Characterization and Properties, Vol. 938 Eds.: K. Oksman, M. Sain, American Chemical Society, New York, USA, 2006.
[93] Ping, L.; You-Lo, H. Carbohydrate Polymers 2010, 82, 329–336.
[94] Habibi, Y.; Chanzy, H.; Vignon, M. R. Cellulose 2006, 13, 679 –687.
[95] Braun, B.; Dorgan, J. R. Biomacromolecules 2009, 10, 334–341.
[96] Heux, L.; Chauve, G.; Bonini, C. Langmuir 2000, 16, 8210-82.
[97] Azizi Samir, M. A. S.; Alloin, F.; Sanchez, J.-Y.; El Kissi, N.; Dufresne, A. Macromolecules 2004, 37, 1386–1393.
[98] Goussè, C.; Chanzy, H.; Exoffier, G.; Soubeyand, L.; Fleury, E. Polymer 2002, 43, 2645-2651
[99] Nishino, T.K.; Takano, J; Nakamae, K. J. J. Polym. Sci. Part B 1995, 33, 1647–1651.
[100] Habibi, Y.; Lucia, L. A.; Rojas, O. J. Chem Rev 2010, 110, 3479–3500.
[101] Nishiyama, Y.; Kim, U. J.; Kim, D. Y.; Katsumata, K. S.; May, R. P.; Langan, P. Biomacromolecules 2003, 4, 1013-1017.
[102] Kai, A. Sen-i Gakkaishi 1976, 32, T326-334.
[103] Shimazaki, Y., Miyazaki, Y., Takezawa, Y., Nogi, M., Abe, K., Ifuku, S., et al. Biomacromolecules 2007, 8, 2976–2978.
[104] Revol, J. F.; Bradford, H.; Giasson, J.; Marchessault, R. H.; Gray, D. G. Int. J. Biol. Macromol. 1992, 14, 170-172.
[105] Orts, W. J.; Godbout, L.; Marchessault, R. H.; Revol, J. F. Macromolecules 1998, 31, 5717-5725.
[106] De Vries, H. I. Acta Crystallogr. 1951, 4, 219-226.
[107] Roman, M., Dong, S. P.; Anjali, H.; Lee, Y. W. "Cellulose Nanocrystals for Drug Delivery," in "Polysaccharide Materials: Performance by Design," American Chemical Society, Washington DC 2010.
[108] Noorani, S.; Simonsen, J.; Atre, S. In Cellulose Nanocomposites: Processing, Characterization and Properties; Oksman, K., Sain, M., Eds.; ACS Symposium Series 938; American Chemical Society: Washington, D.C., 2006.
[109] Morin, A.; Dufresne, A. Macromolecules 2002, 35, 2190-2199.
[110] Azizi Samir, M. A. S.; Alloin, F.; Sanchez, J.-Y.; Dufresne, A. Polymer 2004, 45, 4149-4157.
[111] Paralikar, S. A.; Simonsen, J.; Lombardi, J. J. Membr. Sci. 2008, 320, 248-258.
[112] Petersson, L.; Mathew, A. P.; Oksman, K. J. Appl. Polym. Sci. 2009, 112, 2001-2009.
[113] Roohani, M.; Habibi, Y.; Belgacem, N. M.; Ebrahim, G.; Karimi, A. N.; Dufresne, A. Eur. Polym. J. 2008, 44, 2489-2498.
[114] Ruiz, M. M.; Cavaille, J. Y.; Dufresne, A.; Gerard, J. F.; Graillat, C. Compos. Interfaces 2000, 7, 117-131.
[115] Junior de Menezes, A.; Siqueira, G.; Curvelo, A. A. S.; Dufresne, A. Polymer 2009, 50, 4552-4563.
[116] Bonini, C. Ph.D. Thesis, Joseph Fourier University, Grenoble, France, 2000.
[117] Chazeau, L.; Paillet, M.; Cavaille, J. Y. J. Polym. Sci., Part B: Polym. Phys. 1999, 37, 2151-2164.
[118] Marcovich, N. E.; Auad, M. L.; Bellesi, N. E.; Nutt, S. R.; Aranguren, M. I. J. Mater. Res. 2006, 21, 870-881.
[119] Wang, Y.; Cao, X.; Zhang, L. Macromol. Biosci. 2006, 6, 524-531.
[120] Li, Q.; Zhou, J.; Zhang, L. J. Polym. Sci., Part B: Polym. Phys. 2009, 47, 1069-1084.
[121] Bondeson, D.; Oksman, K. Composites Part A 2007, 38A, 2486-2492.

[122] Zhang, X. L.; Huang, J.; Chang, P. R.; Li, J. L.; Chen, Y. M.; Wang, D. X.; Yu, J. H.; Chen, J. H. Polymer 2010, 51, 4398–4407.
[123] Mahmoud, K. A.; Male, K. B.; Hrapovic, S.; Luong, J. H. T. ACS Appl. Mater. Interfaces 2009, 1, 1383–1386.
[124] Shin, Y.; Exarhos, G. J. Mater. Lett. 2007, 61, 2594–2597.
[125] Fleming, K.; Gray, D. G.; Matthews, S. Chem. Eur. J. 2001, 7, 1831–1836.
[126] Revol, J.-F.; Godbout, L.; Dong, X. M.; Gray, D. G.; Chanzy, H.; Maret, G. Liquid Crystals 1994, 16, 127–134.
[127] Samir, M. A. S. A., Alloin, F.; Sanchez, J.; Dufresne, A. Macromolecules 2004, 37, 4839–4844.
[128] Vandamme, E. J.; De Baets, S.; Vanbaelen, A.; Joris, K.; DeWulf, P. Polym. Degrad. Stab. 1998, 59, 93–99.
[129] Klemm, D.; Schumann, D.; Udhardt, U.; Marsch, S. Prog. Polym. Sci. 2001, 26, 1561–1603.
[130] Bungay, H. R.; Serafica, G. C. (Rensselaer Polytechnic Institute), US-A 6071727, 2000.
[131] Kralisch, D.; Hessler, N.; Klemm, D.; Erdmann, R.; Schmidt, W. Biotechnol. Bioeng. 2010, 105, 740–747.
[132] Fink, H.P.; Purz, H. J.; Bohn, A.; Kunze, J. Macromol Symp 1997, 120,207-217.
[133] Yano, H.; Sugiyama, J.; Nakagaito, A. N.; Nogi, M.; Matsuura, T.; Hikita, M.; Handa, K. Adv Mater 2005 17,153.
[134] Guhados, G.; Wan, W. K.; Hutter, J. L. Langmuir 2005, 21, 6642–6646.
[135] Klemm, D.; Schumann, D.; Kramer, F.; Heßler, N.; Hornung, M.; Schmauder, H. P.; Marsch, S. Adv. Polym. Sci. 2006, 205, 49-96.
[136] Hessler, N.; Klemm, D. In Control of structure and shape of bacterial synthesized nanocellulose. 235th ACS National Meeting, New Orleans, LA, United States 2008.
[137] Heßler, N. PhD thesis, University of Jena, 2008.
[138] Hessler, N.; Klemm, D. Cellulose 2009, 16, 899–910.
[139] Putra, A.; Kakugo, A.; Furukawa, H.; Gong, J. P. Polym. J. 2009, 41, 764–770.
[140] Voss, W.; Dermatest GmbH, Münster, Germany 2001 Report on the testing of moistness.
[141] Xu, C.; Sun, D.; Xu, Chunyuan, CN-A 101365264, 2009.
[142] Zhou, J.; Dong, M.; Jiang, H. Shipin Gongye Keji 2003, 24:25.

CHAPTER IV

NANOCOMPOSITE POLYMERIC MATERIALS

In the last decade, nanomaterials have been the subject of an increasing interest from the scientific community, giving rise to a real technological revolution. These systems are characterized by the presence of at least one dimension below 100 nm and by a high ratio between the surface area and volume. Thanks to the large number of nanomaterials and matrices in which they can be dispersed, such materials can find a lot of applications in different areas, including mechanics, pharmaceutical, biology, medicine, chemistry, engineering, and textile industry.

The development of this kind of materials has also been made possible by the advent of modern technologies such as scanning tunneling microscopy and scanning probe microscopy, which afforded to observe the nature of the surface structure with atomic resolution.[1] Simultaneously, the rapid growth of computer technology has made it easier to characterize and predict the properties at the nanoscale through modeling and simulation.[2]

The potential of this sector are also highlighted by the increasing number of funds that the main countries are assigning to the nanotechnology and nanomaterial sectors in these latest years.

Among them, nanocomposite polymer systems have found particular application in the main industrial fields. They are materials in which inorganic or organic particles, having at least one dimension in the order of 0.1-100 nm, are dispersed in a polymer matrix.[3]

Since many years, the addiction of different microscopic substances into the polymer matrix represents a common practice in the industrial field for the improvement of the polymer properties. In fact, although polymers are characterized by light weight, ease production and often ductility, they exhibit lower modulus and strength as compared to other materials, such as metals and ceramics. Therefore, the introduction of different particles into the polymer leads to the obtainment of a new type of materials, named polymer composites: they show higher mechanical resistance, strength, toughness and impact resistance and lower production cost than the starting polymer materials. Such improvement is mainly due to an increase of material density, which however limits polymer processability. Polymer composites are constituted by a continuous polymeric phase (matrix) and a disperse phase (filler), which generally has inorganic nature, microscopic dimensions and variable aspect ratio: particles, fibers or plates are usually employed as fillers. However, such materials exhibit a complete lack of interaction at the interface between the two components, thus limiting the possibility to obtain significant improvements of the material properties. These limits have been overcome with the advent of polymer nanocomposites. In fact, fillers having dimensions in the order of nanometers are sometimes able to uniformly disperse in the polymer matrix, giving rise to extremely high interfacial area between the two components. With the decrease of filler

dimensions, the number of surface atoms compared to their total amount becomes gradually larger, leading to the enhancement of the interaction between the polymer and fillers.[4] The interaction between polymer and filler are based on the principle of the maximum heterogeneity, which states that nanoparticles must be singularly dispersed so that each of them contributes in the same way to the overall material properties. Depending on the strength of interaction between the filler surface and the matrix, the polymer chains in close proximity to filler will be perturbed with respect to those in the bulk. The thickness *t* of the interfacial region that surrounds the particle is, to first order, independent of the particle size. Accordingly, the relative volume of this interfacial material, $V_{interface}$, with respect to the volume of the particle, $V_{particle}$, will increase as the particle size decreases. In Figure IV.1, $V_{interface}$ / $V_{particle}$ as a function of particle aspect ratio has been reported. The filler size is expressed as δ, the ratio of the thickness of the interface to the smallest dimension of the particle. Fillers having micrometer sizes exhibit $\delta \approx 0.01$, which indicates that, for any aspect ratio, the volume of the particle is higher than that of the interfacial region. When the filler sizes are reduced to the nanoscale, δ is about 1-10 and the volume of the interfacial region exceeds the volume of the particle. In addition, at a fixed value of δ, the aspect ratio has an effect on $V_{interface}$ / $V_{particle}$, which increases from plates to rods to spheres as the fillers change from two–dimensional (plate) to one-dimensional (rod) to zero-dimensional (sphere) objects (Figure IV.1).

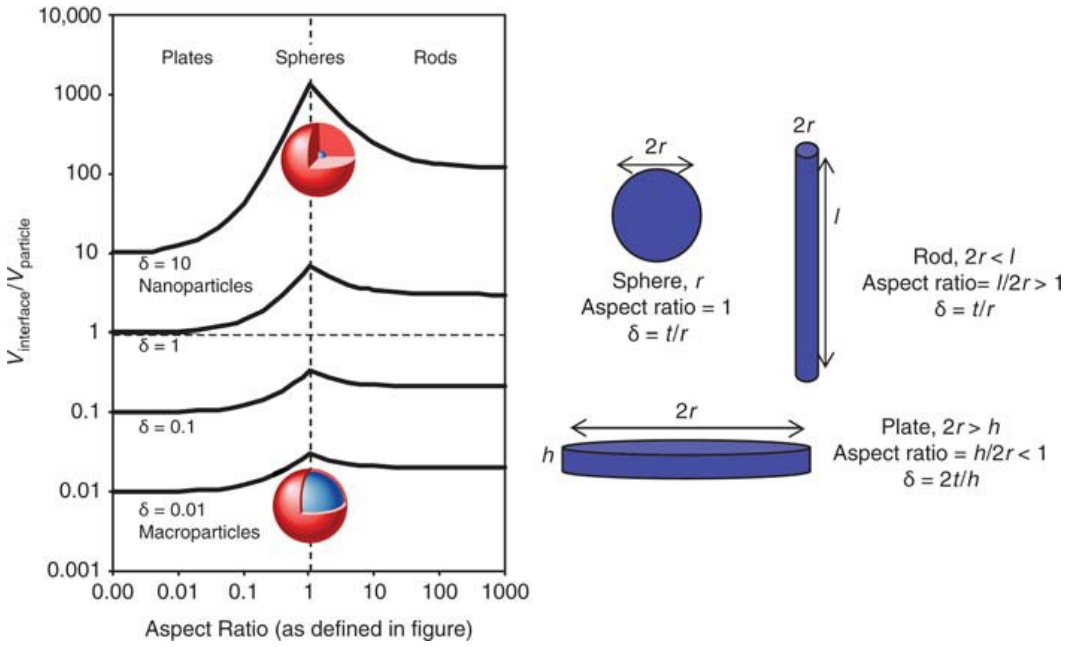

Figure IV.1 The ratio of interfacial volume to the particle volume ($V_{interface}/V_{particle}$) as a function of the particle aspect ratio and the ratio of the interfacial thickness to the particle size (δ). The aspect ratio and δ are defined in the schematic at right (r is radius, l is length, h is height). The interfacial thickness (red shell, t) is assumed to be independent of the particle size. As particles decrease in size to less than 100 nm, the interfacial volume around a particle can dominate the physical properties, and this is particularly evident for spheres and rods.[5]

The extent of this change increases dramatically as the filler size decreases; for example, at δ ≈10, $V_{interface}/V_{particle}$ enhances by two orders of magnitude between plates and spheres. These calculations demonstrate the impact that even a small volume fraction of filler has on the surrounding polymers. For example, if we disperse 1 vol% of nanosphere (radius 2 nm) in a polymer (interfacial thickness ≈ 6 nm), the volume fraction occupied by the interfacial region is about 63 vol%, indicating that more than half of the composite is influenced by the presence of the second-phase particles. When the particle radius increases to 20 nm, without changing the interfacial thickness or particle loading, the volume occupied by the interfacial region would be only ≈ 1.2 vol%.[5]

Therefore, nanometric dimensions and the high surface area of nanofillers afford to obtain a remarkable improvement of material properties when compared with the matrix polymer alone or traditional macro- and micro- composite materials.

Indeed, nanocomposite polymers are characterized by:

- higher mechanical properties, such as moduli, strength, dimensional stability, impact resistance;
- greater thermal stability;
- flame retardance;
- resistance to abrasion and solvents;
- electrical conductivity;
- optical transparency;
- lower gas permeability;
- easy recyclability.

Moreover, the use of nanofillers not only improves the properties of the material but can also confer some features not owned by the starting polymer (e.g., magnetic and optical properties).

The main interesting aspect of using nanofillers is the possibility of drastically reducing their amount into the polymer. The lower loading restricts some side effects, such as the increase of density, the decrease of processability, the alteration of impact resistance and some other superficial aspects of the polymer, which are determined by the addition of traditional additives.[6,7]

For example, low volume additions (1–5%) of nanoparticles, such as layered silicates or carbon nanotubes, provide property enhancements with respect to the neat resin that are comparable to those achieved by conventional loadings (15–40%) of traditional fillers.[5]

Nanofillers can be divided in three different classes, on the base on how many dimensions (width, length, height) of the dispersed particle are in the nanometer range (Figure IV.2):

- zero-dimensional or isodimensional particles (0D), in which all the three dimensions are in the nanometer range, such as silica particles, fullerenes, semiconductor nanoclusters, Polyhedral Oligomeric Silsesquionaxes;

- mono-dimensional particles (1D), in which two dimensions are in the order of nanometers and the third is larger. This kind of particles forms elongated structure such as nanotubes and whiskers. Carbon nanotubes, cellulose whiskers and silicates having a needle-like structure belong to this class;
- bi-dimensional particles (2D), which are characterized by only one dimension in the nanometer range, such as graphene, lamellar silicates and exfoliated clays. This kind of filler is present in the form of sheets of one to a few nanometer thick to hundreds to thousands nanometers wide and long. From these particles, polymer-layered nanocomposite can be obtained through the intercalation of the polymer (or a monomer subsequently polymerized) inside the galleries of layered crystals.

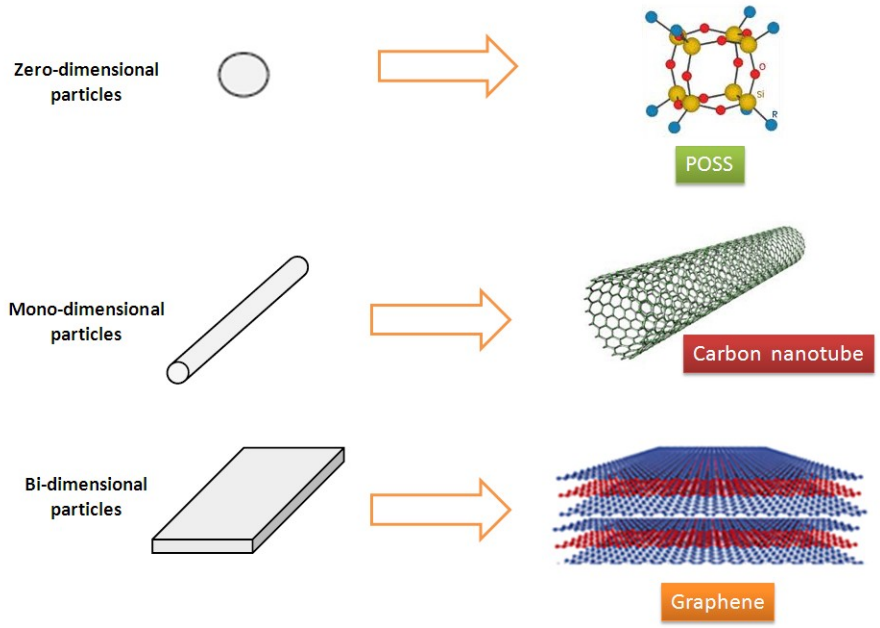

Figure IV.2 Examples of nanoparticles having different dimensions in the nanometer range.

Thanks to the high number of material that can be obtained by introducing various nanofillers in polymer matrices having different nature, polymer nanocomposites have found application in several fields. The main application of such materials is certainly in the automotive area. In fact, most of car components are made with polymer nanocomposites: they show a greater lightness, recyclability, and stiffness similar to that of non filled polymer. For example, car external coating is realized by using nanocomposites of polycarbonate, which have exhibited high resistance to abrasion and atmospheric agents without reducing body brightness.

In the aerospace field, nanocomposite-based coatings are used to improve the resistance of the machine surface from the erosion due to the atmospheric agents.

In pharmaceutical industries, polymer nanocomposites are employed for the development of drug delivery systems, while those containing silver particles have been used in biomedical field to improve the material sterility, thus obtaining safer instruments.
Another promising application of nanocomposites is in the building sector. Currently, the addition of titanium dioxide into paints and solvents allows realizing self-cleaning surfaces and coatings.
In textile field, the introduction of fillers such as silicates, POSS, fullerenes in the polymer matrix affords to improve the flame resistance of tissues.

Here we will discuss about nanocomposites containing nanoparticles characterized by one or two dimensions in the nanometer range; in particular, we will examine graphene nanocomposites and nanocomposites containing nanocellulose, materials studied in this thesis work.

IV. 1 NANOCOMPOSITES WITH 1D- NANOFILLERS

IV. 1. 1 NANOCELLULOSE NANOCOMPOSITES

In recent years, thanks to an increasing interesting toward environmental issues, the use of natural fibers as fillers in polymer nanocomposites has gained much attention.[8]
Among natural fibers, nanocellulose represents an appropriate filler because of its good mechanical properties, biodegradability, renewability, low cost and abundance.[9,10] In fact, the introduction of such nanofiller leads to an improvement of both chemical and physical properties: its nanocomposite materials show better thermal, mechanical and barrier properties as well as superior transparency, recyclability and a low weight, already at low filler concentrations (≤5 wt.-%).
As reported in Chapter III, it is possible to identify three types of nanocellulose on the basis of their dimensions, functions and synthetic methods: MFC, CNC and BNC.
For each of them, I will discuss about the corresponding polymer nanocomposites, their synthetic methods and properties.

MFC nanocomposite materials

MFC can be viewed as a cellulosic material composed of expanded high-volume cellulose, moderately degraded and greatly expanded in surface area, and obtained by a homogenization process. MFC actually consists of aggregates of cellulose microfibrils with a diameter in the range 20–60 nm and a length of several micrometers. MFC is used as filler in nanocomposites to increase their mechanical properties, and because of its ability to produce highly transparent and flexible films. Moreover, it is also used in biodegradable polymers to improve their low thermal stability, fragility and poor barrier properties.

MFC nanocomposites can be usually obtained by six different methods:

- Casting of aqueous MFC dispersion by using water soluble matrix materials
- Casting of MFC dispersion to which a latex dispersion has been added
- Dispersion of MFC and casting of films from a solvent in which the matrix material can be dissolved
- Dispersion of dried MFC into a hydrophobic matrix
- Reinforcement of porous MFC films with an agent to improve their properties
- Use of aqueous MFC dispersions to form composite materials with the matrix in the form of fibers by papermaking, pressing and press molding.

As illustrated in Figure IV.3, MFC nanocomposites have been prepared both with non biodegradable polymers, such as PE, PP, acrylic and epoxy resins, PUs, and with biodegradable polymers such as PLA, PVA and PCL. Below, a brief summary of the main MFC nanocomposites and their corresponding properties is reported.

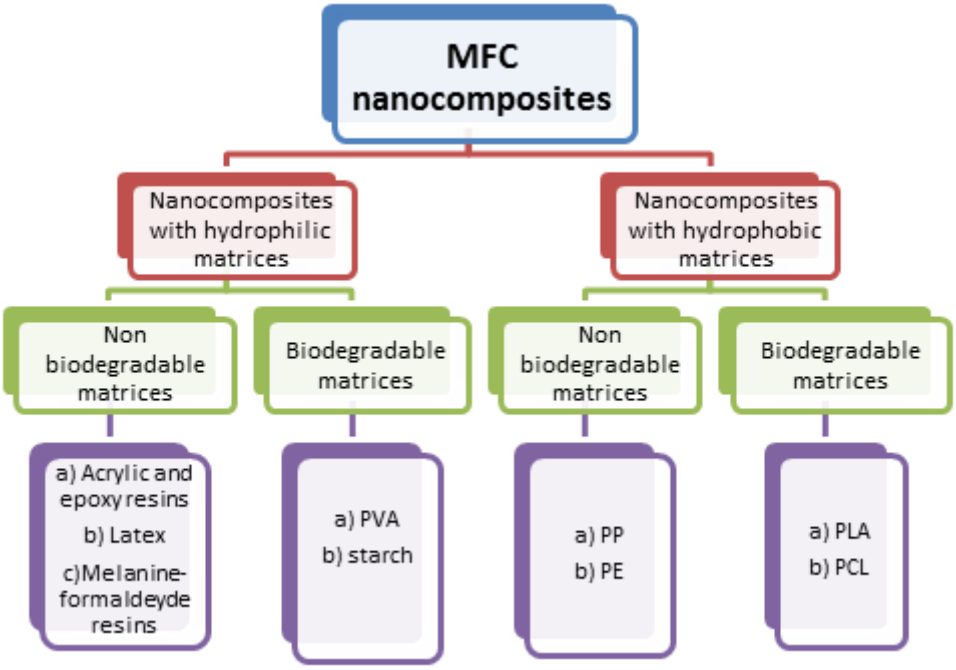

Figure IV.3 Classification of MFC reported in the literature.

MFC/thermosetting resins nanocomposites

In literature, different studies about the employ of MFC as reinforcement agent in thermosetting resins are reported.

Phenol-formaldehyde resin containing MFC have been prepared by Nakagaito et al. by impregnating Kraft pulp with the resin and compressing the obtained material under high pressure. To obtain a complete fibrillation of the pulp fibers, and thus an improvement in the mechanical properties of the initial resin, it is

needed to pass the mixture 16-30 times though a refiner, followed by high pressure homogenization. The nanocomposite obtained exhibited a Young' modulus of about 19 GPa and a bending strength of 370 MPa.[11]

Moreover, it has been noted that reinforcement effect given by MFC introduction on thermosetting resins depends by the pre-treatment subjected by the raw cellulose. In fact, phenolic resins containing MFC obtained by alkali-treated cellulose show tensile strength significantly higher than that of non-treated MFC nanocomposite.[12]

In 2005, Bruce et al. prepared composite materials based on acrylic or epoxy resins and MFC derived from swede root. All the systems showed stiffness and strength higher than that of unmodified resins.[13]

Besides the enhancement of the mechanical properties, MFC can improve the optical feature of some polymer systems. Iwamoto et al. prepared MFC-acrylic resin nanocomposites which are able to retain the transparency of the matrix resin even at high fiber content (70 wt.-%).[14,15]

MFC/PU nanocomposites

The introduction of MFC in PU systems can strongly increase their mechanical properties. In fact, polyurethanes, which are rather polar material, are able to interact with the polar groups of cellulose, leading to good interfacial adhesion, and thus to an increase of mechanical properties.[16]

Seydibeyoglu et al. prepared MFC-polyurethane nanocomposites, which exhibit improved thermal and mechanical properties. With MFC amount of 16.5 wt.-%, the tensile strength and the storage modulus were five and thirty times higher than those of the unmodified polyurethanes, respectively.[17]

MFC/PVA nanocomposites

PVA are a water-soluble, biocompatible and biodegradable polymer, mainly used in biomedical application such as in tissue and cartilage reconstruction, drug delivery systems, soft contact lens, etc. In the latest years, MFC and nanocellulose in general, have been introduced in such systems to improve their mechanical properties and to improve their durability.

Wang and Sain reported that the introduction of soybean MFC in PVA systems led to a two-fold increase in tensile strength if compared with material without fibers.[18,19]

MFC-PVA nanocomposites, with a fiber content of about 20 wt.-%, exhibit a E-modulus and a tensile strength three and five time higher, respectively, than those of PVA.[20]

MFC-PVA nanocomposites with a variable content of fibers (0-90 wt.-%) were prepared by Leitner et al. It was observed that with a MFC amount of 50 wt.-% the tensile strength and the elastic modulus increased of 3.5 and 20 times, respectively. This trend continued with the increasing of the MFC content, demonstrating that the MFC amount is the main crucial factor of nanocomposite mechanical properties.[21]

MFC/poly(styrene-co-butylacrylate) latex nanocomposites

Nanocomposite of poly(styrene-co-butylacrylate), poly(S-co-BuA), latex containing MFC obtained from *Opuntia ficus-indica* cladodes were prepared. The study underlined a strong reinforcing effect of MFC on the matrix: the tensile modulus enhanced from 0.6 to 34.5 MPa with an amount of MFC of ca. 10 wt.-%, while the tensile strength was about 14.5 MPa (Figure IV.4). Moreover, it was found that MFC increased the thermal stability of the composite and that the swelling behavior of the polymer matrix decreased with the increasing of the fiber content.[22]

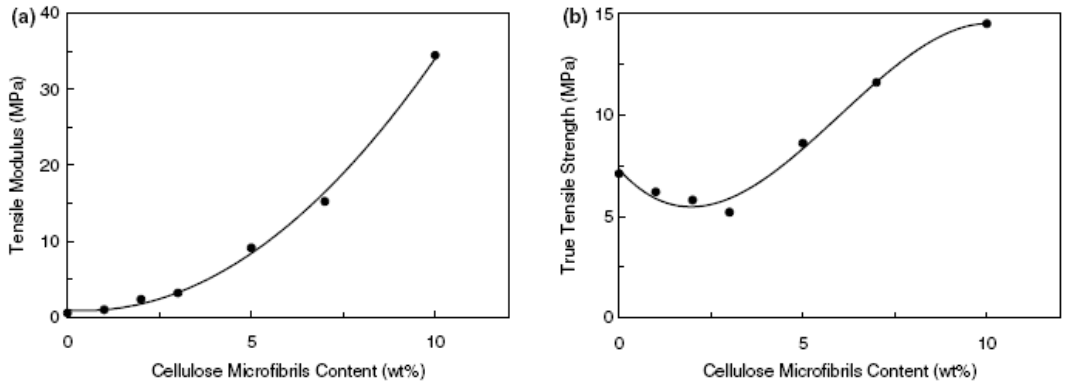

Figure IV.4 Young's modulus, (b) true tensile strength vs cellulose microfibrils content of poly(S-co-BuA)-based composites filled with MFC.

MFC/PE or PP nanocomposites

During these years, several studies have been done to disperse MFC in hydrophobic polymers such as PE and PP.

PP nanocomposites were obtained by MFC and PP fibers by using compression molding. SEM images revealed that MFC were homogeneously dispersed, but the porosity of the PP matrix together with some gaps between fibers and PP matrix suggested a lack of good adhesion. However, the MFC-PP nanocomposite exhibited tensile strength and tensile modulus higher than those of unmodified PP.[23]

MFC/PLA nanocomposites

PLA is one of the most important biopolymer, characterized by optimal physical and mechanical properties. It derives from renewable sources such as wood residues, corn and other biomass, and exhibits some features comparable with those of fossil fuel-based plastics. However, it is characterized by fragility, low thermal stability, poor barrier properties and high cost.

Okubo et al. prepared MFC-PLA nanocomposite by mixing PLA and bamboo MFC in water, followed by vacuum filtration of the resulting dispersion, and hot pressing of the dried filtered sheets. This research

demonstrated that the introduction of MFC increases the mechanical properties of PLA, just at lower concentrations.[24]

MFC-PLA composite have been also synthesized by solvent exchange. Iwatake et al. dispersed MFC in excess acetone, added dissolved PLA and evaporated acetone, kneaded the residue in a twin rotary-roll mixer, and finally compounded this latter at 140 °C. The MFC was uniformly dispersed, while the Young's modulus and the tensile strength are higher than those prepared via direct introduction of MFC to the molten PLA matrix.[25]

PLA fibers and formed papers from a PLA-fiber suspension through the addition of MFC have been used in a process like papermaking, followed by press molding at high temperatures (Figure IV.5).[26]

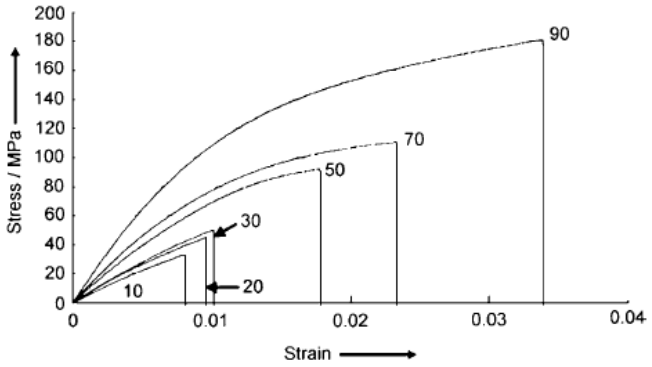

Figure IV.5 Stress–strain curves of MFC/PLA composites at different fiber contents. The percentage indicates the MFC-fiber content.[26]

MFC/PCL nanocomposites

PCL is a biodegradable polymer derived from oil, having good water, solvent and chlorine resistance, low viscosity and melting point. However, it is also characterized by a low tensile strength of about 23 MPa. Therefore MFC can be a great solution to increase the mechanical properties of this material. MFC-PCL nanocomposite were prepared by Loönnberg et al.: MFC was grafted with PCL with the aim to improve compatibility with PCL matrix. The obtained films were hot-pressed together with a PCL film to produce a laminate, which showed an interfacial adhesion higher than that of unmodified systems.[27]

CNC nanocomposite materials

Nanocrystalline cellulose is constituted by rodlike cellulose crystals, having a diameter of 5-70 nm and a length included between 100 nm and several micrometers. They are prepared by the removal of amorphous cellulose fibers through the use of acid hydrolysis.

As a result of their extraordinary properties (see Paragraph III.2.2), CNC are better candidate than MFC as filler in nanocomposite systems. In fact, they exhibit lower dimensions and density (1.61 g/cm^3), higher aspect ratio, better dispersibility, lower susceptibility to bulk moisture absorption, a larger surface area and higher theoretical elastic modulus. Favier et al. reported the first nanocomposite systems containing CNC:

they demonstrated that the introduction of CNC as reinforcing filler in poly(S-co-BuA) latex led to a strong improvement in the matrix modulus in the rubbery state[28] (Figure IV.6). Since then, numerous nanocomposite materials were developed by incorporating CNC into a wide range of polymeric matrices such as polysulfonates,[29] PCL,[30] styrene-butylacrylate latex,[31] polysiloxanes,[32] poly(oxyethylene),[33] CMC,[34] PVA,[35] cellulose acetate butyrate,[36] poly(vinyl acetate),[37] poly(ethylene-vinyl acetate),[38] epoxides,[39] PE,[40] PP,[41] PVC,[42] PU,[43] and WPU.[44] Moreover CNC were also incorporated into biopolymers such as soy protein,[45] chitosan,[46] and biopolymer-like PLA,[47] poly(hydroxyoctanoate),[48] and polyhydroxybutyrates.[49]

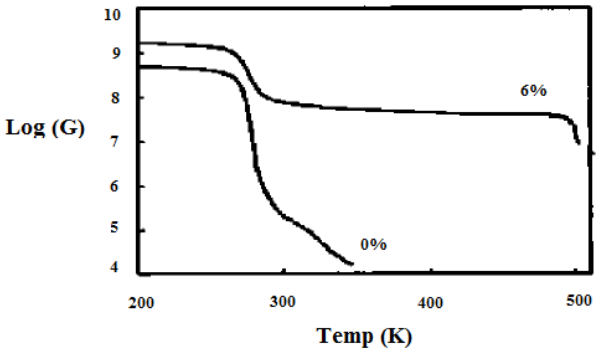

Figure IV.6 Logarithm of storage shear modulus versus temperature for poly(S-co-BuA) nanocomposite reinforced by 6% wt.-% of tunicate CNC.[28]

One of the key steps in the formation of nanocomposite polymer systems containing CNC as filler is the mixing process used to disperse CNC and polymers. As described previously, the hydrophilic nature of CNC allows its dispersion in aqueous system but not in organic media. Several attempts have been done to overcome this problem, thus extending the choice of the matrix also to the hydrophobic polymers. A first example is represented by the use of water dispersed polymers, i.e., latexes, which allows the use of hydrophobic polymers as matrices and ensures a good level of dispersion of CNC. A second valid method consists in dispersing the nanofillers in an adequate (with regard to the matrix) organic medium. This is possible by coating their surface with a surfactant or by chemically modifying their surface. Unfortunately, these techniques show some disadvantages: the high amount of surfactant required prohibits its application in the composite field, while the chemical modification of surface decreases the mechanical properties of the resulting nanocomposites. Recently, it has been found that CNC can be uniformly dispersed in DMF and in DMSO, without any additive or surface modification, opening the way for the using of hydrophobic polymer matrix.

The mixture process between CNC and polymer can be performed by simple stirring at room temperature or under vacuum, to prevent the presence of air bubbles in the final product.

Among the several techniques developed for the obtainment of CNC-nanocomposite systems, the most commonly used are casting evaporation, electrospinning, extrusion and sol gel processes.

Casting evaporation allows preparing nanocomposite systems containing CNC, by solvent evaporation. DMSO,[50] DMF,[51] and THF[52] are the main solvent used for obtaining such systems by casting evaporation. PP containing NCC is prepared by using toluene as solvent for the nanofibers dispersion. Schroers et al. prepared nanocomposite films based on ethylene oxide/epichlorohydrin and CNC, which were produced by dispersion-casting of CNC fillers in THF/water mixtures.[53]

Cao et al. prepared nanocomposite films of PCL-based WPU containing NCC by casting evaporation. The films showed a significant increase in Young's modulus and tensile strength from 0.51 to 344 MPa and 4.27 to 14.86 MPa, respectively, with increasing filler content from 0 to 30 wt.-%. In particular, the Young's modulus increased exponentially with the filler up to a content of 10 wt.-%.[54] (Table IV.1)

Table IV.1 Mechanical properties of WPU and the WPU/CNC nanocomposites obtained from tensile tests: Young's modulus (e), tensile strength (σ_b), and elongation at break (ε_b).[54]

Sample	E (MPa)	σ_B (MPa)	ε_B (%)
WPU	0.5 ± 0.1	4.3 ± 0.8	1086.4 ± 30.3
WPU-CNC 5 wt.-%	0.7 ± 0.3	9.3 ± 1.3	986.6 ± 36.9
WPU- CNC 10 wt.-%	7.8 ± 0.2	10.2 ± 1.9	735.5 ± 32.3
WPU- CNC 15 wt.-%	47.5 ± 1.8	12.1 ± 1.8	614.9 ± 20.6
WPU- CNC 20 wt.-%	116.6 ± 6.7	12.3 ± 2.0	420.8 ± 25.6
WPU- CNC 25 wt.-%	236.9 ± 12.5	14.2 ± 1.4	340.1 ± 18.7
WPU- CNC 30 wt.-%	334.4 ± 10.9	14.9 ± 1.2	186.1 ± 20.1

Electrospinning allows synthesizing fibers with diameters ranging from several micrometers down to 100 nm or less by the action of electrostatic forces. This method is also used for the fast and simple preparation of polymeric filaments. Rojas et al. reported nanocomposite films of polystyrene containing CNC: they found that the dispersion of CNC in hydrophobic matrix can be improved by the addiction of a nonionic surfactant (i.e. sorbitan monostearate).[55]

Electrospinning is also used for the synthesis of PVA[56] and PCL[57] nanofibers containing CNC. The introduction of CNC in such systems increases the storage modulus at all the investigated temperature. Moreover, they show a non linear stress-strain deformation behavior.[56,57]

CNC-based nanocomposites can be also obtained by using twin extrusion as processing method. It consists of pumping an aqueous dispersion of CNC coated with a surfactant or PVA into a melted polymer, such as PLA, during extrusion. However these systems show poor compatibility. Therefore, to overcome this problem, CNC is grafted with a polymer. Junior de Menezes et al. synthesized low density PE (LDPE) containing fatty acid-grafted CNC by extrusion.[40]

An alternative technique for the preparation of such nanocomposites is the sol-gel process. It consists in the formation of a three-dimensional template through self-assembly of CNC, which is filled with a polymer. (Figure IV.7) The first step of this route is characterized by the formation of a homogeneous aqueous CNC dispersion, to which a different solvent, such as acetone, is added. The solvent exchange promotes the self-assembly of a gel of CNC, which is then interpenetrated with a polymer by immersion in a polymer solution. Finally, the resulting nanocomposite is dried and compacted. It should be noted that the polymer solvent must be miscible with the gel solvent and must not redisperse CNC.[58]

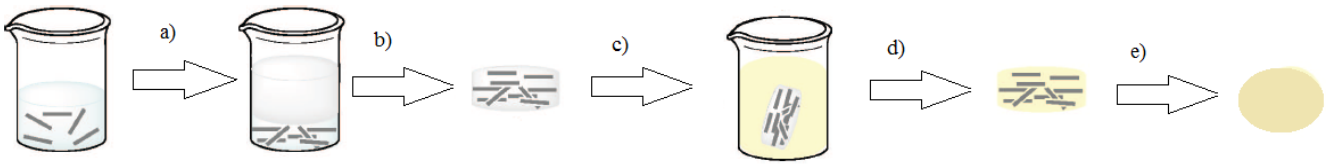

Figure IV.7 Schematic representation of the template approach to obtain polymer/ CNC composites: (a) a non solvent is added to a dispersion of NCCs in the absence of any polymer, (b) solvent exchange promotes the self-assembly of a gel of NCCs, (c) the gelled CNC scaffold is interpenetrated with a polymer by immersion in a polymer solution, before the nanocomposite is (d) dried and (e) compacted.[58]

As described previously, CNC are introduced into polymer matrix to improve their mechanical stiffness and strength. It shows a theoretical Young's modulus higher than that of steel and comparable with that of Kevlar. Different studies have demonstrated how the mechanical properties of nanocomposite containing CNC are better than those expected from theoretical calculations. Theoretically, the performance of reinforced materials is based on the efficiency with which mechanical stress is transferred from an external energy source to the reinforcing phase through the matrix.

The efficiency of the transfer is a function of the quality and the amount of the interfacial area between the reinforcing agent and matrix. The effectiveness of reinforcement can be described by the percolation theory, which can predict long-range connectivity in the matrix during the formation of the nanocomposite.[59] By variation of the number of connections, the material can pass from a state characterized by a disconnected set of components to an infinite connected state. This continuous network is probably generated through hydrogen-bond formation between CNC, whose structure depends on the distribution and orientation of the nanofibers.[60] The presence of such a network was later confirmed by electrical measurements performed on nanocomposites containing CNC that were coated with conductive polypyrrole.[61]

The increasing of the mechanical properties usually occurs at the limit of the percolation threshold, at which just enough CNC have been added to establish connectivity. This percolation threshold was estimated theoretically to be 1% (v/v) for CNC having an aspect ratio of 100.[62]

The percolation network and the efficiency of reinforcement are influenced by different parameters such as the aspect ratio, the technique used for the preparation of the nanocomposite system and the viscosity of the polymer matrix. CNC with high aspect ratio have a greater ability to sustain mechanical stress over the matrix, leading to a better reinforcing effect. However, they are harder to disperse and tend to form entanglements, which limit the mechanical features. Therefore, CNC with an opportune aspect ratio should be used.

Among different methods used for the synthesis of CNC-nanocomposites, sol-gel process and casting evaporation are those that brought more improvements in the mechanical properties. During such slow processing methods, CNC have adequate time to interconnect and form a percolation network. Instead, extrusion causes the gradual breakage of CNC, decreasing their aspect ratio and their efficiency.[63]

Moreover, nanocomposite mechanical properties are influenced by the viscosity of the polymer matrix. Highly viscous systems limit CNC movement and consequently hinder the interconnections among them.

Other important features, such as the nature of the polymer matrix and the surface energy of the CNC, will influence the formation of a network and have a great impact on the mechanical performance of the resulting composites. If CNC and the polymer matrix are not compatible, the nanofibers are extricated from the matrix, resulting in a disastrous decline in the mechanical properties. On the other hand, if CNC and polymer are perfectly compatible, the CNC/polymer interaction are stronger than those between CNC, leading to a surprising decreasing of CNC movement and thus to lower the elastic modulus. [64]

It has also been demonstrated that CNC have better reinforcement effect than MFC and BNC on polyacrylic films.[65]

Besides improving mechanical properties, CNC are able to increase the crystallinity of the polymer matrix: for example, the introduction of CNC in PCL has increased the crystallinity of the polymer matrix, whereas long CNC have no effect on the PCL matrix.[66]

As regarding the thermal properties of nanocomposites containing CNC, different studies have been done to determine the influence of the nanofibers on the T_g. Most of these researches reported that the introduction of CNC in the polymer matrix does not affect the T_g, regardless of the nature of the host polymer, the origin of CNC and the processing conditions.[67,68]

Moreover, it has been reported that the addition of unmodified CNC in semicrystalline polymers does not change the melting temperature (T_m) of the nanocomposite, as has been observed for PEO,[69] cellulose acetate butyrate[70] and PCL-reinforced polymers, etc.[71] However, when chemically modified CNC were used, a variation of T_m was observed.

BNC nanocomposite materials

BNC are cellulose nanofibers, having a diameter of about 20-100 nm, which are secreted extracellularly by specific bacteria, mainly by *Gluconacetobacter* strains.

Similarly to MFC and CNC, the bacterial nanocellulose has been used as nanofiller in nanocomposite materials. Such compounds can be synthesized by *in situ* modification of BNC, that is, by addiction of the composite partners to the culture medium, or by post-processing of BNC synthesized conventionally. Different nanocomposite materials have been prepared by using both organic compounds, such as bioactive agents and polymerizable monomers, polymers (i.e., polyacrylate, resins, polysaccharides and proteins), and inorganic substances, such as metal and metal oxides.

Below, some examples of organic and inorganic nanocomposite systems containing BNC are reported.

Polymer nanocomposites containing BNC have been prepared by introducing acrylate and methacrylate monomers and cross-linkers inside the ethanol-swollen BNC network by solvent exchange and subsequent photo-polymerization. The result was a collagen-like material with high water absorption capacity, strength and elasticity. The essential features of the BNC, i.e., shape, nanofiber network, pore system, and proved biocompatibility remains unchanged during this post-processing.[72]

Yano et al.[73,74] and Nogi et al.[75] have discovered that BNC has an extraordinary potential as reinforcing agent to obtain optically transparent and low thermal expansion materials. The produced BNC-composite resins (epoxy, phenolic and acrylic resin) have exhibited a total light transmittance up to 86% and, in the case of the acrylic resin, the thermal expansion coefficient was reduced to the half.

Figure IV.8 High transparency of a resin containing BNC demonstrated by the view on a flower through a corresponding foil.

In the work of Choi et al. BNC has been modified with cation exchangeable acrylic acid units by UV graft polymerization. First of all, BNC has been dried at 80 °C, immersed in methanol with benzophenone as a photoinitiator for 3h and air-dried for 30 min. To activate the BNC membrane, it has been irradiated with UV light for 3 min under a nitrogen atmosphere. After the addition of an acrylic acid solution, it has been treated with UV light for 5–20 min, purified and stored in NaCl solution. The resulting composite membranes have shown a rising density with increasing UV irradiation time because of the anchorage of

the grafted poly(acrylic acid). Moreover, the modified membranes have exhibited excellent tensile strength due to the high crystallinity of BC.

BNC-chitosan nanocomposites have been prepared by adding chitosan to the culture medium. This systems retains the properties of both components, and shows an extraordinary bactericidal and barrier effect against microorganisms.[76]

BNC nanocomposites with silica, titania and silver nanoparticles have been prepared by using both methods. Yano et al. have produced BNC-nanosilica composite by addiction of silica particle in the culture medium during the biosynthesis of BNC.[77] BNC-silver nanoparticles have been obtained by treating BNC fleeces with aqueous silver nitrate, followed by reduction with $NaBH_4$, leading to the precipitation of silver nanoparticles on BNC fibers. The resulting nanocomposite has shown strong microbial activity against Gram-negative and Gram-positive microorganisms.[78]

In the work of Yamanaka et al., the treatment of BNC fleeces with titanium tetraisopropoxide, followed by its hydrolysis, has resulted in titania-coated BNC fibers. After removal of BNC by heating at 500 °C, TiO_2 nanotubes have been obtained.[79] In this case BNC acted as support for titania and as a precursor.

BNC can be also introduced as nano-scale reinforcement by in situ attaching it to the surface of natural fibers like sisal and hemp. The strong inherence between BNC and the coated fibers surface is caused by the high self-affinity of cellulose through hydrogen bonding. For example, the coating of sisal fibers with BNC during fermentation (Figure IV.9b) leads to better adhesion properties without affecting the strength and biodegradability of the composite materials.

Some authors reported the use of such reinforcing fibers into matrices of PLA and cellulose acetate butyrate. They found that the BNC improved the interaction between the polymer and the fibers, leading to an increasing of the mechanical properties of about 50-60%.[80]

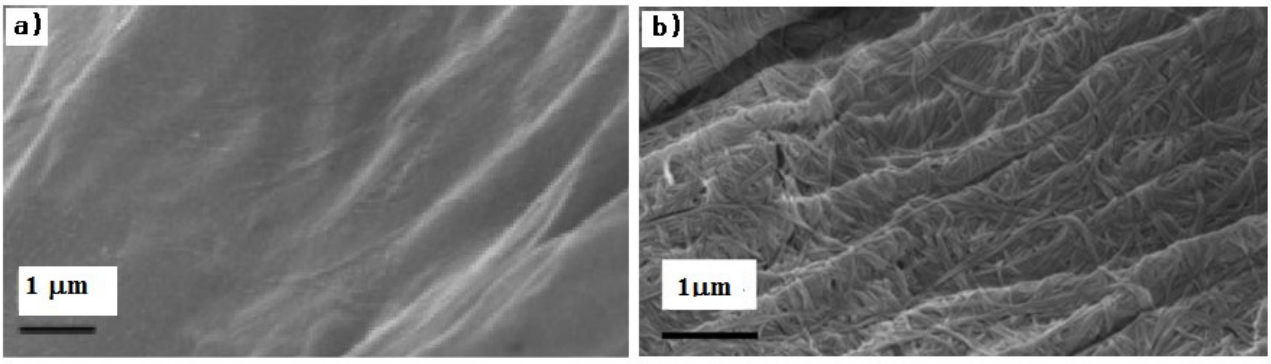

Figure IV.9 SEM images of sisal fiber surfaces: a – natural sisal fiber; b- BNC coating of sisal fiber during fermentation.[80]

IV. 2 NANOCOMPOSITES WITH 2D- NANOFILLERS

IV.2.1 GRAPHENE NANOCOMPOSITES

One of the most important applications of graphene is in the field of polymer nanocomposites, where graphene is introduced as filler with the aim to improve their chemical and physical properties. In fact, thanks to its extraordinary mechanical, electrical and thermal properties as well as its high aspect ratio and large surface area, graphene is a promising replacement of carbon nanotubes, fibers of carbon and Kevlar as filler in nanocomposite polymer systems.

Graphene/polymer composites have found application in high-strength and conductive materials, catalysts, and energy-related systems, especially flexible energy conversion and storage devices. Its reinforcement ability can offer exceptional properties in composites and applications in the field of electronics, aerospace, automotive and green energy.

The improvement in the physicochemical properties of graphene nanocomposite depends on the distribution of graphene layers in the polymer matrix as well as interfacial bonding between the graphene layers and the polymer matrix. The mechanism of interaction between graphene and the host polymer is affected by different factors, such as polarity, molecular weight, hydrophobicity, reactive groups present on the polymer or graphite/graphene surface and solvent, if present.[81]

Top-down methods, based on the exfoliation/separation of graphite, are the most used in the production of graphene-containing nanocomposites because they are suitable for large scale production. In particular, most nanocomposite systems have been produced by using graphene oxide, which has been introduced either directly or after reduction or chemical modification into the polymer matrix. GO has attracted considerable attention as nanofiller for polymer nanocomposites: it is characterized by hydroxyl, epoxide, ketones and carboxyl functional groups, that can alter the Van der Waals interactions, and be more compatible with organic polymers.[82,83] There are also some additional carbonyl and carboxyl groups located at the edge of the sheets, which make graphite oxide sheets strongly hydrophilic, allowing them to readily swell and exfoliate in water and in protic solvents.[84,85] Since GO is constituted by flat sheets, it tends to restack, especially after chemical reduction, reducing significantly its effectiveness. Restacking can be prevented by either use of surfactants that can stabilize the reduced particle suspensions or blending with polymers prior to the chemical reduction.[86]

In recent years, a variety of processes have been reported for dispersing graphene into polymer matrices. Many of these procedures are similar to those used for other nanocomposites systems, even if some of these techniques have been applied uniquely to graphene based nanocomposites. Among them, the most used are the solvent intercalation, *in situ* intercalative polymerization and melt mixing.

Solution intercalation is the most straightforward method for the preparation of polymer nanocomposites. It is based on a solvent system in which the polymer or the pre-polymer is solubilized and graphene or modified graphene layers are dispersed. The polymer is adsorbed onto the delaminated sheets of graphene and when the solvent is evaporated, the sheets reassemble, sandwiching the polymer to form the nanocomposites. Due to the residual oxygen-containing functional groups, GO is one of the most used precursor for preparing graphene polymer nanocomposite. In fact it readily exfoliates in water or in other protic solvents via hydrogen-bonding interaction, and can be mixed with water soluble polymers, such as PVA or PEO, leading to the corresponding nanocomposites.[87] The graphene oxide component in the composite can be converted to conductive r-GO upon chemical or thermal reduction. After removing the solvent, a solid r-GO/polymer composite can be obtained. However, graphene oxide does not dissolve in non-polar solvents and other forms of graphene such as expanded graphite and r-GO show limited solubility in both organic and inorganic solvents. In order to overcome this problem, sonication has been used to produce methastable dispersions of graphene derivatives, which are then mixed with polymer solutions, such as those of PMMA,[88] polyaniline (PANi),[89] PCL,[90] and PU.[91]

Unfortunately, this approach allows restacking, aggregation and folding of the graphene-based nanosheets during the process, reducing the specific surface area of the two-dimensional fillers. Therefore, surface functionalization of graphene-based fillers before solution intercalation must be carried out to provide them with good solubility in various kinds of solvents. For example, isocyanate-modified graphene oxide can be stably dispersed in DMF, and PS was added to its dispersion under stirring to form a mixture. After the reduction of the graphene oxide, a graphene-PS nanocomposite was obtained by adding methanol and after vacuum filtration.[86] The main advantage of this method is that it allows the synthesis of intercalated nanocomposites based on polymers with low or even no polarity. Various polymer composites such as graphene-PVA,[92] GO-PVA,[92] GO -PMMA,[93] GO-PCL,[94] PVDF-thermally reduced graphene (TRG),[95] PP-EG[96] and graphene oxide-PVC.[97]

In situ intercalative polymerization, graphene or chemically modified graphene is first dispersed in the neat monomer (or multiple monomers), or in a solution of monomer. A suitable initiator is then diffused and polymerization is initiated either by heat or radiation.[98,99] Like solution intercalation, functionalized graphene and GO sheets can improve the initial dispersion in the monomer liquid and subsequently in the composites. Many reports using *in situ* polymerization methods have produced composites with covalent linkages between matrix and filler. However, *in situ* polymerization has also been used to produce non-covalent composites of a variety of polymers, such as PE,[100] PMMA,[101] PS[102] and polypyrrole.[103] Extensive research has also been performed on producing epoxy-based nanocomposites using in situ polymerization where sheets are first dispersed into resin followed by curing and by adding hardener.[104]

Finally, in melt mixing, high temperatures and shear forces are used to disperse the reinforcement phase in the polymer matrix. The high temperature liquefies the polymer phase and allows easy dispersion or intercalation of GO and reduced graphene sheets. Hence, it does not require a common solvent for the graphene filler and the polymer matrix. Relative to solution intercalation, melt mixing is often considered a cheaper and more scalable method for dispersing nanoparticles in the polymer. However, because of thermal instability of most chemically modified graphene, its use has so far been limited to a few studies with TRG. Moreover, this technique is less effective in dispersing graphene sheets compared to solvent intercalation, due to the higher viscosity of the composite at increased sheets loading, and the high shear forces used can sometimes result in the breakage of the filler materials. The process can be applied to both polar and non-polar polymers. In particular, this technique is more practical for thermoplastic manufacturing composite in large scale. A wide range of polymer nanocomposites, such as PP-EG,[105] poly(ethyleneterephthalate)-rGO,[106] PC-graphene,[107] PS-EG,[108] PLA-EG[109] etc. have been prepared using this method.

During these years, different nanocomposite materials have been developed by introducing graphene or GO into a wide range of polymeric matrices such epoxy resins, PVA, PU, PS, PC, etc. Below, a brief summary of the main graphene nanocomposites and their corresponding properties is reported.

Epoxy/graphene nanocomposites

The introduction of graphene in epoxy resins leads to a strong increasing of both mechanical and thermal properties of the material. Rafiee et al. have compared mechanical properties of epoxy nanocomposite containing graphene platelets (GPLs), single-walled carbon nanotubes (SWCNTs) and multi-walled carbon nanotubes (MWCNTs) at a nanofiller weight fraction of 0.1 %.[110]

They have found that GPLs significantly out-perform carbon nanotube fillers. The tensile strength of the GPL/epoxy nanocomposite (78 MPa) is about 40% larger than the pristine epoxy (55 MPa), while those containing SWNTs and MWNTs show an increase of about 11 and 14% respectively, if compared to the initial epoxy matrix (Figure IV.10a). Moreover, the introduction of GPLs increases the Young's modulus of the epoxy resin by 31%, from 2.85 to 3.74 GPa. By contrast, the modulus enhancements for SWCNT and MWCNT composites at the same weight fraction are significantly lower (3%; Figure IV.10b).

Epoxy resins containing graphene nanoplatelets have been reported by Yu et al. They have found that the introduction of such filler at a concentration of 25 vol% provides a thermal conductivity enhancement of more than 3000%, and a thermal conductivity of about 6.44 W/mK, drastically higher than that of the pristine epoxy resins (0.21 W/mK). These outstanding thermal properties are probably due to a favorable

combination of the high aspect ratio, two-dimensional geometry, stiffness and low thermal interface resistance of the graphene nanoplatelets.[111]

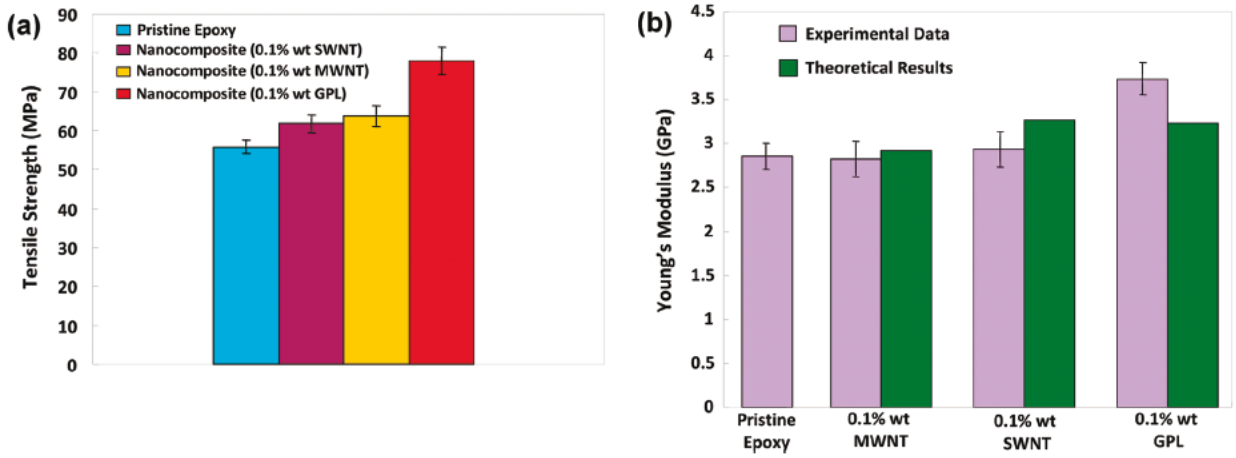

Figure IV.10 Tensile strength (a) and Young' modulus (b) for the pristine epoxy and GPLs/epoxy, MWCNTs/epoxy, and SWCNTs/epoxy nanocomposites. Theoretical predictions using the Halpin-Tsai theory for the nanocomposite samples are also shown in the figure.

PVA/graphene nanocomposites

Liang et al. prepared PVA/graphene nanocomposites by introducing GO into the polymer matrix and using water as solvent.[112] They observed that the mechanical properties are strongly influenced by the presence of graphene: with only 0.7 wt.-% of GO, the tensile strength increases by 76% from 49.9 to 87.6 MPa, and the Young's modulus enhances by 62% from 2.13 to 3.45 GPa (Figure IV.11).

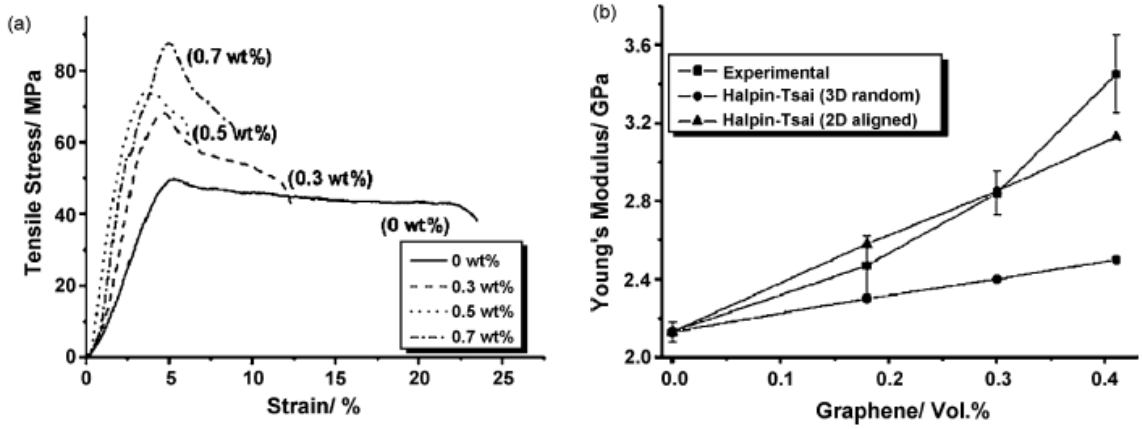

Figure IV.11 (a) Representative stress-strain behavior for PVA/graphene nanocomposites with different GO weight loadings. (b) Experimental Young's modulus of the nanocomposite films, calculated data derived from the Halpin–Tsai model under the hypothesis that GO sheets randomly dispersed as 3D network throughout the polymer matrix, and calculated data derived from the Halpin–Tsai model under the hypothesis that GO sheets aligned parallel to the surface of the composite film.

This significant increase in the mechanical properties arises from the high aspect ratio and the strong interaction between graphene and the PVA matrix. The glass transition temperature (T_g) of the

PVA/graphene nanocomposite with 0.7 wt.-% GO loading increased from 37.5 to 40.8 °C. This increase in T_g was attributed to H-bonding between graphene and PVA. Moreover, the introduction of graphene improved the crystallinity and thermal stability of the resulting nanocomposites.

In the work of Zhou et al. PVA/graphene nanocomposite films are prepared by using two simple steps: the synthesis of PVA/ GO nanocomposite film and immersion of such film in a reducing aqueous solution[113] (Figure IV.12a). They found that the introduction of graphene increased the mechanical properties and the conductivity of the PVA films. The tensile strength increased from 97 to 138 MPa with 0.7 wt.-% of r-GO. The conductivity increased sharply from 1.3 x 10^{-8} to 2.5 10^{-5} S/m when the r-GO content was increased from 0.3 to 0.7 wt.-%. This demonstrated a typical insulating-conductive percolation behavior, where the percolation threshold of r-GO is between 0.3 and 0.5 wt.-%. The highest conductivity achieved was 8.9 x 10^{-3} S/m for the composite containing 3 wt.-% r-GO (Figure IV.12b).

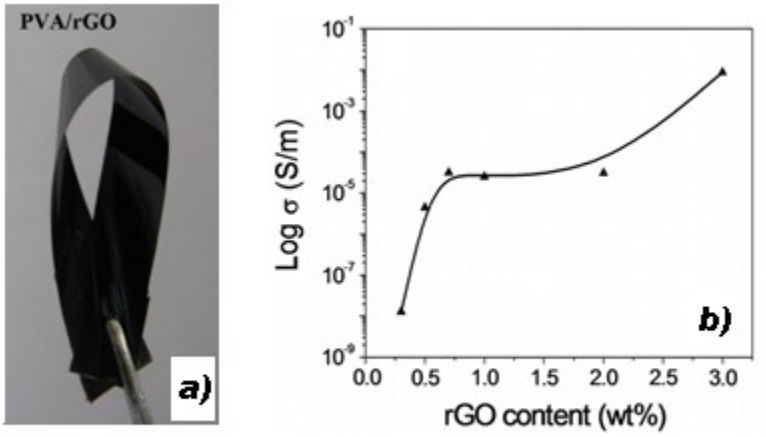

Figure IV.12 PVA/r-GO films and (b) their electrical conductivity as a function of r-GO content.

PU/graphene nanocomposites

Liang et al. prepared three types of nanocomposites by a solution mixing process.[114] They employed isocyanate modified graphene, sulfonated graphene and reduced graphene as nanofiller and thermoplastic polyurethane (TPU) as the matrix polymer. Thermogravimetric analysis (TGA) showed that the rate of thermal degradation for TPU/isocyanate modified graphene nanocomposites are much higher than that of the sulfonated graphene and r-GO based TPU nanocomposites. This suggests that there are fewer functional groups attached to sulfonated graphene sheets than to the isocyanate modified graphene. The TPU/sulfonated graphene nanocomposites showed significant improvement in mechanical properties. The tensile strength of TPU/sulfonated graphene (1 wt.-%) nanocomposites was increased by 75% at a strain of 100% and the Young's modulus was enhanced by 120%. This increase in mechanical properties is considered indirect evidence of the fine dispersion of graphene in the polymer.

Lee et al. prepared nanocomposites of waterborne polyurethane (WPU) with functionalized graphene sheets by using *in situ* polymerization.[115] They found that the electrical conductivity of the nanocomposites was increased 10^5 fold compared to pristine WPU due to the homogeneous dispersion of functionalized graphene sheets (FGS) particles in the WPU matrix. DSC analysis determined that the presence of FGS increased the melting temperature and heat of fusion of the soft segment of WPU in the nanocomposites. Finally, the crystallinity of the hard segments decreased with the graphene amount.

PS/graphene nanocomposites

PS/isocyanate modified graphene composite were prepared by using the solution intercalation method with DMF as solvent, followed by reduction of the composite with dimethyl hydrazine at 80 °C for 24h.[86] The composite appeared to be filled almost completely with graphene sheets at a filler loading of only 2.4 vol% due to the large surface area of modified graphene. The percolation threshold for the electrical conductivity was obtained at 0.1 vol.% GO in PS. This percolation is three times lower than that reported for any other two dimensional fillers due to the homogeneous dispersion and extremely large aspect ratio of graphene. The highest value of electrical conductivity (≈1Sm^{-1}) was obtained with a filler concentration of about 2.5 vol%.

By using a similar method, Li et al. prepared PS/GNP composite.[116] Compression molded thin films (≈ 2μm) of the composite sample were used to measure the electrical conductivity and thermal stability. The introduction of GNP resulted in a sharp increase in the electrical conductivity, from 10^{-4} Sm^{-1} for the neat polymer to 5.77 Sm^{-1} for the nanocomposite material containing 0.38 vol% GNP. Moreover, it was observed that the degradation temperature was 50 °C higher than that of neat PS, indicating a strong interaction between the polymer matrix and the nanofiller at the interface.

PC/graphene nanocomposites

Kim et al. prepared PC composite containing graphite and FGS by using melt mixing.[117] Melt rheology was used to examine the viscoelastic properties of the PC composites: PC-FGS exhibited a percolation threshold lower than that of PC containing graphite. The electrical conductivity measurements showed that percolation in the electrical conductivity could be achieved at a much lower FGS loading than with the graphite filler. The tensile modulus of the PC/FGS nanocomposites was also higher than that of the neat PC. Moreover, PC-FGS avoided N_2 and H_2 permeation, leading to an increasing of the barrier properties of PC.

REFERENCES

[1] Nanoscience and Nanotechnologies, 2004, The Royal Society & the Royal Academy of Engineering.
[2] RTO Lecture Series, EN-AVT-129, May 2005.
[3] Ajayan, P. M.; Schadler, L. S.; Braun, P. V. In Nanocomposite Science and Technology; Wiley-VCH Verlag GmbH &, Ed. 2003.
[4] Wagner, D.; Vaia, R. In Nanocomposites: issues at the interface. Materials Today, November, 2004. ISSN:1369 7021 © Elsevier Ltd.
[5] Winey, K. I.; Vaia, R. A. Mrs Bulletin, 2007, 32, 314-322.
[6] Chang, J. H.; An, Y. U. *J. Polym. Sci. B: Polym. Phys.* 2002, 40, 670–677.
[7] Zavyalov, S. A.; Pivkina, A.N.; Schoonman, J. *Solid State Ionics* 2002, 147, 415–419.
[8] John, M. J.; Thomas, S. *Carbohyd Polym* 2008, 71, 343-364.
[9] Zhang, X.; Huang, J.; Chang, P. R.; Li, J.; Chen, Y.; Wang, D.; Yu, J.; Chen, J. *Polymer* 2010, 51, 4398-4407.
[10]Lin, N.; Huang, J.; Chang, P. R.; Feng, L.; Yu, J. *Colloids and Surfaces B: Biointerfaces* 2011, 85, 270-279.
[11] Nakagaito, A. N.; Yano, H. *Appl Phys A-Mater Sci Process* 2005, 80, 155–159.
[12] Nakagaito, A. N.; Yano, H. Cellulose, 2008, 15, 323–331.
[13] Bruce, D. M.; Hobson, J. W.; Farrent, J. W.; Hepworth, D. G. *Composites Part A* 2005, 36, 1486 – 1493.
[14] Iwamoto, S.; Nakagaito, A. N.; Yano, H.; Nogi, M. *Appl Phys A-Mater Sci Process* 2005, 81, 1109–1112.
[15] Iwamoto, S.; Nakagaito, A. N.; Yano, H. *Appl Phys A-Mater Sci Process* 2007, 89, 461–466.
[16] Aksoy, E. A.; Akata, B.; Bac, N.; Hasirci, N. *J Appl Polym Sci* 2007, 104, 3378–3387.
[17] Seydibeyoglu, M. O.; Oksman, K. *Compos Sci Technol* 2008, 68, 908–914.
[18] Wang, B.; Sain, M. *Polym Int* 2007, 56, 538–546.
[19] Wang, B.; Sain, M. *Compos Sci Technol* 2007,67, 2521–2527.
[20] Zimmermann, T.; Pohler, E.; Geiger, T. *Adv Eng Mater* 2004, 6, 754–761.
[21] Leitner, J.; Hinterstoisser, B.; Wastyn, M.; Keckes, J.; Gindl, W. *Cellulose* 2007, 14, 419–425.
[22] Malainine, M. E.; Mahrouz, M.; Dufresne, A. *Compos Sci Technol* 2005, 65, 1520–1526.
[23] Cheng, Q.; Wang, S. Q.; Rials, T. G.; Lee, S. H. Cellulose 2007, 14, 593–602.
[24] Okubo, K.; Fujii, T.; Thostenson, E. T. *Compos Part A-Appl Sci Manufact* 2009, 40, 469–475.
[25] Iwatake, A.; Nogi, M; Yano, H. *Compos Sci Technol* 2008, 68, 2103– 2106.
[26] Nakagaito, A. N.; Fujimura, A.; Sakai, T.; Hama, Y.; Yano, H. *Compos. Sci. Technol.* 2009, 69, 1293 – 1297.
[27] Loönnberg, H.; Fogelström, L.; Malström, E.; Zhou, Q.; Berglund, L.; Hult, A. Nordic Polymer Days 2008, 11–13 June, Stockholm.
[28] Favier, V.; Chanzy, H.; Cavaille, J. Y. *Macromolecules* 1995,28, 6365 – 6367.
[29] Noorani, S.; Simonsen, J.; Atre, S. In Cellulose Nanocomposites: Processing, Characterization and Properties; Oksman, K., Sain, M., Eds.; ACS Symposium Series 938; American Chemical Society: Washington, D.C., 2006.
[30] Morin, A.; Dufresne, A. *Macromolecules* 2002, 35, 2190-2199.
[31] Paillet, M.; Dufresne, A. *Macromolecules* 2001, 34, 6527-6530.
[32] Grunnert, M.; Winter, W. T. *Polym. Mater. Sci. Eng.* 2000, 82, 232-238.
[33] Azizi Samir, M. A. S.; Alloin, F.; Sanchez, J.-Y.; Dufresne, A. *Polymer* 2004, 45, 4149-4157.
[34] Choi, Y.; Simonsen, J. J. *Nanosci. Nanotechnol.* 2006, 6, 633-639.
[35] Paralikar, S. A.; Simonsen, J.; Lombardi, J. J. *Membr. Sci*. 2008, 320, 248-258.
[36] Petersson, L.; Mathew, A. P.; Oksman, K. *J. Appl. Polym. Sci.* 2009, 112, 2001-2009.
[37] Roohani, M.; Habibi, Y.; Belgacem, N. M.; Ebrahim, G.; Karimi, A. N.; Dufresne, A. *Eur. Polym. J.* 2008, 44, 2489-2498.
[38] Chauve, G.; Heux, L.; Arouini, R.; Mazeau, K. *Biomacromolecules* 2005, 6, 2025-2031.
[39] Ruiz, M. M.; Cavaille, J. Y.; Dufresne, A.; Gerard, J. F.; Graillat, C. *Compos. Interfaces* 2000, 7, 117-131.
[40] Junior de Menezes, A.; Siqueira, G.; Curvelo, A. A. S.; Dufresne, A. *Polymer* 2009, 50, 4552-4563.
[41] Bonini, C. Ph.D. Thesis, Joseph Fourier University, Grenoble, France, 2000.
[42] Chazeau, L.; Paillet, M.; Cavaille, J. Y. *J. Polym. Sci., Part B: Polym. Phys.* 1999, 37, 2151-2164.
[43] Marcovich, N. E.; Auad, M. L.; Bellesi, N. E.; Nutt, S. R.; Aranguren, M. I. *J. Mater. Res.* 2006, 21, 870-881.

[44] Cao, X.; Habibi, Y.; Lucia, L. A. *J. Mater. Chem.* 2009, 19, 7137-7145.
[45] Wang, Y.; Cao, X.; Zhang, L. *Macromol. Biosci.* 2006, 6, 524-531.
[46] Li, Q.; Zhou, J.; Zhang, L. *J. Polym. Sci., Part B: Polym. Phys.* 2009, 47, 1069-1077.
[47] Bondeson, D.; Oksman, K. *Composites Part A* 2007, 38A, 2486-2492.
[48] Dubief, D.; Samain, E.; Dufresne, A. *Macromolecules* 1999, 32, 5765-5771.
[49] Jiang, L.; Morelius, E.; Zhang, J.; Wolcott, M.; Holbery, J. *J. Compos. Mater*. 2008, 42, 2629-2645.
[50] Viet, D.; Beck-Candanedo, S.; Gray, D. G. *Cellulose* 2007, 14, 109-113.
[51] Elazzouzi-Hafraoui, S.; Nishiyama, Y.; Putaux, J. L.; Heux, L.; Dubreuil, F.; Rochas, C. *Biomacromolecules* 2008*,* 9, 57–65.
[52] Schroers, M.; Kokil, A.; Weder, C. *J. Appl. Polym. Sci.* 2004, 93, 2883-2888.
[53] Schroers, M.; Kokil, A.; Weder, C. *J. Appl. Polym. Sci.* 2004, 93, 2883–2888.
[54] Cao, X.; Dong, H.; Li, C. M. *Biomacromolecules* 2007, 8, 899-904.
[55] Rojas, O. J.; Montero, G. A.; Habibi, Y. *J. Appl. Polym. Sci.* 2009, 113, 927–935.
[56] Peresin, M. S.; Habibi, Y.; Zoppe, J. O.; Pawlak, J. J.; Rojas, O. J. Biomacromolecules 2010, 11, 674–681.
[57] Zoppe, J. O.; Peresin, M. S.; Habibi, Y.; Venditti, R. A.; Rojas, O. J. *ACS Appl. Mater. Interfaces* 2009, 1,1996–2004.
[58] Capadona, J. R.; Shanmuganathan, K.; Tyler, D. J.; Rowan, S. J.; Weder, C. *Science* 2008, 319, 1370-1374.
[59] Stauffer, D.; Aharony, A. In Introduction to Percolation Theory; Taylor & Francis: London, 1992.
[60] Balberg, I.; Binenhaum, N. *Phys. Rev. B* 1983, 28, 3799 – 3812.
[61] Flandin, L.; Cavaille´, J. Y.; Bidan, G.; Brechet, Y. *Polym. Compos.* 2000, 21, 165-174.
[62] Favier, V.; Dendievel, R.; Canova, G.; Cavaille, J. Y.; Gilormini, P. *Acta Mater.* 1997, 45, 1557 – 1565.
[63] Hajji, P.; Cavaille, J. P.; Favier, V.; Gauthier, C.; Vigier, G. *Polym. Compos.* 1996, 17, 612–619.
[64] Dufresne, A. J. *Nanosci. Nanotechnol.* 2006, 6, 322-330.
[65] Pu, Y.; Zhang, J.; Elder, T.; Deng, Y.; Gatenholm, P.; Ragauskas, A. J. *Composites Part B* 2007, 38, 360–366.
[66] Siqueira, G.; Bras, J.; Dufresne, A. *Biomacromolecules* 2009, 10, 425–432.
[67] Azizi Samir, M. A. S.; Alloin, F.; Dufresne, A. *Biomacromolecules* 2005, 6, 612-626.
[68] Dufresne, A. *Can. J. Chem.* 2008, 86, 484-494.
[69] Azizi Samir, M. A. S.; Alloin, F.; Sanchez, J.-Y.; Dufresne, A. *Polim.: Cienc. Tecnol.* 2005, 15, 109-113.
[70] Angles, M. N.; Dufresne, A. Macromolecules 2000, 33, 8344-8353.
[71] Habibi, Y.; Goffin, A.-L.; Schiltz, N.; Duquesne, E.; Dubois, P.; Dufresne, A. *J. Mater. Chem.* 2008, 18, 5002-5010.
[72] Kramer, F.; Klemm, D.; Schumann, D.; Hessler, N.; Wesarg, F.; Fried, W.; Stadermann, D. *Macromol. Symp.* 2006, 244, 136-148.
[73] Yano, H.; Nogi, M.; Ifuku, S.; Abe, K.; Takezawa, Y.; Handa, K. WO Patent 2007049666 (2007).
[74] Yano, H.; Nogi, M.; Nakagaito, A. N. WO Patent 2006087931 (2006).
[75] Nogi, M.; Ifuku, S.; Abe, K.; Handa, K.; Nakagaito, A.; Yano, H. *Appl. Phys. Lett.* 2006, 88, 133124-133131.
[76] Ciechanska, D. Fibres Textil Eastern Eur 2004, 12, 69-72.
[77] Yano, S.; Maeda, H.; Nakajima, M.; Hagiwara, T.; Sawaguchi, T. *Cellulose* 2008, 15, 111–120.
[78] Maneerung, T.; Tokura, S.; Rujiravanit, R. *Carbohydr. Polym.* 2008, 72, 43–51.
[79] Yamanaka, S.; Ishihara, M.; Sugiyama, J. *Cellulose* 2000, 7, 213–225.
[80] Pommet, M.; Juntaro, J.; Heng, J. Y. Y.; Mantalaris, A.; Lee, A. F.; Wilson, K.; Kalinka, G.; Shaffer, M. S. P.; Bismarck, A. *Biomacromolecules* 2008, 9, 1643-1651.
[81] Zhang, H. B.; Zheng, W. G.; Yan, Q.; Yang, Y.; Wang, J.W.; Lu, Z. H.; Ji, G. Y.; Yu, Z. Z. *Polymer* 2010, 51, 1191-1196.
[82] Becerril, H.; Mao, J.; Liu, Z.; Stoltenberg, M.; Bao, Z.; Chen, Y. *ACS Nano* 2008, 2, 463–70.
[83] Dikin, A. K.; Stankovich, S.; Zimney, E. J.; Piner, R. D.; Dommett, G. H. B. ; Evmenenko, G. et al. *Nature* 2007, 448, 457–60.
[84] Nethravathi, C.; Rajamathi, J. T.; Ravishankar, N.; Shivakumara, C.; Rajamathi, M. *Langmuir* 2008, 24, 8240–8244.
[85] Szabo, T.; Szeri, A.; Dekany, I. Carbon 2005, 43, 87–94.
[86] Stankovich, S.; Dikin, D.; Dommett, G. H. B.; Kohlhaas, K. M.; Zimney, E. J.; Stach, E. A.; Piner, R. D.; Nguyen, S. T.; Ruoff, R. S. *Nature* 2006, 442, 282-286.
[87] Xu, Y. X.; Hong, W. J.; Bai, H.; Li, C.; Shi, G. Q. *Carbon*, 2009, 47, 3538–3543.

[88] Ramanathan, T.; Stankovich, S.; Dikin, D. A.; Liu, H.; Shen, H.; Nguyen, S. T.; Brinson, L. C. *J. Polym. Sci., Part B: Polym. Phys.* 2007, 45, 2097–2112.
[89] Wu, Q.; Xu, Y. X.; Yao, Z. Y.; Liu, A. R.; Shi, G. Q. *ACS Nano* 2010, 4, 1963–1970.
[90] Cai, D. Y.; Song, M. *Nanotechnology* 2009, 20, 315708-315714.
[91] Cai, D. Y.; Yusoh, K.; Song, M. *Nanotechnology* 2009, 20, 085712-085719.
[92] Liang, J.; Huang, Y.; Zhang, L.; Wang, Y.; Ma, Y.; Guo, T. et al. *Adv Funct Mater* 2009, 19, 2297–2302.
[93] Jang, J. Y.; Kim, M. S.; Jeong, H. M.; Shin, C. M. *Compos. Sci. Technol.* 2009, 69, 186–191.
[94] Kai, W.; Hirota, Y.; Hua, L.; Inoue, Y. *J. Appl. Polym. Sci.* 2008, 107, 1395–1400.
[95] Ansari, S.; Giannelis, E. P. *J Polym Sci Part B - Polym Phys* 2009, 47, 888-897.
[96] Kalaitzidou, K.; Fukushima, H.; Drzal, L. T. *Compos Sci Technol* 2007,67, 2045–2051.
[97] Broza, G.; Piszczek, K.; Schulte, K.; Sterzynski, T. *Composites Science and Technology* 2007, 67, 890-894.
[98] Zheng, W.; Lu, X.; Wong, S. C. *J Appl Polym Sci* 2004, 91, 2781–2788.
[99] Lianga, J.; Wanga, Y.; Huanga, Y.; Maa, Y.; Liua, Z.; Caib, J. et al. *Carbon* 2009, 47, 922–5.
[100] Fim, F. C.; Guterres, J. M.; Basso, N. R. S.; Galland, G. B. *J Polym Sci Part A Polym Chem* 2010, 48, 692-698.
[101] Jang, J. Y., Kim, M. S.; Jeong, H. M.; Shin, C. M. *Compos Sci Technol* 2009,69, 186-191.
[102] Hu, H.; Wang, X.; Wang, J.; Wan, L.; Liu, F.; Zheng, H.; Chen, R.; Xu, C. *Chemical Physics Letters* 2010, 484, 247-253.
[103] Gu, Z.; Zhang, L.; Li, C. *J Macromol Sci Part B Phys* 2009, 48, 1093-1102.
[104] Rafiee, M. A.; Rafiee, J.; Srivastava, I.; Wang, Z.; Song, H.; Yu, Z. Z, et al. *Small* 2010,6,179-183.
[105]Kalaitzidou, K.; Fukushima, H.; Drzal, L. T. *Carbon* 2007, 45, 1446–1452.
[106] Zhang, H. B.; Zheng, W. G.; Yan, Q.; Yang, Y.; Wang, J. W.; Lu, Z. H.; Ji, G. Y.; Yu, Z. Z. *Polymer* 2010, 51, 1191–1196.
[107] Kim, H.; Macosko, C. W. *Polymer* 2009, 50,3797-3809.
[108] Chen, G.; Wu, C.; Weng, W.; Wu, D.; Yan, W. *Polymer* 2003; 44:1781–1784.
[109] Kim, I. H.; Jeong, Y. G. *J. Polym. Sci., Part B: Polym. Phys.* 2010, 48, 850–858.
[110] Rafiee, M. A.; Rafiee, J.; Wang, Z.; Song, H.; Yu, Z. Z.; Koratkar, N. *ACS nano* 2009, 3,3884-3890.
[111] Yu, A. P.; Ramesh, P.; Itkis, M. E.; Bekyarova, E.; Haddon, R. C. *J Phys Chem C* 2007,111,7565-7569.
[112] Liang, J.; Huang, Y.; Zhang, L.; Wang, Y.; Ma, Y.; Guo, T. et al. *Adv Funct Mater* 2009, 19, 2297–302.
[113] Zhou, T.; Chen, F.; Tang, C.; Bai, H.; Zhang, Q.; Deng, H.; Fu, Q. *Composites Science and Technology* 2011,71, 1266–1270.
[114] Liang, J.; Xu, Y.; Huang, Y.; Zhang, L.; Wang, Y.; Ma, Y. et al. *J Phys Chem* 2009, 113,9921–9927.
[115] Lee, Y. R.; Raghu, A. V.; Jeong, H. M.; Kim, B. K. *Macromol Chem Phys* 2009, 210, 1247–1254.
[116] Liu, N.; Luo, F.; Wu, H.; Liu, Y.; Zhang, C.; Chen, J. *Adv Funct Mater* 2008, 18, 1518–1525.
[117] Kim, H.; Macosko, C. W. *Polymer* 2009, 50, 3797–3809.

CHAPTER V

THE FRONTAL POLYMERIZATION

During the lasts decades, significant advances in the chemistry of polymer synthesis have been done, not only through the preparation of well-characterized materials, but also developing new general methods able to accelerate and simplify polymerization routes without compromising the required properties. However, to obtain advanced materials with specific features, a complete knowledge of the polymerization kinetics and of the influence of reaction conditions (i.e., temperature, monomer, initiator, etc.) is required. With the aim to achieve this purpose, numerous studies have been focused on the developing of synthetic methods able to control morphology, microstructure, molecular weight etc. Among them, FP is an advantageous and already widely studied technique for synthesizing uniform polymers and polymer networks in a rapid way. FP is an approach to macromolecular synthesis which exploits the exothermicity of the reaction itself for the rapid conversion of monomer into polymer. The heat released during the reaction generates a polymerization front able to self sustain and propagate along the reactor. Indeed, if the heat dissipated is not excessive, a sufficient amount of energy able to induce the polymerization of the monomer close to the hot zone is provided.

There are three types of FP:

- Thermal Frontal Polymerization, in which front propagates due to the heat released by the polymerization reaction itself;[1-4]
- Photofrontal Polymerization, in which the front is driven by the continuous flux of radiation, usually UV light;[5-9]
- Isothermal Frontal Polymerization, which is based on the gel effect (also known as Trommsdorff-Norrish effect)[10,11] that occurs when monomer and initiator diffuse into a pre-formed polymer.[12]

FP is the result of the application of *Self-propagating High temperature Synthesis* (SHS) to polymer synthesis. Examples of SHS reactions are the synthesis of intermetallic compounds (i.e., nickel and aluminum)[13] and the synthesis of boride (niobium and boron).[14] In these reactions, the reactants are placed in a cylinder as powders, and one end is heated to an ignition temperature, initiating a travelling front. This approach to ceramic synthesis has the advantage over uniformly heating a reaction mixture, due to the low amount of energy and time required. Moreover, such fronts demonstrate a rich variety of dynamical behavior, including planar fronts, spin modes[15-17] and chaotic reaction waves.[18]

Most of the nanocomposite materials prepared during this research have been obtained by using thermal frontal polymerization as synthetic method. FP is generally carried out in a glass test tube, filled with the appropriate monomeric mixture in which an initiator or catalyst have been previously dissolved. The vessel

is shaken in order to obtain a homogeneous mixture, and a thermocouple junction, located at about 1 cm from the bottom of the tube and connected to a digital thermometer, is used to monitor the temperature change. The reaction starts by heating the external wall of the tube through a soldering iron, in correspondence of the upper surface of the monomeric mixture, until the formation of the front becomes evident. Moreover, the position of the front, easily visible through the glass wall of test tubes, against time was measured (Figure V.1).

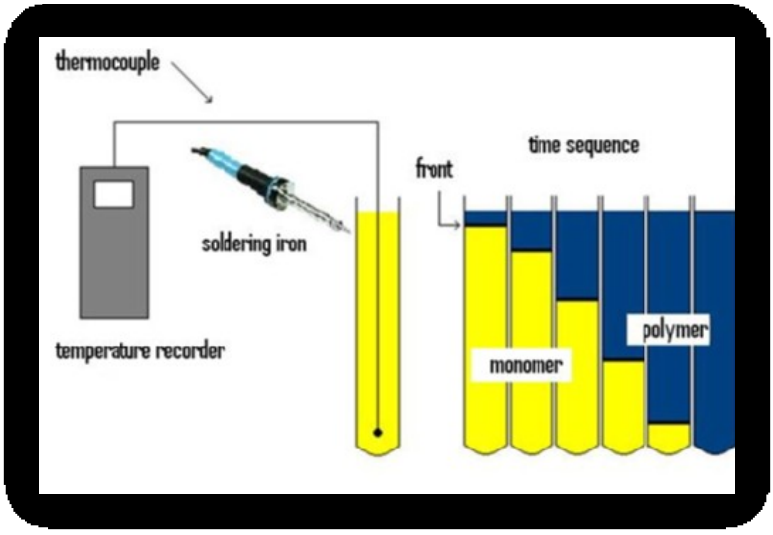

Figure V.1 Apparatus of a typical FP experiment

If compared with the traditional polymerization methods, FP generally exhibits many advantages that make it an advantageous technique of macromolecular synthesis:

- shorter reaction times: a typical FP run takes only a few minutes, whereas classical polymerization often need hours or days;
- low energy consumption: FP is an environmentally friendly technique inasmuch as it does not need external energy supplying except that necessary to locally ignite it (ignition times takes only a few seconds);
- easy and simple protocols even without special apparatuses and generally without involving the use of solvents;
- thermal and mechanical properties are comparable or better than those of materials traditionally obtained;
- monomer can be used as received, i.e. without the usual elimination of the dissolved inhibitor, due to the high temperature reached by the front;
- conversions are often almost quantitative, thus making the final common purification procedures not necessary.

V. 1 STATE OF ART

The first study on FP was carried out in 1975 by Chechilo and Enikolopyan, who synthesized poly(methylmethacrylate) by a homogeneous bulk process in adiabatic conditions and under high pressure (>3000 atm).[19,20] In this case, FP was performed under high pressure to eliminate double-diffusive instabilities and monomer boiling. They also found that front velocity increased with the enhancement of both initiator concentration and pressure.

After this preliminary work, different studies have been focused on the discovery of other monomers suitable for FP: they had to be characterized by boiling temperatures higher than that of the front and had to be able to ensure front stability. Pojman et al. found that methacrylic acid fulfills the above requirements, leading to the obtainment of stable fronts and thus uniform products.[21] Lately, they exploited FP for polymerizing, at ambient pressure, different vinyl monomers,[22-25] epoxy resins[26] and their IPNs.[27]

Morbidelli et al. reported on the advantageous application of FP to the obtainment of poly(methylmethacrylate)/polystyrene blends.[28] Namely, it was found that such systems were characterized by reduced phase separation if compared with those obtained either by mechanical mixing and the classical synthetic route. In this work, phase separation was limited by the high conversion rate which “freezes” the various components of the mixture in a methastable situation.

FP was also employed for the production of copolymers: high front temperatures make both reactivity monomer ratios equal to the unity. Accordingly, all copolymer chains were characterized by the same composition independently of monomer conversion.[29]

Washington and Steinbock were the first to apply FP for the obtainment of temperature-sensitive hydrogels,[30] while Fortenberry et al. used FP for the synthesis of polyacrylamide without any solvent.[31]

Chen et al. frontally polymerized 2-hydroxyethyl acrylate[32] and methyloacrylamide;[33] furthermore, they exploited this technique for obtaining epoxy resin/PU networks,[34] PVP[35] and PU-nanosilica hybrid nanocomposites.[36]

Our research group has widely studied FP polymerization as an alternative macromolecular synthetic technique.

For the first time FP was used to carry out the ring opening metathesis polymerization of dicyclopentadiene (DCPD)[37] and, subsequently to prepare its IPNs with acrylates.[38] In particular, in this latter work it was found that the heat released by DCPD polymerization affords to sustain the front of a second monomer (methylmethacrylate), which is not able to frontally polymerize alone. PUs,[39,40] poly(diurethane diacrylates),[41] unsaturated polyester/styrene resins,[42] epoxy-amine systems,[43-46] hybrid organic-inorganic epoxy resins[47] and phosphonium-based ionic liquids as radical initiators[48] for FP have been prepared by

using such technique. FP can also be applied to the synthesis of polymer hydrogels and drug delivery systems: stimuli responsive hydrogels of poly(N,N-dimethylacrylamide),[49] poly(acrylamide-co-3- sulfopropyl acrylate),[50] poly (NIPAAm-co-3-sulfopropyl acrylate)[51] and P(NIPAAm-co-NVCL)[52] were successfully obtained. FP was also exploited for stone consolidation,[53,54] and for preparing polymer based nanocomposites with montmorillonite[44] or polyhedral oligomeric silsequioxanes.[55] Recently, we have also proposed FP for the obtainment of nanocomposite hydrogels based on PNIPAAm and containing graphene[56] or partially exfoliated graphite.[57]

V.2 FUNDAMENTAL PARAMETERS AND PROPERTIES OF FP

The maximum temperature reached by the polymerization front and the velocity at which the thermal wave moves along the reactor are two fundamental parameters in the study of FP. As described previously, temperature profiles are obtained by using a thermocouple located within the monomer mixture and connected to a digital thermometer, whereas front velocity is monitored through the use of a simple chronometer.

Front temperature and velocities are extremely important because afford to determine if the frontal polymerization is *pure* or accompanied by other concomitant reactions. *Pure* FP indicates the process in which the conversion of monomer into polymer is only due to the FP reaction, at a given time. For pure FP to occur, the investigated chemical system must be almost inert at relatively low temperature but very reactive at the temperature reached by the front (generally much higher than 100 °C). That means that sufficiently long pot-lives are necessary. However, the polymerizing system does not always have this requisite and, sometimes, a proper additive has to be added. Indeed, if a temperature increase happens in regions distant from the hot travelling zone, spontaneous polymerization (SP) is probably taking place. For the above reasons, temperature of the monomer far from the incoming front is a more significant parameter to be checked. In a pure FP, temperatures recorded in regions far from the hot travelling zone, are almost constant, suggesting the absence of concomitant SP. When the polymerization front is near the thermal junction, it can be suddenly observed a temperature enhancement. The higher the front velocity, the higher the increment of the temperature. Temperature continues to rise until it reaches its maximum value (T_{max}), which is strongly influenced by both the monomeric mixture and the type of initiators and additives used. Moreover, it is also related to the degree of conversion and crosslinking, the onset of polymer degradation and bubble formation. Once reached T_{max}, a thermal decrease due to heat dissipation is observed. (Figure V.2)

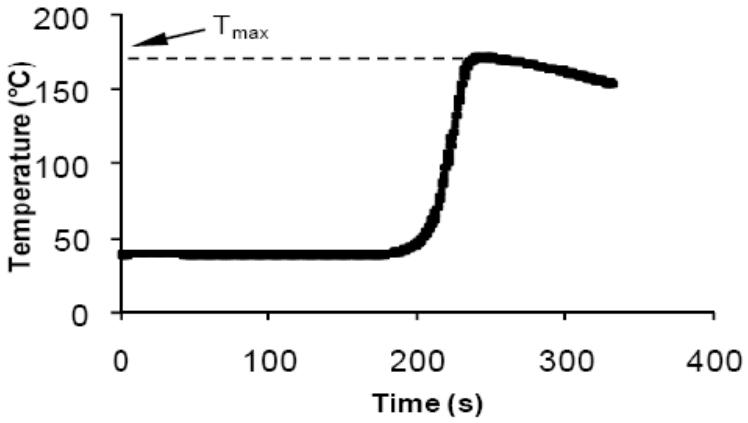

Figure V.2 Temperature profile recorded during a typical pure FP experiment.

The temperature profile for an ideal system is reported in Figure V.3a: temperature remains constant at room temperature until front crosses the thermocouple junction, and after temperature remains constant at T_{max}. This system is adiabatic and heat diffusion is not present. In this system only FP is occurring. For real systems, the temperature profiles are similar to that showed in Figure V.2. If other reactions are present, for example SP, the temperature profile has different characteristics, like those shown in Figure V.3b and V.3c: the temperature increase happens in regions distant from the hot travelling zone and SP is probably taking place.

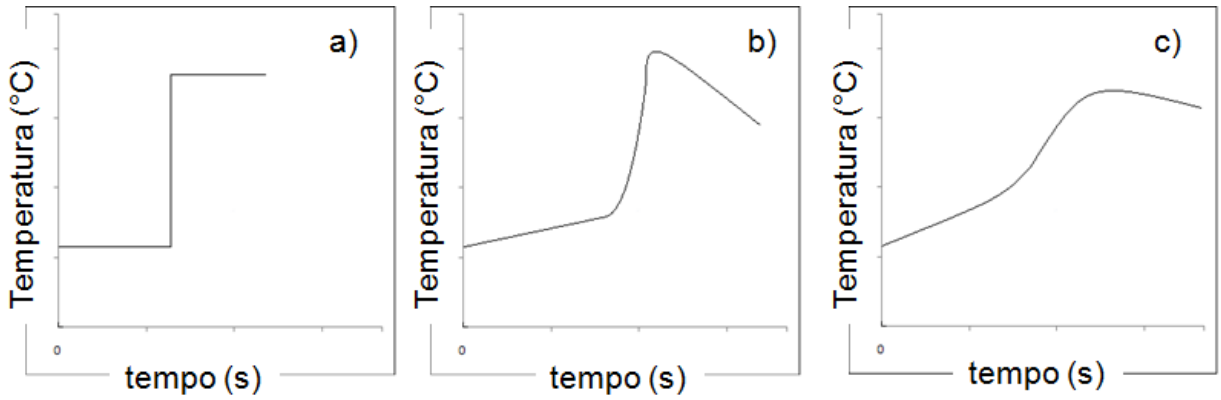

Figure V.3 Temperature profile : a)adiabatic system without SP ; b) non adiabatic real system and c) real system with SP.

In a pure FP, the hot travelling front moves along the reactor with a constant velocity, V_f, even if such behavior is not always found. (Figure V.4a) The presence of bubbles, generated during the process, sometimes impart a non-uniform and non-constant movement to the front. (Figure V.4b) However, a linear dependence between front position and time can be found also if SP is simultaneously occurring. For instance, that happens if FP is relatively fast if compared with SP in the time scale needed to complete the

polymerization in a reactor of a certain geometry (the longer a reactor is, the more crucial this point becomes). The front position as a function of time deviates if other phenomena are occurring.

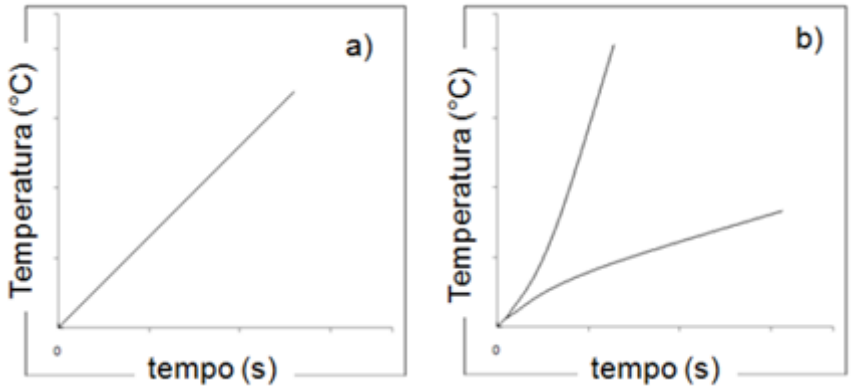

Figure V.4 Front position as a function of time: a) ideal FP, b) deviation from ideality.

As previously described, another important parameter for the study and the development of a pure FP is the choice of the monomer system.

There are three classes of monomers used in FP, which differ basically by their physical properties:

- monomers that form thermoset polymers;
- monomers that form thermoplastic polymers;
- monomers that form phase-separated polymers.

This classification was introduced by the Pojman's group at the University of Southern Mississippi, one of the most active in this field.

The first group includes crosslinking monomers such as tri(ethylene glycol)dimethacrylate (TGDMA), di(ethyleneglycol) dimethacrylate, divinylbenzene, etc. In such monomer systems, the polymerization develops in three dimensions to yield strongly crosslinked polymer networks. A sharp frontal interface propagated along the reactor media as polymerization and crosslinking occurring simultaneously. The products of these reactions are rigid thermosets, capable of withstanding high temperature. Some of these monomers are very viscous (i.e., TGDMA) and allow ascending and horizontally propagating fronts because the natural convection is reduced.

The second group of monomers includes all highly reactive monomers that produce thermoplastic polymers, which are molten at the front temperature. Among them, acrylates are by far the most studied systems because of their reactivity and the availability of kinetic data for numerical studies. Other acrylates that have been frontally produced include benzyl acrylate, hexyl acrylate and butyl methacrylate. During the front propagation of some monoacrylates the so-called *"fingering"* can be observed: it is a phenomenon that happens when, during the polymer formation, its simultaneous solubilization into the

monomer mixture occurs, leading to non homogeneous and instable front. This phenomenon is also observed when the front temperature is higher than polymer melting temperature. To reduce or prevent the formation of *fingering*, an inert filler such as an ultra-fine silica gel (Cabosil) may be added: this increases the medium viscosity, stabilizing the front, even if the homogeneity is greatly compromised.[59] Pojman et al. overcame such problem carrying out FP under microgravity conditions.[58]

The third group includes monomers having limited miscibility with their polymers. Good examples are acrylic and methacrylic acid.[3,24,59] The homogeneous systems become heterogeneous due to the insolubility of the growing polymer in the reaction media. Insoluble polymer particles coagulate and adhere to each other during their formation and stick to the reactor or test tube walls. This provides a mechanical durable phase and a discernible polymer-monomer interface, whereby the heat of reaction can easily diffuse into the unreacted zone to proliferate further polymer growth. Nevertheless, front instabilities partially develop in such systems, manifesting themselves as *fingering*.[21,22] To suppress this phenomenon, the technique of rotating the reactor around the axis of propagation was devised. The instabilities yielded to the centrifugal forces such that stable front were established.[60]

In recent years, different studies have been conducted for the development of a reliable and effective method for FP. However, the determination of the general conditions for the obtainment of a stable front have not been found, because each monomer requires an opportune combination of initiator, solvent, concentration, initial temperature, etc. Accordingly, to obtain polymers with the desired features a wide study about each component is needed. In particular, some salient aspects of FP should be emphasized:

the monomer and the solvent, if present, should have a boiling temperature higher than front temperature, in order to prevent boiling. In fact bubbles can interfere with front velocity, leading to heterogeneous products. Sometimes, bubbles formation can be related to the decomposition of organic initiators. For example, the byproducts of the homolytic cleavage of peroxide and nitriles are carbon dioxide and nitrogen gases, respectively. On the contrary, persulfate initiators generate free radicals upon heating, thus resembling the organic peroxides. However, persulfate does not decompose into any gaseous products. Therefore such initiators have been used in conjunction with dimethylsulfoxide (DMSO) or DMF for the obtainment of non porous materials. Moreover, Masere et al. have developed various gas-free initiators for FP.[61] In addition, our research group have been synthesized two ionic liquids as a new type of free-gas radical initiators that exhibit many advantages if compared with the traditional ones and APS. Namely tetrabutylphosphonium persulfate (TBPPS) and trihexyltetradecylphosphonium persulfate (TETDPPS).[48] If compared with Aliquat persulfate (APS) and the traditional initiators, benzoyl peroxide (BPO) and AIBN, they are soluble in a much larger number of reaction media, thus allowing their use with an increased number of monomers, and show a higher thermal stability toward thermal degradation. The maximum

temperature reached in the presence of TETDPPS or TBPPS were lower than those recorded with the other initiators mentioned above, but front velocities were in the same range, thus indicating that the same reaction times can be used without occurring in polymer degradation. Furthermore, the minimum molar concentration of these new initiators able to sustain the front is particular low (i.e. a fifth of that of AIBN and BPO and a half of those of APS), still preserving the mechanical properties of the polymer.

The polymerization rate should be almost zero at room temperature and increase sharply at the front temperature. Therefore, no bulk polymerization takes place and polymerization starts after that a sufficient thermal energy has been provided. The thermal energy released during the FP polymerization must be sufficient to sustain the propagating front.

In some case, phenomena of heat dissipation can be solved by using reactors with larger dimensions, pre-heating the reactants or employing insulation systems.

V.3 KINETICS AND MECHANISM OF FP

Most of the typical reactive systems used in FP follow free-radical mechanism. Once FP is started by reaction of the initiating species with the monomer functional groups, a chain reaction proceeds very much as in classical thermal polymerization, except for the control in synthesis temperature and the localized reaction zone. The synthesis of high polymers by free-radical method occurs by a path involving the repetitive addition of a monomer to the growing radicals, generated from a reactive initiator. In particular, this mechanism can be described into three main steps: initiation, propagation and termination. (Scheme V.1)

$$Initiation: \quad I \rightarrow f2R\cdot$$
$$Propagation: R\cdot + M \rightarrow P_1\cdot$$
$$P_n\cdot + M = P_{n+1}\cdot$$
$$Termination: P_{n+1}\cdot + P_m\cdot \rightarrow P_n + P_m \ (or\ P_{n+m})$$

Scheme V.1 The three main steps of a free-radical chain polymerization.

In the first step, unstable compound, such as peroxide or azo-compound, decomposes to produce radicals; f represents the efficiency, which is strongly influenced by the initiator type and solvent. During the propagation, a radical can then add to a monomer to initiate a growing polymer chain. This step continues until a chain terminates by reacting with another chain, or with an initiator radical.

The major heat release in the polymerization reaction occurs in the propagation step, even if it does not have sufficiently high activation energy to provide a frontal regime (i.e. a significant reaction rate difference between the reaction and cold zones). Frontal polymerization autocatalysis occurs through the initiator

decomposition step, because the initiator radical concentration is the main control for the total polymerization rate, compared to the gel effect or direct thermal polymerization that may also be present in the frontal polymerization process. The steady-state assumption in the polymerization model gives an approximate relationship between the effective activation energy of the entire polymerization process and activation energy of the initiator decomposition reaction:

$$E_{eff} = \frac{1}{2}E_i + E_p - \frac{1}{2}E_t$$

where E_i, E_p and E_t are referred to initiation, propagation and termination steps respectively. E_p and E_t are normally small, so that for thermally initiated reactions, E_i is often the largest, thus determining the effective activation energy. Because of this, the initiator plays a significant role in determining if a front will exist and, if so, the temperature profile in the front and how fast the front will propagated.

REFERENCES

[1] Peppas, N. A.; Mikos, A. G. In Hydrogels in Medicine and Pharmacy, edited by N. A. Peppas, CRC Press, Boca Raton, 1986.
[2] Davtyan, S. P.; Zhirkov, P. V.; Vol'fson, S. A. *Russian Chemical Reviews* 1984, 53, 150-153.
[3] Chechilo, N. M.; Khvilivitskii, R. J.; Enikolopyan, *N. S. Doklady Akademii Nauk SSSR* 1972, 204, 1180-1181.
[4] Pojman, J. A.; Ilyashenko, V. M.; Khan, A. M. J. Chem. Soc., Farad. Trans. 1996, 92, 2826-2836.
[5] Pearlstein, A.J. J. Phys. Chem. 1985, 89, 1054–1058.
[6] Briskman, V.A. In Polymer Research in Microgravity: Polymerization and Processing, Acs Symposium Series No. 793 (eds J.P. Downey and J.A. Pojman), American Chemical Society, Washington, DC, 2001.
[7] Cabral, J.T.; Hudson, S.D.; Harrison, C.; Douglas, J.F. *Langmuir* 2004, 20, 10020–10029.
[8] Cheng, J.; Han, S.; Yan, Y. *Physical Reviews A* 2005, 72, 021801-021804.
[9] Cabral, J. T.; Hudson, S. D.; Harrison, C.; Douglas, J. F. *Langmuir* 2004, 20, 10020-10029.
[10] Norrish, R. G. W.; Smith, R. R. *Nature* 1942, 150, 336-337.
[11] Trommsdorff, E.; Khole, H.; Lagally, P. *Makromolekulare Chemie* 1948, 1, 169-198.
[12] Lewis, L. L.; DeBisschop, C. S.; Pojman, J. A.; Volpert, V. A. *J. Polym. Sci. Part A: Polym. Chem.* 2005, 43, 5774-5786.
[13] Anselm-Tamburini, U.; Munir, Z. A. *J. Appl. Phys.* 1989, 66, 5039-5045.
[14] Puszynski, J.; Degreve, J.; Hlavacek, V. *Ind. Eng. Chem. Res.* 26, 1424-1434.
[15] Merzhanov, A. G.; Dvoryankin, A. V.; Strunina, A. G. *Dokl. Phys. Chem.* 1982, 267, 869-872.
[16] Sivashinsky, G. I. *J. Appl. Math*, 1981, 40, 432-434.
[17] Volpert, A. I.; Volpert, V. A. In Traveling Wave Solutions of Parabolic Systems. American Mathematical Society, Providence, RI, 1994.
[18] Strunin, D. V.; Strunina, A. G.; Rumanov, E. N.; Merzhanov, A. G. *Phys. Lett. A* 1994, 192, 361-363.
[19] Chechilo, N. M.; Enikolopyan, N. S. *Dokl. Phys. Chem.* 1975, 221, 392-394.
[20] Chechilo, N. M.; Enikolopyan, N. S. *Dokl. Phys. Chem.* 1976, 230,840-843.
[21] Pojman, J. A. *J. Am. Chem. Soc.* 1991, 113, 6284-6286.
[22] Pojman, J. A.; Craven, R.; Khan, A.; West, W. W. *J. Phys. Chem* 1992, 96, 7466-7472.
[23] Pojman, J. A.; Willis, J. R.; Khan, A. M.; West, W. W. *J. Polym. Sci., Part A: Polym. Chem.* 1996, 34, 991-995.
[24] Pojman, J. A.; Willis, J.; Fortenberry, D.; Ilyashenko, V.; Khan, A. M. *J. Polym. Sci., Part A: Polym. Chem.* 1995, 33, 643-652.
[25] Pojman, J. A.; Nagy, I. P.; Salter, C. C. *J. Am. Chem. Soc.* 1993, 115, 11044-11045.
[26] Chekanov, Y.; Arrington, D.; Brust, G.; Pojman, J. A. *J. App. Polym Sci.* 1997, 66, 1209-1216.
[27] Pojman, J. A.; Elcan, W.; Khan, A. M.; Mathias, L. *J. Polym. Sci., Part A: Polym. Chem.* 1997, 35, 227-230.
[28] Tredici, A.; Pecchini, R.; Sliepcevich, A.; Morbidelli, M. *J. Appl. Polym. Sci.* 1998, 70, 2695-2702.
[29] Tredici, A.; Pecchini, R.; Morbidelli, M. *J. Polym. Sci., Part A: Polym. Chem.* 1998, 36, 1117-1126.
[30] Washington, R. P.; Steinbock, O. *J. Am. Chem. Soc.* 2001, 123, 7933-7934.
[31] Fortenberry, D. I.; Pojman, J. A. *J. Polym. Sci., Part A: Polym. Chem.* 2000, 38, 1129-1135.
[32] Hu, T.; Chen, S.; Tian, Y.; Chen, L.; Pojman, J. A. *J. Polym. Sci. Part A: Polym. Chem.* 2007, 45, 873-881.
[33] Chen, L.; Hu, T.; Yu, H.; Chen, S.; Pojman, J. A. *J. Polym. Sci. Part A: Polym. Chem.* 2007, 45, 4322-4330.
[34] Chen, S.; Tian, Y.; Chen, L.; Hu, T. *Chem. Mater*. 2006, 18, 2159-2163.
[35] Cai, X.; Chen, S.; Chen, L. *J. Polym. Sci. Part A: Polym. Chem.* 2008, 46, 2177-2185.
[36] Chen, S.; Sui, J.; Chen, L.; Pojman, J. A. *J. Polym. Sci. Part A: Polym. Chem.* 2005, 43, 1670-1680.
[37] Mariani, A.; Fiori, S.; Chekanov, Y.; Pojman, J. A. *Macromolecules* 2001, 34, 6539-6545.
[38] Fiori, S.; Mariani, A.; Ricco, L.; Russo, S. *e-Polymers* 2002, 29, 1-10.
[39] Mariani, A.; Bidali, S.; Fiori, S.; Malucelli, G; Sanna, E. *e-Polymers* 2003, 44, 1-9.
[40] Fiori, S.; Mariani, A.; Ricco, L.; Russo, S. *Macromolecules* 2003, 36, 2674-2679.
[41] Mariani, A.; Fiori, S.; Bidali, S.; Alzari, V.; Malucelli, G. *J. Polym. Sci. Part A: Polym. Chem.* 2008, 46, 3344-3352.
[42] Fiori, S.; Malucelli, G.; Mariani, A.; Ricco, L.; Casazza, E. *e-Polymers* 2002, 57, 1-10.
[43] Frulloni, E.; Salinas, M. M.; Torre, L.; Mariani, A.; Kenny, J. M. *J. Appl. Polym. Sci.* 2005, 96, 1756-1766.

[44] Mariani, A.; Bidali, S.; Caria, G.; Monticelli, O.; Russo, S.; Kenny, J. M. *J. Polym. Sci. Part A: Polym. Chem.* 2007, 45, 2204-2211.
[45] Mariani, A.; Bidali, S.; Fiori, S.; Sangermano, M.; Malucelli, G.; Bongiovanni, R.; Priola, A. *J. Polym. Sci. Part A: Polym. Chem.* 2004, 42, 2066-2072.
[46] Mariani, A.; Alzari, V.; Monticelli, O.; Pojman, J. A.; Caria, G. *J. Polym. Sci. Part A: Polym. Chem.* 2007, 45, 4514-4521.
[47] Scognamillo, S.; Alzari, V.; Nuvoli, D.; Mariani, A. *J. Polym. Sci. Part A: Polym. Chem.* 2010, 48, 4721-4725.
[48] Mariani, A.; Nuvoli, D.; Alzari, V.; Pini, M. *Macromolecules* 2008, 41, 5191-5196.
[49] Caria, G.; Alzari, V.; Monticelli, O.; Nuvoli, D.; Kenny, J. M.; Mariani, A. *J. Polym. Sci. Part A: Polym. Chem.* 2009, 47, 1422-1428.
[50] Scognamillo, S.; Alzari, V.; Nuvoli, D.; Mariani, A. *J. Polym. Sci. Part A: Polym. Chem.* 2010, 48, 2486-2490.
[51] Scognamillo, S.; Alzari, V.; Nuvoli, D.; Illescas, J.; Marceddu, S.; Mariani, A. *J. Polym. Sci. Part A: Polym. Chem.* 2011, 49, 1228-1234.
[52] Alzari, V.; Monticelli, O.; Nuvoli, D.; Kenny, J. M.; Mariani, A. *Biomacromolecules* 2009, 10, 2672-2677.
[53] Brunetti, A.; Princi, E.; Vicini, S.; Pincin, S.; Bidali, S.; Mariani, A. *Nucl. Instrum. Methods Phys. Res. Sec.t B-Beam Interactinos with Materials and Atoms* 2004, 222, 235-241.
[54] Vicini, S.; Mariani, A.; Princi, E.; Bidali, S.; Pincin, S.; Fiori, S.; Pedemonte, E.; Brunetti, A. *Polym. adv. technol.* 2005, 16, 293-298.
[55] Mariani, A.; Alzari, V.; Monticelli, O.; Pojman, J. A.; Caria, G. *J. Polym. Sci. Part A: Polym. Chem.* 2007, 45, 4514-4521.
[56] Alzari, V.; Nuvoli, D.; Scognamillo, S.; Piccinini, M.; Gioffredi, E.; Malucelli, G.; Marceddu, S.; Sechi, M.; Sanna, V.; Mariani, A. *J. Mater. Chem.* 2011, 21, 8727-8733.
[57] Alzari, V.; Mariani, A.; Monticelli, O.; Valentini, L.; Nuvoli, D.; Piccinini, M.; Scognamillo, S.; Bon, S. B.; Illescas, J. *J. Polym. Sci. Part A: Polym. Chem.* 2010, 48, 5375-5381.
[58] Pojman, J. A.; Khan, A. M.; Mathias, L. *Microgr. Sci. Tech.* 1997, X, 36–40.
[59] Pojman, J. A. *J. Am. Chem. Soc.* 1991, 113, 6284–6286.
[60] Nagy, I. P.; Pojman, J. A. *J. Phys. Chem.* 1996, 100, 3299-3304.
[61] Masere, J.; Chekanov, Y. A.; Warren, J. R.; Stewart, F.; Al-Kaysi, R.; Rasmussen, J. K.; Pojman, J. A. *J. Polym. Sci. Part A: Polym. Chem.* 2000, 38, 3984–3990.

CHAPTER VI

EXPERIMENTAL PART

VI.1 POLYMER HYDROGELS OF 2-HYDROXYETHYL ACRYLATE AND ACRYLIC ACID OBTAINED BY FRONTAL POLYMERIZATION

In this work, homopolymer and copolymer hydrogels of acrylic acid and 2-hydroxyethylacrylate were prepared by using FP as macromolecular synthetic technique. DSC was used to estimate the conversion degree and to determine the T_g of each sample. The swelling behavior of the corresponding hydrogels was studied as a function of the pH. Moreover, SEM analysis was done to investigate the morphology of such systems at varying the pH.

MATERIALS

2-hydroxyethyl acrylate (HEA, MW = 116.12 g/mol, d = 1.011 g/mL, Figure VI.1a), AAc (MW = 72.06 g/mol, d = 1.050 g/mL, Figure VI.1b), tetraethylenglycoldiacrylate (TEGDA, MW = 302.33 g/mol, d =1.11 g/mL), BPO (FW = 242.23 g/mol), potassium hydrogen phthalate (MW =204.22 g/mol), sodium dihydrogen phosphate (MW = 137.99 g/mol), potassium nitrate (MW = 101.103 g/mol), and sodium tetraborate decahydrate (MW = 381.37 g/mol) were purchased from Sigma Aldrich and used as received without any further purification.

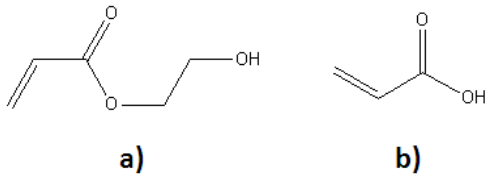

Figure VI. 1 Structures of: a) HEA and b) AAc.

SYNTHESIS OF HOMOPOLYMERS AND COPOLYMERS OF AAc AND HEA

The polymer samples were synthesized keeping constant the total molar amount of the two monomers (6.96×10^{-2} mol), the amounts of crosslinker and of initiator (5 mol % and 1 mol % referred to the total amount of the two monomers, respectively). HEA and/or AAc were introduced in a common glass test tube (i.d. = 1.5 cm, length = 16 cm) and were sonicated in an ultrasonic bath for 1 min. Then, TEGDA and BPO were added, and the solution was again sonicated for other 2 min to have a homogeneous mixture. A thermocouple junction was located at about 1 cm from the bottom of the tube and connected to a digital temperature recorder. Front started by heating the external wall of the tube in correspondence of the upper surface of the monomer mixture until the formation of the front became evident. The position of the front (easily visible through the glass wall of test tubes) against time was measured. Front temperature

measurements were performed by using a K-type thermocouple connected to a digital thermometer (Delta Ohm 9416) used for temperature reading and recording (sampling rate: 1 Hz). For all samples, front temperature (T_{max}, ±10 °C) and front velocity (V_f, ±0.5 cm/min) were measured. Each sample was synthesized in triplicate, and all the experimental data were averaged.

CHARACTERIZATION

Differential Scanning Calorimetry analyses

Thermal analyses were performed using a DSC Q100 Waters TA Instruments calorimeter, with a TA Universal Analysis 2000 software. Dried samples were placed in closed 40 mL aluminum crucibles and subjected to two DSC scans from -80 to 300 °C, with a scan rate of 20 °C/min and in inert atmosphere (argon flux: 40 mL/min): the first scan was performed to determine monomer conversion, and the second one was to establish T_g. In particular, conversions were calculated by using the following equation:

$$C\% = \left(1 - \frac{\Delta H_r}{\Delta H_{100}}\right) \cdot 100$$

where ΔH_r (residual) is the peak area obtained for the residual polymerization occurred during the first thermal scan, and ΔH_t (total) is the area under the curve when the polymerization was carried out in the DSC instrument.

SEM analyses

SEM analyses of the hydrogels were executed using a Zeiss EVO LS10.

Swelling Experiment

To study the swelling behavior at different pH values, the hydrogels were immersed in buffer solutions of the desired pH (1–13) and containing KNO_3 at the constant concentration of 0.1 mol/L, necessary to have a sufficiently high ionic strength. Buffer solutions were prepared by using various combinations of potassium hydrogen phthalate, sodium dihydrogen phosphate, sodium tetraborate decahydrate, NaOH, and HCl. When the equilibrium was attained, the samples were weighed and their swelling ratio (SR%) at different pH was calculated applying the following equation:

$$SR\% = \frac{M_s - M_D}{M_S} \cdot 100$$

where M_s and M_d are the hydrogel masses in the swollen and in the dried state, respectively. The reported data are an average of three measurements (reproducibility was about ±10%).

VI. 2. ORGANIC-INORGANIC IPNs AND HYBRID POLYMER MATERIALS PREPARED BY FRONTAL POLYMERIZATION

Novel polyacrylamide-based hydrogels containing 3-(trimethoxysilyl)propyl methacrylate, 3-TMeOSi, and/or tetraethoxy silane, TEtOSi, were synthesized by means of frontal polymerization, using ammonium persulfate as initiator, BIS as crosslinking agent and DMSO as solvent. The swelling ratio of the obtained hydrogels was determined at two different pH values: 2 and 5. The occurrence of this reaction was assessed by solid state NMR. Moreover, the thermal properties of the dry materials were studied by DSC and TGA, and their water contact angles (WCAs) were measured.

MATERIALS

AAm (MW = 71.8 g/mol, Figure VI.2a), TEtOSi (MW = 208.33 g/mol, d = 0.933 g/mL, Figure VI.2b), 3-TMeOSi (MW = 248.35 g/mol, d = 1.045 g/mL, Figure VI.2c), BIS (MW = 154.17 g/mol), AmPS (MW = 228.20 g/mol) and DMSO (MW = 78.13 g/mol, d = 1.101 g/mL) were purchased from Sigma-Aldrich and used as received.

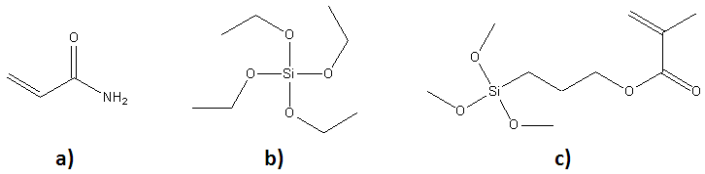

Figure VI. 2 Structures of: a) AAm, b) TEtOSi and c) 3-TMeOSi.

HYDROGEL SYNTHESIS

Hydrogels were prepared using different molar fractions of AAm, TEtOSi and 3-TMeOSi, from the AAm homopolymer to copolymers containing up to 1.7 mol% of TEtOSi and 6.9 mol% of 3-TMeOSi (Table VI.1), keeping constant the amounts of crosslinker (BIS, 0.25 mol % referred to the amount of AAm), initiator (0.50 mol% referred to the amount of AAm) and DMSO (2.5 mL).

A common glass test tube (i.d. = 1.5 cm, length = 16 cm) was filled with the appropriate amounts of AAm, TEtOSi, 3-TMeOSi, BIS and DMSO. The mixture was sonicated in an ultrasonic bath at 25 °C until the mixture became homogeneous. Then, AmPSA was added. A thermocouple junction was located at about 1.5 cm from the bottom of the tube and connected to a digital thermometer in order to monitor the temperature. Frontal polymerization started by heating the external wall of the tube at the upper surface of the monomer mixture with the tip of a soldering iron until the formation of the front became evident. The position of the front, visible through the glass wall of the test tube, was measured as a function of time.

Front temperature measurements were performed by using a K-type thermocouple connected to a digital thermometer, Delta Ohm 9416, employed for temperature reading and recording (sample rate = 1 Hz). The front velocity, V_f, (± 0.5 cm/min) and the front temperature, T_{max} (± 15 °C) were measured for all samples. Once achieved the frontal polymerization, all samples were washed with distilled water in order to remove DMSO.

Tabella VI.1 Composition of hybrid hydrogels.

Sample code	TEtOSi (mol%)	[3TMeOSi]/[TEtOSi] (mol%)
A1	0	0
B1	0.35	0
B2	0.35	1
B3	0.35	2
B4	0.35	3
B5	0.35	4
C1	0.70	0
C2	0.70	1
C3	0.70	2
C4	0.70	3
C5	0.70	4
D1	1.7	0
D2	1.7	1
D3	1.7	2
D4	1.7	3
D5	1.7	4
E1	3.5	0

CHARACTERIZATION

Swelling experiments

All samples were allowed to swell at pH 2 and 5 and the swelling behavior of the resulting hybrid hydrogels was measured at various time intervals using the following equation:

$$SR\% = \frac{M_S - M_D}{M_S} \cdot 100$$

where M_d and M_s are the hydrogel masses in the swollen and in the dried state, respectively. The reported data are an average of three measurements (reproducibility was about ±10%).

Thermal analyses

DSC thermal characterization was performed by means of a Q100 Waters TA Instruments calorimeter, using TA Universal Analysis 2000 software. Two heating ramps from -80 to 300 °C, employing a heating rate of 10 °C/min, were carried out on dry samples. The first scan was carried out in order to remove traces of residual solvent and to determine monomer conversion by calculating the residual polymerization heat. The second was recorded to determine the T_g.

The thermo-oxidative stability of the hydrogels was evaluated by TGA in air (gas flow: 60 mL/min), from 50 to 800 °C with a heating rate of 10 °C/min. A TAQ500 analyzer was used, placing the samples (ca. 10 mg) in open alumina pans.

SEM analyses

The morphological characterization of polymer hydrogels was carried out using a SEM JEOL 7600. Before the analysis, samples were lyophilized, fractured in liquid nitrogen, and the fractured surface was coated with gold.

Water contact angle measurements

WCAs were determined by a Dataphysics OCA 5, 10 instrument on the above samples previously treated at both pH 2 and 5 and desiccated before the measurement.

^{29}Si NMR analyses

High resolution NMR spectra were collected using a Varian UNITY INOVA Spectrometer with a 9.39 T wide-bore Oxford magnet. The ground samples were analyzed by ^{29}Si Cross Polarization Magic Angle Spinning (CP/MAS) by packing each sample into a 7 mm ZrO_2 rotor at a spinning rate of 5 KHz. The ^{29}Si CP/MAS experiments were run with a contact time of 1 ms, recycle time of 2 s, 90° pulse lengths, a 100 kHz bandwidth and 2000 scans in each experiment. ^{29}Si chemical shifts were referenced to that of tetramethylsilane.

VI.3 MULTISTIMULI-RESPONSIVE HYDROGELS OF POLY(2-ACRYLAMIDO-2-METHYL-1-PROPANESULFONIC ACID) CONTAINING GRAPHENE

In this work, nanocomposite hydrogels of PAMPS containing graphene were prepared by free radical polymerization. Graphene was obtained through exfoliation of graphite in DMF, and was characterized by

TEM and Raman spectroscopy. The swelling properties of the resulting nanocomposites in response to ionic strength and electrical stimuli were investigated. Moreover, SEM analyses were performed to study the influence of graphene on the nanocomposite morphology.

MATERIALS

AMPSA (MW = 207.25 g/mol, d 1.1 g/mL, Figure VI.3), DMF (MW =73.08 g/mol, d = 0.944 g/mL), BIS (MW = 154.17 g/mol), potassium nitrate (MW = 101.10 g/mol), calcium nitrate tetrahydrate (MW = 236.15 g/mol) and graphite flakes (+100 mesh) were purchased from Sigma-Aldrich and used as received. TETDPPS (MW = 1159 g/mol) was used as the radical initiator and synthesized according to the method described in the literature.[1]

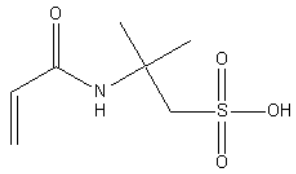

Figure VI.3 AMPSA structure.

SYNTHESIS

Graphene dispersion in DMF

Graphite (5.0 g) dispersed in 100 g of DMF was introduced in a 250-mL flask; the mixture was sonicated in an ultrasonic bath (EMMEGI, 0.55 kW, water temperature ≈ 25 °C) for 24 h. Then, the dispersion was centrifuged for 30 min at 4000 rpm, and the residual solid graphite was removed. The concentration, calculated by gravimetry after filtration through polyvinylidene fluoride (PVDF) filters (pore size 0.22 µm), was found to be equal to 0.35 mg/mL.

Synthesis of PAMPSA hydrogels

In order to prepare hydrogels containing various amounts of graphene, the above stock dispersion was properly diluted with suitable amounts of DMF. The desired quantities of AMPSA were added to the obtained graphene dispersion, and the new resulting mixture was sonicated for 15 min. Then, the crosslinker (BIS, 5 mol% with respect to the molar concentration of AMPSA) and the initiator (TETDPPS, 0.5 mol% with respect to the molar concentration of AMPSA) were added. The investigated formulations are listed in Table VI.2.

A common test tube (inner diameter=1.5 cm, length= 16 cm) was filled with the reacting mixture (Table VI.2). The polymerization was performed by keeping the tube immersed in an oil bath at 80 °C for 1 h.

Table VI.2 Amount of graphene present in each nanocomposite hydrogel.

Sample	Graphene content (wt.-% respect to monomer weight)
A	0
B	0.01
C	0.02
D	0.06

CHARACTERIZATION

Graphene/DMF dispersion characterization

The graphene stock dispersion in DMF was analyzed by UV–Vis spectroscopy using the Hitachi U-2010 spectrometer (1 mm cuvette), following the method described in the literature.[2-4] Namely, a calibration line for graphene concentration was used (wavelength was 660 nm). The calculated absorption coefficient was 2498 mL mg^{-1} m^{-1}. This was used to determine the actual graphene concentrations in any diluted dispersion derived from the stock one.

TEM measurements were performed on the JEOL JEM-2100 TEM instrument (JEOL Ltd., Akishima, Tokyo, Japan), with the LaB6 filament, with an operating voltage of 200 kV. For TEM analysis, the solutions have been cast directly on the 200-mesh cooper grid and followed by solvent evaporation at ambient conditions for 24 h. Raman analysis was performed with a Bruker Senterra Raman microscope, using an excitation wavelength of 532 nm at 5 mW. The spectra were acquired by averaging five acquisitions of 5 s with a ×50 objective.

Hydrogel characterization

After freeze-drying, the hydrogels were analyzed by SEM using the ZEISS DSM 962 CSEM scanning electron microscope. Prior to examination, all samples were fractured in liquid nitrogen, and the fractured surface was coated with gold. To determine the SR% as a function of the ionic strength, the hydrogels were immersed in aqueous solutions of KNO_3 and $Ca(NO_3)_2$, to evaluate the influence of the type of cation. In particular, the ionic strength was varied from 0 to 0.1, and the pH was kept constant at 3; when the equilibrium was attained, the samples were weighed, and the SR% was calculated applying the following equation:

$$SR\% = \frac{M_S - M_D}{M_S} \cdot 100$$

where M_s and M_d are the hydrogel masses in the swollen and dry states, respectively. The reported data are an average of three measurements (reproducibility was about ±10%).

To determine the SR% as a function of the variation of an electrical stimulus, the hydrogels were immersed in deionized water for 2 h. Then, they were cut into rectangular shaped blocks (10 x 10 x 5 mm). After precise weighing, each hydrogel sample was placed between the two metal electrodes. Since during the measurement the hydrogels deswell, the electrodes were forced to remain in contact with the sample during the whole experiment duration. The voltage applied was constant at 5, 15, or 30 V and applied for 30 s. Finally, the samples were weighed at the end of each test.

The relative weight change (RWC) due to the variation of the electrical field was calculated by the following equation:

$$RWC = 1 - \left(\frac{M_i - M_f}{M_i}\right)$$

where M_f is the weight of the sample after treatment with the electric field, and M_i is the weight of the sample before treatment (conventionally, the weight of the sample not subjected to the electric field is equal to 1).

VI. 4 SYNTHESIS AND CHARACTERIZATION OF GRAPHENE-CONTAINING THERMORESPONSIVE NANOCOMPOSITE HYDROGELS OF POLY(*N*-VINYLCAPROLACTAM) PREPARED BY FRONTAL POLYMERIZATION

In this work, FP was used to synthesize stimuli responsive nanocomposite hydrogels of PNVCL, containing graphene. This latter was obtained by direct graphite sonication in the self-same liquid monomer. Furthermore, the corresponding nanocomposites were fully characterized by Raman, SEM, and TEM, and their swelling behavior and rheological properties were investigated.

MATERIALS

N-vinylcaprolactam (NVCL, MW = 139.2 g/mol, d = 1.029 g/mL, Figure VI.4) and TEGDA (MW = 302.33 g/mol, d = 1.11 g/mL) were purchased from Sigma Aldrich and used as received. TETDPPS (MW = 1115 g/mol) was prepared following the method reported in a previous study.[1] Graphite flakes were purchased from Aldrich and used as received.

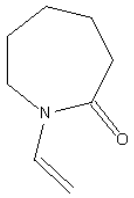

Figure VI.4 NVCL structure.

SYNTHESIS

Graphene Dispersion Preparation

A graphene masterbatch dispersion was prepared by dispersing 5.0 wt.-% graphite flakes in NVCL, placed into a tubular plastic reactor (i.d. 15 mm) and ultrasonicating it for 24 h at 40 °C (Ultrasound bath EMMEGI, 0.55 kW). Then, the dispersion was centrifuged for 30 min at 4000 rpm and the gray to black liquid phase containing graphene was recovered. The concentration of the graphene dispersion was obtained by gravimetric filtration through PVDF filters (pore size 0.22 μm).

Synthesis of PNVCL Hydrogels

The nanocomposite polymer hydrogels of PNVCL containing graphene were prepared by varying the amount of the nanofiller from 0.0088 to 0.44 wt.-% (corresponding to 0.10 and 5.0 mg/mL, respectively, referred to NVCL monomer), and keeping constant the amount of crosslinker (TEGDA), and initiator (TETDPPS), both at 1.0 mol% referred to the amount of NVCL (Table 1). The graphene masterbatch dispersion in NVCL was diluted with suitable amounts of NVCL, thus obtaining dispersions containing a different concentration of graphene. Each dispersion was poured into a common glass test tube (i.d. = 1.5 cm, length = 16 cm), and added of TEGDA and TETDPPS. A thermocouple was located at about 1 cm from the bottom of the tube and connected to a digital temperature recorder (Delta Ohm 9416, sampling rate: 1 Hz). FP started by heating the external wall of the tube in correspondence of the upper surface of the monomeric mixture. The position of the front (easily visible through the glass wall of test tubes) vs. time was also monitored. For all the samples, front temperature (T_{max}, ±10 °C) and front velocity (V_f, ±0.5 cm/min) were measured.

CHARACTERIZATION

Graphene/NVCL dispersion characterization

The graphene–NVCL masterbatch dispersion was submitted to UV–Vis spectroscopic analysis, using a Hitachi U-2010 spectrometer (1 mm cuvette) and following the method described in the published reports.[2-4] A calibration curve was constructed for the wavelength of 660 nm, to evaluate the molar extinction coefficient of the dispersion (which was found to be equal to 1502 mL/(m mg)) and to determine the graphene concentration in all the diluted dispersions derived from the masterbatch (Figure VI.5).

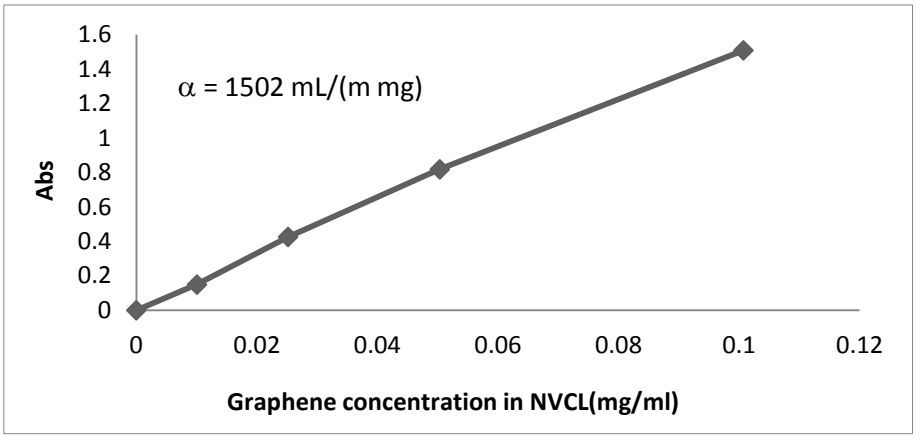

Figure VI. 5 Calibration lines for graphene dispersion in NVCL and its corresponding absorption coefficient.

Raman analyses were performed using a Bruker Senterra Raman microscope with an exciting radiation of 532 nm at 5 mW. The spectra were acquired by averaging five acquisitions of 5 s with a x50 objective.

Hydrogel characterization

The morphological characterization of polymer hydrogels was carried out using a SEM Zeiss EVO LS10.

The swelling behavior as a function of temperature of the PNVCL–graphene nanocomposite hydrogels was measured in water from 3 to 55 °C using a thermostatic bath. To this aim, three different heating rates were used, namely 3 °C/day (from 3 to 9 °C), 1 °C/day (from 25 to 35 °C), and 5 °C/day (from 35 to 55 °C). The SR% was calculated by the following equation:

$$SR\% = \frac{M_S - M_D}{M_S} \cdot 100$$

where M_s and M_d are the hydrogel masses in the swollen and in the dried state, respectively. The reported data are an average of three measurements (reproducibility was about ±10%).

Rheological measurements were carried out on a strain controlled rheometer (ARES, TA Instruments, Waters LLC) with a torque transducer range of 0.2–2000 gf cm, using 25 mm parallel plate geometry. Frequency sweep tests were carried out in the linear viscoelastic region for all the samples, at 25 °C, 0.1–100 rad/s. Strain has been chosen to have a torque within the sensitivity of the instrument in the linear viscoelastic region. To assure reproducibility, at least four measurements were performed on each sample.

TEM studies were performed on a JEOL JEM-1011 working at an accelerating voltage of 100 kV. Ultrathin sections (nominal thickness of 100 nm) of either dried or swollen hydrogels were cut at 120 °C using a Leica Ultracut UCT microtome with a EMFCS cryo kit equipped with a diamond knife, and collected onto formvar-coated 400 mesh copper grids. The sections from dried samples were difficult to handle because of the accumulated static charge and had to be removed from the knife edge with an eyelash, transferred to an

ipersaturated sucrose solution and then placed on the grids. In the case of swollen gels, a drop of a sucrose solution was used to collect the cuts directly from the microtome and to transfer them to the grids. Finally, the sucrose was washed away with deionized water, and the grids dried at room temperature. Apart from the direct visualization of different graphene morphologies, TEM images were also analyzed to offer a qualitative determination of the amount of isolated few-layer graphene sheets to aggregated graphene, in a series of at least 10 images per sample.

VI. 5 SYNTHESIS AND CHARACTERIZATION OF THERMORESPONSIVE NANOCOMPOSITE HYDROGELS OF POLY(*N*-VINYLCAPROLACTAM) CONTAINING NANOCRYSTALLINE CELLULOSE

In this work, PNVCL nanocomposite hydrogels containing CNC were prepared by the use of the frontal polymerization technique. CNC were obtained by acid hydrolysis of commercial microcrystalline cellulose and dispersed in DMSO. The dispersion was characterized by TEM analysis and mixed with suitable amounts of NVCL for the synthesis of PNVCL nanocomposite hydrogel having a CNC concentration ranging between 0.10 and 2.0 wt.-%. The nanocomposite hydrogels were analyzed by SEM and their swelling and rheological features were investigated.

MATERIALS

NVCL (MW = 139.2 g/mol; d = 1.029 g/mL), BIS (MW = 154.17 g/mol), DMSO (MW = 78.13 g/mol; d = 1.101 g/mL) and microcrystalline cellulose (MCC, dimensions of 10-15 μm) were purchased from Sigma Aldrich and used as received. TETDPPS (MW = 1115) was prepared following the method reported in our previous study.[5]

SYNTHESIS

Synthesis of cellulose nanocrystals

CNC suspension was prepared from MCC by acid hydrolysis following the recipe used by Cranston and Gray.[5] Hydrolysis was carried out with 64 wt.-% sulphuric acid at 45 °C for 30 min with vigorous stirring. After removing the acid, dialysis and ultrasonic treatment were performed. The resultant cellulose nanocrystals aqueous suspension was approximately 0.50 wt.-% while the hydrolysis yield was about 20 %.

Synthesis of PNVCL nanocomposite hydrogels

The nanocomposite polymer hydrogels were synthesized by varying the amount of CNC from 0.20 to 2.0 wt.-% (referred to the amount of NVCL monomer), and keeping constant the amount of crosslinker (BIS) and initiator (TETDPPS) to 2.5 and 0.50 mol% (referred to NVCL), respectively.

CNC dispersions were prepared by dissolving the appropriate amount in 3 ml of DMSO, and sonicating it in an ultrasonic bath for 5 minute. Then, CNC dispersions in DMSO and liquid NVCL were introduced in a common glass test tube (i.d. = 1.5 cm, length = 16 cm) and sonicated for 1 minute. After that, BIS and TETDPPS were added, and the solution was sonicated again for 30 s to remove any bubbles present in it. A thermocouple junction was located at about 1 cm from the bottom of the tube and connected to a digital temperature recorder (Delta Ohm 9416). Front started by heating the external wall of the tube in correspondence of the upper surface of the monomer mixture, until the formation of the front became evident. Front velocity, V_f, was determined by measuring front positions as a function of time. Front temperature, T_{max}, was obtained by using a K-type thermocouple connected to the above digital thermometer (sampling rate: 1 Hz). For all samples, T_{max} (±10 °C) and V_f (± 0.05 cm min^{-1}) were measured. After polymerization, all samples were washed in water for several days to remove DMSO and allow them to swell.

CHARACTERIZATION

CNC characterization

The nanocrystals in water and DMSO suspensions were examined by transmission electron microscopy (TEM, JEOL JEM-1010), using an accelerating voltage of 100 kV. One drop of each sample was directly placed in the electron microscopic grid and dry at room temperature.

Hydrogel characterization

The swelling behavior of the CNC-PNVCL nanocomposite hydrogels was measured in water from 3 to 50 °C, using a thermostatic bath. Three different heating rates were used: 3 °C/day (from 3 to 9 °C), 1 °C/day (from 26 to 36 °C) and 5 °C/day (from 36 to 51 °C). The SR% for each sample was calculated by applying the following equation:

$$SR\% = \frac{M_s - M_D}{M_S} \cdot 100$$

where M_s and M_d are the hydrogel masses in the swollen and in the dry state, respectively. All measurements were performed in triplicate.

Rheological tests were performed in a rotational rheometer ARES, with parallel plate geometry (ϕ 8 mm). Dynamic measurements have been performed in order to analyze the viscoelastic properties of the materials and the influence of CNC. Preliminary strain sweep tests to determine the liner viscoelastic region were done. Frequency sweep measurements at room temperature (25 °C) with a strain of 2% in the frequency range of 0.03 – 100 rad/sec were performed. A special tool was used in order to maintain the

sample immersed in water during the test thus avoiding any change in mechanical response due to sample drying.

The surface morphology was assessed by scanning electron microscopy (FE-SEM, Supra 25 Zeiss, Germany). Before the analysis, samples were lyophilized, fractured in liquid nitrogen, and the fractured surface was coated with gold.

VI. 6 THE PRODUCTION OF CONCENTRATED DISPERSIONS OF FEW-LAYER GRAPHENE BY THE DIRECT EXFOLIATION OF GRAPHITE IN ORGANOSILANES

In this work, highly concentrated dispersions of graphene have been prepared by direct exfoliation of graphite in two reactive organosilanes. The concentration of graphene dispersions was determined by gravimetry, while TEM and Raman spectroscopy were used to confirm the presence of few-layer graphene.

MATERIALS

Phenyl triethoxysilane (PhTES, MW = 240.37 g/mol, d = 0.99 g/mL, Figure VI.6a), 3-glycidoxypropyl trimethoxysilane (GPTMS, MW = 236.34 g/mol, d = 1.07 g/mL, Figure VI.6b) and graphite flakes (+100 mesh) were purchased from Sigma Aldrich and used as received without further purification.

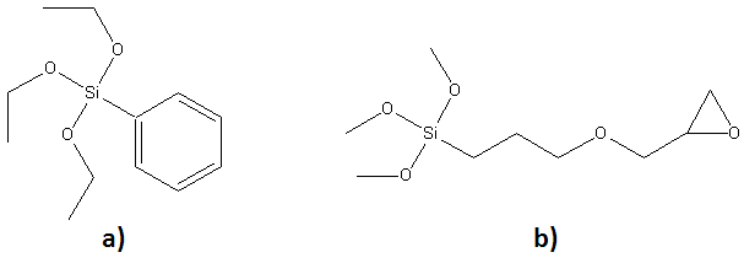

Figure VI.6 Structures of: a) Phenyl triethoxysilane and b) 3-glycidoxypropyl trimethoxysilane.

SYNTHESIS

Graphene dispersions

Mixtures containing various amounts of graphite flakes and organosilane (5.00 g) were put in a tubular plastic reactor (i.d. 15 mm) and placed in an ultrasonic bath (Ultrasound bath EMMEGI, 0.55 kW, water temperature ≈ 25 °C) for 24 h. Then, after they were centrifuged for 30 min at 4000 rpm, the gray to black liquid phase containing graphene was recovered.

CHARACTERIZATION

In order to determine the graphene concentration, the above dispersion was divided into two fractions with a known volume. The first one was filtered through PVDF (pore size of 0.22 μm) in order to directly weigh the amount of dispersed graphene and determine the actual graphene concentration.

The above gravimetric data allowed us to determine the absorption coefficient α: the second aliquot of the above dispersion was diluted several times, and for each of them the absorbance at a wavelength of 660 nm was measured by using a spectrophotometer UV Hitachi U-2010 spectrometer (1 cm cuvette), following the method reported in literature. [2-4] Absorbance versus concentration plots gave the absorption coefficient α value of about 4710 $ml \cdot mg^{-1} \cdot m^{-1}$ and 2415 $ml \cdot mg^{-1} \cdot m^{-1}$ for graphene dispersion in PhTES and GPTMS respectively. (Figure VI.7)

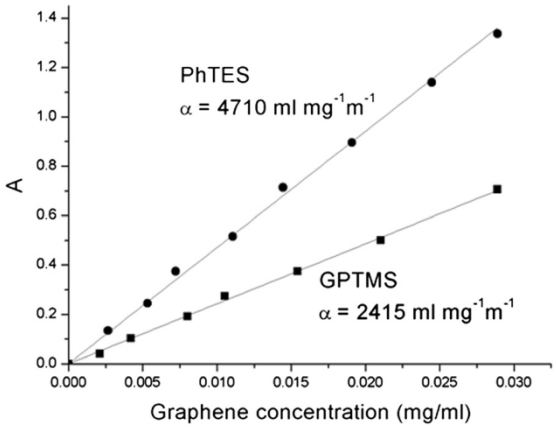

Figure VI.7 Calibration lines for graphene dispersion in PhTES and GPTMS, and their corresponding absorption coefficients.

TEM analyses

TEM measurements were performed on a JEOL JEM-2100 TEM instrument (JEOL Ltd., Akishima, Tokyo, Japan), with a LaB6 filament, with an operating voltage of 200 kV. For the TEM analysis, the solutions were sonicated for 5 min and then cast directly on the 200 mesh cooper grid; eventually, the solvent was evaporated at ambient conditions for 24 h.

Raman spectroscopy

Analyses were performed on graphene flakes obtained after vacuum filtration of dispersions on PVDF filters (pore size 0.22 μm), with a Bruker Senterra Raman microscope, using an excitation wavelength of 532 nm at 5 mW. The spectra were acquired by averaging five acquisitions of 5 s with a ×50 objective.

VI. 7 IN SITU PRODUCTION OF HIGH FILLER CONTENT GRAPHENE-BASED POLYMER NANOCOMPOSITES BY REACTIVE PROCESSING

In this work, graphene containing nanocomposites of poly(tetraethyleneglycol diacrylate), PTEGDA, were obtained by direct exfoliation of graphite in TEGDA and subsequent polymerization of the latter to the corresponding polymer nanocomposites. The concentration of the dispersions was calculated by gravimetry and UV-Vis measurements, while TEM and Raman analyses were performed to confirm the presence of graphene. Graphene-based polymer nanocomposites were characterized by DSC, thermogravimetry, dynamic mechanical thermal analysis (DMTA), Raman and TEM.

MATERIALS

TEGDA (MW = 302.32 g/mol, d = 1.11 g/mL, Figure VI.8) and graphite flakes (+ 100 mesh) were purchased from Sigma Aldrich and used as received without further purification. TETDPPS was used as the radical initiator and was synthesized according to the method described in the literature.[5]

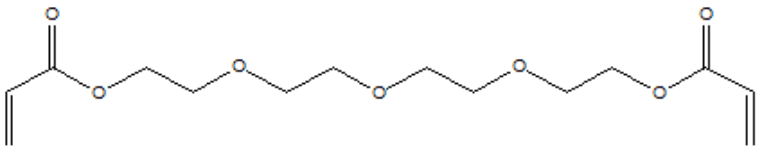

Figure VI.8 TEGDA structure

SYNTHESIS

Graphene Dispersion Preparation

In order to prepare a graphene masterbatch dispersion, 5.0 wt.-% of graphite flakes were added to TEGDA, placed into a tubular plastic reactor (i.d. 15 mm) and ultrasonicated (Ultrasound bath EMMEGI, 0.55 kW, water temperature ~40 °C) for 24 h. Then the dispersion was centrifuged for 30 min at 4000 rpm; finally, the gray to black liquid phase containing graphene was recovered. The concentration of the dispersion, calculated by gravimetry after filtration through PVDF filters (pore size 0.22 μm), was 9.5 mg/mL.

Synthesis of Poly(TEGDA) nanocomposites

The TEGDA/graphene masterbatch was further diluted with suitable amounts of TEGDA; then, 0.50 wt.-% of TETDPPS initiator was added and the polymerization was performed in Pasteur pipettes, used as tubular reactors, in an oven at 80 °C for 2 hours. Any run was repeated at least three times.

CHARACTERIZATION

Graphene/TEGDA dispersion characterization

The above graphene masterbatch dispersion in TEGDA was analyzed by UV-Vis spectroscopy, using a Hitachi U-2010 spectrometer (1 mm cuvette), following the method reported in the literature.[2-4] Namely, a calibration line for graphene concentration was used, at a wavelength of 660 nm (Figure VI.9). The calculated absorption coefficient was 436 mL mg^{-1} m^{-1}: this value was used for determining the actual graphene concentrations in any diluted dispersion derived from the masterbatch one.

Raman spectra were obtained with a Bruker Senterra Raman microscope, using an excitation wavelength of 532 nm at 5 mW. They were acquired by averaging 5 acquisitions of 5 seconds with a x50 objective.

High resolution TEM images were obtained with JEOL equipment, model JEM-2010 operating with an acceleration voltage of 200 kV. TEM analyses were performed on the samples after solvent evaporation under vacuum, performed at room temperature for 2 h.

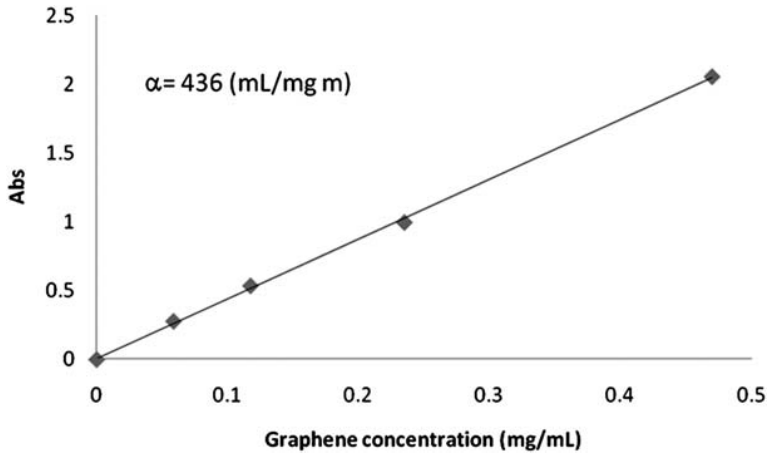

Figure VI.9 Calibration curve for graphene/TEGDA dispersion

Graphene-based polymer nanocomposite characterization

The surface morphology of the samples was investigated using a scanning electron microscope (SEM, LEO 1450VP), equipped with an X-ray probe (INCA Energy Oxford, Cu-Ka X-ray source, k = 1.540562 Å), in order to perform elemental analysis. The specimens (0.5 X 0.5 mm^2) were fractured in liquid nitrogen, fixed to conductive adhesive tapes and gold-metallized.

The thermo-oxidative stability of the samples was evaluated by TGA performed from 50 to 800 °C with a heating rate of 10 °C/min, using a Pyris1TGA Q 500 analyzer. The samples were placed in open alumina pans and analyzed in air atmosphere (gas flux: 60 mL/min).

DSC scans were performed on a DSC Q20 TA Instrument, from -50 to 200 °C, with a heating rate of 20 °C min^{-1}. The samples were placed in closed 40 mL aluminium crucibles and analyzed in inert atmosphere (nitrogen flux: 40 mL/min).

DMTA measurements were performed with a DMA Q800 TA Instrument, at a constant frequency of 1 Hz, strain amplitude of 15 mm with a preload of 0.01 N, and a temperature range from -90 to 180 °C, with a heating rate of 10 °C min^{-1}. Cylindrical samples (length: 35 mm, diameter: 4.8 mm) were analyzed in bending (dual cantilever) mode. Three DMTA tests were repeated for each material in order to have reproducible and significant data. Standard deviation for the storage modulus (G') values was within 5%.
Three point bending flexural tests, according to ASTM D790, were performed, using a Zwick-Roll Z010 apparatus, equipped with a 5 kN load cell, 30 mm support span, at 23 ± 2 °C and 50 ± 5% relative humidity. At least five tests were repeated for each material in order to have reproducible and significant data.

VI.8 SYNTHESIS AND CHARACTERIZATION OF GRAPHENE-BASED NANOCOMPOSITES WITH POTENTIAL USE FOR BIOMEDICAL APPLICATIONS

In the present study, graphene-based nanocomposites containing different amounts of nanofiller dispersed into Bisphenol A glycerolate dimethacrylate/TEGDA (Bis-GMA/TEGDA) polymer matrix have been prepared. In particular, the graphene dispersions, produced by simple sonication of graphite in TEGDA monomer, have been used for the direct preparation of nanocomposite copolymers with Bis-GMA. The morphology of the obtained nanocomposites has been investigated as well as their thermal and mechanical properties.

MATERIALS

TEGDA (MW = 302.32 g/mol, d = 1.11 g/mL), triethyleneglycol dimethacrylate (TEGDMA, MW = 286.32 g/mol, d = 1.092 g/mL), Bis-GMA (MW = 512.6 g/mol, d = 1.161 g/mL), BPO (MW = 242.23 g/mol), and graphite flakes (particle size, +100 mesh) were purchased from Sigma-Aldrich and used as received.

SYNTHESIS

Preparation of graphene dispersions in TEGDA

Graphene dispersions in TEGDA were prepared following the method reported in the previous work. The graphene concentration, calculated by gravimetry after filtration through PVDF filters (pore size 0.22 μm), was 6.0 mg/mL.

Synthesis of Bis-GMA/TEGDA nanocomposites

Polymer resins were prepared as follows: the graphene masterbatch dispersion in TEGDA was diluted with suitable amounts of this latter liquid monomer for achieving the desired concentration (for the neat resin, pure TEGDA was employed); an appropriate amount of Bis-GMA was added for obtaining a 1:1 w/w mixture, then 1 wt.-% (referred to the total weight) of BPO was added and the mixture was homogenized.

Polymerization was performed in silicone molds (1 x 1 x 0.3 cm^3) at 80 °C for 24 h. For comparative purposes, TEGDA was replaced with TEGDMA, following the same procedure described above.

CHARACTERIZATION

Graphene/TEGDA dispersion characterization

Graphene dispersions in TEGDA were characterized by UV-Vis and Raman spectroscopy as reported in the previous work.

Characterization of Bis-GMA/TEGDA nanocomposites containing graphene

Thermal analysis on the resins and their nanocomposites were performed by using DSC Q100 Waters TA Instruments calorimeter, equipped with TA Universal Analysis 2000 software. Dried samples were placed in closed 40 mL aluminum crucibles and subjected to two DSC scans from 30 to 300 °C, with a scan rate of 20 °C/min, in inert atmosphere (nitrogen flux: 40 mL/min): the first scan was performed to determine monomer conversion, and the second one was to establish T_g.

The surface morphology of the samples was investigated using a scanning electron microscope (SEM, LEO 1450VP). The specimens (0.5 x 0.5 mm^2) were fractured in liquid nitrogen, fixed to conductive adhesive tapes and gold-metallized.

Compression tests, according to ASTM D695, were performed, using a Zwick-Roll Z010 apparatus, equipped with a 5 kN load cell, at 23 ± 2 °C and 50 ± 5 % relative humidity. At least five tests were repeated for each material to have reproducible and significant data. Standard deviation was always below 5 %. The surface hardness of the samples was measured according to ASTM D2240 (Shore A) at 23 ± 2 °C and 50 ± 5 % relative humidity. At least one measurement at each of five different points distributed over the specimen was performed, using the median of these hardness measurements as the hardness value. Standard deviation was always below 2 %.

VI.9 SYNTHESIS AND CHARACTERIZATION OF NANOCOMPOSITES OF THERMOPLASTIC POLYURETHANE WITH BOTH GRAPHENE AND GRAPHENE NANORIBBON FILLERS

TPU nanocomposites containing graphene and graphene nanoribbons were obtained by polymerizing 1,4-butanediol (BD) with two diisocyanates (namely, 1,6-hexane diisocyanate (HDI) or isophorone diisocyanate (IPDI)), in which the nanofillers were previously dispersed. Raman spectroscopy and TEM analysis were performed to demonstrate the formation of few-layer graphene and graphene nanoribbons dispersed in the monomers. Thermal and rheological behavior of the nanocomposites containing graphene was also investigated.

MATERIALS

BD (MW =90.12 g/mol, d = 1.047 g/mL, Figure VI.10a), HDI (MW = 168.19 g/mol, d = 1.047 g/mL, Figure VI.10b), IPDI (MW = 222.28 g/mol, d = 1.049 g/mL, Figure VI.10c), NMP (MW = 99.13 g/mol, d = 1.028 g/mL), pyrocatechol (PCC, MW = 110.11 g/mol), dibutyltindiacetate (DBTDAc, MW = 351.03 g/mol, d = 1.32 g/mL^{-1}) and graphite flakes (+100 mesh) were purchased from Sigma Aldrich and used as received without further purification.

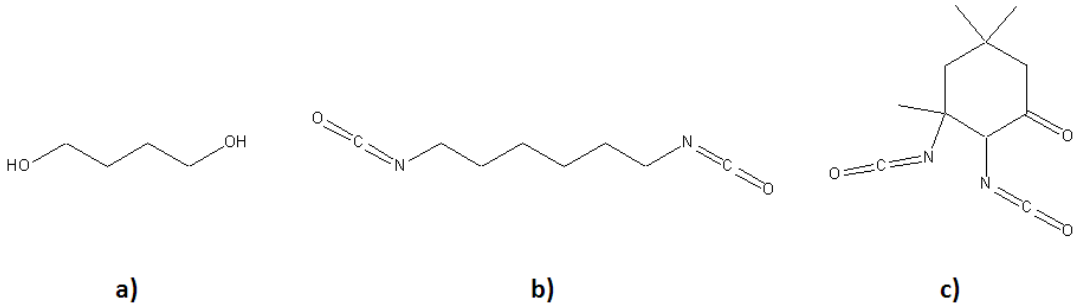

a) b) c)

Figure VI.10 Structures of: a) 1,4-butanediol, b) 1,6-hexane diisocyanate and c) isophorone diisocyanate.

SYNTHESIS

Graphene dispersions

A mixture of diisocyanates or diol (100 mL) and graphite flakes (5.0 wt.-%, 5.0 g) was put into four different tubular plastic reactors (i.d.: 15 mm) and placed in an ultrasonic bath (Emmegi, 0.55 kW) for 24 h, at 40 °C. Then, the reactors were centrifuged for 30 min at 4000 rpm; the gray liquid phase containing graphene was then recovered. The graphene concentrations in BD, HDI and IPDI, calculated by gravimetry after filtration through PVDF filters (pore size 0.22 μm), were 1.1, 1.9 and 3.8 mg/mL respectively.

Synthesis of the polyurethane nanocomposites

The dispersions of graphene were mixed together according to the following molar ratios: diisocyanate/diol (1:1), diisocyanate/ DBTDAc (1:0.01), DBTDAc/PCC (1:30) and diisocyanate/NMP (1:0.1). The mixtures were heated at 70 °C for 1 h, then cooled down to room temperature; finally, the solvent was removed by Soxhlet extraction and the obtained products analyzed.

CHARACTERIZATION

Graphene dispersion characterization

Several dilutions from the second aliquot of the above dispersions were analyzed by UV-Vis spectrometry with a Hitachi U-2010 Instrument (1 cm cuvette). The above gravimetric data allowed us to determine the absorption coefficient: from a known volume of initial dispersion, several dilutions were carried out and the

absorbance at a wavelength of 660 nm was measured.[2-4] Absorbance vs. concentration plots gave the absorption coefficient α.

Raman analyses were performed on graphene flakes obtained after vacuum filtration of the dispersions on PVDF filters (pore size: 0.22 μm), with a Bruker Senterra Raman microscope, using an excitation wavelength of 532 nm at 5 mW. The spectra were acquired by averaging 5 acquisitions of 5 s with a x50 objective.

TEM studies were performed on a JEOL JEM-1011 or a Libra 200 FE OMEGA, working with an accelerating voltage of 100 or 200 kV, respectively. Samples were prepared by dropping 20 mL of dispersion onto carbon-coated 400 mesh copper grids (15-25 nm carbon layer thickness, Ted Pella Inc.), and analyzed after solvent evaporation under vacuum at room temperature for 1 h. TEM images were also analyzed to evaluate the percentage of nanoribbons, i.e. graphene (planar) structures with a large aspect ratio, which may also be partially rolled up, in a series of at least 10 images per sample. Even though the total area covered by such number of images is very small to carry high statistical significance, it was sufficient to enlighten the presence of approximately a half of the few layers of graphene sheets with a large aspect ratio into the HDI/graphene dispersions. Ultrathin sections (nominal thickness of 80 nm) of polyurethane systems were cut at -80 °C using a Leica Ultracut UCT microtome with an EM-FCS cryo kit equipped with a diamond knife, and collected onto formvar-coated copper grids.

Graphene-containing TPU nanocomposite characterization

A Fourier transform infrared (FT-IR) spectroscope (JASCO FT 480 spectrometer) was used for recording the FT-IR spectra of the samples. The powders were ground into a dry KBr disk and 32 scans at a resolution of 4 cm^{-1} were used to record the spectra.

DSC measurements on the TPUs and their nanocomposites were performed by means of a Q100 Waters TA Instruments calorimeter, equipped with a TA Universal Analysis 2000 software. Two heating ramps, from 80 to 250 °C, with a heating rate of 10 °C min^{-1}, were carried out on dry samples: the first scan was performed to remove eventual residual solvent and to assess the extent of monomer conversion, while the second one was to establish T_g.

The rheological measurements were carried out on a strain-controlled rheometer (ARES, TA Instruments Inc., Waters LLC) with a torque transducer range of 0.2-2000 gf cm, using a 25 mm parallel plate geometry. The rheometer was equipped with a convection oven in nitrogen to avoid the thermal degradation of the samples. The rheological characterization was performed in frequency sweep tests at 160 °C (frequency ranging from 0.1 to 100 rad s^{-1}). Strain has been chosen in order to have a torque within the sensitivity of the instrument in the linear viscoelastic region. Furthermore, regression lines were used for interpolating viscosity data and giving an indication of the non- Newtonian behavior of the materials. Suitable disk

specimens of the TPUs and their nanocomposites used for the rheological tests were obtained by compression molding at 100 bar and 160 °C.

TEM analyses were also carried out on TPUs and their nanocomposites by using the same condition above described. Ultrathin sections (nominal thickness of 80 nm) of polyurethane systems were cut at -80 °C using a Leica Ultracut UCT microtome with an EM-FCS cryo kit equipped with a diamond knife, and collected onto formvar-coated copper grids.

VI.10 EXFOLIATED GRAPHENE EMBEDDED INTO HIGHLY ORDERED MESOPOROUS TITANIA FILMS WITH ENHANCED PHOTOCATALYTIC ACTIVITY

Graphene - titania mesoporous nanocomposite films with highly ordered porosity are obtained through evaporation-induced self-assembly from a solution containing graphene sheets. The calcination treatment in inert atmosphere was performed in order to remove the templates from the pores and induce crystallization into anatase phase. The films are finally patterned by deep-x-rays lithography to integrate the synthetic pathway with top-down processes.

MATERIALS

1-vinyl-2-pyrrolidone (NVP, MW = 111.14 g/mol , d = 1.04 g/mL, Figure VI.11a), titanium tetrachloride (MW = 189.68 g/mol, d= 1.73 g/mL), block-copolymer pluronic F127 (Figure VI.11b), ethanol (EtOH, MW = 46.07 g/mol , d = 0.789 g/mL), distilled water, and stearic acid (MW = 284.48 g/mol, Figure VI.11c) and graphite flakes (+100 mesh) were purchased from Sigma Aldrich and used as received without further purification. P-type/boron doped, (100) oriented, 400 µm thick silicon wafers (Si-Mat) and 1.2 mm thick silica slides (UV grade form Heraeus) were used as substrates.

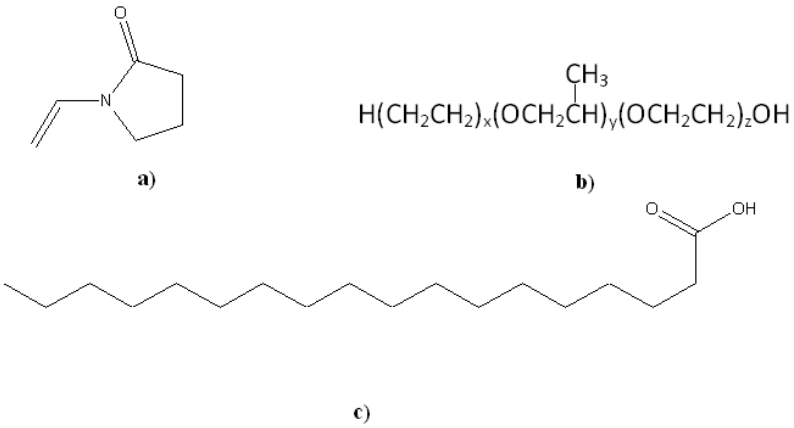

Figure VI.11 Structure of a) NVP, b) pluronic F127 and c) stearic acid.

SYNTHESIS

Sol preparation

A graphene masterbatch dispersion was prepared by dispersing 5 wt.-% graphite flakes in NVP, placed into a tubular plastic reactor (inner diameter 15 mm) and ultra-sonicating it for 24 h at 25 °C (Ultrasound bath EMMEGI, 0.55 kW). Then, the dispersion was centrifuged for 30 min at 4000 rpm and the gray to black liquid phase containing graphene was recovered. The concentration of the graphene dispersion, obtained by gravimetric filtration through polyvinylidene fluoride filters (pore size 0.22 μm), was 2.3 g/mL.

The precursor sol for the deposition of nanocomposite titania films was prepared by adding dropwise 1.1 mL of $TiCl_4$ into a mixture of 23.4 mL of EtOH and 0.65 g of Pluronic F127. After stirring for 15 min at room temperature, 1.8 mL of distilled water was added. The molar ratio of the reagents in the film solution were $TiCl_4$: EtOH : F127 : H2O: = 1 : 40 : 0.005 : 10. As final step, increasing amount of graphene dispersion were added to 2 mL of precursor sol in a volume range from 0 up to 200 μl and the mixture was left under stirring for other 10 minutes before film deposition.

Nanocomposite Film preparation

The nanocomposite titania films were prepared by spin coating 50 μl of solution on 2 x 2 cm^2 monocrystalline silicon and fused silica substrates at relative humidity of 30%. The revolutions per minute was set at 3000 rpm for 40 s followed by 300 rpm for 30 s. After spinning, the as-deposited films were treated in oven at 100 °C for 12 hours. Then, to check the photocatalytic properties, the nanocomposite titania films were fired in a tubular reactor with an argon flux (50 mL/min) with the following heating ramp: from room temperature up to 400 °C with a rate of 10 °C/min, 1 hour at 400 °C, heating up to 450 °C with a rate of 5 °C/min, 2 hours at 450 °C. After this time, the furnace was turned off so that the samples were slowly cooled down to room temperature.

CHARACTERIZATION

Graphene/NVP dispersion characterization

The graphene–NVP masterbatch dispersion was submitted to UV–Vis spectroscopic analysis, using a Hitachi U-2010 spectrometer (1 mm cuvette) and following the method described in the published reports.[2-4] A calibration curve was constructed for the wavelength of 660 nm, to evaluate the molar extinction coefficient of the dispersion (which was found to be equal to 6357 mL/(m mg)) and to determine the graphene concentration in all the diluted dispersions derived from the masterbatch (Figure VI.12).

Raman analyses were performed using a Bruker Senterra Raman microscope with an exciting radiation of 532 nm at 5mW. The spectra were acquired by averaging five acquisitions of 5 s with a x50 objective.

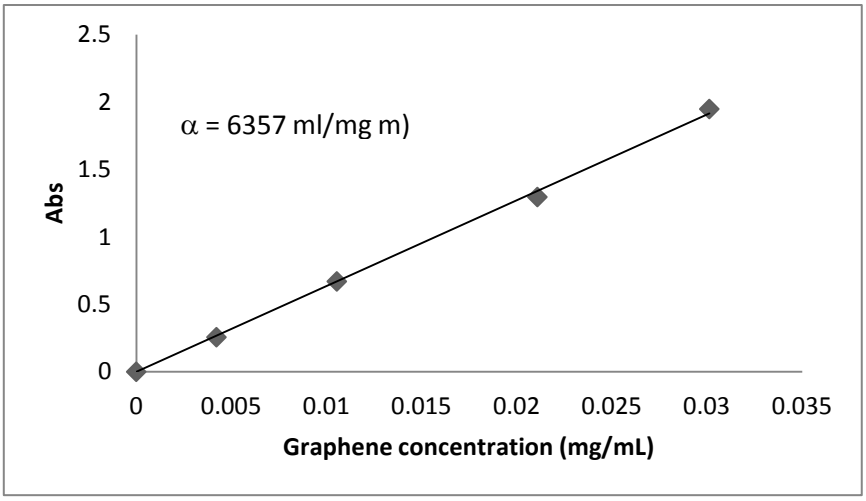

Figure VI.12 Calibration curve for graphene/NVP dispersion.

Graphene- titania mesoporous nanocomposite film characterization

FT-IR measurements were obtained by using a Vertex 70 Bruker spectrophotometer equipped with a RT-DTGS detector and a KBr beam splitter. The spectra were recorded in the 400−4000 cm^{-1} range with a resolution of 4 cm^{-1}, by using a silicon wafer as the background reference. The baseline was corrected using a concave rubber-band method (OPUS 6.5 software) using 64 baseline points and 1 iteration.

Optical properties have been measured by a Nicolet Evolution 300 UV−Vis spectrophotometer and silica glass has been used as background reference.

The film thickness has been estimated by an α-SE Wollam spectroscopic ellipsometry using a fitting model for absorbing films as deduced by UV-Vis characterization. Plots of ψ and Δ as a function of incident wavelength from 400 and 900 nm have been simulated using the "CompleteEASE v. 4.2" software from Wollam. The results of the fits have been evaluated on the basis of the mean squared error (MSE), which was maintained below 9.

XRD patterns of nanocomposite and pure titania films were collected with a Bruker D8 Discover instrument working in grazing incidence geometry with a Cu Kα line (λ = 1.54056 Å); the X-ray generator was set at 40 kV and 40 mA. The patterns were recorded in 2θ ranging from 10 to 100° with a step size of 0.02° and a scan speed of 0.5 s by a repetition mode for 12 h until maximization of the signal-to-noise ratio. The XRD data were analyzed with the MAUD software according to the Rietveld method.

TEM images were obtained by using a JEOL 200CX microscope equipped with a tungsten cathode operating at 200 kV and a JEOL JEM-2200FS microscope, provided with a field emission electron gun and a spherical aberration corrector and operating at 200 kV. Two different sample preparations were used depending on the type of measurements. For general measurements film fragments, scratched from the substrate, were dispersed in ethanol by sonication and then dropped on a carbon-coated copper grid and dried for observations. For cross section measurements, two small plates were prepared by cutting the sample at a

fixed height of the substrate. A roughly mechanical polishing procedure was carried out on all the samples to achieve around 50 μm in thickness: in the direction parallel to the substrate cut for the cross-section sample and in the direction perpendicular to the substrate cut for the planar view sample. Final thinning to electron transparency was achieved by precision ion milling with a JEOL IS (Ion Slicer).

A Bruker Senterra confocal Raman microscope working with a laser excitation wavelength of 532 nm at 5 mW of nominal power was used for Raman characterization. Raman mapping was obtained with a 10x objective and an array of 60 x 30 points was defined to cover an area of 120 x 60 μm^2 with a step of 2 μm. Each spectrum of the map was obtained by averaging 5 acquisitions of 4 s.

Patterning process: After deposition, the nanocomposite films were directly exposed to hard X-rays using the Deep X-ray Lithography beam line (DXRL) at Elettra synchrotron facility (Trieste, Italy). For Raman and FT-IR spectroscopy the films were irradiated with optimized X-ray dose without lithographic mask by changing the exposure time. The energies per unit area incident to the samples surface were 550, 1100 and 2000 J cm^{-2}. The sample for Raman mapping was irradiated with 1100 J cm^{-2} through a test mask. The samples were mounted on the top of a water cooled stainless steel plate (scanner), which was continuously rastering the sample to obtain a homogeneous exposure of areas larger than the beam size, the scanner rate was set to 20 mm s^{-1}. After exposing to X-ray radiation, the sample was dipped in ethanol for around 30 s. Rinsing was done in isopropyl alcohol for 15 s, and finally, the sample was dried with flowing nitrogen to avoid remaining residuals.

Photocatalytic activity measurements: 100 μl of a solution of stearic acid in ethanol were spin-coated of the nanocomposites titania films by applying a speed rate of 1500 rpm for 30 s. The samples were then placed for increasing time (15, 30, 45, 60 and 75 min) under an UV lamp (λ_{ex} = 365 nm, nominal power density of 470 μW cm^{-2} at 15 cm) at a distance of 0.5 cm.

REFERENCES

[1] Mariani, A.; Nuvoli, D.; Alzari, V.; Pini, M. *Macromolecules* 2008, 41, 5191–5196.

[2] Hernandez, Y.; Nicolosi, V.; Lotya, M.; Blighe, F. M.; Sun, Z. Y.; De, S.; McGovern, I. T.; Holland, B.; Byrne, M.; Gun'Ko, Y. K.; Boland, J. K.; Niraj, P.; Duesberg, G.; Krishnamurthy, S.; Goodhue, R.; Hutchison, J.; Scardaci, V.; Ferrari, A. C.; Coleman, J. N. *Nat Nanotechnol* 2008, 3, 563–568.

[3] Lotya, M.; King, P. J.; Khan, U.; De S.; Coleman, J. N. *ACS Nano* 2010, 4, 3155–3162.

[4] Nuvoli, D.; Valentini, L.; Alzari V.; Scognamillo, S.; Bittolo Bon, S.; Piccinini, M.; Illescas, J.; Mariani, A. *J Mater Chem* 2011,21, 3428-3431.

[5] Cranston, E. D.; Gray, D. G. Biomacromolecules 2006, 7, 2522–30.

[6] Alzari, V; Nuvoli, D; Scognamillo, S.; Piccinini, M.; Gioffredi, E.; Malucelli, G.; Marceddu, S.; Sechi, M.; Sanna, V.; Mariani, A. J Mater Chem 2011, 21, 8727–8733.

CHAPTER VII

RESULTS AND DISCUSSION

VII. 1 POLYMER HYDROGELS OF 2-HYDROXYETHYL ACRYLATE AND ACRYLIC ACID OBTAINED BY FRONTAL POLYMERIZATION

The aims of this work were to prepare homopolymer and copolymer hydrogels of HEA and AAc by using FP as an alternative, easy and cheap synthetic technique, and to study their swelling behavior at various pH values. PAAc is one of the most studied pH-responsive polymer systems: it generally swells at neutral and high pH and deswells in acid condition. Poly(2-hydroxyethyl acrylate), PHEA, was used as hydrophilic component because of its high hydrophilicity: it is able to form hydrogen bonds with water and with polymer having carboxylic groups.
The obtained copolymer materials were characterized and compared in terms of thermal properties, swelling behavior and morphology.

First of all, the influences exerted by all components on the synthetic and morphological characteristics were investigated. Samples were prepared by varying the ratio between AAc and HEA, and keeping constant all the other parameters such as the total molar amount of the two monomers (6.96 x 10^{-2} mol), the amounts of initiator and of crosslinker (5 mol % and 1 mol % referred to the total amount of the two monomers, respectively). All samples were obtained with high conversion, always included between 90 and 96% (Table VII.1).

Table VII.1 Compositions, conversions and Tg values of the polymer samples prepared in this work.

Sample code	χAAc	T_g (°C)	Conversion (%)
FP1	0	13.0	96
FP2	0.25	71.0	92
FP3	0.50	155	90
FP4	0.75	168	96
FP5	1.0	135	96

In Figure VII.1, the values of the front temperatures and velocities as functions of the molar fraction of acrylic acid (χAAc) are reported. It can be noticed that the front temperatures exhibit a trend characterized by a maximum: they range from 278 °C for the homopolymer of HEA (FP1) to 214 °C for the PAAc (FP5),

with a maximum value of 296 °C corresponding to the copolymer having χAAc = 0.50. As far as the front velocities are concerned, they increase from 4.00 to 10.8 cm/min for the samples having a molar fraction of AAc included between 0 and 0.75 (FP1-4), whereas PAAc (FP5) shows a front velocity of 3.90 cm/min. Moreover, all the samples show high front velocities with their maximum value (10.8 cm/min) recorded for the sample having χAAc = 0.75 (FP4). It should be also highlighted that 10.8 cm/min is one of the highest V_f values reported so far in the FP literature.[1,2]

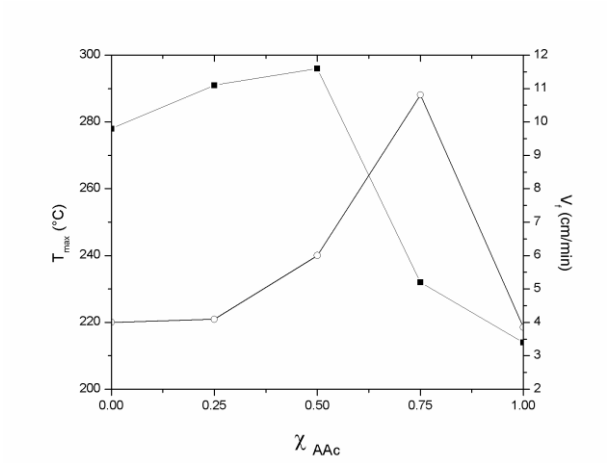

Figure VII.1 T_{max} (■) and V_f (○) as functions of the molar fraction of AAc in the poly(AAc-co-HEA) copolymers.

As reported in the Experimental part, the swelling studies on the copolymer hydrogels at different pH were done by immersing any sample into buffer solutions at various pH (1–13), until they achieved the equilibrium. As can be seen in Figure VII.2, the swelling ratio of all the samples remains almost constant along all the pH range included between 1 and 5 (SR% is always around 100–200%). Instead, due to the deprotonation reaction and the subsequent electrostatic repulsion among COO^- groups, from pH 6 to 8, the swelling ratio of the hydrogels starts to increase up to values that are higher for the hydrogels containing larger amounts of AAc. For instance, at pH 8, the SR% goes from 230%, for the hydrogel with χAAc = 0.25 (sample FP2), to 260%, for the sample with a molar fraction of AAc equal to 0.75 (FP4). Moreover, at pH around 12–13, apart from the very large SR% reached by the AAc and HEA homopolymers (1200% and 1400%, respectively), the swelling ratio of the copolymers reached the maximum values of 600–720% due to alkoxylate group formation. To check whether such a large increase might be due to the occurrence of partial hydrolysis (mainly because of the presence of TEGDA ester groups), all samples allowed to swell at the highest pH values (12–13) were successively equilibrated at pH = 7 (not shown). In all cases, the SR% was almost equal (610%) to that of the same sample previously swollen at this latter pH, thus indicating that no significant hydrolysis occurred. The above results suggest classifying these polymer hydrogels among those exhibiting a pH responsive behavior, with two critical pH values: one at about 6 and the second at about 11–13, depending on their composition (Figure VII.2).

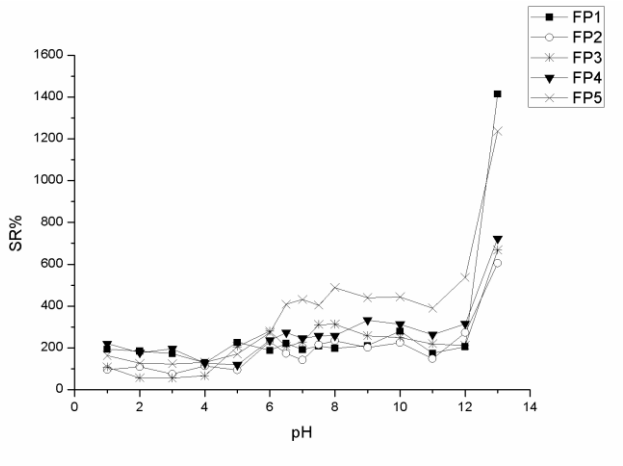

Figure VII.2 SR% as function of pH for samples having a different monomer ratio.

In Figure VII.3, the glass transition temperatures of all samples after swelling at pH 2 and pH 12 and successively dried are reported together with those of the samples which did not undergo any swelling treatment.

First of all, it can be seen that the recorded T_g for the non-treated samples tend to increase with the amount of AAc from 13.0 °C for the homopolymer of HEA up to a maximum at 168 °C for the sample having χAAc = 0.75, and then to decrease again to 135 °C for the AAc homopolymer. As one may expect, this behavior is qualitatively similar to that of the series comprising the samples swollen at pH 2. Indeed, because these copolymers are characterized by the presence of acid protons, they were not influenced by the treatment at low pH. However, the T_g values of these materials are generally lower than those of the non-treated materials probably because of the presence of residual water, which might have some plasticizing effect.

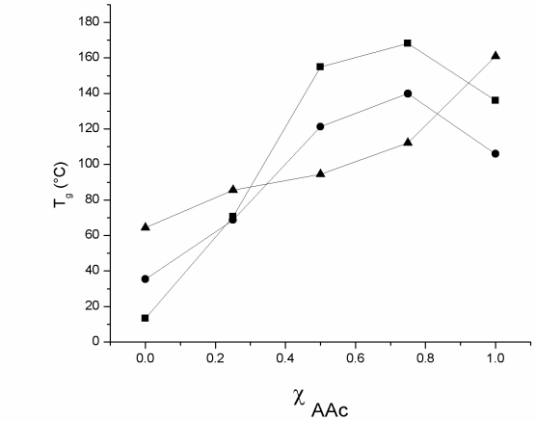

Figure VII.3 T_g of the non-treated samples (■), dried samples after swelling at pH 2 (●) and dried samples after swelling at pH 12 (▲) as functions of the molar fraction of AAc.

By considering the series of samples which were dried after swelling at pH 12, it can be noticed that the glass transition temperature monotonically increases with the molar fraction of AAc from 64.0 to 161 °C, thus clearly confirming that the presence of an increasing amount of carboxylate groups enhances the interactions among the macromolecular chains, thus reducing the general mobility.

The morphological characteristics of the obtained hydrogels were investigated by SEM analysis (Figure VII.4). By comparing the 1:1 AAc-HEA copolymer with the corresponding homopolymers, all swollen at pH 2 (respectively: b_2, a_2 and c_2 images in Figure 4), it can be noticed that both the HEA homopolymer and the copolymer are characterized by a hydrogel structure with relatively large pores, whereas the AAc homopolymer has pores having much smaller dimensions. This finding is in agreement with the relatively larger SR% found for this sample at this pH value. Indeed, as we reported in our previous work on thermoresponsive polymer hydrogels, the smaller the pore dimension is, the larger SR% is.[3] Quite surprising, the discussed pore structure is not held at pH 12. Namely, in these conditions, all hydrogels exhibit a much denser and more compact aspect. However, again, the lack of relatively large pores results in an increase of the swelling ratio.

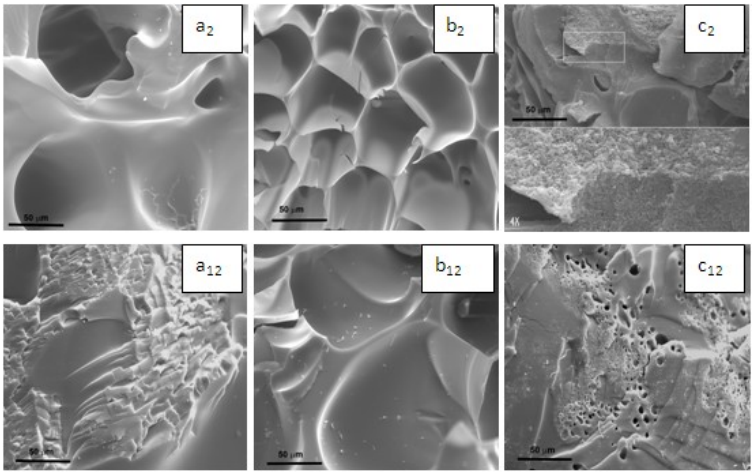

Figure VII.4 SEM micrographs of: a) PHEA (sample FP1); b) poly(AAc-co-HEA) (sample FP2); c) PAAc (sample FP5), swollen at pH 2 (a_2,b_2,c_2) and swollen at pH 12 (a_{12}, b_{12}, c_{12}).

In conclusion, homopolymers and copolymers of AAc and HEA were successfully prepared by FP. As expected, it was found that both T_{max} and V_f are dependent on the ratio between the monomers. The front temperatures range from 278 °C for the homopolymer of HEA to 214 °C for the PAAc, with a maximum value of 296 °C corresponding to the copolymer having χAAc = 0.50. It is noteworthy that all the samples show high front velocities with the maximum value of 10.8 cm/min recorded for the sample having χAAc = 0.50, which is one of the highest values reported so far in the FP literature. The obtained materials were allowed to swell in aqueous solutions at different pH values. The resulting hydrogels were found to exhibit

a pH-responsive behavior at two critical values located at pH ≈ 6 and ≈ 11–13, respectively, depending on the composition.

VII.2 ORGANIC-INORGANIC IPNs AND HYBRID POLYMER MATERIALS PREPARED BY FRONTAL POLYMERIZATION

In this work, novel polyacrylamide-based hydrogels containing 3-TMeOSi and/or TEtOSi, were obtained by means of FP, using AmPS as initiator, BIS as crosslinking agent and DMSO as solvent. The obtained materials are both organic-inorganic IPNs and hybrid polymer at the same time. Hybrid hydrogels are referred to systems that possess organic polymers and inorganic moieties, covalently interconnected. IPNs are a class of polymer blends that can be defined as a combination of two (or more) polymers in a network form, in which one is synthesized or cross-linked in the presence of the other(s).
The samples were submitted to swelling studies at two different pH (2 and 5). The occurrence of this reaction was assessed by solid state NMR. Moreover, the corresponding dried materials were characterized by thermal and morphological analyses and their contact angles were measured.

Two different series of samples were synthesized: the first one deals about the obtainment of composite materials by the frontal polymerization of AAm and TEtOSi; the second one pertains the frontal copolymerization of AAm and 3-TMeOSi in the presence TEtOSi, thus leading to the obtainment of hybrid composite materials.

Frontal polymerization of AAm and TEtOSi: obtainment of composite materials
In this series of experiments, samples composed of PAAm and TEtOSi, were prepared. This latter compound was chosen in that it is able to undergo sol-gel reaction in acidic conditions.[4,5] It should be noticed that, after the latter condensation reaction, a composite material is obtained, which is constituted of an organic polymer matrix and crosslinked silica as inorganic filler, not directly linked to each other. Moreover, since after sol-gel reaction both AAm and TEtOSi give rise to crosslinked structures, the resulting materials can be classified as organic-inorganic interpenetrating polymer networks.
The effect of the concentration of TEtOSi (which was allowed to range from 0 to 3.5 mol%) on the main FP parameters (V_f and T_{max}) was studied by keeping constant the amounts of BIS (0.25 mol%) and AmPS (0.50 mol%) as the radical initiator (all concentrations are referred to the amount of AAm). As can be seen in Table VII.2, V_f increases with TEtOSi concentration from 3.8 to 5.9 cm/min. However, since the samples containing 0 and 3.5 mol% TEtOSi underwent evident degradation due to the excessive front temperature (ca. 220 °C), the following research was focused on the hydrogels having 0.35, 0.70 and 1.7 mol% of TEtOSi, only.

Table VII.2 Experimental data for the FP of AAm/TEtOSi hydrogels prepared in this work.

Sample	TEtOSi (mol%)	BIS (mol%)	V_f (cm/min)	Tmax (°C)	T_g (°C)
A1	0	0.25	3.8	220	226
B1	0.35	0.25	4.0	202	243
C1	0.70	0.25	4.4	192	246
D1	1.7	0.25	4.8	209	252
E1	3.5	0.25	5.9	221	255

Frontal copolymerization of AAm and 3-TMeOSi in the presence TEtOSi: obtainment of hybrid composite materials

These materials contain a constant amount of AAm, which was copolymerized with 3-TMeOSi in the presence of TEtOSi. The concentration of these two latter compounds was allowed to vary by taking into account that the subsequent sol-gel condensation reaction may involve from one to four Si linkages of TEtOSi. For such a reason, the molar ratio between TEtOSi and 3-TMeOSi was varied from 1 to 4.

In Table VII.3, results from three different sets of hybrid copolymers are presented. In the first series (B1-B5), containing 0.35 mol% of TEtOSi, the molar fraction of the comonomer 3-TMeOSi was varied from 0 to 1.4 mol%. In these samples V_f ranged from 3.5 to 5.4 cm/min. In the same interval of concentrations, T_{max} ranges from 202 to 225 °C.

The second series (C1-C5) collects polymers containing 0.70 mol% of TEtOSi and 3-TMeOSi in concentration from 0 to 2.8 mol%. V_f increases from 4.4 to 5.8 cm/min and T_{max} values range from 192 to 211 °C. However, while front velocity increases monotonically with 3-TMeOSi, T_{max} drops down in correspondence of its highest concentration (182 °C; 2.8 mol%).

In the third series (D1-D5), data of samples containing 1.7 mol% of TEtOSi and 3-TMeOSi ranging from 0 to 6.9 mol% are grouped. V_f and T_{max} were found to vary from 3.0 to 5.7 cm/min and from 208 to 225 °C, respectively, without any apparent relation with the ratio between TEtOSi and 3-TMeOSi.

Table VII.3 Experimental Data obtained for the FP of AAm, TEtOSi and 3-TMeOSi.

Sample	TEtOSi (mol%)	[3-TMeOSi]/[TEtOSi] (mol%)	V_f (cm/min)	T_{max} (°C)	T_g (°C)
B1	0.35	0	4.0	202	243
B2	0.35	1	5.4	216	245
B3	0.35	2	4.2	215	243
B4	0.35	3	4.1	210	247
B5	0.35	4	3.5	225	242
C1	0.70	0	4.4	192	246
C2	0.70	1	4.9	208	265
C3	0.70	2	5.3	209	256
C4	0.70	3	5.6	211	237
C5	0.70	4	5.8	192	257
D1	1.7	0	4.8	209	252
D2	1.7	1	3.0	208	275
D3	1.7	2	4.2	225	264
D4	1.7	3	5.7	211	272
D5	1.7	4	3.7	208	283

All samples were allowed to swell at pH 2 and 5 and the swelling behavior of the resulting hydrogels was studied. In order to achieve the conversion of organo-silane to Si-OH groups, by sol-gel reaction, acidic conditions were used.

In Figure VII.5, the swelling ratio of the hydrogels made of AAm and TEtOSi as a function of time is reported for the first 2880 min (48 h). The equilibrium swelling for both pH values has been achieved approximately after 24 h. As can be seen, after reaching the equilibrium, SR% was always comprised between ca. 2000 and 2700 % (pH 5, Figure VII.5a) or between ca. 1400 and 2200 % (pH 2, Figure VII.5b). This difference may be imputable to a larger conversion of the silane groups when stronger acidic conditions are used,[4,5] they resulting in a more compact crosslinked structure.

Furthermore, in both series the increasing of the TEtOSi content results in an initial increase of SR%, which is then followed by a decrease down to values that are even lower than that of the neat polymer hydrogel.

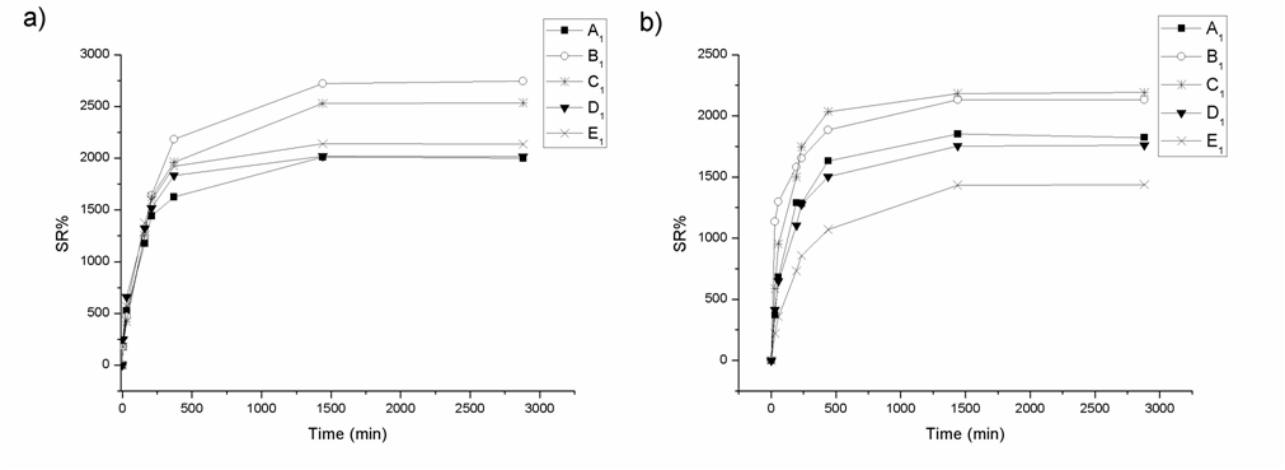

Figure VII.5 SR% as a function of time for the samples swollen at pH 5 (a) and pH 2 (b).

When TEtOSi is dispersed in the 3-TMeOSi/AAm copolymer instead of PAAm, SR% changes. Figure VII.6 shows the resulting trend as a function of the 3-TMeOSi concentration. TEtOSi was kept constant and equal to 0.35 mol % (Figure VII.6a) or 0.70 mol% (Figure VII.6b); moreover, data refer to samples swollen at pH 2 and pH 5. As expected, because of the sol-gel crosslinking, in all cases the swelling ratio decreases as the amount of 3-TMeOSi increases. However, similarly to what mentioned above, since at pH 2 the efficiency of such a reaction is higher,[4,5] samples allowed swelling in stronger acidic conditions swell less than the others.

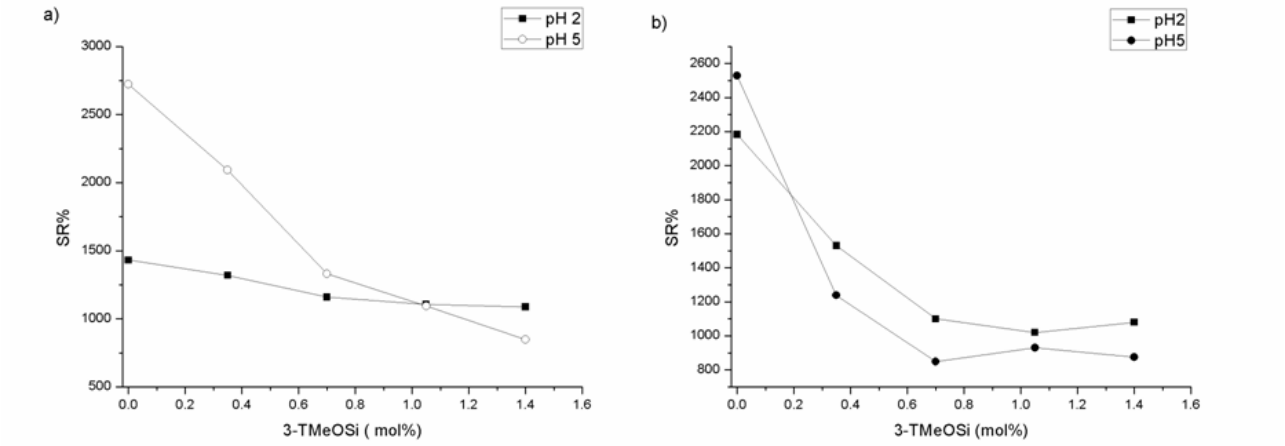

Figure VII.6 SR% as a function of the molar amount of 3-TMeOSi for the samples swollen at pH 2 and pH 5: a) [TEtOSi] = 0.35 mol%; b) [TEtOSi] = 0.70 mol%. Data are taken at equilibrium conditions, after 48 h.

The clear confirmation of these results came from the ^{29}Si CP/MAS NMR experiments. The pertinent results of the samples swollen at pH 2 and pH 5 are reported in Figure VII.7.

Either spectra show three partially overlapping signals in the region between -40 to -70 ppm related to the silane organic moieties incorporated as a part of the silica wall structure. According to the literature, they

are assigned to T1 [$SiC(OH)_2(OSi)$] (-46 ppm), T2[$SiC(OH)(OSi)_2$] (-56 ppm) and T3 [$SiC(OSi)_3$] (-66 ppm) groups.[6,7]

In particular, the spectrum of the sample swollen at pH 2 shows an intense signal attributed to T3 (-66 ppm), a smaller signal attributed to T2 (-56 ppm) and a very small signal attributed to T1 (-46 ppm). This indicates a higher degree of condensation and crosslinking and means that most of silicon atoms do not have any free hydroxyl group. This spectrum shows also a signal at -101 ppm, ascribed to a Q3-type crosslinker moiety [$Si(OSi)_3(OH),$], indicating the presence of a small fraction of silica that is not involved in the bond with adjacent tetrahedral units.[8]

The sample swollen at pH 5 shows T1 (-36 ppm) and T2 signals (-56 ppm) that are more intense than the T3 one (-66 ppm). The presence of a higher concentration of free hydroxyl groups, resulting from T1 and T2 units, indicates a lower degree of condensation and crosslinking compared to the sample swollen at pH 2.

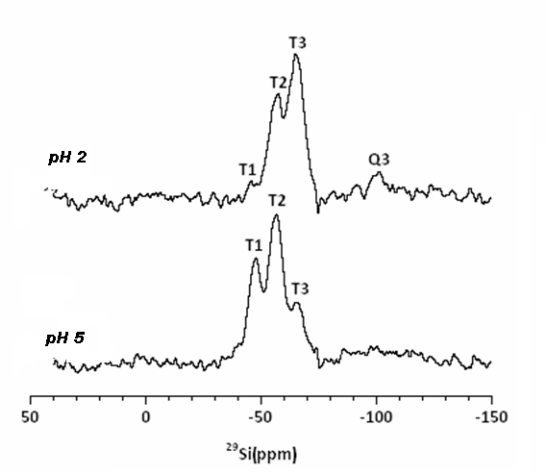

Figure VII.7 ^{29}Si CP/MAS NMR spectra for the samples D5 swollen at pH2 and pH5.

Furthermore, the thermal properties of the obtained polymer samples were evaluated by DSC. Conversion was determined by the following equation:

$$C\% = \left(1 - \frac{\Delta H_r}{\Delta H_t}\right) \cdot 100$$

Where ΔH_r (residual) is the peak area obtained for the residual polymerization occurred during the first thermal scan, and ΔH_t (total) is the area under the curve when the polymerization was carried out in the DSC instrument. Conversion was always comprised between 90 and 95%.

As far as the T_g values is concerned (Tables VII.2 and VII.3), these were in the range of 226-283 °C, depending on the TEtOSi and 3-TMeOSi concentrations. In particular, as expected PAAm is characterized by the lowest T_g value, located at 226 °C (sample A1). Indeed, the addition of TEtOSi results in its significant

increase to 243 °C for the sample containing 0.35 mol% of this filler; further addition gradually increases T_g up to the value of 255 °C for the sample containing 3.5 mol% TEtOSi (sample E1).

The glass transition temperature of the hybrid samples is also strongly affected by the presence of Si; in fact, as a general trend, the higher its content is, the higher T_g is. Moreover, a significant effect is due to the crosslinking extent; indeed, as can be seen by comparing samples containing different amounts of TEtOSi, the larger its amount is, the higher T_g is. For example, by comparing samples having [3- TMeOSi] / [TEtOSi] = 4 it goes from 242 °C when TEtOSi is equal to 0.35 mol% (sample B5) to 283 °C when TEtOSi is 1.7 mol% (sample D5).

As far as the thermo-oxidative stability of the hydrogel is considered, TGA analyses in air were performed. Table VII.4 collects the obtained values, referring to T_{10} (i.e. the temperature, at which the sample loses 10% mass) residue. It is noteworthy that the samples that did not undergo any acidic treatment, which is necessary to induce the sol-gel synthesis, exhibited a thermal stability that was even lower than that of the neat polymer matrix.

At variance, all samples treated at pH 2 and 5 are characterized by a T_{10} higher than that of neat sample; namely, from 196 to 245 °C, even if the corresponding trend is not well defined.

This is a further confirmation that the sol-gel reaction is promoted during the swelling process.

The morphological structures of the PAAm/TEtOSi composite hydrogel and the hybrid composite hydrogel containing 3-TMeOSi were investigated by SEM. The analyses were carried out on samples treated at pH 2 and pH 5, but micrographs did not show any significant difference among them. Therefore, it can be concluded that pH does not influence the hydrogel structure, at least at this level. This is also confirmed by what shown in Figure VII.8, which is a comparison between the cross-sectional SEM images of the composite (sample E1, Figure VII.8a) and the hybrid hydrogel (sample D5, Figure VII.8b).

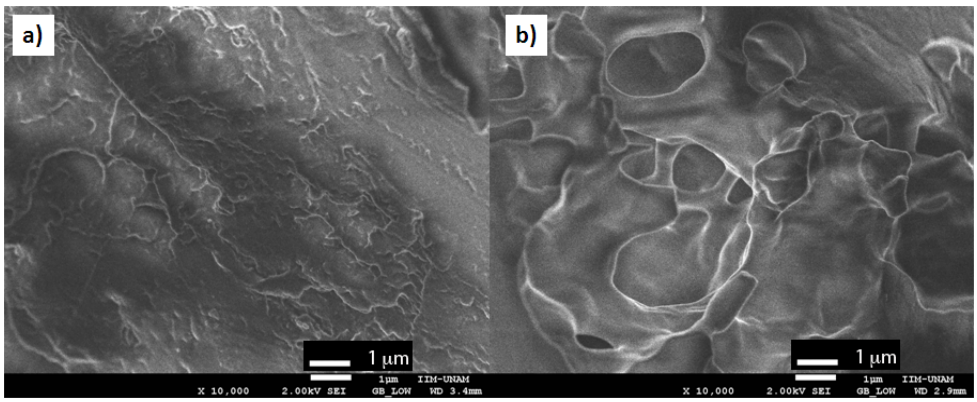

Figure VII.8 SEM images at pH 5 of: a) cross-sectional PAAm-TEtOSi hydrogel (sample E1) and b) cross-sectional PAAm-TEtOSi-3TMeOSi hybrid composite (sample D5), having the highest Si content.

Table VII.4 TGA data of the obtained samples.

Sample Code	% Si (w/w)	T_{10} (°C)
A1	0	183
B1	0.133	149
C1	0.263	130
D1	0.634	152
B5	0.638	163
C5	1.21	155
D5	2.59	197
B1[a]	0.133	196
C1[a]	0.263	203
D1[a]	0.634	192
B5[a]	0.638	221
C5[a]	1.21	245
D5[a]	2.59	222
B1[b]	0.133	198
C1[b]	0.263	233
D1[b]	0.634	217
B5[b]	0.638	196
C5[b]	1.21	232
D5[b]	2.59	219

[a] sample swollen at pH 2
[b] sample swollen at pH 5

Finally, WCA data as a function of the total Si amount are shown in Figure VII.9. It is evident that, if the Si percentage in the hydrogels is increased, for both the series of samples swollen in solutions of pH 2 and 5, the contact angle diminishes, thus accounting for an increased hydrophilicity. It is also noteworthy that WCA values of the samples swollen at pH 2 is slightly lower than those swollen at pH 5, thus confirming that stronger acidic conditions result in a larger hydrolysis extent.[4,5]

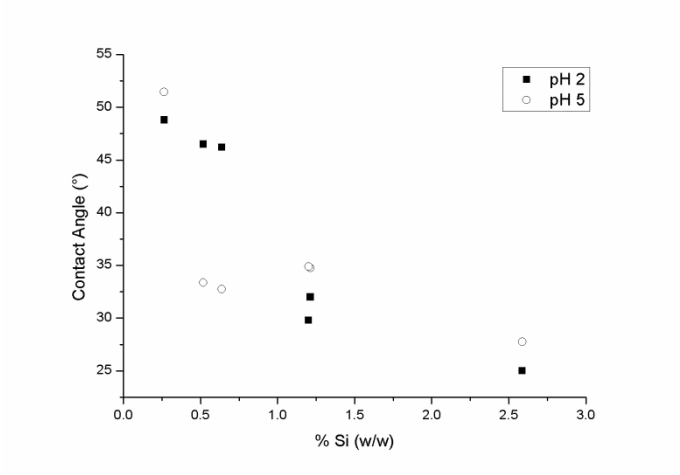

Figure VII.9 WCA for hybrid hydrogels having different amount of silica and swollen at pH 2 (■) and pH 5 (○).

In conclusion, hybrid and composite IPN hydrogels of PAAm were successfully synthesized through the frontal polymerization technique.

In the composite hydrogel, the increasing of the TEtOSi content results in an initial increase of SR% in water, which is then followed by a decrease down to values that are even lower than that of the neat polymer hydrogel.

At variance, in the hybrid system the swelling ratio decreases as the amount of 3-TMeOSi increases.

In both systems, it was found that, when the swelling experiments were carried out at pH 2, the SR% was less than what found at pH 5. This finding is due to a larger conversion of the silane groups when stronger acidic conditions are used,[4,5] which results in a more compact crosslinked structure. This statement was also confirmed by ^{29}Si CP/MAS NMR experiments, which evidenced the different extent of the sol-gel reaction. Finally, by contact angle characterization, it was found that an increment of Si into hydrogel structure increases the hydrophilicity of the materials.

VII.3 MULTI*STIMULI*-RESPONSIVE HYDROGELS OF POLY(2-ACRYLAMIDO-2-METHYL-1-PROPANESULFONIC ACID) CONTAINING GRAPHENE

In the present study, nanocomposite polymer hydrogels of PAMPSA, containing graphene as nanofiller were prepared by radical polymerization.

In particular, neat PAMPSA hydrogel is a very interesting and widely studied system: it is a superabsorbent and *stimuli*-responsive polymer material, which is able to change its size and shape as a function of pH, ionic strength, and electrical field. Graphene was obtained through an easy and convenient method lately developed by our research group, which consists in the exfoliation of graphite by sonicating it in a proper solvent medium. In this case, DMF was chosen as dispersing medium of graphene. The resulting dispersion

was directly used for the synthesis of the nanocomposite hydrogels: in fact, DMF acts both as dispersing medium of graphene and as solvent for AMPSA. The swelling behavior of the obtained nanocomposites in response to ionic strength and electrical *stimuli* was investigated. Moreover, the influence of graphene amount on their swelling properties and their morphological features was studied.

First of all, graphene dispersion in DMF was analyzed by UV-Vis spectroscopy; in particular, the absorbance at different graphene concentrations was registered, and the calibration curve of the dispersion was obtained (Figure VII.10). The system exhibits Lambert–Beer behavior, with an absorption coefficient of 2498 mL mg^{-1} m^{-1} and a concentration of graphene, calculated by gravimetry, equal to 0.35 mg/mL.
Then, graphene dispersion in DMF was subjected to Raman analysis with the aim to confirm the presence of graphene itself and to determine the number of graphene layers. In fact, such technique allows an unambiguous distinction among single layer, bi-layer, and multilayer graphene.[9] This is possible through a comparison of the relative intensity of the characteristics G peak (at ~1580 cm^{-1}) and 2D peak (at ~2700 cm^{-1}) and by the symmetry of the 2D peak in the Raman spectra. The Raman spectrum of graphene obtained by filtration of its dispersion in DMF, compared with that of graphite (Figure VII.11), shows that the 2D peak of graphite is made of two components; by contrast, the peak of graphene is symmetric, and its shape and position suggest that the sample under examination is constituted of few-layer graphene.[10] The disorder related D peak at ca. 1350 cm^{-1} is present also in the pristine graphite powder, but its intensity is higher for graphene; this finding is in agreement with what reported in the literature in those cases in which graphene was produced by sonication of graphite and can be attributed to the new edges produced during the sonication process; the ultrasonic treatment causes the decrease in size of the flakes compared to the original graphite, with a consequent increase of the total edge length.[11,12]

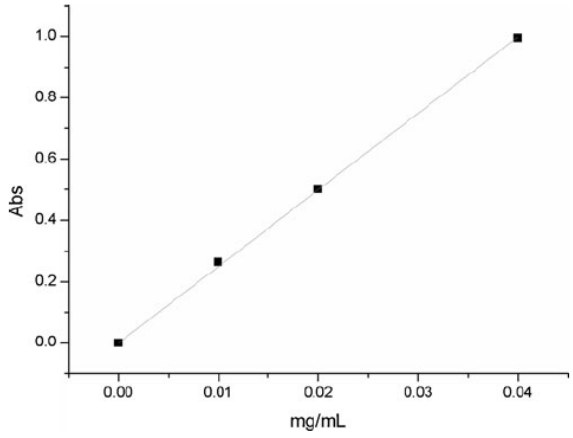

Figure VII.10 Optical absorbance (660 nm) as a function of graphene concentration in DMF. The Lambert–Beer behavior is exhibited, with an absorption coefficient of 2498 mL mg^{-1} m^{-1}.

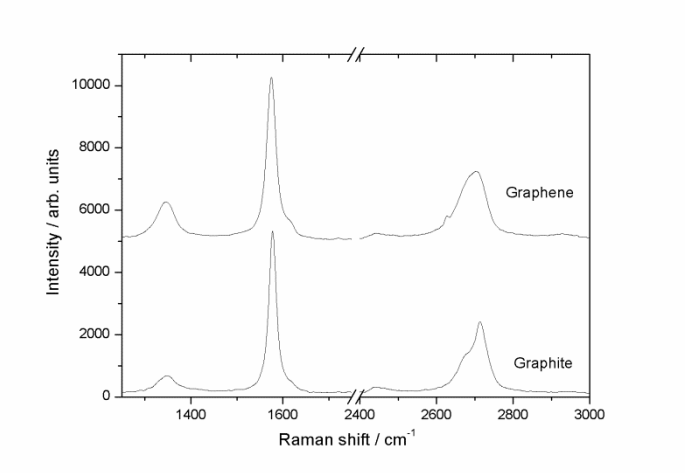

Figure VII.11 Raman spectra of graphene obtained from DMF dispersion (top line) and graphite (bottom line).

TEM analysis is usually employed for the investigation of graphene dispersions.[13-15] As shown in Figure VII.12, the micrographs evidence the formation of few-layer graphene. In particular, well-defined graphene sheets are clearly visible. It should be underlined that in all cases, graphite aggregates were not observed.

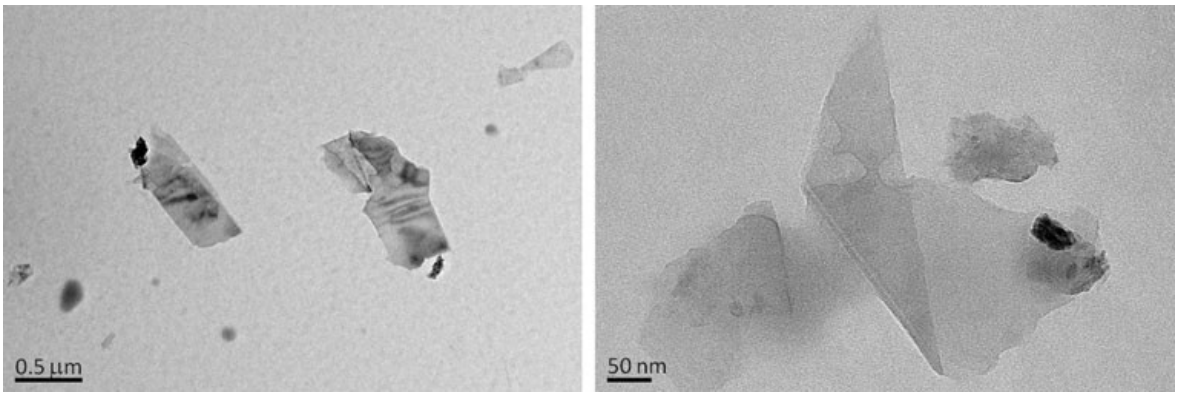

Figure VII.12 TEM images of some graphene sheets (from the stock DMF/graphene dispersion diluted 1:10).

Once confirmed the obtainment of graphene, the above dispersion in DMF were employed for the synthesis of several nanocomposite hydrogels of PAMPSA, having a graphene amount ranging from 0.01 to 0.06 wt.-% respect to the monomer weight (see Table VI.2 in the Experimental Part).

Afterwards, the resulting hydrogels were subjected to swelling studies at varying of ionic strength and of the applied electric field. In addition, the influence of graphene on these properties was investigated, in terms of emphasis or reduction of the SR% as a function of these two stimuli. Various experiments were performed, in which only one of the above parameters was varied at once, while the others were kept constant.

The influence of ionic strength on SR% was studied by keeping the pH value constant and equal to 3, which is the natural pH of the aqueous medium resulting from the immersion of the hydrogels. For this

experiment, two different salts were used—KNO_3 and $Ca(NO_3)_2$. They were chosen in order to investigate the different effects of a mono- or bivalent cation on the hydrogel swelling properties.

By using KNO_3, the ionic strength was varied from 0 to 0.1 M. The SR% decreases as the ionic strength increases, as shown well in Figure VII.13. The swelling behavior mainly depends on the diffusion of the ions and the fluid. By adding salt, a gap in the ionic concentration is created between the interior hydrogel and the external solution. The osmotic pressure due to the ionic concentration gap drives the ions to move from the solution into the hydrogel, in order to eliminate this concentration difference and to reach a dynamic equilibrium. This is achieved when the driving force is balanced by the elastic one; in consequence, the hydrogel shrinks.[16]

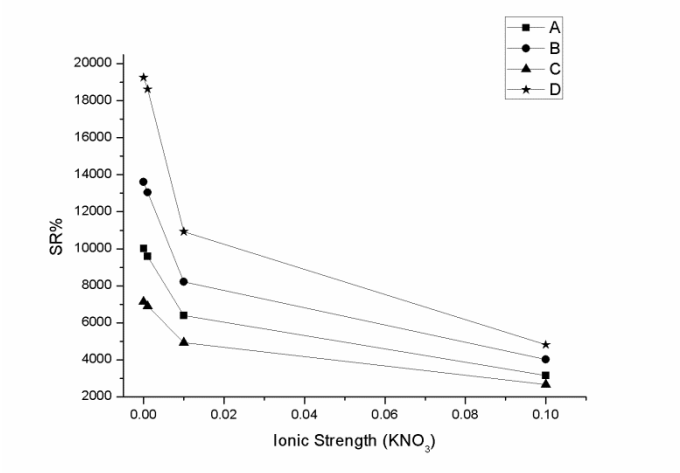

Figure VII.13 SR% as a function of ionic strength for different graphene amounts (KNO_3 solution, sample A = 0 wt.-% of graphene, sample B = 0.01 wt.-% of graphene, sample C = 0.02 wt.-% of graphene, sample D = 0.06 wt.-% of graphene).

The introduction of graphene within the hydrogel matrix does not influence the shrinking of hydrogels with increasing the ionic strength, but allows the materials swelling more than the filler-free hydrogel, up to a minimum threshold value. As can be seen from the Figure VII.13, at ionic force zero the samples having the lowest amount of graphene (sample B and C) show a swelling behavior not particularly influenced by the presence of the nanofiller. On the contrary, SR% undergoes a drastic enhancement when the graphene concentration was about 0.06 wt.-% (sample D). This finding might be attributed to the presence of graphene sheets that separate close macromolecular chains, thus reducing the cross-linking extent.[17]

Since a bivalent cation as Ca^{2+} can complex the hydrogel stronger than what K^+ can do, by using a solution of $Ca(NO_3)_2$, the hydrogels deswell more as the salt content raised; for such a reason, the influence of graphene on SR% is less pronounced (Figure VII.14), and the samples had approximately the same swelling capacities regardless of the graphene content.

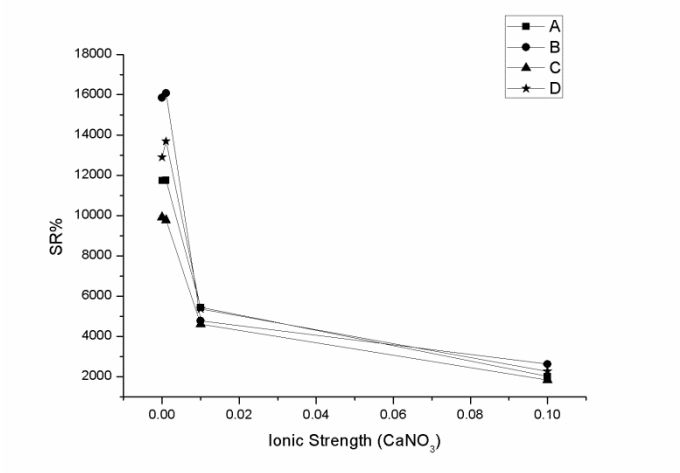

Figure VII.14 SR% as a function of ionic strength for different graphene amounts ($Ca(NO_3)_2$ solution, sample A = 0 wt.-% of graphene, sample B = 0.01 wt.-% of graphene, sample C = 0.02 wt.-% of graphene, sample D = 0.06 wt.-% of graphene).

As can be seen in Figure VII.15, PAMPSA hydrogels exhibit a variation of their size in response to a variation of an external electrical field. This type of behavior is due to a migration of the cations present inside the hydrogel toward the cathode, thus resulting in a partial shielding of the sulfonate group, which causes the decrease of gel hydration.[18] So, the hydrogels deswell with increasing the applied voltage (from 5 to 30 V).

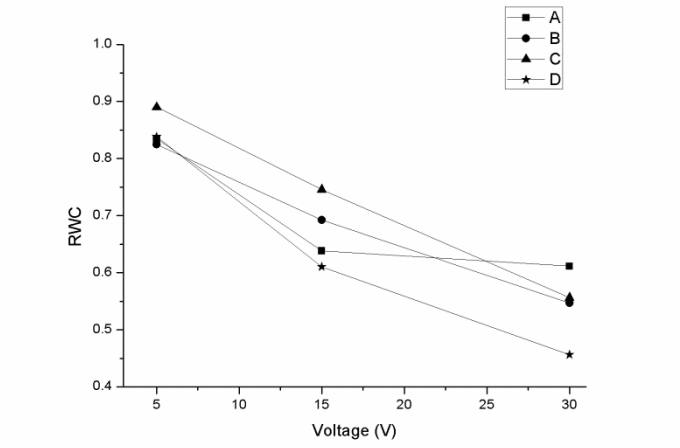

Figure VII.15 RWC of hydrogels as a function of the voltage applied for different graphene amounts (sample A = 0 wt.-% of graphene, sample B = 0.01 wt.-% of graphene, sample C = 0.02 wt.-% of graphene, sample D = 0.06 wt.-% of graphene).

As reported in the literature for polyelectrolyte hydrogels, the extent of deswelling increases with the magnitude of the electric field but is not linearly proportional to it; in particular, the behavior is characterized by an asymptotic trend for higher voltages.[19] Indeed, at the regimes, when gels are deswollen to a certain extent, their resistivity to the passage of a charge increases as the content of “free” water

decreases. Subsequently, a smaller amount of a charge passes through the gel whose response is proportionally smaller. In particular, accordingly to the above statement, at higher voltages, the response magnitude of the filler-free sample tails off. At variance, the deswelling behavior of the nanocomposite hydrogels studied in the present work is different. Indeed, graphene influences this behavior—the neat polymer (sample A) deswells as the applied voltage increases, up to 15 V. This fact indicates that the equilibrium swelling capability of this sample is exhibited at 15 V. At variance, the other samples, which contain graphene in different amounts, continue to deswell by increasing voltage, at least up to the limit of 30 V used in our experiments.

Finally, the morphology of the hydrogels was investigated by SEM analysis. In particular, no differences among samples containing graphene and filler-free samples were found; the hydrogel nanocomposites having different amounts of graphene are characterized by the typical hydrogel porous morphology, consisting of a spongy structure. All hydrogels prepared in the present work are characterized by inhomogeneous morphology independent of the graphene amount, with small pores having dimensions smaller than 250 μm, together with others that are larger than 500 μm (Figure VII.16).

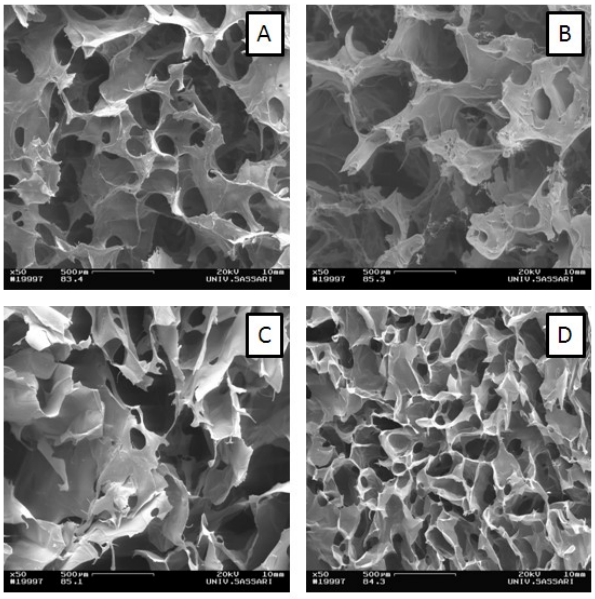

Figure VII.16 SEM micrographs of hydrogel samples (sample A = 0 wt.-% of graphene, sample B = 0.01 wt.-% of graphene, sample C = 0.02 wt.-% of graphene, sample D = 0.06 wt.-% of graphene).

In conclusion, multi*stimuli* responsive polymeric nanocomposite hydrogels of PAMPSA-containing graphene were synthesized by free radical polymerization. It was found that they are responsive to variations of both ionic strength and electrical field, thus changing their swelling capability in aqueous solutions. In particular, the introduction of graphene in the hydrogel matrix increased the SR% of these materials and influenced its variation in response to the application of the stimuli. As a matter of fact, by increasing the ionic strength of

the solution in which they are immersed, they deswell. Moreover, the use of a Ca^{2+} instead of a K^{+} resulted in an increase of deswelling, which might be attributed to the larger coordinating capability of the bivalent cation as compared with the monovalent one and to the consequent different extents of non-covalent crosslinking. Besides, graphene influence the swelling behavior even if up to a minimum threshold value locate at 0.06 wt.-%.

Furthermore, the polymer hydrogels studied here exhibited a response to the application of an electrical field. Namely, they contracted in different ways, depending on the graphene content and the applied voltage. It is noteworthy that the hydrogel sample that does not contain graphene exhibits an equilibrium swelling capability at 15 V, while the other samples, which contain different amounts of graphene, continue to deswell as voltage raises (up to 30 V, the highest voltage used in our experiments). These findings suggest that the neat hydrogel behaves as the typical dielectric materials do,[20] while those that contain graphene are characterized by a completely different behavior.

VII.4 SYNTHESIS AND CHARACTERIZATION OF GRAPHENE-CONTAINING THERMORESPONSIVE NANOCOMPOSITE HYDROGELS OF POLY(*N*-VINYLCAPROLACTAM) PREPARED BY FRONTAL POLYMERIZATION

In this work, thermoresponsive nanocomposite hydrogels of poly(*N*-vinylcaprolactam) containing graphene were prepared for the first time by using FP as synthetic technique. PNVCL is a thermoresponsive polymer hydrogel that is attracting much attention in the last years as a valid alternative to PNIPAAm, the most studied *stimuli* responsive polymer hydrogel. PNVCL is a non-ionic, water-soluble, non-adhesive polymer belonging to the group of poly(*N*-vinylamide) macromolecular compounds. Moreover, PNVCL is non-toxic and, unlike PNIPAAm, is stable against hydrolysis and biodegradable.

High concentration of graphene was obtained by simple sonication of graphite directly in the liquid NVCL monomer, thus avoiding any chemical manipulation and obtaining ‘‘real’’ graphene as nanofiller instead of one of its more or less oxidized derivatives, which is what generally reported in published reports. This synthetic strategy has significantly limited the reaggregation phenomena to graphite, which may occur during the nanofiller recovery in the solid-state. Moreover, the corresponding nanocomposites were obtained without using any solvent to be eventually removed. Finally, the influence of graphene on the swelling behavior of the obtained hydrogels at different temperatures and on the rheological and morphological features was thoroughly investigated.

First, graphene dispersions in NVCL were subjected to Raman analysis to confirm the presence of graphene itself and to determine the number of graphene layers.[9,21] In Figure VII.17, a comparison between the

Raman spectra of graphite and graphene obtained by gravimetric filtration of its dispersion in NVCL is reported. As can be seen, both the spectra exhibit three typical signals, namely the D band at 1350 cm^{-1}, the G band at 1580 cm^{-1} and the disorder-related 2D peak at a frequency of ca. 2700 cm^{-1}. The 2D band is a diagnostic signal for the identification of graphene because its shape differs from that of graphite; indeed, it can: (i) be fully symmetrical (in mono-layer graphene), or (ii) have a shoulder (in graphite), or (iii) be characterized by an intermediate shape depending on the number of layers.

In the example reported in Figure VII.17, the shape and position of the 2D band suggest that the sample under examination consists of few-layer graphene, this name refers to graphene flakes made up of five to seven layers. On the contrary, graphite shows a very different 2D band, which consists of two components with a stronger peak at 2713 cm^{-1}.[22] The graphene concentration in NVCL was also estimated using the method reported in previous studies[17,23] and was found to be 5.0 mg/mL, one of the highest reported so far in published reports with any method and in any liquid.

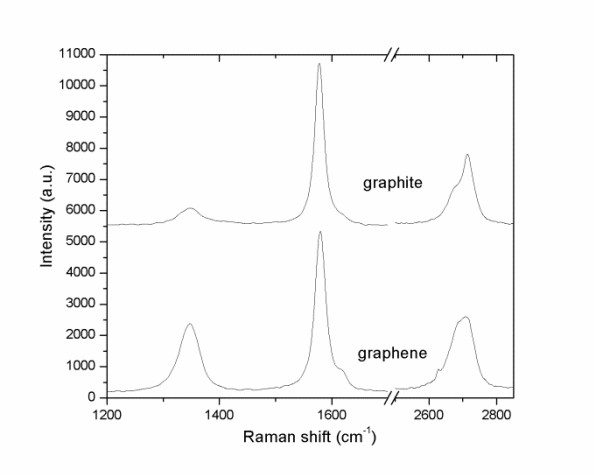

Figure VII.17 Raman spectra of graphene obtained after filtration of the NVCL dispersion (bottom) and pristine graphite (top).

Another proof of the nanometric dimensions of the dispersed graphene particles was provided by the occurrence of the Tyndall effect (Figure VII.18). NVCL dispersion shows graphene light scattering, thus confirming the colloidal nature of this system.

From the above graphene dispersions in NVCL, several polymer nanocomposites having graphene concentrations ranging from 0.0088 to 0.44 wt.-% were prepared by FP. As can be seen in Table VII.5, front temperatures are not affected by the presence of graphene and T_{max} values are always comprised between 161 and 166 °C. At variance, a relatively larger range characterizes V_f: namely, the addition of graphene results in decreasing V_f from 1.50 cm/min for the neat polymer to values ranging from 1.03 to 1.40 cm/min for the nanocomposites.

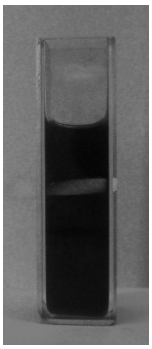

Figure VII.18 Tyndall effect exhibited by graphene dispersion in NVCL.

Besides, all the samples showed an almost quantitative conversion, which is independent of graphene concentration and is much higher than that previously reported in the published reports for the classical polymerization of NVCL, performed in solution at 60 °C for 192 h (<90%).[24]

The formation of the polymer was confirmed by FT-IR spectroscopy (Figure VII.19); namely, the typical PNVCL peaks were found at 700 cm^{-1} (δ-N-C=O), 1447 cm^{-1} (δ-CH_2), 1629 cm^{-1} (ν–C=O), 2927 cm^{-1} (ν-CH_2). Unfortunately, because of the superposition of graphene bands with those of PNVCL, only the peaks of this latter are visible in all the spectra of graphene-containing samples. This finding confirms the reliability of FP as a convenient alternative polymerization technique.

Table VII.5 Composition and conversions of the polymer nanocomposites prepared in this study, and temperatures and velocities of the polymerization fronts.

Sample	Graphene concentration in NVCL (mg/mL)	Graphene concentration in PNVCL (wt.-%)	T_{max} (°C)	V_f (cm/min)	Conversion (%)
FP1	0	0	166	1.50	98.0
FP2	0.10	0.0088	161	1.05	98.0
FP3	0.20	0.018	166	1.24	99.0
FP4	0.50	0.044	162	1.40	99.0
FP5	1.0	0.088	165	1.32	100
FP6	2.0	0.18	165	1.32	100
FP7	5.0	0.44	164	1.03	100

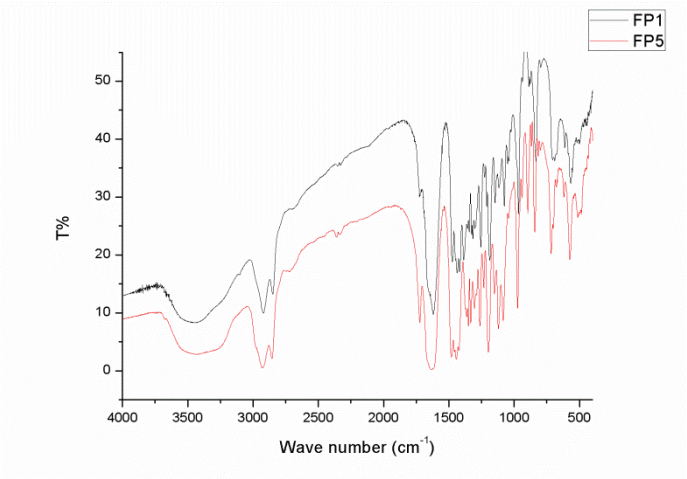

Figure VII.19 FT-IR spectra of the neat polymer (sample FP1, black line) and PNVCL containing 0.088 wt.-% of graphene (sample FP5, red line).

The swelling ratio of the nanocomposite polymer hydrogels as a function of temperature was measured from 3 to 53 °C in a thermostatic bath. As depicted in Figure VII.20, at 3 °C the swelling ratio is strongly influenced by the concentration of graphene embedded in the nanocomposite hydrogels. Namely, SR% increases from 1700% for the neat polymer to 2400% for the nanocomposite having the lowest graphene content (0.0088 wt.-%, sample FP2). Such an SR% increase is a clear indication that graphene largely interacts with the polymer matrix, affecting its typical properties even if present in small quantities. SR% increases with increasing graphene content and reaches a maximum value (3300%) for the hydrogel containing 0.088 wt.-% graphene (sample FP5). Furthermore, the increase of SR% as graphene increases may be attributed to the disturbance of this nanoparticle on the crosslinking occurrence.

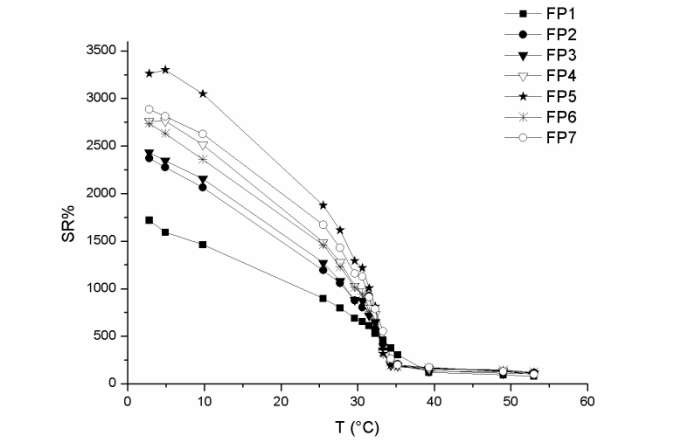

Figure VII.20 SR% as a function of temperature for samples containing different graphene amounts (see Table VII.4 for compositions).

On the other hand, when graphene concentration exceeds 0.088 wt.-%, SR% decreases down to 2700% (for sample FP6, which contains 0.18 wt.-% graphene) and to 2900% (sample FP7, which contains 0.44 wt.-% graphene). This last finding might be related to the decrease of the whole hydrophilic character of the nanocomposite polymer hydrogel, which, in turns, can be attributable to the presence of the relatively large amount of highly hydrophobic graphene sheets. Furthermore, the nanofiller does not affect the LCST, always located at ca. 32–33 °C, a value that is close to the physiological one.

The dispersion state of the graphene sheets and the morphological structure of the polymer nanocomposite hydrogels were assessed by TEM and SEM, respectively. As shown in TEM images, the nanofiller consists of flakes with an average length below 1 μm and a number of sheets roughly evaluated from the edges, which tend to fold back in between two and several layers (Figure VII.21a,b). The ratio of isolated to aggregated graphene sheets was difficult to evaluate over very large areas, mainly because of the big difference of contrast and brightness. Nevertheless, approximately 1 μm-size graphene particle (example in Figure VII.19c) any tens of well-dispersed structures was observed. The concentration of such graphene granes in ultra-microtomed samples from dried hydrogel was qualitatively higher than in those obtained by direct cryogenic sectioning of the swollen gel. This finding possibly indicates that aggregation takes place during the drying process, as a direct consequence of shrinkage, especially in the case of bulk samples. As a matter of fact, such tendency was more apparent for nanocomposites having higher graphene content, and especially for sample FP7.

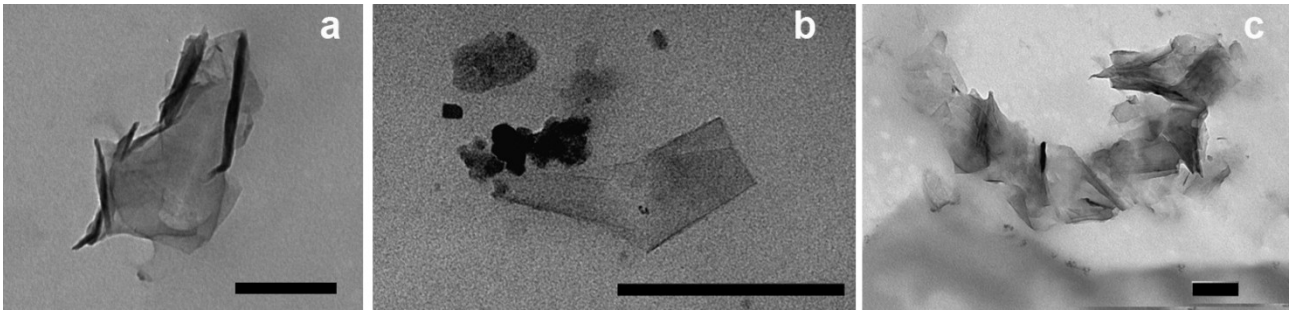

Figure VII.21 TEM images of few layer graphene sheets (a,b) and a graphene aggregate (c) in sample FP7. Scale bar: 200 nm.

The morphological structure of the obtained polymer nanocomposite hydrogels was investigated by SEM. First, it had to be noticed that this technique does not allow detecting the presence of graphene; furthermore, both the neat polymer (sample FP1) and the nanocomposites show a highly micro-porous structure (see Figure VII.22). It is worthy to note that the pore diameters of the neat polymer (sample FP1, Figure VII.22a) are much smaller than those of graphene-containing hydrogels (sample FP2, Figure VII.22b).

This difference may be attributed to the presence of graphene sheets, which partially disturb the crosslinking. This assumption is in agreement with what stated above about the influence of graphene in the swelling behavior of the prepared hydrogels.

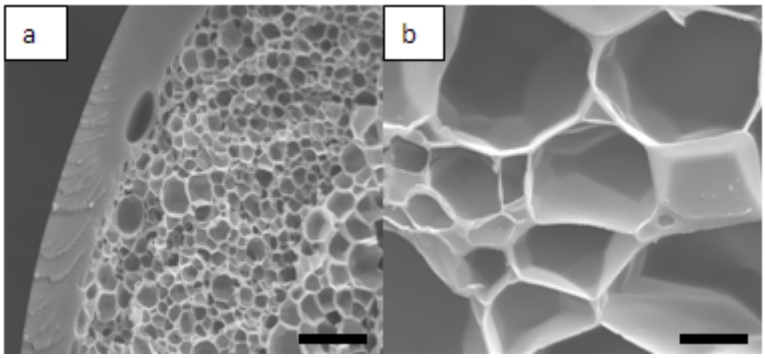

Figure VII.22 SEM micrographs of: (a) sample FP1 (neat polymer), and (b) sample FP2 (containing 0.0088 wt.-% graphene). Scale bar: 200 nm.

As far as the rheological characterization is concerned, Figure VII.23a plots the storage modulus (G') as a function of frequency for neat PNVCL and some PNVCL/graphene hydrogels. The neat polymer shows the presence of a horizontal plateau, which refers to a typical crosslinked material. The presence of the filler does not affect the elastic response of all the tested compositions: indeed, G' remains constant within the frequencies range explored. The lubrication effect induced by graphene sheets, which has been already observed for other polymer matrices,[17] promotes a decrease of G' with increasing graphene content (Figure VII.23a): unlike PNIPAAm hydrogels,[18] a threshold filler concentration is not present in the systems under study, so that the complex viscosity curves are continuously shifted toward lower values with increasing the nanofiller content (Figure VII.23b).

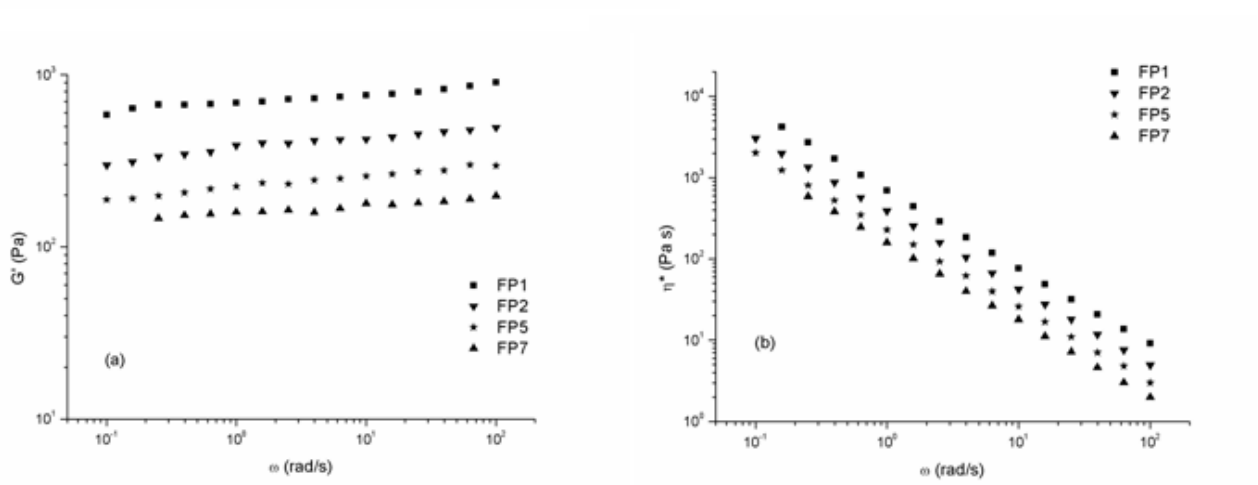

Figure VII.23 (a) Storage modulus G' and (b) complex viscosity as a function of frequency for some investigated PNVCL (see Table VII.4 for compositions).

Furthermore, the slope of the regression lines, which gives an indication of the non-Newtonian behavior of the hydrogels, is in the same range (~0.95) for all the compositions investigated and further confirms the unchanged viscoelastic behavior of all the nanocomposites with respect to the unfilled counterpart.

In conclusion, FP was successfully exploited for the synthesis of thermoresponsive graphene-based PNVCL nanocomposite hydrogels. This is the first time that NVCL was frontally polymerized; furthermore, the monomer to polymer conversions were always almost quantitative, thus confirming the feasibility of FP in the easy, short time consuming macromolecular synthesis.

At variance to the most commonly reported methods, which are more complicated and often less effective, the one used in the present study easily allows obtaining defect-free graphene by direct graphite sonication. In particular, when compared with the other route for obtaining graphene in liquid dispersion, which consists of graphite oxide partial reduction, no chemical modification was used, thus achieving ‘‘real’’ graphene. Besides, the utilized dispersing medium was the self-same liquid monomer. In such a method, the graphene/monomer dispersion was directly polymerized to achieve the corresponding nanocomposites, thus avoiding solvent removal, which is a process that may result in graphene aggregation to form graphite. Graphene concentration in NVCL was one of the highest reported so far in published reports using any method and any liquid (5.0 mg/mL). As far as the material properties are concerned, it is noteworthy that graphene influences the swelling ratio of the obtained hydrogels; namely, at 3 °C, SR% ranges from 1700% for the neat polymer to 3260% for one of the graphene-containing nanocomposites. However, all the materials exhibit the same LCST at ca. 32–33 °C, independently of the presence of graphene and its concentration. Taking into account that this value is closer to the physiological temperature than the LCST of PNIPAAm itself, PNVCL can be considered a much safer and cheaper polymer and should be preferred especially in biomedical applications.

Furthermore, similarly to what already reported in Ref. 18, the study on the rheological properties evidenced that the G' modulus and complex viscosity of the hydrogels decrease as the amount of nanofiller increases, thus indicating that graphene exerts a lubrication effect.

VII.5 SYNTHESIS AND CHARACTERIZATION OF THERMORESPONSIVE NANOCOMPOSITE HYDROGELS OF POLY(*N*-VINYLCAPROLACTAM) CONTAINING NANOCRYSTALLINE CELLULOSE

In this work, FP was used for the synthesis of thermoresponsive nanocomposite hydrogels of PNVCL containing cellulose nanocrystals as nanofiller. CNC are constituted of rodlike cellulose crystals, having a width of 5-70 nm and a length included between 100 nm and several micrometers.[25,26] They were used as

reinforcing agents with the aim of improving the poor mechanical properties of hydrogels, which is something that strongly limits their use in structural applications. Among the natural fibers, nanocrystalline cellulose represents an appropriate filler for hydrogels because of its good mechanical properties and renewability. In fact, it is characterized by high aspect ratio, high bending strength (10 GPa), high Young's modulus (150 GPa), large surface area, low density, low extension to break, biodegradability and biocompatibility.[27,28]

The nanofibers were prepared by acid hydrolysis of microcrystalline cellulose, and then dispersed in DMSO. TEM analysis was performed on CNC to determine their dimensions and structures. The CNC dispersion in DMSO was then mixed with the opportune amount of NVCL for the synthesis of the corresponding nanocomposite hydrogels, whose swelling behavior, rheological properties and morphologies were widely studied.

Figure VII.24 shows TEM analysis of pristine cellulose nanocrystals in aqueous suspension obtained after acid hydrolysis, and the freeze-dried CNC re-dispersed in DMSO for the PNVCL nanocomposite hydrogel production. The hydrolysis process allowed obtaining well individualized CNC (Figure VII.24a) that showed the typical acicular structure and dimensions ranging from 100 to 200 nm in length and 5–10 nm in width, as previously reported.[29,30]

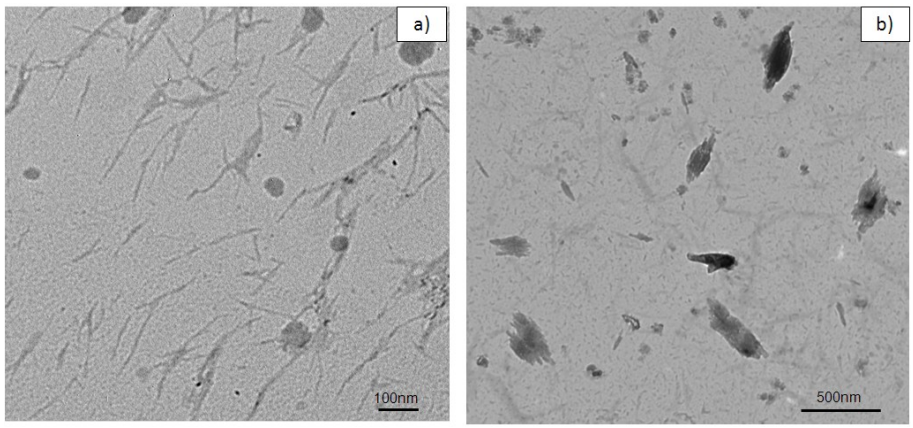

Figure VII.24 TEM analysis of pristine cellulose nanocrystals suspensions in water (a) and CNC re-dispersed in DMSO by ultrasonic treatment (b).

Prior to the PNVCL nanocomposite hydrogel production process, the CNC suspension was freeze-dried, and then re-dispersed in DMSO. During the freeze-drying process, CNC tended to agglomerate and form strong hydrogen bonds as water sublimates. Results obtained for crystal shape and size after the re-dispersion in DMSO (Figure VII.24b) highlighted that no particular morphological modifications occurred and CNC maintained its original acicular structure. The dispersion and self-ordering properties of cellulose

nanocrystals are restricted to aqueous suspensions and the high tendency to agglomeration of these materials in non polar solvents is usually due to their electrostatic character. However their dispersion in some specific organic solvents with high dielectric constant, such as DMSO or ethylene glycol, was previous proved.[31]

FP was used to prepare nanocomposite polymer hydrogels of PNVCL containing different amounts of CNC, which are included between 0.20 and 2.0 wt.-% referred to the monomer. As can be seen from Table VII.6, the frontal polymerization temperature increases of 15 °C introducing CNC in the polymer matrix, and remains constant around 116-120 °C when the CNC amount is further increased. At variance, front velocity is not significantly affected by the CNC content (0.30-0.33 cm/min). This behavior is in agreement with the V_f trend observed in our previous work about nanocomposite polymer hydrogels of PNIPAAm containing graphene as nanofiller.[17]

Table VII.6 Composition of the polymer nanocomposites prepared in this study, and temperatures and velocities of the polymerization fronts

Sample	CNC Concentration (wt.-% referred to NVCL)	T_{max} (°C)	V_f (cm/min)
FP1	0	101	0.30
FP2	0.20	113	0.33
FP3	0.50	120	0.33
FP4	1.0	114	0.33
FP5	2.0	117	0.37

As reported in the Experimental part (paragraph VI.5), the swelling behavior of CNC-containing PNVCL hydrogels in water as a function of temperature was measured from 3 to 50 °C, using three different heating rates. As shown in Figure VII.25, SR% decreases from 1200% for the neat polymer to 970% for the nanocomposite containing the lowest amount of CNC (sample FP2). The introduction of nanocrystalline cellulose involves a strong increase of the hydrophobic character of the polymer, leading to its sharp contraction. Moreover, CNC can act as a physical crosslinker, giving rise to more junctions in the hydrogel network and thus increasing the crosslink density.

With the enhancement of the CNC amount, SR% decreases and reaches the minimum value of 870% for the hydrogel containing 1.0 wt.-% of CNC (sample FP4). However, when CNC content is 2.0 wt.-% (sample FP5), SR% exhibits a slightly increase up to 940%. This behavior is probably due to the negative interference of

cellulose nanocrystals in the crosslinking process within the polymer matrix, as observed in the work described in paragraph VII.4, in which graphene was used as nanofiller. Moreover, the introduction of CNC in PNVCL hydrogels does not influence the LCST, located around 33-34 °C, a temperature that is very close to that of the human body.

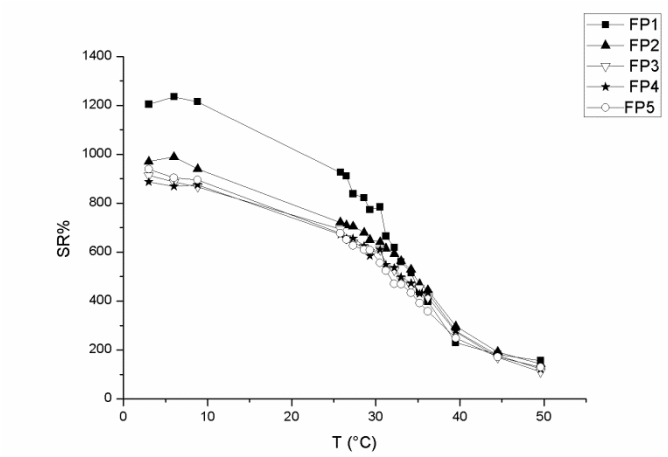

Figure VII.25 SR% as a function of temperature for samples containing different CNC amounts (see Table 1 for compositions).

The morphological characterization of the obtained nanocomposite polymer hydrogels were carried out by FE-SEM analysis. Unfortunately, by this technique it was not possible to detect the presence of nanocrystalline cellulose. In Figure VII.26, FE-SEM images of the neat polymer (sample FP1, Figures VII.26a_1 and a_2) and of the corresponding nanocomposite containing 0.2 (sample FP2, Figure VII.26 b_1 and b_2) and 0.50 wt.-% (sample FP3, Figure VII.26 c_1 and c_2) of cellulose nanocrystals, respectively, are reported. It can be seen that all the samples analyzed show the typical hydrogel structures, with pores having dimension of 5-20 μm.

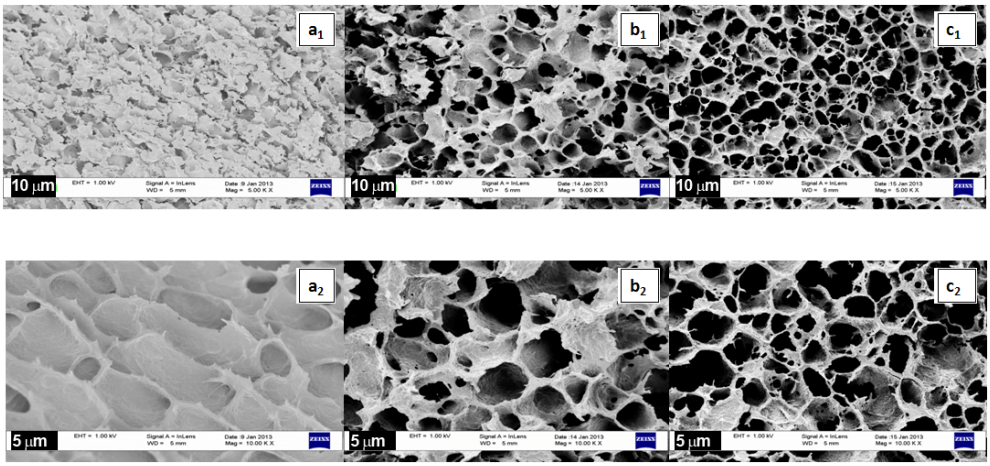

Figure VII.26 FE-SEM micrographs of: PNVCL (a_1 5000 X, a_2 10000 X, sample FP1), (b) PNVCL-0.20 wt.-% CNC (b_1 5000 X, b_2 10000 X, sample FP2), and (c) PNVCL-0.50 wt.-% CNC (c_1 5000 X, c_2 10000 X, sample FP3).

The results of rheological analysis in terms of G' and loss moduli (G'') are reported in Figure VII.27. As can be observed, G' is always higher than G'' for pristine PNVCL and all nanocomposites in the whole frequency range, thus indicating that the material response is prevalently elastic.

As expected, nanocomposites have higher moduli than pure PNVCL, which increase with the CNC concentration. The effect on G' is more pronounced and this is due to the mechanical behavior of CNC, which is characterized by high stiffness and therefore low viscous response.[30] The increase in G' confirms that cellulose nanocrystals act as reinforcement of PNVCL hydrogels improving their stiffness.

It is important to note that at low frequencies the viscoelastic properties of the nanocomposites deviate from the PNVCL behavior; indeed, they have a pronounced solid-like behavior with a clear tendency to reach a plateau for both G' and G''. This is probably due to the CNC-CNC and PNVCL-CNC interactions that are responsible for the formation of an interconnected structure[32,33] that strongly affects the viscoelastic properties of the hydrogel matrix. In fact, cellulose nanocrystals are nanoparticles with high aspect ratio, this allows the formation of a network that induces the solid-like behavior. On this respect, it should be reminded here that several authors observed the same behavior in other systems reinforced with nanoparticles having high aspect ratio.[34]

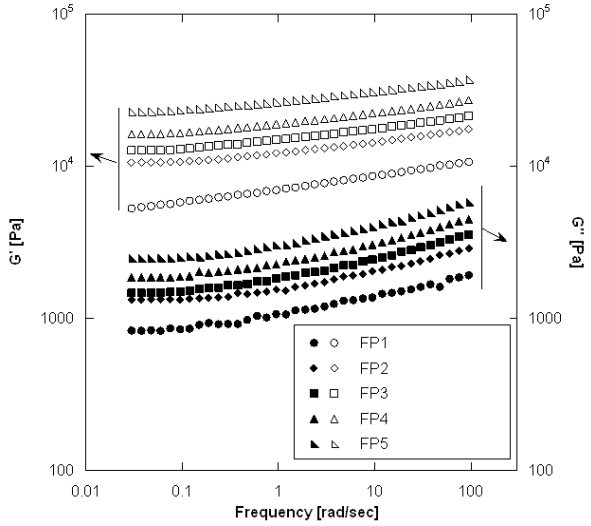

Figure VII.27 Storage (G') and loss (G'') moduli behavior as functions of frequency.

In Figure VII.28, the complex viscosity curves are reported. The viscosity of CNC-filled formulations is higher than that of the pristine hydrogel and, as expected, increases with the nanocrystalline cellulose concentration (Figure VII.28a).

The analysis of the complex viscosity as a function of stress confirms that the CNC dispersed into the matrix generates an interconnected structure that strongly affects the viscoelastic response of the hydrogel hindering the mobility of the network of hydrogel chains. In fact, in Figure VII.28b it is possible to observe that nanocomposites show a clear deviation from the matrix behaviour with an asymptotic tendency

indicating the presence of a yield stress for these formulations. Several authors[35-39] previously observed the presence of yield stress in nanocomposite systems with an interconnected structure, suggesting that this kind of structure is present also in the analyzed systems.

This rheological behaviour also suggests that CNC are well dispersed into the hydrogel matrix; in fact, agglomerated systems with low aspect ratio have lower tendency to induce solid-like behaviour and yield stress, with the consequence that these phenomena became relevant only at high filler concentration. In the present case, solid-like behaviour and yield stress are observed also at very low concentration (0.20 wt.-%) and became more relevant when the CNC content increases, suggesting the presence of low filler agglomeration.[40-43]

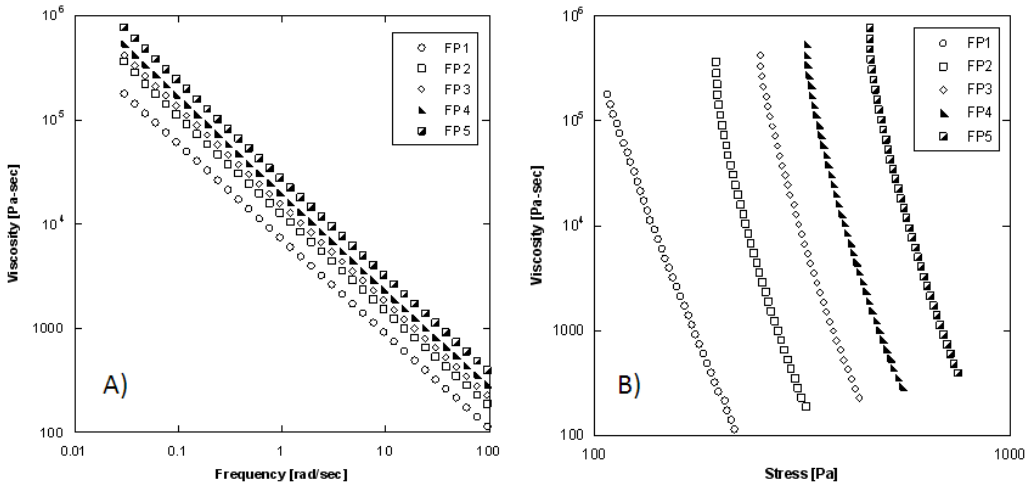

Figure VII.28 Results of complex viscosity from frequency sweep tests: A) Viscosity vs. Frequency curves; B) Viscosity vs. Stress curves.

In conclusion, different nanocomposite hydrogels containing CNC were successfully prepared by exploiting FP. This very easy technique was chosen also because is considered “greener” than most of the classical methods in that it is faster and requires only very low amounts of energy.

Moreover, CNC was easily prepared by commercial microcrystalline cellulose hydrolysis, and its formation was confirmed by TEM. They exhibited the typical acicular structure and the dimensions ranging from 100 to 200 nm in length and 5–10 nm in width.

The introduction of CNC in the polymer matrix strongly influenced the swelling ratio of the obtained hydrogels; namely, at 3 °C SR% ranges from 1200% for the neat polymer to 890% for the nanocomposite containing 1.0 wt.-% of CNC. This decreasing of SR% with the enhancement of CNC amount is probably due to the fact that the nanofiller acts as a physical crosslinker, giving rise to more junctions in the hydrogel network and thus increasing the crosslink density. However, all the resulting PNVCL nanocomposites showed an LCST located at ca. 33-34 °C, independently of the presence of CNC and its concentration.

The rheological analyses indicated that CNC gives a significant contribution to the viscoelastic modulus, even at very low concentration: both G' and G'', and the viscosity increase with CNC content, although the enhancement of viscosity with the filler concentration is less pronounced than in G' and G''. These results show that CNC improves the mechanical properties of PNVCL hydrogels, demonstrating a great potential as reinforcing agent in nanocomposite materials.

VII. 6 THE PRODUCTION OF CONCENTRATED DISPERSIONS OF FEW-LAYER GRAPHENE BY THE DIRECT EXFOLIATION OF GRAPHITE IN ORGANOSILANES

In this work, graphene dispersions were obtained by sonicating graphite in two reactive organosilanes: phenyl triethoxysilane and 3-glycidoxypropyl trimethoxysilane. This preparation method was mild, easy and does not produce any chemical modification of graphite. Moreover, it affords to obtain graphene also in reactive media, which can be directly used for the synthesis of polymeric materials, without any solvent removal and purification processes. The alkoxy group is the reactive site of such class of compounds: hydrolysis of the methoxy or ethoxy groups of GPTMS and PhTES gives rise to silanol groups which can condense to form silicate networks. Furthermore, GPTMS has an epoxy ring that can be used for organic network formation, for instance, through condensation with diethylenetriamine or ethylenediamine at room temperature. In particular, PhTES and GPTMS were tested with the aim of preparing graphene dispersions that could be directly utilized for further uses without recovering graphene in the solid state, thus avoiding any possible restacking of it to pristine graphite and compromising any previous successful exfoliation process.

Graphene dispersions in organosilanes were thoroughly characterized by using Raman and UV-Vis spectroscopies, while TEM was used for the statistical analysis concerning the distribution among single and few-layer graphene.

Graphene dispersion in PhTES and GPTMS were prepared by using a simple method based on direct exfoliation of graphite in organosilanes.

A first indication of the nanometric dimensions of the dispersed graphene particles was provided by the occurrence of the Tyndall effect.[44] Both GPTMS (Figure VII.29) and PhTES dispersions exhibit graphene light scattering, thus confirming the colloidal nature of these systems.

With the aim of determine the best initial graphite/liquid medium ratio that allows obtaining the highest graphene concentration, a series of dispersions with different amounts of graphite was prepared for each of the two organosilanes. In order to find the absorption coefficient α and set-up a reliable method for the determination of graphene concentration in the above media, UV-Vis and gravimetric analysis were carried

out (see Experimental part). Figure VII.30 shows the Lambert-Beer behavior and the different slopes of the two suspensions, thus indicating that the two media have different dispersibility.

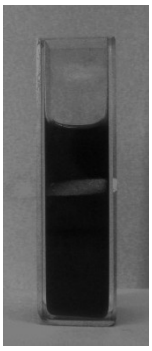

Figure VII.29 Tyndall effect exhibited by graphene dispersion in GPTMS. When the red laser light passes through the dispersion, it is scattered and becomes visible.

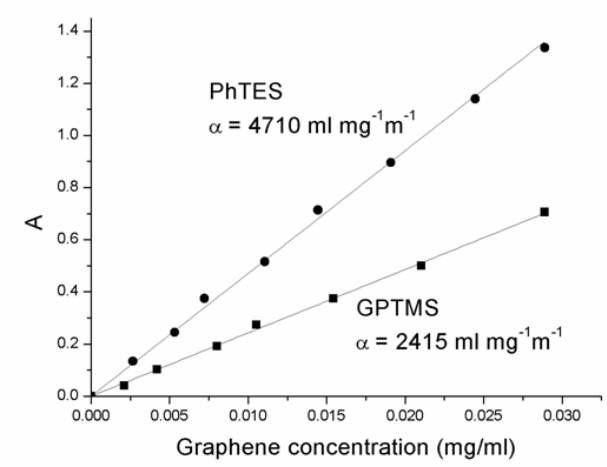

Figure VII.30 Absorption coefficient α determination. Optical absorbance (660 nm) as a function of graphene concentration in
PhTES and GPTMS.

Namely, for GPTMS and PhTES, an absorption coefficient of 2415 and 4710 ml·mg^{-1}·m^{-1} was respectively found.

The concentrations of graphene in GPTMS and PhTES as functions of the initial graphite concentration are reported in Figures VII.31a and 31b, respectively. As far as the GPTMS dispersion is concerned, a direct proportionality between initial graphite and graphene seems to exist up to 5.0 wt.-% of the initial graphite (Figure VII.31a). After this value, a decrease of graphene concentration was found. This is probably due to the following observed phenomenon: when high concentrations of graphite are added to the used plastic reactor, it tends to precipitate thus making the subsequent sonication process less effective. It should be highlighted that the maximum concentration of graphene here obtained is one of the highest reported so far by any method.[13,45-47] An analogous trend was observed also in the case of PhTES (Figure VII.31b), for

which the maximum graphene concentration (0.66 mg/mL) was found when the initial graphite concentration was 2.5 wt.-%. Besides, the maximum amount of graphene that can be dispersed in PhTES is much lower than in the case of GPTMS, 0.66 mg/mL instead of 8.0 mg/mL, thus indicating that this latter liquid medium is more effective than PhTES in dispersing graphene.

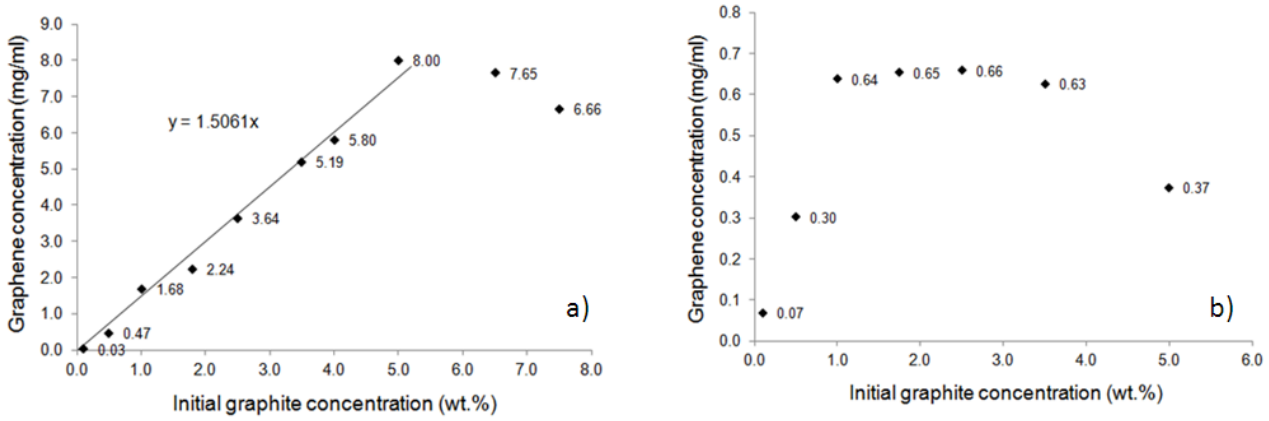

Figure VII.31 Graphene concentration in GPTMS (a) and in PhTES (b) as a function of initial graphite concentration.

TEM was used to investigate the state of the graphene particles dispersed in organosilanes; indeed, this technique is usually employed for the investigation of graphene dispersions.[13-15,48]

As shown in Figure VII.32, the images revealed a large quantity of flakes of different types. A larger proportion of flakes were few-layer graphene of various dimensions: in particular, very large flakes (lateral size approximately 1 µm) and smaller flakes with an average lateral size of 100 to 200 nm.

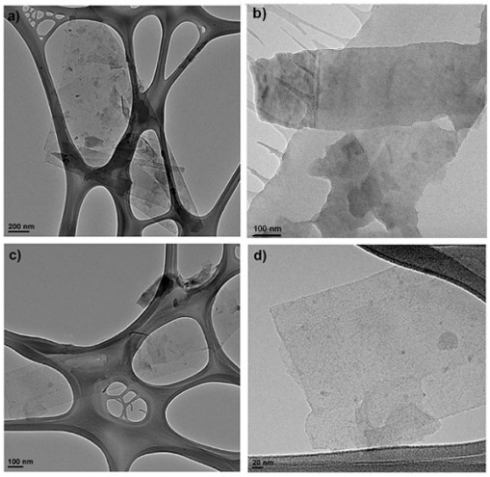

Figure VII.32 Graphene dispersed in GPTMS (a,b) and in PhTES (c,d).

It should be underlined that, in all cases, we did not observe graphite aggregates. Despite of what was reported in other applications, a relatively large size distribution is generally not considered a drawback in

polymer nanocomposites in which the nanometric dimensions of the filler is the predominant factor influencing the properties of the resulting material.[17]

A statistical analysis on TEM data was performed in order to verify the exfoliation, thus analyzing carefully the edge of the graphene flakes and measuring the number of layers presented in each flake.[15] At this regards about fifty different images have been observed in order to obtain a significant number of flakes for the statistical analysis. The results are reported in Figure VII.33.

The flakes present good exfoliation degree with an average number of layers of 2.7 for GPTMS and 2.4 for PhTES; standard deviation was about 0.4 and 0.5, respectively. In both cases, only 14% of the flakes were made of more than three layers. Moreover, no more than five layers have been counted in very few flakes thus indicating a narrow dispersion. These results confirm that the exfoliation process was very effective.

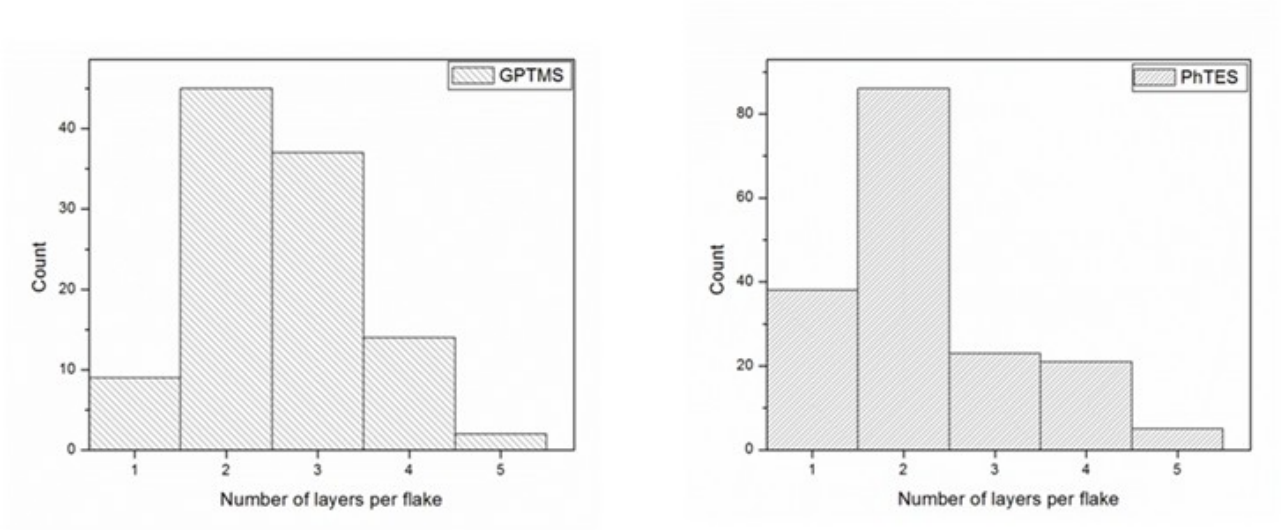

Figure VII.33 Statistical analysis. Histograms showing the number of layers per flake measured for graphene obtained by exfoliation of graphite in GPTMS (left) and PhTES (right).

Subsequently, graphene dispersion was characterized by Raman spectroscopy to verify the presence of graphene itself and to determine the number of graphene layers. Moreover, such technique is considered one of the best characterization techniques for discriminating between graphite and graphene.[10,49,50]

As shown in Figure VII.34a, typical Raman signals of graphene recovered from the dispersions of GPTMS and PhTES are very similar, both exhibiting the characteristic graphene peaks. In particular, as far as PhTES is concerned, the G band at 1577 cm^{-1}, the 2D band at 2696 cm^{-1}, and the disorder-related D peak at approximately 1346 cm^{-1} are evident. Similarly, graphene obtained from GPTMS shows the G band at 1574 cm^{-1}, the 2D band at 2701 cm^{-1}, and the disorder-related D peak at approximately 1345 cm^{-1}. The shape and position of the 2D peaks (Figure VII.34b) is typical of bilayer graphene (four components with the main peak at approximately 2701 cm^{-1}, as confirmed by a deconvolution process).[10]

As a comparison, the 2D peak of graphite consists of two components and the main peak is upshifted to 2713 cm^{-1}.

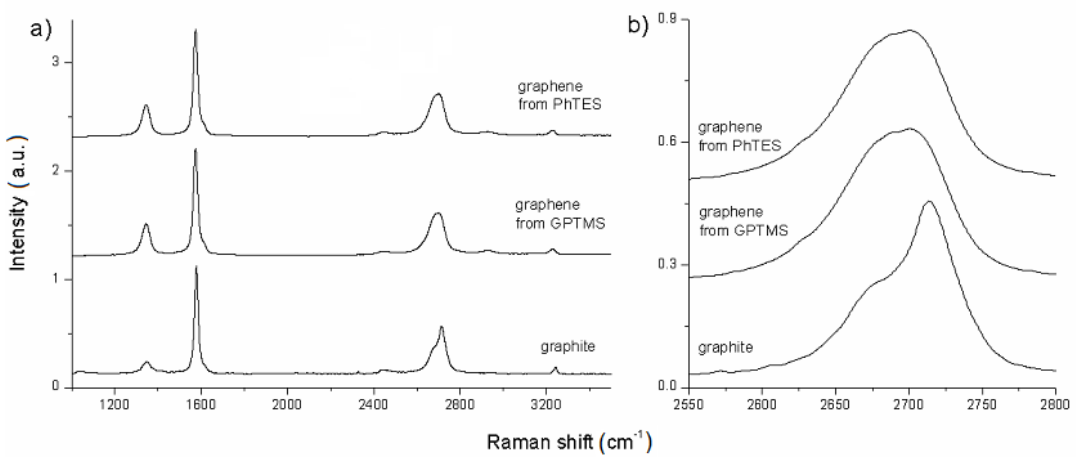

Figure VII.34 Raman analysis. Spectra of graphene obtained by sonication in PhTES and GPTMS from 5 wt.-% of the initial graphite compared with graphite (a). 2D peaks evaluation for this systems (b).

The disorder-related D peak is present also in the initial graphite powder, but its intensity is higher for graphene.

This finding was already reported in other works in which graphene was produced by sonication of graphite and can be attributed to the new edges produced during the sonication process. In fact, ultrasonic treatment causes the decrease in size of the flakes compared to the original graphite, with a consequent increase of the total edge length.[11,12,15] Comparing the intensity of the peaks and the *D/G* ratio found in the case of graphene obtained in GPTMS and PhTES, only little differences can be found, thus indicating that the disorder induced by the exfoliation process is very similar. Namely, the *D/G* ratio is 0.47 for graphene dispersed in GPTMS and 0.65 for that dispersed in PhTES, while the reference value for graphite powder is 0.14. On the basis of the above concentration results, some considerations about the use of the Hildebrand solubility parameters δ should be done. Indeed, Hernandez et al.[51] stated that these parameters could be the key for envisaging the best graphene solvent media. In particular, they calculated a δ value for graphene equal to ca. 23 $MPa^{1/2}$, this value being the same of *N*-methyl-2-pyrrolidone.[17] However, GPTMS, the best solvent medium reported here, is characterized by δ = 14.5 $MPa^{1/2}$.[48] This value suggests that graphene solubility parameters should be revised and/or that they are not adequate for any reliable solubility prediction on this respect.

In conclusion, graphene were efficiently dispersed in two organosilanes by using a simple and cheap method based on graphite exfoliation in the self-same liquids. This technique allows avoiding any chemical manipulation of graphite and its re-aggregation, leading to the obtainment of defect-free graphene.

Namely, the two organosilanes in which graphene was dispersed are GPTMS and PhTES, which are commonly used in sol–gel synthesis, and for the preparation of polymer hybrids.

In detail, PhTES and GPTMS resulted to be one of the most effective media found so far for dispersing graphene, allowing for a concentration of this material equal to 8.0 mg/mL.

The concentration value found for PhTES is much lower (0.66 mg/mL) but, especially if compared with that of most the reported data,[13,52-54] it can be considered of interest; for instance, for the preparation of polymer composites, in which an even lower concentration of graphene might result in peculiar final properties of the resulting material.[17,55-57]

VI. 7 IN SITU PRODUCTION OF HIGH FILLER CONTENT GRAPHENE-BASED POLYMER NANOCOMPOSITES BY REACTIVE PROCESSING

In the present work, high concentration graphene was obtained for the first time by exfoliation of graphite in an acrylic monomer, TEGDA. As described in the previous work, graphene was obtained directly in the monomer, allowing synthesizing the corresponding polymer nanocomposites without solvent removal or additional processes. The resulting materials, obtained from classical polymerization, were analyzed from the morphological, thermal and mechanical point of view, with the aim to investigate the influence of graphene on the polymer properties.

The concentration of graphene, determined by gravimetry after filtration, was as high as 9.5 mg/mL, which represents the highest value reported so far in any solvent and obtained by any method. It is noteworthy that our approach is not only very effective but also as simple as possible and by-passes the recovering of graphene from a non-reactive solvent, which partially compromises any previous successful step, since a partial reaggregation of the nanofiller to graphite flakes occurs.

In Figure VII.35, the UV-Vis calibration curve for graphene/TEGDA dispersions is plotted: the system shows Lambert–Beer behavior, with an absorption coefficient of 436 mL mg^{-1} m^{-1}.

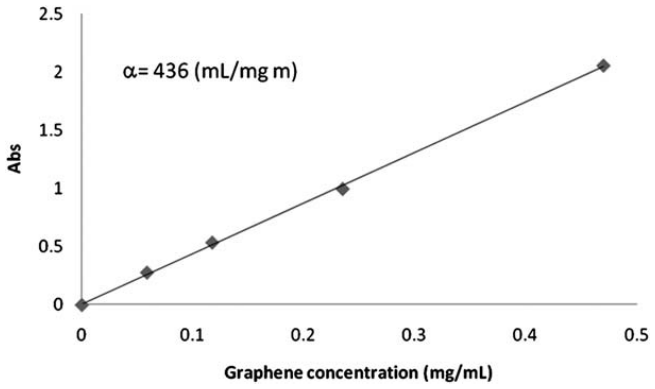

Figure VII.35 Calibration curve for graphene/TEGDA dispersion.

A first indication of the nanometric dimensions of the dispersed graphene particles can be provided by the occurrence of the Tyndall effect. As shown in Figure VII.36, light scattering confirms the colloidal nature of our TEGDA/graphene dispersion.

Figure VII.36 Tyndall effect measured on TEGDA/graphene dispersion (diluted 1 : 20)

The presence of graphene was also confirmed by Raman spectroscopy, which can discriminate not only between graphene and graphite, but also allows determining the number of layers.[9,10,57,58] As shown in Figure VII.37, the Raman spectrum of graphene obtained by filtration of its dispersion in TEGDA shows the typical graphene bands, namely: G at 1574 cm^{-1}, 2D at 2703 cm^{-1} and the disorder-related D band at 1350 cm^{-1}. The shape and position of the 2D band suggest that the sample under examination is constituted of few-layer graphene.[10] As a comparison, the shape of the 2D band of pristine graphite is very different and consists of two components with a stronger peak at 2713 cm^{-1}.

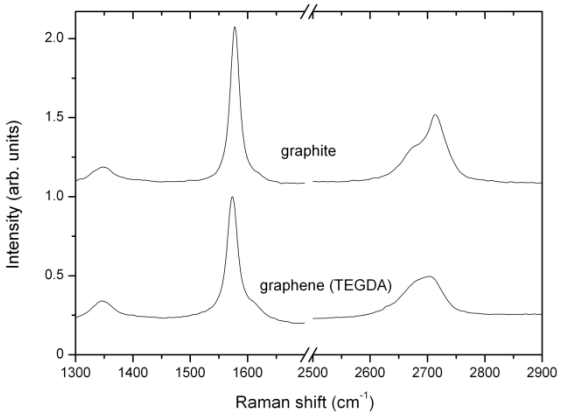

Figure VII.37 Raman spectra of graphite (top line) and of the graphene obtained from TEGDA dispersion (bottom line).

TEM analyses were also carried out on TEGDA/graphene dispersion (diluted 1:40) to further confirm graphene formation. Figure VII.38a shows a few flakes of few-layer graphene, and Figure VII.38b evidences the presence of some nanoribbons. It is worthy to note that this is the first reported example in which

graphene nanoribbons are obtained directly by simple graphite sonication; in addition, for the first time, graphene nanoribbons are obtained directly in a monomer. Indeed, these nanomaterials were previously obtained by a chemical route,[59] by sonochemically cutting chemically derived graphene sheets,[60] by unzipping of nanotubes,[61] by using chlorosulfonic acid[62] and by a few other methods.[63]

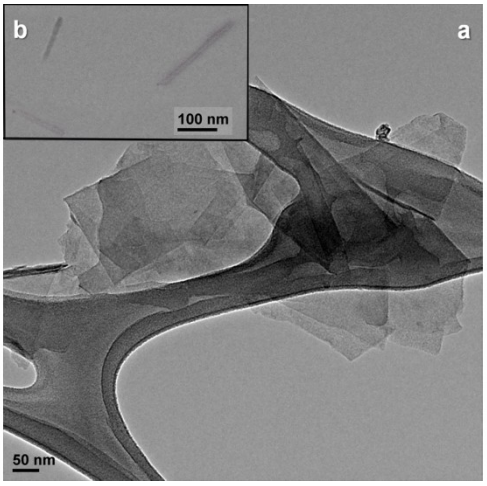

Figure VII.38 TEM images of TEGDA/graphene dispersion (diluted 1 : 40): (a) a few sheets of few-layer graphene; (b) some nanoribbons.

Table VII.7 Graphene concentration in the obtained polymer nanocomposites

Sample Name	Graphene concentration in TEGDA (mg/mL)
A	0
B	0.12
C	0.43
D	4.7
E	9.5

Once prepared graphene dispersion in TEGDA, nanocomposite polymers having five different concentrations of graphene were synthesized. Their compositions are listed in Table VII.7.

First, all samples were analyzed by Raman spectroscopy, to assess the absence of graphene aggregates, which could be formed during the polymerization reaction.

Figure VII.39 shows the Raman spectra of PTEGDA (dashed line, sample A) and PTEGDA containing graphene (solid line, sample D); the spectra are normalized to the peak at 1730 cm^{-1}. The differences between these spectra are mainly due to graphene bands, in particular, the G band at 1580 cm^{-1} and the

disorder-related D band at ~1350 cm^{-1}, which is superimposed on the PTEGDA spectrum. Furthermore, the other disorder-related D' band peaked at 1630 cm^{-1} is now well visible. D and D' bands are shifted and result better separated with respect to the spectrum of the graphene dispersion obtained from TEGDA monomer: such shift can be ascribed to the interaction between graphene and PTEGDA. Unfortunately, the 2D band at ~2700 cm^{-1} appears as a shoulder of the very strong PTEGDA Raman band peaked at ~3100 cm^{-1}; nevertheless, such a band is still typical of few-layer graphene because of its broadness and flatness, whereas the main peak of the graphite band would be much more intense and narrower.

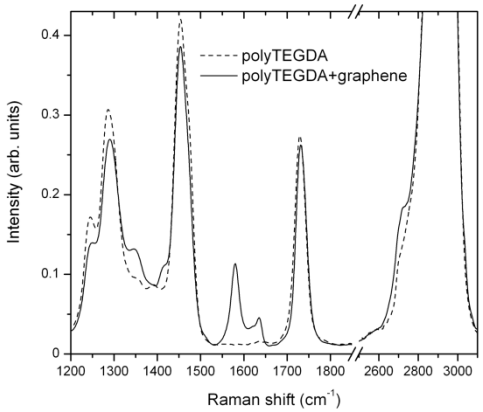

Figure VII.39 Raman spectra of PTEGDA (dashed line, sample A) and PTEGDA containing graphene (solid line, sample D).

Two typical SEM images of the fracture surfaces of neat PTEGDA (sample A) and of a typical graphene-containing nanocomposite (sample D) are displayed in Figure VII.40. In the latter, the presence of graphene sheets is clearly evident; in addition, while the surface of neat PTEGDA is quite smooth that of the nanocomposite sample is very rough.

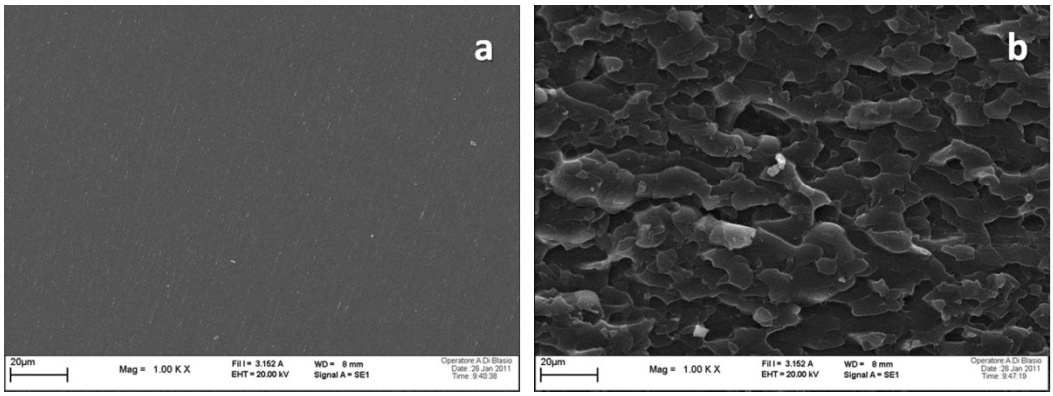

Figure VII.40 SEM micrograph of the neat polymer (a) and of the sample containing 4.7 mg/mL of graphene (b).

In Table VII.8, both T_g values calculated by DSC and/or DMTA, and the elastic moduli (G') values of the neat PTEGDA and of its nanocomposites are reported.

It is also worthy to note that, regardless of their concentration in the polyacrylate network, a very homogeneous distribution of graphene sheets within the polymer matrix is achieved for all the filled systems investigated, also including that characterized by the highest graphene content.

As concerning the transition glass temperatures, the data clearly indicate that they are strongly affected by the presence of graphene nanosheets: indeed, T_g increases from 1 °C, for neat PTEGDA, up to 27 °C for sample D, which contains 4.7 mg/mL of graphene. This finding is a clear indication of the effect of the nanofiller, which induces the formation of constraints that reduce polymer segment mobility. Furthermore, the observed T_g trend seems to indicate that the interactions between graphene and the polymer matrix occur even at very low nanofiller content.

Indeed, a significant 10 °C T_g increase is observed at the lowest graphene concentration (0.12 mg/mL, sample B). In contrast, the presence of a very high amount of graphene (sample E of Table VII.7) causes a drastic reduction of the T_g value, which approaches that of pure PTEGDA. This finding can be attributed to the high concentration of graphene sheets within the polymer, which are responsible for a lubrication effect, thus increasing the mobility of the polymer segments and decreasing T_g.

A similar behavior was evidenced by investigating the rheological properties of graphene-containing nanocomposite hydrogels of PNIPAAm prepared by frontal polymerization.[17]

Such a behavior was confirmed by DMTA analysis, which also pointed out a substantial increase in the storage modulus, both in the glassy state and in the rubbery plateau, where the influence of the nanofiller on the mechanical behavior of the polymer matrix becomes larger (see Table VII.9 and Figure VII.41). Once again, the only exception is observed for the sample with the highest graphene content (sample E), which exhibits the T_g and G' values of the neat cured resin.

Table VII.8 Glass transition temperatures (T_g) and storage modulus (G') of the cured nanocomposites

Sample	Description	Tg/DSC (°C)	Tg/DMTA (°C)	G' (-50 °C) (MPa)	G' (-100 °C) (MPa)
A	Neat TEGDA	1.20	4.90	1639	11.40
B	TEGDA + graphene (0.12 mg/ml)	10.7	13.8	1860	16.00
C	TEGDA + graphene (0.43 mg/ml)	15.2	31.2	2370	26.30
D	TEGDA + graphene (4.67 mg/ml)	26.9	48.7	2960	39.00
E	TEGDA + graphene (9.45 mg/ml)	2.80	7.80	1715	13.00

In order to further confirm the strong polymer/filler interactions, which graphene nanosheets are responsible for, flexural three point bending tests were performed at room temperature on all the

prepared nanocomposites and the obtained results were compared with the unfilled counterpart. As collected in Table VII.8, a strong increase in flexural modulus is observed when graphene is added to the acrylic system: indeed, flexural modulus almost triples in the case of the nanocomposite with high nanofiller content (4.7 mg/mL), with respect to the unfilled material. In addition, a significant increase in the σ_{max} is achieved, as well. Also in this case, when the highest graphene content is added to the acrylic monomer (9.5 mg/mL), a strong decrease in the mechanical behavior (flexural modulus and σ_{max}, Table VII.8) is observed, in agreement with its T_g decrease (Table VII.8).

Table VII.9 Flexural modulus and σ_{max} for the cured samples.

Sample	Graphene content in PTEGDA (mg/ml)	Flexural modulus (MPa)	σmax (MPa)
A	0	58.7	6.4
B	0.12	51.2	6.6
C	0.43	80.6	9.1
D	4.7	171	15
E	9.5	56.9	6.2

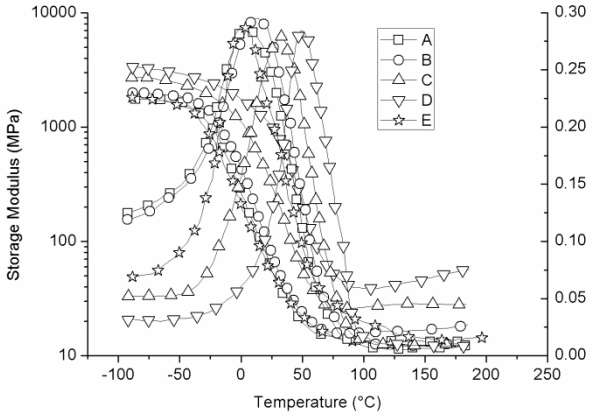

Figure VII.41 DMTA traces of cured PTEGDA and its graphene polymer nanocomposites

Finally, in Table VII.10, the results of TGA analyses performed in air are collected in terms of T_5, T_{10} and T_{50}, i.e. the temperatures at which the weight loss corresponds to 5, 10 or 50%, respectively.

The collected data clearly indicate that the thermo-oxidative stability of the polymer is substantially not affected by the presence of graphene nanosheets, irrespective of the nanofiller content.

Table VII.10 TGA data of samples

Samples	Graphene content in PTEGDA mg/mL	T_5 (°C)	T_{10} (°C)	T_{50} (°C)	Residue at 800 °C (%)
A	0	345	375	419	1.7
B	0.12	356	380	416	0.50
C	0.43	354	378	414	0.80
D	4.7	351	376	418	1.1
E	9.5	348	372	416	1.2

In conclusion, in this work, nanocomposite systems of PTEGDA containing different amounts of graphene were prepared by using radical polymerization. Graphene was obtained by exfoliation of graphite directly in the acrylic monomer, which is then polymerized, leading to the formation of the corresponding nanocomposites. In addition, for the first time a certain amount of graphene nanoribbons was also obtained through colloidal solution of graphene.

Raman spectroscopy demonstrated that the graphene directly formed within TEGDA does not undergo oxidation to graphite oxide and is made of a very limited number of graphene layers. Regardless of their concentration in the polyacrylate network, a very homogeneous distribution of graphene sheets within the PTEGDA matrix was obtained for all the systems investigated.

DSC analyses and thermo-mechanical tests indicated the occurrence of strong polymer/filler interactions: in particular, a significant increase in the T_g values was assessed also in the presence of very low graphene content, together with a strong increase in flexural and storage moduli.

Finally, the thermo-oxidative stability of the PTEGDA was not affected by the presence of graphene nanosheets.

Since the nanocomposite containing the highest graphene concentration (9.5 mg/mL) exhibits properties that approach those typical of the filler-free polymer, the corresponding highest concentration liquid dispersion might be used in copolymer synthesis in order to increase the final graphene content.

VII.8 SYNTHESIS AND CHARACTERIZATION OF GRAPHENE-BASED NANOCOMPOSITES WITH POTENTIAL USE FOR BIOMEDICAL APPLICATIONS

In this work, graphene dispersion in TEGDA, prepared by using the method reported in the previously work, was exploited for the development of nanocomposite copolymers of 2,2'-*bis*-[4-(methacryloxypropoxy)-

phenyl]-propane, which might be of interest in biomedical applications. In fact, Bis-GMA has been widely used as an important dental base monomer, which combines its mechanical characteristics with the advantage of limiting the volumetric shrinkage upon polymerization and enhancing the resin reactivity.[64,65] However, because of its high viscosity, monomers as TEGDMA, which are less viscous, are usually added to the resin for improving the handling features and increasing the double-bond conversion.[66] For this reason, 50/50 (w/w) Bis-GMA/TEGDMA mixtures are those that are used most for the preparation of dental composites, where the final properties are enhanced by the addition of large amounts of inorganic fillers, such as micro- or nano-sized SiO_2, ZrO_2, Al_2O_3, and silicate glasses. [67-69]

Taking into account the above consideration, and knowing the outstanding properties of graphene, the present study focused on the use of graphene as novel and alternative nanofiller for the production of resins based on Bis-GMA for possible dental and biomedical application.

However, TEGDA was used instead of TEGDMA because of its superior characteristics as an effective dispersing medium for graphene and its quite similar structure.

Morphology, thermal and mechanical properties of the resulting nanocomposites were investigated and correlated with the nanofiller content.

Graphene dispersions in TEGDA with high nanofiller loadings were obtained by sonication of graphite flakes in TEGDA and subsequently characterized by TEM (Figure VII.38) and Raman spectroscopy (Figure VII.37), as reported in the previous work (see paragraph VII.7).

For this study, several copolymers (PBTs) made of Bis-GMA/TEGDA (constant ratio: 50:50 w/w), were prepared varying graphene concentration (from 0 to 0.3 wt.-%), by properly diluting a TEGDA masterbatch dispersion (graphene concentration: 6.0 mg/mL, Table VII.11).

Table VII.11 Graphene concentration in the liquid dispersions and in the final nanocomposite materials.

Sample	Graphene concentration in TEGDA (mg/mL)	Graphene concentration in PBT (wt.-%)
A1	0	0
A2	0.060	0.003
A3	0.24	0.01
A4	1.2	0.05
A5	6.0	0.3

Figure VII.42 shows the typical SEM micrographs of A3, A5 samples (both are graphene-filled) and of the corresponding neat polymer (sample A1). While the surface of the neat PBT appears completely smooth

and homogeneous, it becomes as rougher as the graphene content increases. This finding can be explained by taking into account the strong interactions occurring between graphene and polymer matrix, which obstacle the straight propagation of the fracture that, otherwise, would result in a smooth surface. It is also worthy to note that a very homogeneous distribution of the graphene sheets within the polymer matrix is achieved for all the filled systems investigated, also including that characterized by the highest graphene content, as already reported in the previous work about graphene containing nanocomposite of PTEGDA (see paragraph VII.7).

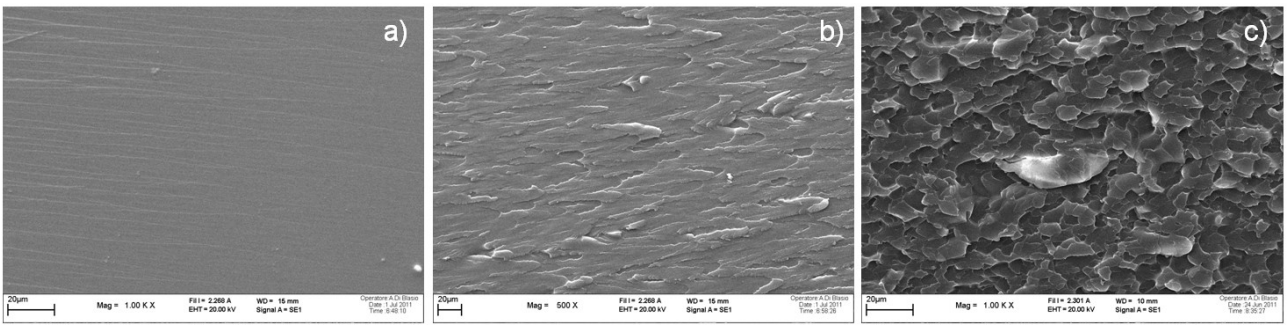

Figure VII.42 SEM micrographs of Bis-GMA/TEGDA copolymers with different amounts of graphene: neat PBT (A1, a), 0.011 wt.-% (A3, b), and 0.270 wt.-% (A5, c).

In order to investigate the effect of graphene on the mechanical properties, hardness and compression tests were carried out on PBT copolymers containing different amounts of nanofiller, as listed above. Table VII.12 collects the obtained values of Shore A hardness and modulus of elasticity. For comparison, values referred to the unfilled resin prepared with TEGDMA instead of TEGDA are also presented (see R sample). First of all, a comparison between the neat polymer matrices was made. As can be seen in Table VII.12, Shore A hardness values indicate that the replacement of TEGDMA with TEGDA results in an increase of the hardness from 80 to 84. When graphene is embedded into the polymer matrix, the measured hardness turns out to depend on the nanofiller content; in particular, Shore A hardness increases up to 94 (12 % increase with respect to the unfilled PBT) for the sample containing 0.01 wt.-% graphene (sample A3), and to 96 (when the nanofiller concentration reaches 0.3 wt.-%; sample A5), thus indicating that hardness reaches a plateau in the presence of relatively low nanofiller amounts. This behavior can be ascribed to the formation of a percolated interphase region, occurring even at very low graphene concentrations, upon which the effect of the nanofiller on the thermal and mechanical properties is less pronounced.[55]

As far as compression tests are concerned, the replacement of TEGDMA with TEGDA worsens the compression strength, which, however, is compensated by the addition of the nanofiller. Indeed, graphene exerts a strong reinforcing effect on the polymer matrix even at very low concentration: the modulus of elasticity increases with increasing graphene concentration, with a trend similar to that found for the hardness values.

Table VII.12 Hardness and modulus of elasticity for PBT filled with different amounts of graphene.

Sample	Hardness-Shore A	Modulus of Elasticity[a] (MPa)
R[b]	80	630
A1	84	542
A2	87	550
A3	94	658
A4	95	730
A5	96	839

[a] From compression test

[b] Bis-GMA/TEGDMA (50/50)

Table VII.13 Degree of conversion and T_g values for PBT filled with different amounts of graphene.

Sample	Conversion (%)	T_g (°C)
R	97	46
A1	94	99
A2	94	99
A3	98	99
A4	95	99
A5	97	98

DSC analyses were carried out to assess the degree of conversion (C%) and the glass transition temperature of PBT samples, which are listed in Table VII.13. For all samples, the degree of conversion was larger than 90% regardless of the amount of graphene and the type of polymer matrix (i.e., TEGDMA- or TEGDA-based). At variance, the replacement of TEGDMA with TEGDA resulted in a significant T_g increase (from 46 to 99 °C for R and A1 samples, respectively).

It is noteworthy that the presence of graphene does not influence the glass transition temperature (and therefore the crosslinking density of the cured network), which is stable around 99 °C. A similar behavior has been already assessed by other groups.[70,71]

In conclusion, in this study, graphene has been used as reinforcing nanofiller in polymeric materials having potential applications for biomedical purposes. Bis-GMA/TEGDA has been chosen as polymer system because its structure is similar to that of Bis-GMA/TEGDMA copolymer (widely used in biomedical field);

furthermore, TEGDA monomer is one of the best exfoliating media for graphene, as confirmed from the previous study (see paragraph VII.7).

Graphene dispersions at high concentration were obtained by simple sonication in TEGDA monomer and directly used for synthesizing Bis-GMA/TEGDA nanocomposites. The homogeneous dispersion of the nanofiller within the polymer matrix has been confirmed by SEM analyses, which showed rougher surfaces for all the nanocomposites with increased graphene concentration.

As far as the mechanical properties of the nanocomposites are concerned, graphene has been found to exert interesting reinforcing effects on the cured copolymers: indeed, both modulus of elasticity and surface hardness turned out to significantly increase even in the presence of small amounts of graphene.

Finally, the glass transition temperature and hence the crosslinking density of the obtained nanocomposite networks were found to be substantially independent of the nanofiller content (T_g ~ 99 °C).

VII.9 SYNTHESIS AND CHARACTERIZATION OF NANOCOMPOSITES OF THERMOPLASTIC POLYURETHANE WITH BOTH GRAPHENE AND GRAPHENE NANORIBBON FILLERS

In the present work, thermoplastic polyurethanes containing both graphene and graphene nanoribbon fillers were prepared, by polymerizing 1,4-butanediol with two diisocyanates (namely, 1,6-hexane diisocyanate or isophorone diisocyanate), in which graphene was dispersed. Graphene dispersions in BD, HDI and IPDI were characterized by TEM and Raman spectroscopy to confirm the presence of graphene and determine the number of layers. Once graphene dispersions were prepared, the corresponding polyurethanes were synthesized by heating at 70 °C for 1 h in presence of dibutyltindiacetate as catalyst and pyrocatechol as the inhibitor of the latter.

The influence of the graphene content on the thermal and mechanical properties of such compounds were also investigated.

The first goal of the work was to obtain graphene by direct graphite sonication in the self-same monomer to eventually polymerize: as described in the other works concerning graphene, this was achieved without any physical or chemical manipulation and confirmed by experimental evidences.

The first indication of the presence of graphene was provided by the occurrence of the Tyndall effect[45] in all the obtained monomer dispersions, which is a typical light scattering phenomenon confirming the presence of nanometric structures (Figure VII.43).

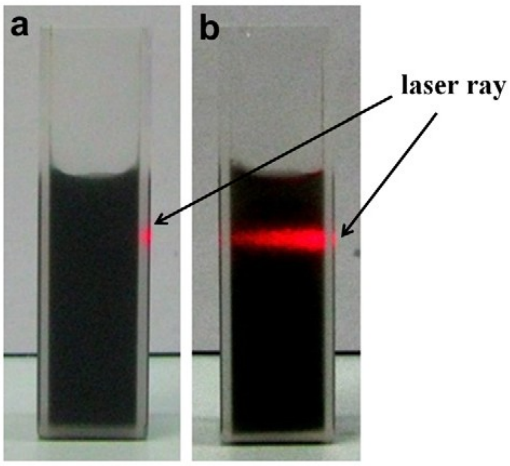

Figure VII.43 Tyndall effect on dispersions of a) graphite and b) graphene in HDI.

The effect of the type of monomer medium on the dispersion of graphene was investigated by adding a constant amount of graphite (5.0 wt.-%) to BD or diisocyanates (HDI or IPDI) and obtaining the graphene concentrations reported in Table VII.14.

Table VII.14 Compositions, regression lines slope and flow behavior of the investigated TPUs.

Sample	Graphene concentration (mg/mL)	Slope	Non-Newtonian behavior of the polymer system
HDI + BD systems			
A1	0	-0.98	Plastic
A2	0.80	-0.96	Plastic
A3	0.40	-0.98	Plastic
A4	0.20	-0.98	Plastic
A5	0.080	-0.99	Plastic
IPDI + BD systems			
B1	0	-0.53	Plastic
B2	1.1	-0.060	Newtonian
B3	0.28	-0.16	Newtonian
B4	0.11	-0.43	Pseudoplastic

In order to find the absorption coefficient α and the graphene concentration in such monomers, gravimetric analysis and UV-Vis spectroscopy measurements were carried out. The obtained data are collected in Table VII.15 and show a Lambert-Beer behavior for all the dispersions investigated. It is noteworthy that a concentration as high as 3.8 mg/mL was achieved when IPDI was used as the dispersing

medium. However, also HDI and BD turned out to be very effective dispersing media (indeed, concentrations of 1.9 and 1.1 mg/mL were obtained in these monomers, respectively). It should be highlighted that these values are among the highest reported so far, independently of the solvent and method used for graphene preparation.[11,13-15,72]

The formation of few-layer graphene sheets within the monomer dispersions was demonstrated by means of Raman spectroscopy. This technique is able to discriminate between graphite and graphene and allows determining the number of graphene layers within an acceptable error range. As shown in Figure VII.44, the Raman signals for the dispersions obtained from HDI and IPDI are very similar to those of BD diol: all the spectra show the three typical graphene peaks at ~1334 cm^{-1} (D peak), ~1561 cm^{-1} (G peak) and ~2700 cm^{-1} (2D peak). In comparison with graphite, for which the diagnostic 2D peak consists of two components and the main peak is upshifted to 2714 cm^{-1}, the corresponding 2D peak of the monomers dispersions exhibit a sharp size and a downshifting, as it is expected in the presence of a few graphene layers. As far as the diisocyanates dispersions are concerned, the 2D signal is located at ca. 2680 cm^{-1}, whereas for BD it is around 2690 cm^{-1} (Figure VII.44). In addition, the 2D peak downshifting is much more evident in the presence of diisocyanates: such behavior indicates that diisocyanates are capable to better disperse graphene with respect to diols.

Besides, as expected, the D/G ratio values of graphene are higher than that of pristine graphite. Furthermore, it is worth mentioning that HDI and IPDI graphene dispersions are characterized by almost the same D/G ratio (ca. 0.2), while it is significantly higher in the BD system, thus indicating that a larger degree of disorder results from the dispersion of graphene in this latter liquid medium.

Table VII.15 Graphene concentrations in the monomer dispersions and the corresponding UV-Vis absorption coefficients and Raman peaks (D, G, and 2D).

Sample	Absorption coefficient α (mL/mg m)	Graphene concentration (mg/mL)	D peak (cm-1)	G peak (cm-1)	2D peak (cm-1)	D/G peak
BD	4165	1.1	1344	1572	2697	0.34
HDI	3211	1.9	1334	1561	2675	0.20
IPDI	8725	3.8	1344	1572	2686	0.19
Graphite	-		1347	1576	2314	0.11

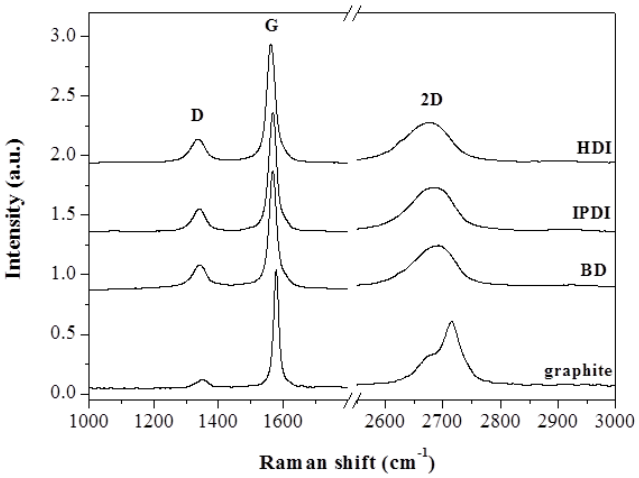

Figure VII.44 Raman spectra of the graphene dispersions in the monomers: the diagnostic 2D peak (~2700 cm^{-1}), which, at variance to what happens for graphite, is symmetrical in graphene, indicates the presence of few-layer graphene.

The morphology of graphene sheets was assessed by TEM. All the dispersions showed the presence of large amounts of graphene sheets, such as those visible in Figure VII.45. Furthermore, in the case of IPDI, and in particular for the HDI/graphene dispersion, the formation of graphene nanoribbons was extensively observed (Figure VII.45b). Differently from what reported in literature, in which very complicated methods for their obtainment are described,[59,61,63,73] the formation of small amounts of graphene nanoribbons as a result of a simple graphite sonication in a polar liquid has been already reported by us[24] and lately by Ling et al. who also used a polymer surfactant.[74]

In the present work, HDI turned out to be a very effective medium, as approximately half of the flakes resulted to be nanoribbons.

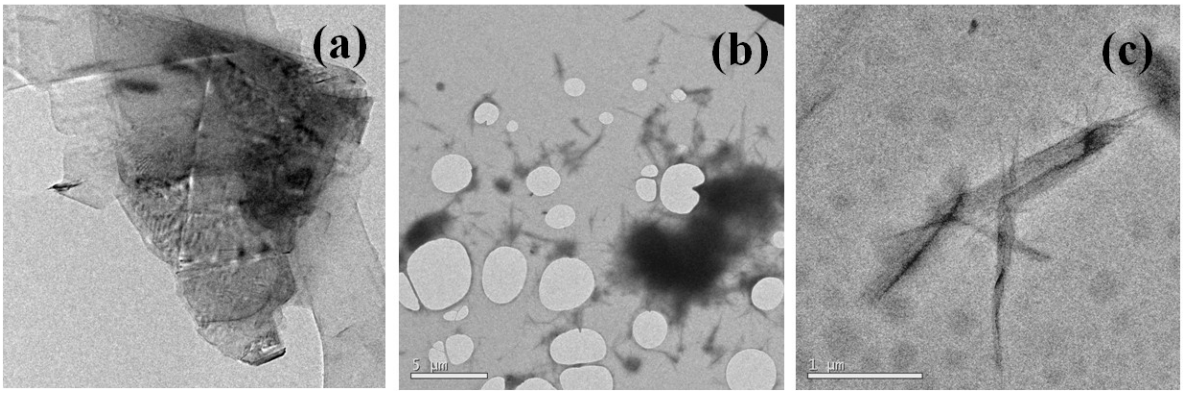

Figure VII.45 TEM images of graphene structures in different dispersions: (a) few layers of graphene in an IPDI/graphene dispersion (diluted 1:100), (b) graphene nanoribbons in an HDI/graphene dispersion (diluted 1:10), and (c) HDI/BD polymer matrix containing graphene (0.80 mg/mL, sample A2).

The graphene diisocyanate (HDI or IPDI) dispersions obtained by sonication were allowed to react with BD in order to get the two polyurethane systems. The adopted synthetic batch allowed achieving an almost full

conversion of the monomers, as clearly indicated by FT-IR spectroscopy (Figure VII.46): indeed, the FT-IR spectra indicate the disappearance of the NCO signal (~ 2270 cm^{-1}) and the formation of the urethane groups (peaks at 3320 and 1720 cm^{-1}). In both cases, the graphene morphologies did not change after polymerization, as shown in Figure VII.46 for the HDI-BD system.

The completeness of the monomer conversion was also assessed through DSC analyses, which were performed also to assess the ability of graphene to modify the thermal properties of the TPUs. As indicated in the experimental, all the DSC traces did not evidence any exothermic peak during the first heating up, thus further confirming the completeness of the polymerization reaction.

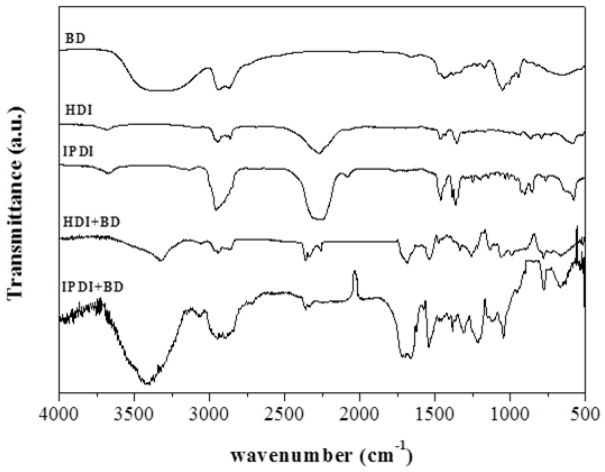

Figure VII.46 FT-IR spectra of BD, HDI and IPDI monomers and of the corresponding polyurethanes (samples A1 and B1).

Figure VII.47 plots the T_g values for the HDI-BD and IPDI-BD polyurethane systems as a function of graphene concentration. It can be observed that the T_g of the IPDI-BD systems tends to increase even in the presence of very low amounts of graphene, reaching a sort of horizontal plateau as graphene concentration increases. This behavior indicates that, for this composite system, the nanofiller has the capability to interact with the matrix, acting as a reinforcing agent. The limit of the reinforcing capability can be probably ascribed to the lubrication effect exerted by graphene nanosheets, as already reported in the literature,[17] which balances the reinforcing effect, so that T_g remains practically unchanged. On the other hand, for the HDI-BD systems, the lubrication/plasticization effect of the nanofiller overcomes its reinforcing feature, so that T_g decreases in the presence of very low amounts of graphene achieving a horizontal plateau (Figure VII.47).

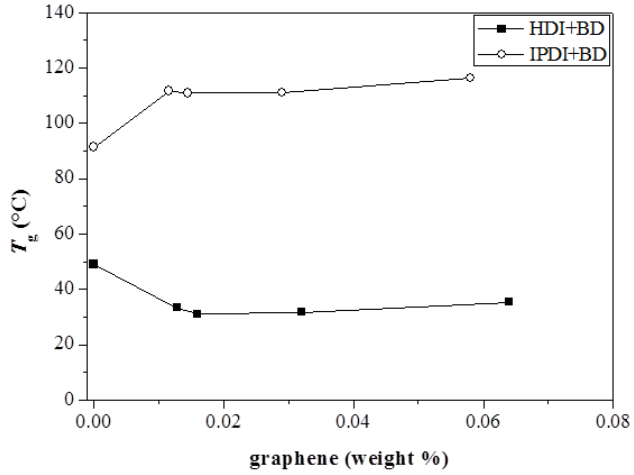

Figure VII.47 T_g values (from DSC analysis) of HDI-BD and IPDI-BD polyurethane systems, as a function of graphene concentration.

In Figure VII.48a, the storage and loss *moduli* are plotted as a function of frequency for the HDI-BD system. In addition, G' is also included for some compositions containing graphene. The unfilled polymer (sample HDI-BD, A1) shows an elastic response, which is generally typical for cross-linked materials (even though the systems under study are thermoplastic), as confirmed by the presence of a horizontal plateau. The addition of graphene does not affect the viscoelastic properties of all tested TPUs: indeed, G' remains constant within the range of frequencies explored and decreases with increasing the nanofiller content. As already observed, this behavior can be ascribed to a lubrication effect induced by graphene sheets:[17] the only difference concerns the lack of a threshold of graphene concentration, which promotes the lubrication effect, at least within the investigated graphene concentration range. Indeed, a very small amount of nanofiller (0.080 mg/mL) is already capable to strongly lower the G' values of the composite.

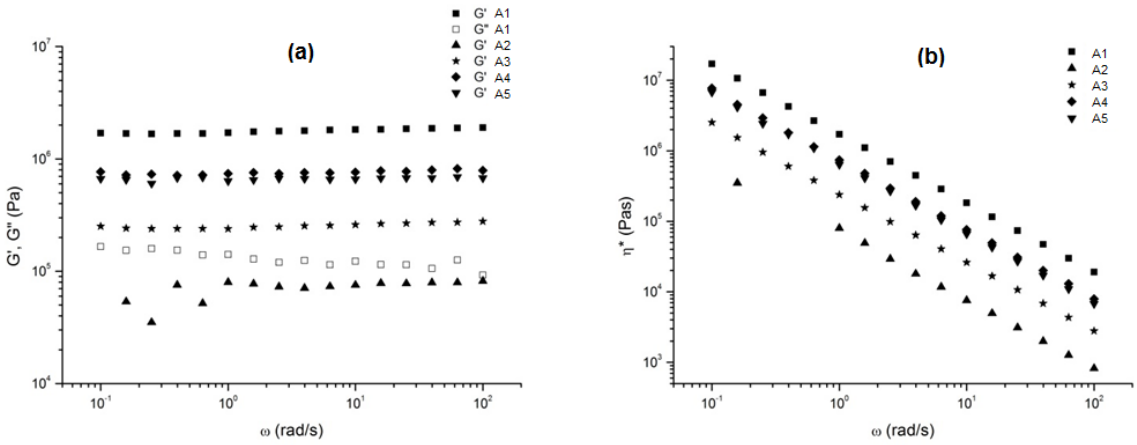

Figure VII.48 Viscoelastic moduli (a) and complex viscosity (b) vs. frequency for some investigated TPU systems (their compositions are listed in Table VII.13).

The complex viscosity curves, plotted in Figure VII.48b, indicate that the viscosity decreases with increasing the graphene content; furthermore, the slope of the regression lines, which were used for interpolating viscosity data and giving an indication of the non-Newtonian behavior of the materials, remains constant for all the compositions investigated (Table VII.13). As already discussed for G', these results further confirm the lubrication effect exerted by graphene and the unchanged viscoelastic behavior of all the nanocomposites with respect to the unfilled counterpart.

Figure VII.49a plots G' and G'' vs. frequency for the IPDI-BD system and for some of its nanocomposites. Unlike the HDI-BD systems previously discussed, the viscoelastic behavior of the unfilled polymer (sample IPDI-BD, B1) is substantially thermoplastic-like and the moduli are frequency-dependent. The presence of graphene induces some changes in the viscoelastic behavior of the nanocomposites: indeed, the crossover point is within the considered frequencies range for TPUs containing small amounts of graphene (0.11 mg/mL), whereas the moduli tend to diverge by increasing the nanofiller content. Furthermore, it can be observed that both G' and the complex viscosity (Figure VII.49b) abruptly fall off in presence of graphene, thus confirming a lubrication effect of the nanofiller for all the concentrations investigated. The viscosity at 0.1 rad/s decreases by more than three orders of magnitude moving from the TPU matrix (106 Pa s) to the composite having the highest graphene content (1.1 mg/mL, 300 Pa s). A significant change in viscoelastic behavior is also evident, since the plastic IPDI-BD system becomes Newtonian at high graphene contents, i.e. η^* becomes independent of the frequency (the parameters of the regression lines are collected in Table VII.14).

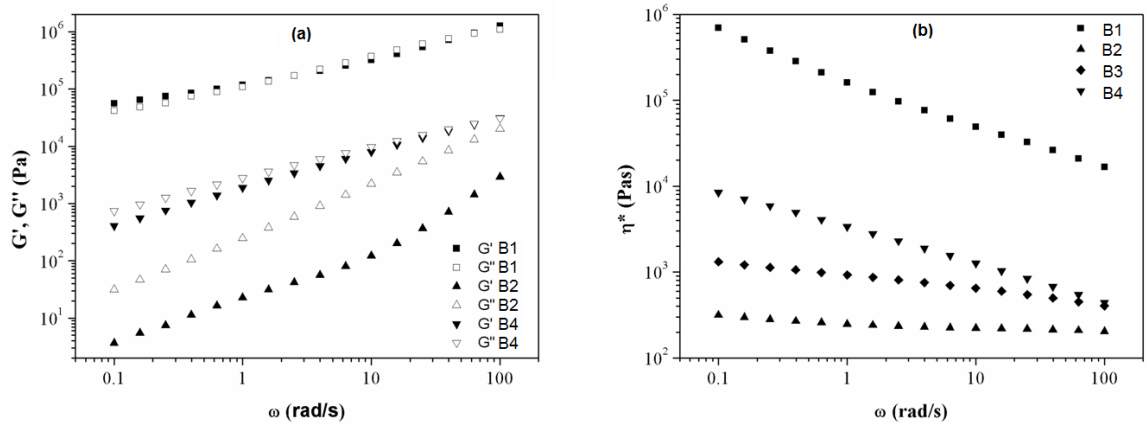

Figure VII.49 Viscoelastic moduli (a) and complex viscosity (b) as a function of frequency for some investigated TPU systems (their compositions are listed in Table VII.13).

In conclusion, graphene and graphene nanoribbon/polyurethane thermoplastic nanocomposites were obtained through the polymerization of 1,4-butanediol with 1,6-hexane diisocyanate or isophorone diisocyanate.

Very high nanofiller concentrations were achieved by directly sonicating graphite in the starting diols and diisocyanates, exploiting the strategy previously proposed for preparing polymer nanocomposites. In particular, it is worth mentioning that, at variance to the most commonly reported methods, which involve the oxidation of graphite to graphite oxide, its dispersion to get graphene oxide and the reduction of this latter, the process here reported does not make use of any chemical manipulation.

Furthermore, it should be highlighted that by the same method, a significant amount of graphene nanoribbons was also obtained in HDI, thus paving the way for their production through a much easier and effective technique than those reported in the literature so far.

The T_g values and the rheological features of the nanocomposites turned out to be strongly affected by the type of polyurethane system and by the concentration of the nanofiller used: indeed, graphene substantially acted as a lubricant for the HDI-BD system, whereas it was found to exert a reinforcing effect in the case of the IPDI-BD matrix.

VII.10 EXFOLIATED GRAPHENE EMBEDDED INTO HIGHLY ORDERED MESOPOROUS TITANIA FILMS WITH ENHANCED PHOTOCATALYTIC ACTIVITY

In the present study, a new protocol for the fabrication of highly ordered mesoporous films made by nanocrystalline TiO_2 doped with exfoliated graphene sheets was proposed. In fact, carbon-based nanostructures, such as nanotubes and graphene sheets, have recently shown to strongly boost the functional properties of hybrid organic-inorganic nanocomposites due to their extraordinary electron mobility. Graphene-titania nanomaterials, for example, appear of paramount interest because of their electrical,[75,76] sensing,[77] photovoltaic,[78,79] and, in particular, photocatalytic properties.[80]

The nanocomposite films were obtained through evaporation–induced self-assembly from a solution containing graphene sheets. In particular graphene was prepared by direct exfoliation of graphite in 1-vinyl-2-pyrrolidone (NVP), following the method reported in the previous works. A calcination treatment in inert atmosphere was done with the aim to remove the templates from the pores and induce crystallization into anatase phase with no-damage of graphene. The films are finally patterned by deep-X-rays lithography to integrate the synthetic pathway with top-down processes.

First of all, graphene dispersions in NVP were subjected to Raman analysis to confirm the presence of graphene itself and to determine the number of graphene layers.[9,21] In Figure VII.50, the Raman spectra of graphene obtained by gravimetric filtration of its dispersion in NVP is reported. As can be seen, the spectra exhibits the three typical signals, namely the D band at 1346 cm^{-1}, the G band at 1579 cm^{-1} and the disorder-related 2D peak at a frequency of ca. 2701 cm^{-1}. The D band is particularly pronounced: this is due

to the increasing of the disorder induced by the sonication process. Moreover, the shape and the position of the 2D band suggest that the sample under examination consists of few-layer graphene, this name referring to graphene flakes made up of five to seven layers. The graphene concentration in NVP was also estimated using the method reported in previous studies[17,23] and was found to be 2.3 mg/mL.

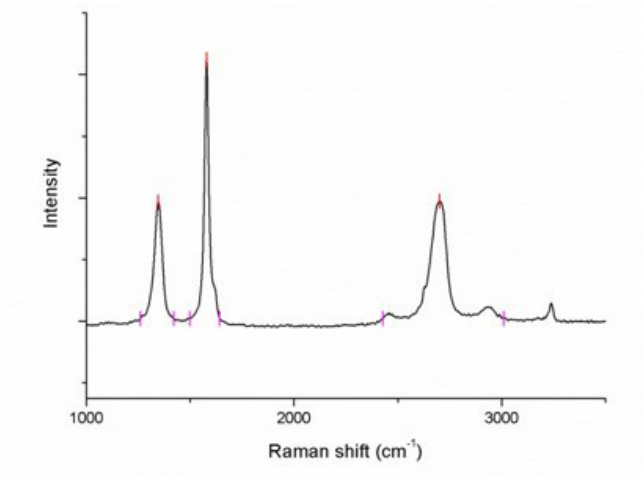

Figure VII.50 Raman spectra of graphene obtained from NVP dispersion.

The high concentrated graphene dispersion in NVP was used as dispersing medium for the preparation of the titania sols. Since the effect of the monomer on the self-assembly kinetics of titania sols has not been yet studied, a systematic investigation about the influence of the graphene solution into the titania sol has been realized to identify the best conditions for the synthesis of highly ordered mesoporous titania-graphene films. The volume of the graphene dispersion in the sol has been changed from 0 up to 10% without observing a significant sedimentation of the graphene sheets within 10 hours.

The influence of graphene colloidal suspensions on the pore organization of the nanocomposites films has been evaluated by Small Angle X-ray scattering (SAXS) in grazing incidence (Figure VII.51). Between 0 and 5% in volume, the titania films show the typical (101) spots due to a body centered cubic structure ($Im\bar{3}m$ space group) with the (110) perpendicular to the substrate. [81] However, within this range we observe an almost linear increase of the $d_{(101)}$-spacing (Figure VII.52) and a decrease in the intensity spot which is caused by the insertion of graphene and polymers into the inorganic organized matrix. Further increase of graphene suspension up to 10 % causes the complete loss of organization with the appearance of a diffuse faint halo in the SAXS pattern.

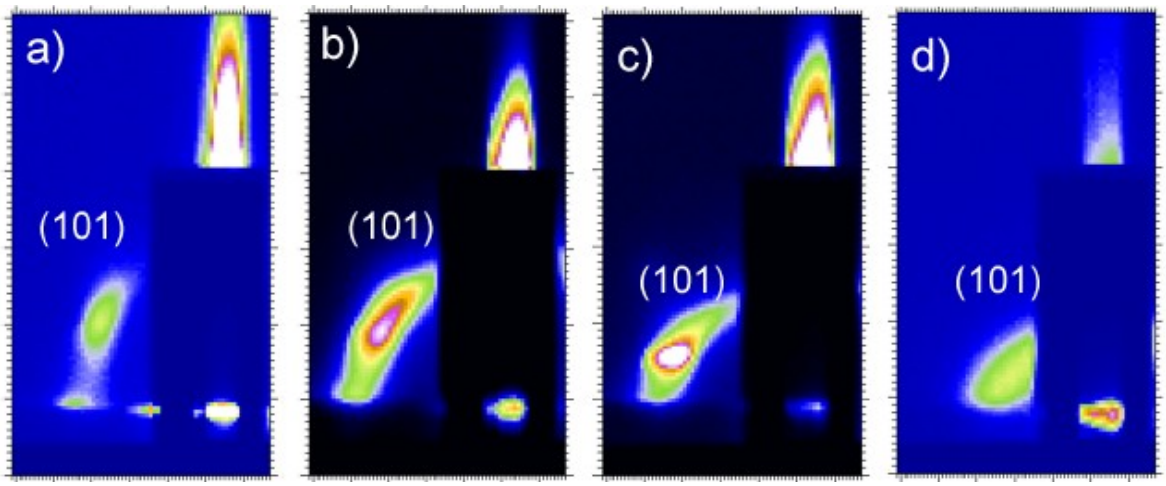

Figure VII.51 Grazing incidence SAXS patterns of graphene-titania mesoporous nanocomposites treated at 150 °C as a function of the graphene-NVP volume fraction: a) no graphene, b) 12.5 µL, c) 25.0 µL, d) 50.0 µL.

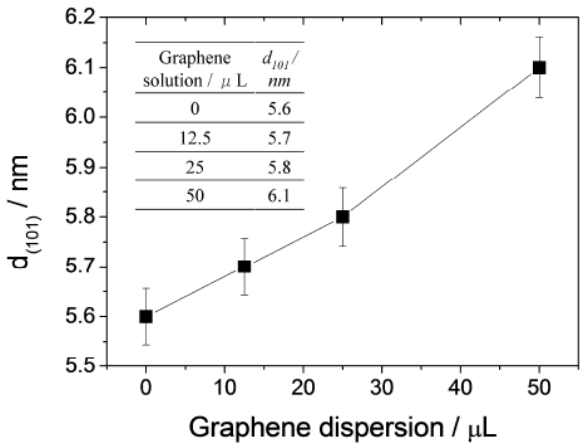

Figure VII.52 Evolution of the d-spacing of the (101) spot in the SAXS patterns of the graphene-titania mesoporous nanocomposites as a function of the graphene-NVP volume fraction. The data are reported as an inset.

The pore organization has been cross-checked by TEM; Figure VII.53 shows some representative pictures of the order observed in the films prepared with a 2.5% of graphene suspension volume fraction. Figure VII.53a and b reveal the simultaneous presence of graphene layers (indicated by arrows) and a highly ordered mesoporous titania structure for both not-calcined and calcined films. The presence of graphene has been homogeneously detected in the fragments and does not seem to affect the organization; Figure VII.51c provides an emphasized scheme of the nanocomposite structure. Although an unambiguous attribution of the pore symmetry cannot be provided only by TEM characterization, the pore organization appears close-packed cubic, in agreement to the space group symmetry identified by SAXS measurements, while the thermal treatment does not affect the pore order even after titania crystallization. This effect of thermal treatment on the mesoporous structure has been investigated in more detail by cross-section TEM;

Figure VII.53d shows the flawless pore organization of the film after thermal treatment while the crystalline structure of the inorganic matrix can be deduced by comparing the bright and dark field images of a film fragment (Figure VII.53e and f).

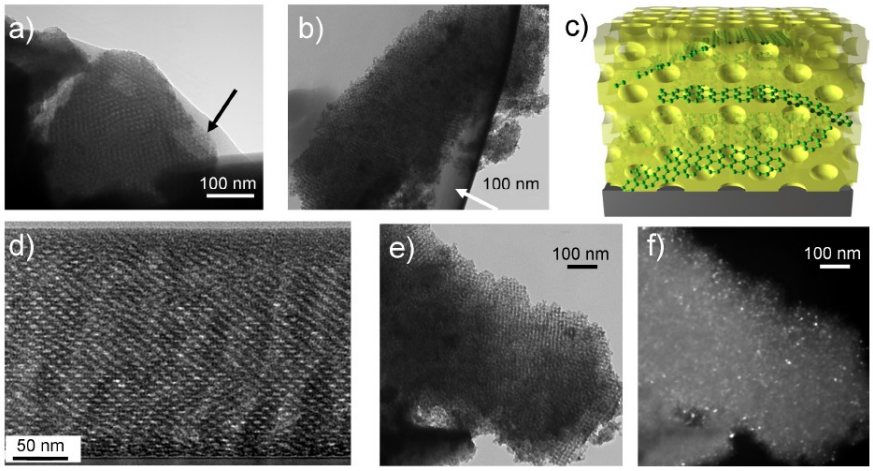

Figure VII.53 TEM images of representative areas taken from mesoporous graphene-titania nanocomposite films. a, b) film fragments before calcination, the arrow indicate the graphene sheets; c) drawing of the nanocomposite morphology; d) cross-section TEM of the films after calcination. The dimension of the elliptical pores has been evaluated as 6.4 ± 1.4 nm for the major axis and 3.8± 0.8 nm for the minor axis.; e, f) bright and dark field images showing the crystallinity of the titania matrix after thermal treatment.

Such level of pore organization in titania crystalline mesostructured films is one of the highest reported in the current literature, to our knowledge; the crystallization of the titania pore walls into anatase phase usually affects, in fact, the periodicity and mesostructure with a loss of order.[82] The enhanced resistance of the pore organization towards the thermal treatment is attributed to a delayed removal of the template scaffold from the porous structure. In an inert atmosphere, in fact, the thermal degradation of block copolymers, which usually occurs below 350 °C,[83] is strongly slowed down because of the oxygen deficiency. This allows preserving the template scaffold even after thermal treatments at temperatures higher than 350 °C, when nucleation and growth of the anatase phase occurs.

Spectroscopic ellipsometry has been used to determine the film thickness before and after firing, the as-deposited films have an average thickness of 340 nm while, after calcination, they shrink up to 150 nm roughly; similar values have been also obtained from pure mesoporous titania films subjected to the same treatment.

The nanocomposite films have been also characterized by a set of analytical techniques to assess the chemical modification in the materials under thermal calcination and to check the presence of graphene layers inside the structure. The infrared absorption spectra of the films before and after firing show that the

thermal treatment strongly increases the polycondensation degree of the titania network and degrades almost completely the block copolymer and NVP (Figure VII.54a and b).

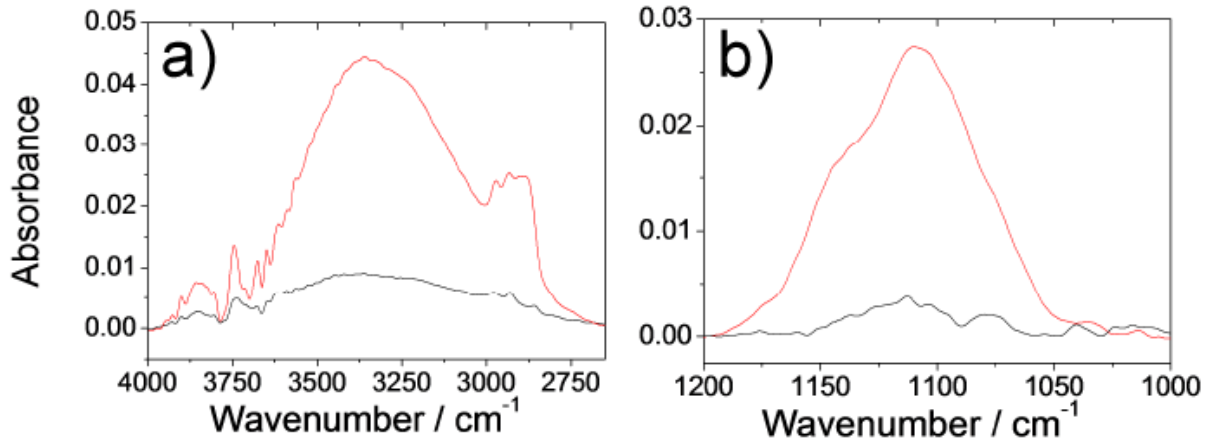

Figure VII. 54 a) FT-IR spectra of the mesoporous graphene-titania nanocomposite films before (red line) and after (black line) thermal treatment.

The film crystallinity has been cross-checked through XRD by comparing the pure and graphene-doped mesoporous titania films (Figure VII.55a). After calcination, the two samples show a crystalline structure with the appearance of the (101) peak of the anatase phase; Rietveld refinement has allowed to estimate the nanocrystals size as 8 nm.

Figure VII.55b shows the Raman spectra of the nanocomposites after thermal treatment in the range of the G' band which peaks around 2700 cm^{-1}.[10] This phonon band, which comes from the inter-valley scattering of two in plane transverse optical phonons, provides unambiguous information about the number of constituent graphene layers. In fact, the number of graphene sheets aggregated in the form of platelets controls the number of Lorentzian curves that are experimentally required to fit the Raman band. The best curve fit of the spectra is obtained using four curves, indicating the presence of bi-layer graphene and similar results have been also obtained for the not-treated film (Figure VII.56). This analysis has been performed with a confocal microscope by systematic sampling the film surface but, however, we do not exclude that the nanocomposite is formed by aggregates of few-layers with different numbers of graphene sheets.[84]

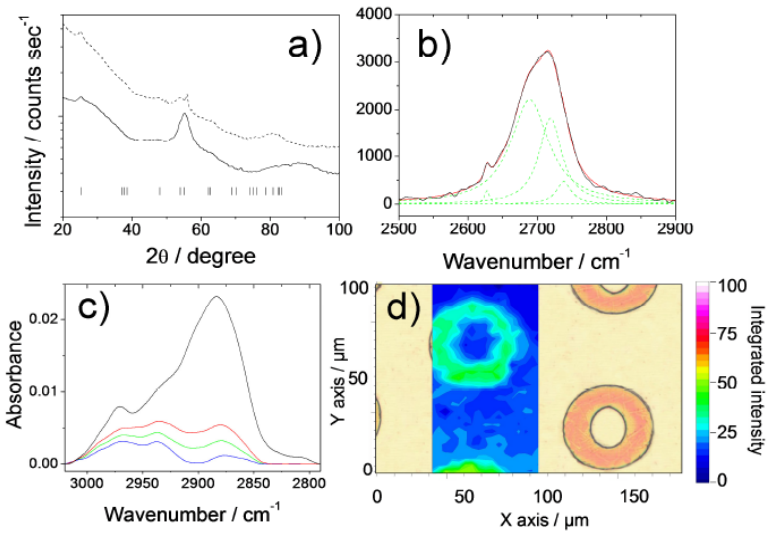

Figure VII.55 a) XRD patterns of pure titania (dotted line) and graphene-titania (full line) film after calcination. b) Raman spectra (full black lines), global fit (full red lines) and single Laurentian fit curves (green dotted lines) of the G' band attributed to bi-layer graphene embedded in the mesoporous crystalline titania before treatment at 450 °C. c) FT-IR spectra of the mesoporous graphene-titania nanocomposite exposed at increasing X-ray doses; as-deposited (black line), 550 (red line), 1100 (green line) and 2200 (blue line) J cm^{-2}. d) Raman mapping obtained from a patterned films exposed to 1000 KJ cm^{-2} and then developed. The chemical images, reported in false color scale, has been obtained by integration of the graphene G' band.

The mesoporous titania-graphene films can be easily processed by lithographic techniques before thermal treatment to produce patterned functional area.[85] Deep X-ray Lithography (DXRL) using a synchrotron source with increasing X-ray doses has been applied to study the chemical changes occurring upon exposure and to pattern the films in form of micrometer arrays. FT-IR (Figure VII.55c) spectra reveal that the lithographic process produces in the matrix chemical changes similar to the thermal treatment, in particular the band attributed to block-copolymers and NVP almost disappears at the highest exposure dose. In contrast, no changes in the Raman bands of graphene have been observed suggesting a higher radiation threshold of this nanostructure. After etching, a "chemical picture" of the pattern has been taken by sampling a sub-millimeter area with a confocal Raman microscopy and integrating the spectra in the G' band range. The results are shown in Figure VII.55d, where the chemical and the optical images can be completely overlapped.

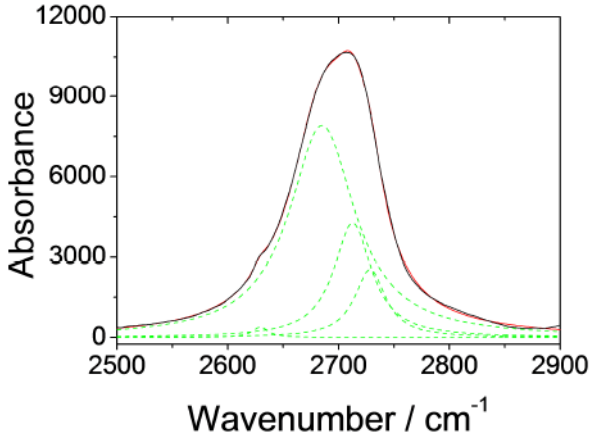

Figure VII.56 Raman spectra (full black lines), global fit (full red lines) and single Laurentian fit curves (green dotted lines) of the G' band attributed to few layers graphene embedded in the matrix contained into the nanocomposites before thermal treatment.

The mesoporous titania-graphene films have been finally tested as functional coatings for self-cleaning surfaces by measuring their photocatalytic activity. In most part of the cases, self-cleaning coatings require easy scalability to cover large substrates, such as panels for glassy facades, and a good optical transparency. Despite the small coloration given by the graphene sheets to the titania sol, the transmittance of the nanocomposite films remains very high even after calcination (inset of Figure VII.57), thanks to the small film thickness. The photocatalytic activity of the samples has been evaluated by monitoring the degradation of stearic acid by FT-IR. The ratio between the integrals of the bands in the 3010-2800 cm^{-1} range before and after UV-Vis-exposure has been used as a benchmark for evaluating the kinetic of photodegradation (Figure VII.57). Contrary to previous findings, a sensitive difference in the photocatalytic activity of pure and graphene-doped titania films has been observed.[81] After 45 minutes, for instance, the nanocomposites degrade the 85% of the initial amount of stearic acid while the pure titania less than 65%. Up to date, only one attempt of producing hierarchical porous titania films containing reduced GO has been reported and no differences in photocatalytic activity between pure and graphene-loaded mesoporous titania has been detected. For this reasons Du and co-authors designed thicker nanocomposite coatings with hierarchical porosity to overcome the problem of the mass transfer that very likely hampered the photodegradation.[86]

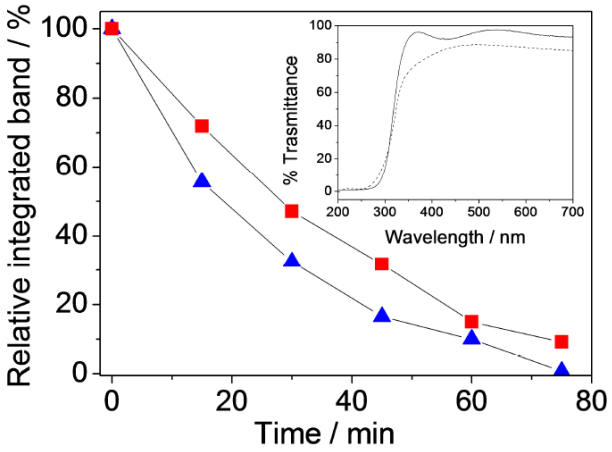

Figure VII.57 Kinetics of photodegration of stearic acid deposited on pure titania (red squares) and graphene-titania (blue triangles) mesoporous nanocomposites. Inset: UV-Vis spectroscopy of graphene-titania mesoporous films before (full line) and after (dotted line) thermal calcination.

Despite the small thickness, the proposed system has shown a remarkable photocatalytic activity and, because of the high degree of pore organization, no larger pores have been necessary to reach a complete photodegradation of the benchmark molecules. The enhanced photocatalytic activity compared to similar systems is due to the specific properties of the exfoliated graphene in combination of anatase titania and the highly degree of organization of the porous matrix in a cubic fashion that offers a higher diffusivity inside the hybrid matrix. It has been observed from electrochemical-permeability measurements and electrochemical-impedance spectroscopy experiments that the diffusivity of a cubic porous is highest in comparison to the other mesostructures.[87,88]

In conclusion, titania mesostructured films with an unprecedented level of organization after crystallization have been used as the matrix for the insertion of exfoliated graphene sheets through a one pot synthesis. Graphene is well dispersed and the mesoporous film does not loose cubic ordered structure. The advantage of a high structural mesopore order in crystalline anatase films combined with the presence of graphene layers is experimentally confirmed by the enhanced photocatalytic properties exhibited by the material with respect to undoped titania films. This system opens a new scenario for developing high performances self-cleaning coatings in that the material is almost optically transparent and is compatible with lithographic techniques that allows developing different types of integrated devices.

REFERENCES

[1] Caria, G.; Alzari, V.; Nuvoli, D.; Monticelli, O.; Mariani, A. J. *Polym. Sci. Part A: Polym. Chem.* 2009, 47, 1422–1428.
[2] Nason, C.; Roper, T.; Hoyle, C.; Pojman, J. A. Macromolecules 2005, 38, 5506–5512.
[3] Fiori, S.; Malucelli, G.; Mariani, A.; Ricco, L.; Casazza, E. *e-Polymers* 2002, 057, 1–10.
[4] Wen, J.; Wilkes, G. L. *Chem. Mater.* 1996, 8, 1667-1681.
[5]Hench, L. L.; West, J. K.; *Chem. Rev.* 1990, 90, 33-72.
[6] Llusar, M.; Monros, G.; Roux, C.; Pozzo J. L.; Sanchez, C. *J. Mater. Chem.* 2003, 13, 2505–2514.
[7] Wang, Y. Q.; Yang, C. M.; Zibrowius, B.; Spliethoff, B.; Linden, M.; Schüth, F. *Chem. Mater.* 2003, 15, 5029–5035.
[8] Lipmaa, E.; Magi, M.; Samson, A.; Engelhardt, G.; Grimmer, A.R. *J Am Chem Soc* 1980, 102, 4889–4893.
[9] Ferrari, A. C.; Meyer, J. C.; Scardaci, V.; Casiraghi, C.; Lazzeri, M.; Mauri, F.; Piscanec, S.; Jiang, D.; Novoselov, K. S.; Roth S.; Geim, A. K. *Phys Rev Lett* 2006, 97, 187401/1–187401/4.
[10] Ferrari, A. C. Solid State Commun 2007, 143, 47–57.
[11] Lotya, M.; King, P. J.; Khan, U.; De, S.; Coleman, J. N. *ACS Nano* 2010, 4, 3155–3162.
[12] Casiraghi, C; Hartschuh, A.; Qian, H.; Piscanec, S.; Georgi, C.; Fasoli, A.; Novoselov, K. S.; Basko, D. M.; Ferrari, A. C. *Nano Lett* 2009, 9, 1433–1441.
[13] Hernandez, Y.; Nicolosi, V.; Lotya, M.; Blighe, F. M.; Sun, Z. Y.; De, S.; McGovern, I. T.; Holland, B.; Byrne, M.; Gun'ko, Y. K.; Boland, J. J.; Niraj, P.; Duesberg, G.; Krishnamurthy, S.; Goodhue, R.; Hutchison, J.; Scardaci, V.; Ferrari, A. C.; Coleman, J. N. *Nat Nanotechnol* 2008, 3,563–568.
[14] Lotya, M.; Hernandez, Y.; King, P. J.; Smith, R. J.; Nicolosi, V.; Karlsson, L. S.; Blighe, F. M.; De, S.; Wang, Z.; McGovern, I. T.; Duesberg, G. S.; Coleman, J. N. *J Am Chem Soc* 2009, 131,3611–3620.
[15] Khan, U.; O'Neill, A.; Lotya, M.; De, S.; Coleman, J. N. Small 2010, 6,864–871.
[16] Lai F.; Li, H. *Eur Phys J E* 2010, 31,269–274.
[17] Alzari, V.; Nuvoli, D.; Scognamillo, S.; Piccinini, M.; Gioffredi, E.; Malucelli, G.; Marceddu, S.; Sechi, M.; Sanna, V.; Mariani, A. *J Mater Chem* 2011, 21, 8727–8733.
[18] Kim, S. J.; Lee C. K.; Kim, S. I. *J Appl Pol Sci* 2004, 92, 1731–1736.
[19] Murdan, S. *J Control Release* 2003, 92, 1–17.
[20] Wang, Z.; Nelson, J. K.; Hillborg, H.; Zhao, S.; Schadler, L. S. Adv Mater 2012, 24, 3134–3137.
[21] Karmakar, S.; Kulkarni, N. V.; Nawale, A. B.; Lalla, N. P.; Mishra, R.; Sathe, V. G.; Bhoraskar, S. V.; Das, A. K. J. *Phys. D: Appl. Phys.* 2009, 42, 115201/1–11501/14.
[22] Sun, Z.; Hasan, T.; Torrisi, F.; Popa, D.; Privitera, G.; Wang, F.; Bonaccorso, F.; Basko, D. M.; Ferrari, A. C. *ACS Nano* 2010, 4, 803–810.
[23] Nuvoli, D.; Valentini, L.; Alzari, V.; Scognamillo, S.; Bittolo Bon, S.; Piccinini, M.; Illescasd, J.; Mariani, A. *J. Mater. Chem.* 2011, 21, 3428–3431.
[24] Kozanoglu, S.; Ozdemir, T.; Usanmaz, A. J. *Macromol. Sci. A Pure Appl. Chem.* 2011, 48, 467–477.
[25] Dong, X. M.; Kimura, T.; Revol, J. F.; Gray, D. G. *Langmuir* 1996, 12, 2076 – 2082.
[26] Klemm, D.; Kramer, F.; Moritz, S.; Lindstrom, T.; Ankerfors, M.; Gray, D.; Dorris, A. *Angew Chem Int Ed* 2011, 50, 5438 – 5466.
[27] Sturcova, A.; Davies, G. R.; Eichhorn, S. J. *Biomacromolecules* 2005, 6, 1055-1061.
[28] Samir, M. A. S. A.; Alloin, F.; Dufresne, A. *Biomacromolecules* 2005, 6, 612-626.
[29] Fortunati, E.; Armentano, I.; Zhou, Q.; Iannoni, A.; Saino, E.; Visai, L.; et al. *Carbohyd Polym* 2012, 87, 1596-1605.
[30] Fortunati, E.; Armentano, I.; Zhou, Q.; Puglia, D.; Terenzi, A.; Berglund, L. A.; Kenny, J. M. *Polymer Degradation and stability* 2012, 97, 2027-2036.
[31] Turbak, A. F.; Snyder, F. W.; Sandberg, K. R; *J. Appl. Polym. Sci. Appl. Polym. Symp.* 1983, 3, 815–827.
[32] Pötschke, P.; Fornes, T. D.; Paul, D. R. *Polymer* 2002, 43, 3247-3255.
[33] Valentino, O.; Sarno, M.; Rainone, N. G.; Nobile, M. R.; Ciambelli, P.; Neitzert, H. C.; Simon, G. P. *Physica E* 2008, 40, 2440–2445.
[34] Lin, J. C.; Nien, M. H.; Yu, F. M. *Composite Structures* 2005, 71, 78–82.
[35] Mitchell, C. A.; Krishnamoorti, R. *J Polym Sci Part B: Polym Phys* 2002, 40, 1434–1443.

[36] Abbasi, S.; Carreau, P. J.; Derdouri, A.; Moan, M. *Rheol Acta* 2009, 48, 943–959.
[37] Mobuchonn C.; Carreaun, P. J.; Heuzeyn M. C. *Rheol Acta* 2007, 46, 1045–1056.
[38] Galgali, G.; Ramesh, C.; Lele, A. *Macromolecules* 2001 34: 852-858.
[39] Rignot, E. L.; Joughin, I.; Aubry, D. Geographical research letters 2005 DOI: 10.1029/2004GL021693.
[40] Wagener, R.; Reisinger T. J. G. *Polymer* 2003, 44, 7513-7518.
[41] Kotsilkova, R. *Dependent Materials* 2002, 6, 283-300.
[42] Zhao, J.; Morgan, A. B.; Harris, J. D. *Polymer* 2005, 46, 8641-8660.
[43] Koo, C. M.; Kim, M. J.; Choi, M. H.; Kim, S. O.; Chung, I. J. *J Appl Polym Sci* 2003, 88, 1526-1535.
[44] Li, D.; Müller, M. B.; Gilje, S.; Kaner, R. B; Wallace, G. G. *Nat Nanotechnol* 2008, 3, 101–105.
[45] Schottner, G. *Chem Mater* 2001, 13, 3422–3435.
[46] Yang, Q.; Pan, X.; Huang, F.; Li, K. *J Phys Chem C* 2010, 114, 3811–3816.
[47] Khan, U.; Porwal, H.; O'Neill, A.; Nawaz, K.; May, P.; Coleman, J. N. *Langmuir* 2011, 27, 9077–9082.
[48] Scognamillo, S.; Alzari, V.; Nuvoli, D.; Mariani, A. *J Polym Sci Part A: Polym Chem* 2010, 48, 4721–4725.
[49] Green, A. A.; Hersam, M. C. *Nano Lett* 2009, 9, 4031–4036.
[50] Nemanich, R. J.; Solin, S. *Phys Rev B* 1979, 20, 392–401.
[51] Hernandez, Y.; Lotya, M.; Shane, D. R.; Bergin, D.; Coleman, J. N. *Langmuir* 2010, 26, 3208–3213.
[52] Suzuki, N.; Ishida, H. *J Appl Polym Sci* 2003, 87, 589–598.
[53] Davis, S. R.; Brough, A. R.; Atkinson, A. *J Non-Cryst Solids* 2003, 315, 197–205.
[54] Yang, Q.; Pan, X.; Huang, F.; Li, K. *J Phys Chem C* 2010, 114, 3811–3816.
[55] Ramanathan, T.; Abdala, A. A.; Stankovich, S.; Dikin, D. A.; Herrera-Alonso, M.; Piner, R. D.; Adamson, D. H.; Schniepp, H. C.; Chen, X.; Ruoff, R. S.; Nguyen, S. T.; Aksay, I. A.; Prud'Homme, R. K.; Brinson, L. C. *Nat Nanotechnol* 2008, 3, 327–331.
[56] Rafiee, M. A.; Rafiee, J.; Wang, Z.; Song, H.; Yu, Z. Z.; Koratkar, N. *ACS Nano* 2009, 3, 3884–3890.
[57] Verdejo, R.; Barroso-Bujans, F.; Rodriguez-Perez, M. A.; De Saja, J. A.; Lopez-Manchado, M. A. *J Mater Chem* 2008, 18, 2221–2226.
[58] Green, A. A.; Hersam, M. C. *Nano Lett*. 2009, 9, 4031-4036.
[59] Li, X.; Wang, X.; Zhang, L.; Lee, S.; Dai, H. *Science* 2008, 319, 1229-1232.
[60] Wu, Z. S.; Ren, W.; Gao, L.; Liu, B.; Zhao, J.; Cheng, H. M. *Nano Res.* 2010, 3, 16-22.
[61] Jiao, L.; Wang, X.; Diankov, G.; Wang, H.; Dai, H. *Nat. Nanotechnol*. 2010, 5, 321-325.
[62] Behabtu, N.; Lomeda, J. R.; Green, M. J.; Higginbotham, A. L.; Sinitskii, A.; Kosynkin, D. V.; Tsentalovich, D.; ParraVasquez, A. N. G.; Schmidt, J.; Kesselman, E.; Cohen, Y.; Talmon, Y.; Tour, J. M.; Pasquali, M. *Nat. Nanotechnol.* 2010, 5, 406-411.
[63] Terrones, M.; Botello-Mèndez, A. R.; Campos-Delgado, J.; Lòpez- Urìas, F.; Vega-Cantù, Y. I.; Rodrìguez-Macìas, F. J. ; Elìas, A. L.; Munoz-Sandoval, E.; Cano-Màrquez, A. G.; Charlier, J. C.; Terrones, H. *Nano Today* 2010, 5, 351-372.
[64] Bowen, R. L. U.S. Patent 3066112, 1962.
[65] Bowen, R. L. *J Am Dent Assoc* 1963, 66, 57–64.
[66] Bowen RL U.S. Patent 3179623, 1965.
[67] Antonucci, J. M.; Stansbury, J. W. In Molecular designed dental polymer. In: Arshady R (ed) Desk reference of functional polymers: synthesis and application. American Chemical Society, Publication, 1997.
[68] Roberson, T. M.; Heyman, H.; Swift, E. J. In Sturdevant's art and science of operative dentistry, 4th edn. Mosby Elsevier, St Louis, 2002.
[69] Chen, M.; Chen, C.; Hsu, S.; Sun, S. H.; Su, W. *Dent Mater* 2005, 22, 138–145.
[70] Ansari, S.; Giannelis, E. P. J Polym Sci Part B Polym Phys 2009, 47, 888–897.
[71] Garboczi, E. J.; Snyder, K. A.; Douglas, J. F.; Thorpe, M. F. Phys Rev E 1995, 52, 819–828.
[72] Behabtu, N.; Lomeda, J. R.; Green, M. J.; Higginbotham, A. L.; Sinitskii, A.; Kosynkin, D. V.; et al. *Nat Nanotechnol* 2010, 5, 406-411.
[73] Valentini, L; Trentini, M.; Mengoni, F.; Alongi, J.; Armentano, I.; Ricco, L.; et al. *Diam Relat Mater* 2007,16,658-663.
[74] Monticelli, O; Mendichi, R.; Bisbano, S.; Mariani, A.; Russo, S. *Macromol Chem Phys* 2000, 201, 2123-2127.

[75] Yang, S.; Feng, X.; Mullen, K. *Adv. Mater.* 2011, 23, 3575-3579.
[76] Cao, H.; Li, B.; Zhang, J.; Lian, F.; Kong, X.; Qu, M. J. *Mater. Chem.* 2012, 22, 9759-9766.
[77] Tang, L. A.; Wang, J.; Lim, T. K.; Bi, X.; Lee, W. C.; Lin, Q.; Chang, Y. T.; Lim, C. T.; Loh, K. P. *Anal. Chem.* 2012, 84, 6693-6700.
[78] Stefik, M.; Yum, J.H.; Hu, Y.; Graetzel, M. *J. Mater. Chem*. A 2013, ASAP DOI: 10.1039/C3TA01635H.
[79] Ng, Y. H.; Lightcap, I. V.; Goodwin, K.; Matsumura, M.; Kamat, P. V. *J. Phys. Chem. Lett*. 2010, 1, 2222-2227.
[80] Liang, Y. T.; Vijayan, B. K.; Gray, K. A.; Hersam, M. C. *Nano Lett.* 2011, 11, 2865-2870.
[81] Crepaldi, E. L.; Soler-Illia, G. J. J. A.; Grosso, D.; Cagnol, F.; Ribot, F.; Sanchez, C. *J. Am. Chem. Soc.* 2003, 125, 9770-9786.
[82] Grosso, D.; Soler-Illia, G. J. J. A.; Crepaldi, E. L.; Cagnol, F.; Sinturel, C.; Bourgeois, A.; Brunet-Bruneau, A.; Amenitsch, H.; Albouy, P. A.; Sanchez, C. *Chem. Mater*, 2003, 15, 4562-5470
[83] Malfatti, L.; Falcaro, P.; Amenitsch, H.; Caramori, S.; Argazzi, R.; Bignozzi, C. A.; Enzo, S.; Maggini, M.; Innocenzi, P. *Micropor. Mesopor. Mater*. 2006, 88, 304-311
[84] Malard, L. M.; Pimenta, M. A.; Dresselhaus, G.; Dresselhaus, M. S. *Phys. Rep*. 2009, 473, 51-87.
[85] Falcaro, P.; Malfatti, L.; Vaccari, L.; Amenitsch, H.; Marmiroli, B.; Grenci, G.; Innocenzi, P. *Adv. Mater.* 2009, 21, 4932-4936.
[86] Du, J.; Lai, X.; Yang, N.; Zhai, J.; Kisailus, D.; Su, F.; Wang, D.; Jiang, L. *ACS Nano* 2010, 5, 590-596.
[87] Etienne, M.; Quach, A.; Grosso, D.; Nicole, L.; Sanchez, C.; Walcarius, A. *Chem. Mater*. 2007, 19, 844-856.
[88] Wei, T. C.; Hillhouse, H. W. *Langmuir* 2007, 23, 5689-5699.

CONCLUSIONS

In this thesis work, different typologies of polymeric materials such as *stimuli* responsive hydrogels, organic-inorganic IPNs, and diacrylic- and polyurethane-based nanocomposites were developed. Specifically, this work has been divided in two main threads: in the first one, electric field-, ionic force-, pH- and thermo-responsive hydrogels were prepared, whose thermal and mechanical properties, as well as the swelling behavior were strongly improved by the introduction of graphene or CNC into the polymer matrix; in the second one, a simple and efficient method for graphene production was developed and used for the obtainment of the corresponding polymer nanocomposites. Moreover, the effect of the nanofillers on the general properties of these materials was also widely investigated.

Most of the stimuli responsive hydrogels were synthesized by using FP as a "green" technique of macromolecular synthesis, which has proved to be extremely advantageous, thanks to its low energy consumption, high yields, short reaction times and simple protocols.
In particular, for the first time FP was successfully exploited for the synthesis of pH- responsive polymer hydrogels of HEA and AAc. It was observed how the copolymerization of HEA, which is usually employed as hydrophilic component in polymer hydrogels, with the AAc afforded to obtain a material exhibiting a pH-responsive behavior at two critical values located at pH ≈ 6 and ≈ 11–13, respectively, depending on the composition. Instead, due to the deprotonation reaction and the subsequent electrostatic repulsion among COO^- groups, from pH 6 to 8, the SR% of the hydrogels starts to increase up to values that are higher for hydrogels containing larger amounts of AAc. Moreover, at pH around 12–13, the SR% of the copolymers reaches the maximum values due to alkoxylate group formation. In addition, all the samples exhibit high front velocities, with the maximum value of 10.8 cm/min recorded for the samples having the χAAc = 0.50, which is one of the highest values reported so far in the FP literature.

Afterwards, FP was used for the preparation of novel polyacrylamide-based hydrogels containing 3-TMeOSi and/or TEtOSi: the obtained materials are both organic-inorganic IPNs and hybrid polymers at the same time. These materials were able to swell in acid conditions thanks to the hydrolysis of the silane groups along the polymer chains. It was found that, when the swelling experiments were carried out at pH 2, the SR% was less than that found at pH 5, which is probably due to a larger conversion of the silane groups when stronger acidic conditions are used. ^{29}Si CP/MAS NMR experiments further confirmed this finding. Moreover, it was found that an increment of Si into the hydrogel structure increases the hydrophilicity of the materials.

FP was also used for the production of PNVCL nanocomposite hydrogels containing graphene or CNC, with the aim to improve their poor mechanical properties, which are typical of such materials. Also in this case, FP has proved to be an advantageous technique because it afforded to synthesize PNVCL in high yields, without the use of solvents and in short times, unlike the traditional ones, which are characterized by lower velocities and higher energy consumption.

Even if the LCSTs of the nanocomposite hydrogels of PNVCL, located at ca. 32-34 °C, are not influenced either by the nature or the amount of the nanofiller, the swelling behavior drastically changes when graphene was replaced with CNC.

The introduction of graphene into the polymer matrix allowed an increment of the SR% of about 50% compared to that of neat PNVCL. This value tends to enhance with the increasing of the nanofiller concentration, thus indicating the strong interference exerted by graphene on the crosslinking occurrence. However, when graphene content reaches a certain value, SR% starts to decrease: this might be related to the reduction of the whole hydrophilic character of the nanocomposite polymer hydrogel, which, in turns, can be attributed to the presence of the relatively large amount of highly hydrophobic graphene sheets.

On the contrary, the replacement of graphene with CNC involves a strong increase of the hydrophobic character of the polymer, leading to its sharp contraction and a decrease of the SR%, already at low concentrations (0.20 wt.-%). In fact, CNC can act as a physical crosslinker, giving rise to more junctions in the hydrogel network and thus increasing the crosslinking density. Similarly to what seen in graphene-containing PNVCL hydrogels, once it has been reached a certain amount of CNC, SR% exhibits a slightly increase, which is probably due to the negative interference of cellulose nanocrystals in the crosslinking process within the polymer matrix.

As concerning the rheological analysis of the obtained nanocomposites, a different effect of graphene and CNC on their mechanical properties was observed. Indeed, graphene exerts a lubricant effect, that is, the value of both G’ and the complex viscosity decreases as its amount increases. Instead, the use of CNC allows an enhancement of G’, G’’ and of the complex viscosity already at low concentrations, thus showing a strong reinforcing effect on the polymer matrix, which increases with the enhancement of CNC amount.

Taking into account the above considerations, it was possible to modulate the swelling behavior and the mechanical properties of PNVCL hydrogel, according to the used nanofiller. In particular, CNC demonstrated its great potential as reinforcing agent in nanocomposite materials. Nanocomposites containing CNC also represent a good example of green chemistry, because the final products are biodegradable, biocompatible and were obtained by using an environmental friendly technique. Moreover, both PNVCL nanocomposite systems are characterized by an LCST value closer to the physiological temperature than that of PNIPAAm, thus indicating that PNVCL could be an advantageous alternative to it, especially in biomedical applications.

Graphene was also used to improve general properties of PAMPSA hydrogels, which have proved to be sensible to ionic force and electric field variations. In particular, the introduction of graphene in the hydrogel matrix increased the SR% of these materials, and also influenced its variation in response to the applied stimuli. In fact, by increasing the ionic strength of the solution in which they are immersed, they deswell. Moreover, the extent of deswelling changed accordingly to the used salt. In addition, the investigated polymer hydrogels exhibited a response to the application of an electrical field. Namely, they contracted in different ways, depending on the graphene content and the applied voltage. The swelling tests suggested that the neat hydrogel behaves as typical dielectric materials do, while those containing graphene are characterized by a completely different behavior.

As reported in the second part of this work, a simple and efficient method for graphene production was developed. This nanofiller was produced by sonication of graphite in different reactive media, such as GPTMS, PhTES, TEGDA, HDPI, IPDI, BD, which can be directly used for the synthesis of polymeric materials, without any solvent removal and purification processes. If compared with the other method reported in literature until now, this method affords to obtain defect free graphene in high concentrations and without any chemical manipulation, and not one of its more or less oxidized derivatives. Raman and TEM analysis have further confirmed the presence of few-layer graphene.

Among the different reactive media used for graphene production, TEGDA has shown to be the best, with a nanofiller concentration of about 9.5 mg/mL.

The corresponding polymer nanocomposites were obtained through the introduction of graphene in the reaction mixture, after dispersion in an appropriate solvent or directly in the monomer.

For all the developed nanocomposite systems, it was observed that graphene exerts a particular influence on the features of the nanocomposites themselves. As concerning the PTEGDA and the Bis-GMA-co-TEGDA systems, it was found that both G' and T_g increase with both the introduction and the enhancement of graphene amount, indicating a strong reinforcing effect exerted by it. This finding is a clear indication of the influence of the nanofiller, which induces the formation of constraints that reduce polymer segment mobility. However, for the sample containing the highest amount of graphene, a decrease of T_g and mechanical properties was recorded. This is probably due to the high concentration of graphene sheets within the polymer, which are responsible for a lubrication effect, thus increasing the mobility of the polymer segments and decreasing T_g.

When graphene was employed for the production of polyurethane-based nanocomposites, their T_g values and the rheological features turned out to be strongly affected by the type of polyurethane system and by the concentration of the nanofiller used: indeed, graphene substantially acted as a lubricant for the HDI-BD system, whereas it was found to exert a reinforcing effect in the case of the IPDI-BD matrix.

Finally, the graphene dispersion in NVP was also successfully employed for the obtainment of highly ordered titania mesostructured films, through the use of an one pot synthesis. It was found that graphene is well dispersed in the matrix and the cubic ordered structure of mesoporous films has remained unchanged. The highly structural mesopore order in crystalline anatase films, together with the introduction of graphene, afforded to an enhancement of the photocatalytic properties exhibited by the material. Thanks to its almost optical transparence and compatibility with lithographic techniques, this system can be used for the development of new high performance self-cleaning coatings.